APPLICATION OF IMPEDANCE TUBE TECHNIQUE IN THE MEASUREMENT OF BURNING SOLID PROPELLANT ADMITTANCES

A THESIS

Presented to

The Faculty of the Division of Graduate

Studies and Research

by

Mohammed Salikuddin

In Partial Fulfillment

of the Requirements for the Degree

Doctor of Philosophy

in the School of Aerospace Engineering

Georgia Institute of Technology

April, 1978

APPLICATION OF IMPEDANCE TUBE TECHNIQUE IN THE

MEASUREMENT OF BURNING SOLID PROPELLANT ADMITTANCES

Approved:

Ben T. Zinn, Chairman

Warren C. Strahle

E. W. Price

Date Approved by Chairman: April 26, 1978

ACKNOWLEDGMENTS

I hereby express my sincere appreciation to Dr. Ben T. Zinn for his suggestion of the dissertation topic, for his sustained guidance and encouragement during this investigation and for his scrutiny of the manuscript. I also thank Dr. Warren C. Strahle and Prof. E. W. Price for their careful examination of the manuscript and for their constructive comments. I also thank Drs. S. V. Shelton and P. Durbetaki for being the members of the reading committee.

The expert assistance of Mr. Brady R. Daniel while conducting the experiments was invaluable and I earnestly thank him for his generous help and cooperation. Also I thank Dr. William A. Bell for writing the program for Analog to Digital Converter and Dr. B. A. Janardan for providing me some of the data from Gaseous Rocket Injector Experiment. I am extremely thankful to my wife Naseem whose cooperation, help and tolerance made my work a success. I also thank all my friends who helped me directly and indirectly toward the completion of my dissertation.

The financial assistance provided by a research assistantship in the Aerospace School of the Georgia Institute of Technology and the Air Force Office of Scientific Research, Aerospace Sciences Directorate, Arlington, Virginia for financing this project are acknowledged.

TABLE OF CONTENTS

TABLE OF CONTENTS (Continued)

LIST OF TABLES

LIST OF TABLES (Continued)

LIST OF ILLUSTRATIONS

LIST OF ILLUSTRATIONS (Continued)

LIST OF ILLUSTRATIONS (Continued)

LIST OF ILLUSTRATIONS (Continued)

LIST OF ILLUSTRATIONS (Continued)

LIST OF ILLUSTRATIONS (Continued)

LIST OF ILLUSTRATIONS (Continued)

GLOSSARY OF SYMBOLS

Symbol	
A_{ij}	coefficients defined in Equations (3-31)
A_+, A_-	complex integration constants
C	heat transfer parameter
$\bar{c}$	velocity of sound, ft/sec.
C_p	specific heat at constant pressure, Btu/lbm. °R
C'_p	specific heat of solid particles, Btu/lbm. °R
C_v	specific heat at constant volume, Btu/lbm. °R
D	diameter of the impedance tube, ft.
F	losses due to viscosity and gas phase damping
F_p	drag force per particle, lbf./particle
f	frequency, Hz.
G	bulk loss coefficient
h	heat transfer coefficient, Btu/sec.ft.^{2} °R
I	unit or identity matrix
i	imaginary unit, $\sqrt{-1}$
k	wave number, $w/\bar{c}$, rad./ft., also coefficient of Thermal Conductivity, Btu/sec.ft. °R
L	length, ft.
M	Mach number
m	mass flow rate per unit cross sectional area, lbm./ft.^{2}
m_p	particle mass, lbm./particle
$\bar{n}$	number of particles per unit volume

GLOSSARY OF SYMBOLS (Continued)

Symbol	
P_r	Prandtl number
p	pressure, lbf./ft.^{2}
Q	volumetric heat source
Q_p	heat transfer per particle
R	specific gas constant, ft.-lbf./slug. °R, also solid propellant response factor
R_0	radius of the impedance tube, ft.
r	burning rate, ft./sec.; also radial distance, ft., also particle radius, ft.
s	entropy, Btu./lbm. °R
T	temperature, °R; also Transmission matrix
$\overline{T}_A$	weighted mean temperature, °R
T_{wo}	wall temperature at x = 0, °R
$\overline{T}_c$	weighted mean temperature at x = 0, °R
t	time, sec.
u	axial velocity, ft./sec.
V_p	particle volume, ft.^{3}
x	axial distance along the impedance tube, ft.
Y	specific admittance
Z	variable used to represent oscillatory quantities (see Equations (3-31))
α, β	parameters defined in Equations (4-2) through (4-10)
α_g	growth rate constant
α_d	decay rate constant

GLOSSARY OF SYMBOLS (Continued)

Symbol

ϕ	phase angle
ρ_s	density of solid propellant, slug/ft.^{3}
γ	ratio of specific heats
λ	wave length, ft.
μ	viscosity coefficient, lbm./ft. sec.
ν	particle loading
Λ	heat transfer parameter
ρ	density, slug/ft.^{3}
ω	angular frequency, rad./sec.; also temperature exponent of viscosity law
τ_d	dynamic relaxation time, sec.
τ_t	thermal relaxation time, sec.

Superscripts

$\bar{(\ )}$	variable describing steady state conditions
$(\ )'$	a perturbation quantity

Subscripts

$(\ )_c$	quantity evaluated at the propellant surface
$(\ )_r$	real part of a complex quantity
$(\ )_i$	imaginary part of a complex quantity
$(\ )_a$	amplitude of a complex quantity
$(\ )_\phi$	phase of a complex quantity
$(\ )_w$	quantity evaluated at the wall
$(\ )_p$	quantity represents particle property

GLOSSARY OF SYMBOLS (Continued)

Subscripts

$( )_I$	incident quantity
$( )_R$	reflected quantity
$( )_T$	transmitted quantity
$( )_e$	experimentally evaluated quantities (see Equations (3-58) and (3-59))

SUMMARY

The primary objective of the research work presented here is the development and the application of the impedance tube technique in the measurement of the admittances of combustion processes such as the one at the surface of a burning solid propellant. While the experimental efforts discussed in this thesis are primarily concerned with the measurement of the admittance at the surface of a burning solid propellant, exposed to oscillatory flow conditions simulating those observed in unstable solid rockets, the developed measurement technique has a much wider range of applications. The impedance tube technique has been chosen for this purpose, because, in principle it can be used for measuring the admittances of a variety of solid propellants including weakly unstable and aluminized propellants. Finally, the impedance tube technique determines the unknown admittances of various propellants under identical oscillatory flow conditions, a situation which is often not duplicated with other test methods. In the impedance tube technique a burning solid propellant is placed at one end of a tube and a sound source at the other end. It can be shown that the structure of a standing wave setup in such a tube by the acoustic driver depends upon the admittance of the burning solid propellant. Hence, by measuring the structure of this standing wave, the unknown admittance of the burning solid propellant can be determined. With this experimental setup, a single tube can be used to determine the propellant admittance over a desired frequency range, since in the impedance tube setup the acoustic

driver and not the burning propellant is primarily responsible for maintaining the tube oscillation.

In this study, a modified impedance tube technique was employed in which several microphones were mounted along the length of the tube instead of traversing a microphone inside the tube, as is done in the classical impedance tube technique. An experimental setup consisting of a circular tube, a propellant sample and its holder, two acoustic drivers, and a pressure regulating exhaust valve was used to obtain the admittance values at low pressures. A high pressure facility designed for operating pressures up to 500 psig. has been developed to simulate actual rocket motor operating conditions. In this experimental setup the driven burner tube with the propellant sample-holder, the pressure transducers, and the acoustic drivers were all contained within the 0 to 500 psig. pressurization tank equipped with high pressure hinged ports to allow easy access for propellant sample changes, burner tube removal, and general maintenance.

In addition to the above mentioned experimental facilities, an analytical procedure and numerical methods had been developed for determining the unknown admittance of a burning solid propellant from the measured acoustic pressure data. Also, analytical studies that were concerned with the dependence of the impedance tube wave structure upon the propellant surface boundary conditions, particulate matter-acoustic wave interaction and the propellant self-noise had been conducted. The development and the results of the above mentioned analytical studies are described in this thesis. Finally, results obtained in impedance

tube experiments conducted at both low and high pressures are discussed. Attached appendix contains descriptions of the mean temperature behavior in the impedance tube.

CHAPTER I

INTRODUCTION

The research work presented in this thesis describes the adaptation of the impedance tube technique in the measurement of admittances under high temperature conditions. The developed measurement technique is primarily concerned with the experimental determination of the admittances of burning solid propellants, which are needed either as inputs for solid rocket stability analysis or as means for evaluating the relative driving capabilities of various solid propellants.[1] While the research described herein is specifically concerned with solid propellant admittances, the developed measurement technique is quite general and it is applicable to other situations involving high temperature admittance measurements. As a matter of fact, the developed measurement technique has recently been used, successfully, in the measurement of the admittances of gaseous rocket injectors.[2] Other examples of such applications include the determination of the impedances of fibrous materials that are used in exhaust silencers.[3,4]

Combustion instability has seriously hindered the development and operation of many solid and liquid propellant rocket motors and air breathing propulsion systems for many years. Combustion instability is the result of the interaction between the combustion process and disturbances within the rocket motor -- an interaction which often leads to the amplification of these disturbances into finite amplitude oscillations. Combustion instability may lead to mechanical failure of engine components, extremely high heat-transfer rates fo the combustor's

walls and interference with the control and guidance system.

Instabilities occurring in solid propellant rocket motors are broadly classified under three categories;[5] namely, (a) high frequency instabilities; (b) intermediate frequency instabilities; and (c) low frequency instabilities. High frequency instability is encountered in the frequency range of 1 to 100 kHz., and it usually involves the excitation of one of the transverse acoustic modes of the chamber. Intermediate frequency instability is observed in the frequency range of 100 to 1000 Hz. This type of instability is generally encountered in large rocket motors. Also, in contrast to the high frequency instability, intermediate frequency instability usually involves the excitation of one of the longitudinal modes of the chamber. Low frequency instability occurs at frequencies in the range of 1 to 100 Hz., usually in large rocket motors.

In recent years, several methods have been developed to suppress high frequency combustion instability. Among them, the addition of powdered metals or oxides to the propellant[5] has been highly successful. However, contrary to expectations, such additives sometimes aggravate the intermediate frequency instability. Hence, the intermediate frequency instability is currently a key factor in the development of solid rockets.

To determine the susceptibility of a given propulsion system to combustion instability, it is necessary to determine the energy balance that exists between the various sources of wave energy gains and losses that are present within the combustor. Wave energy loss mechanisms are convective energy losses caused by the mean flow, energy

dissipation processes associated with viscosity and heat transfer and losses resulting from the interaction of the disturbance with various mechanical components of the engine such as the exhaust nozzle. On the other hand, wave energy gains tend to amplify the engine disturbances and thus exert a destabilizing influence upon the combustor. The primary source of wave energy gain is the unsteady combustion process. If the energy gains outweigh the energy losses, an initial disturbance will amplify and lead to undesirable self-sustained oscillations inside the combustor.

To evaluate the stability of a given solid propellant rocket motor it is necessary to quantitatively determine the characteristics of the various gain and loss mechanisms that are present in the system. The wave energy gain in a solid rocket motor may be determined from either theoretical or experimental investigations of the interaction between a burning solid propellant and an oscillatory gas phase. This interaction can be described by means of the admittance or the response factor of the burning surface which, in turn, can be used to compute the wave energy gain resulting from the above mentioned interaction. Defined as the ratio of the normal velocity perturbation to the pressure perturbation at the burning propellant surface, the propellant admittance also describes the boundary condition that the combustor oscillation must satisfy at the propellant surface in combustion instability analysis.

The non-dimensional form of the admittance of a burning propellant is often expressed in the following form:

$$Y = \frac{\overline{\gamma p}}{\overline{c}} \cdot \frac{u'}{p'} \qquad (1\text{-}1)$$

where the various quantities are defined in the nomenclature. As mentioned earlier, the interaction between the combustion process and the gas phase oscillations can also be described by means of the response factor of the propellant. The latter is defined as the complex ratio of the propellant burning rate perturbation to the pressure perturbation, evaluated at the burning surface. The non-dimensional form of the response factor is given by

$$R = \frac{\bar{p}}{\bar{r}} \cdot \frac{r'}{p'} = \frac{\bar{p}}{\bar{m}} \cdot \frac{m'}{p'} \qquad (1\text{-}2)$$

The relationship between the propellant response factor and its admittance is of interest. Using the definition of the mass flux, $m = \rho u$, the relationship between Y and R can be expressed as follows:

$$R = \frac{Y}{\gamma \bar{M}} + \frac{\rho'/\bar{\rho}}{p'/\bar{p}} \qquad (1\text{-}3)$$

If the oscillation is isentropic, the above relationship reduces to

$$R = \frac{1}{\gamma \bar{M}} [Y + \bar{M}] \qquad (1\text{-}4)$$

Since instability is often caused by small differences between wave energy gains and losses, it is imperative that the contributions from all processes affecting the stability of a rocket motor be known as accurately as possible. Hence, it is of utmost importance that an experimental technique capable of accurate determination of the response of burning solid propellants be available. The development of such an

experimental technique, based upon a modified version of the impedance tube method,[7] is the main objective of this work.

CHAPTER II

BACKGROUND

Because of the complexity of the combustion process, no satisfactory theoretical analysis currently exists for the accurate determination of the admittance of a burning solid propellant. Instead, various experimental techniques are used to determine the admittance of burning propellants. The most widely used method is the T-burner.[8] Although considerable data have been obtained utilizing various T-burner configurations, the accuracy of the results is open to question because of experimental uncertainties. For background information and further reference existing methods for measuring solid propellant admittances are discussed below.

Self-Excited T-Burners

The self-excited T-burner (see Figure 2-1) consists of a cylindrical tube with disc-shaped propellant samples located at both ends.[9] An exhaust vent is located at the center of the tube. The propellant samples are ignited and under certain conditions the interaction between the combustion process and gas phase disturbances results in the development of a pressure oscillation in the tube whose amplitude increases exponentially with time until a certain maximum amplitude is reached. The oscillation decays once the propellant samples are completely burnt out. The experimental procedure consists of measuring the exponential growth rate of the oscillation, and once the combustion is completed,

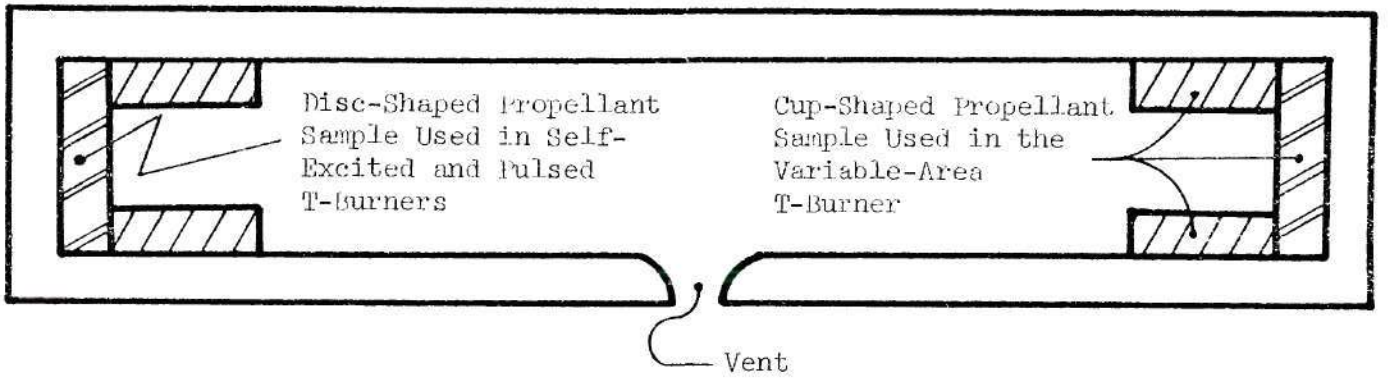

Figure 2-1. T-Burner

measuring the decay rate of the oscillation. The measured growth and decay rates are then used to determine the unknown propellant admittance.

When energy gains in a T-burner are larger than the acoustic losses the interaction of a disturbance with the combustion process would result in disturbance amplification and the corresponding pressure oscillation exhibits the following time dependence:

$$p' \sim e^{\alpha_g t} \tag{2-1}$$

When the burning of the propellant samples is completed, the acoustic losses present in the system will result in the exponential decay of the oscillation which exhibits the following time dependence:

$$p' \sim e^{-\alpha_d t} \tag{2-2}$$

where the positive constant α_d is the system's "decay constant."

In the T-burner experiment, the observed growth rate α_g, presumably represents the difference between the gain provided by the burning propellant and the losses present in the system. For such a situation, the measured growth rate can be related to the real part of the propellant admittance by the following relationship.[9]

$$\alpha_g = \frac{2\bar{c}}{L} (Y_r + \bar{M}) - \alpha_d \tag{2-3}$$

or

$$Y_r = \frac{L}{2\bar{c}} (\alpha_g + \alpha_d) - \bar{M} \tag{2-4}$$

The real part of the response factor can be obtained from the following expression when the oscillation is isentropic:

$$R_r = \frac{\bar{p}}{4\rho_s r C} \cdot \frac{2L}{\bar{C}} (\alpha_g + \alpha_d), \text{ since } \bar{M} = \frac{\rho_s \overline{r c}}{\gamma \bar{p}} \qquad (2\text{-}5)$$

In the determination of the admittance of the burning solid propellant, the critical assumption made is that the causes and magnitude of the loss of the acoustic energy in the T-burner are the same during the growth and decay phases of oscillation. However, since the flow field, temperature and frequency are not the same during the growth and decay periods, this assumption is at best open to question. Another limitation of this technique is that the frequency of the oscillation is determined by the length of the tube, therefore, several T-burners of different lengths are necessary to cover a certain range of frequencies.

Since the admittance of a burning solid propellant is expected to depend on both the frequency and growth rate of the gas oscillation, in comparing the driving capabilities of different solid propellants it is important that their responses be determined under identical conditions. This practice has not been followed to date. Instead, the relative driving capabilities of different propellants have been determined by comparing their responses at the same frequency and completely ignoring the different growth rates of the oscillations for which these responses were measured. An alternate way to resolve this difficulty is to develop an experimental technique in which the responses of different

solid propellants can be measured under the same oscillatory flow conditions. Finally, in reducing the T-burner data, it is customarily assumed that the mean gas temperature in the T-burner is uniform and that the spatial wave structure is isentropic. In fact, the mean gas temperature in the T-burner is not uniform and hence the wave structure is not the same as in the classical acoustic case.

Variable-Area T-Burner

The variable-area T-burner is an alternate approach for determining the admittances of burning solid propellants.[10] Whereas the self-excited T-burner usually employs propellant discs with the same cross-sectional area as the tube, with the variable-area T-burner cup-shaped propellant samples, whose burning surface area may be varied, are used (see Figure 2-1). The desired propellant admittance is obtained by running a series of experiments and varying the area of the burning propellant surface between experiments. The critical assumption with this technique is that the admittance of the burning solid propellant and the system damping remain constant from test to test for all values of the area ratio S_b/S_c where S_b is the area of the burning surface and S_c is the cross-sectional area of the tube. If this assumption is valid, then one can write[10]

$$\alpha_g + \alpha_d = \frac{2\bar{c}}{L} (Y_r + \bar{M}) \cdot \frac{S_b}{S_c} \qquad (2\text{-}6)$$

Using Equation (2-6), a plot of measured growth rate constants α_g versus S_b/S_c should yield a straight line. Extrapolation of this line

to $S_b/S_c = 0$ should give the value of α_d. The slope of this line is $(Y_r + \overline{M})$ and this value can be used to determine the desired solid propellant admittance. However, data have been obtained which indicate that a plot of α_g versus S_b/S_c does not produce a straight line. In addition, data scatter limits the accurate determination of α_g and the slope of the line from which the admittance is determined. Also, a number of experiments is required to produce a single point on the propellant admittance versus frequency curve.

To date, the variable-area method has been used to determine the admittances of aluminized and weakly unstable propellants. This method requires the use of large burning surface area to derive sufficient energy from the combustion process to overcome the wave energy losses in the T-burner so that pressure oscillations can be excited. This necessitates the use of the cup-shaped grains which extend over different lengths of the tube. However, the characteristics of the combustion and damping process vary along the length of the tube, and the use of cup-shaped samples also introduce two dimensional effects. These phenomena are not accounted-for in the derivation of Equation (2-6) and their omission causes inaccuracies and uncertainties in data interpretation.

Pulsed T-Burner

In addition to the variable-area T-burner, the pulsed T-burner[8,11,12] is also used to determine the admittances and system losses for aluminized propellants. With this method it is not necessary for the combustion process to generate and sustain oscillations in the

burner. Instead, a charge is fired into the T-burner during and immediately after completion of the propellant combustion. The difference in the decay rates of the resulting pressure oscillations is used to determine the admittance of the burning propellant surface. The principal disadvantages of this technique are the introduction of foreign particles by the charge into the burner, the inability to control the frequency of the oscillations, the uncertainty whether the system damping is the same after the firing of both the first and second charges and the marginal difference between the observed decay rates of both pulses that leads to considerable scatter in the measured admittance data. Because of these difficulties, the accuracy of the admittance results obtained from pulsed T-burners is limited.

Forced Oscillation Methods

Because of the limitations of the various T-burner techniques, investigators[13,14,15] have resorted to the use of forced oscillation experiments to measure the admittances of burning solid propellants. In a recent study[13] the experimental set-up (see Figure 2-2) consisted of a short tube whose walls were lined with a solid propellant. An exhaust nozzle at the end of the tube controlled the combustor pressure and a rotating valve produced periodic blocking and opening of a small orifice which, in turn, produced a small amplitude pressure oscillation of desired frequency in the chamber. Assuming that the combustor length is short compared with the acoustic wave length, the oscillating pressure is taken to be spatially uniform in the chamber. Under these conditions the admittance of the burning propellant can be determined from

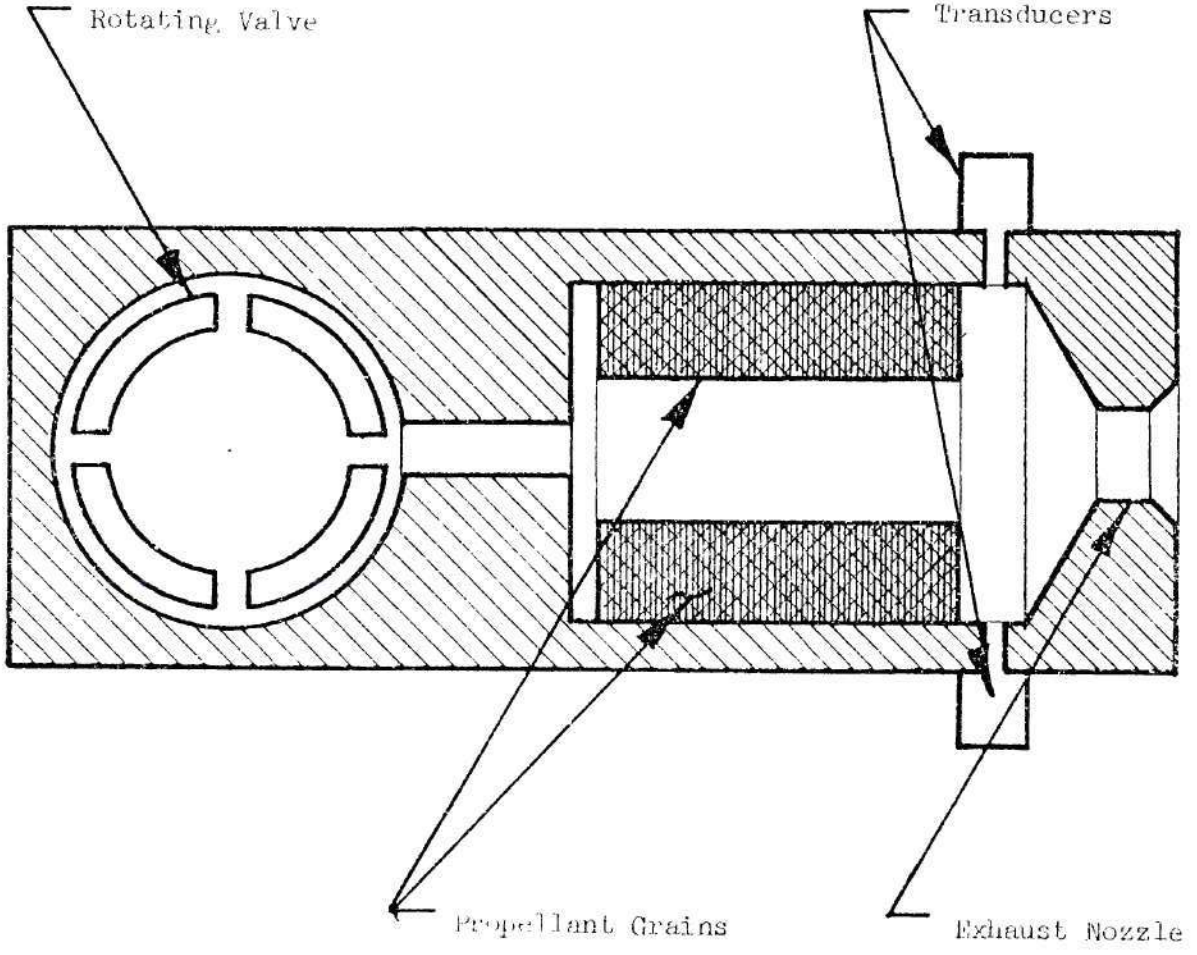

Figure 2-2. Forced Oscillation Method

measurement of the amplitude ratio and phase difference between the area oscillation at the rotating valve and the pressure oscillation in the chamber.

The principal disadvantage of the above mentioned experiment is that due to the short motor assumption employed in the development of its theory this experimental set-up can only be used for admittance measurements at low frequencies. This set-up is basically a driven L*-burner. Other disadvantages are that particle damping associated with aluminized propellants can not be determined and in its present configuration both velocity and pressure oscillations affect the measured combustion response function and it is impossible with this method to evaluate the contribution of each one of these effects.

Forced oscillation experiments have also been conducted by investigators in France[14] and investigators at the Applied Physics Labs in the U.S.[15] In the French study, oscillations were generated in a cylindrical rocket motor having a tubular propellant by periodically and partially blocking the exhaust nozzle throat area. However, the propellant admittance values could not be deduced from the measured data, since this study was in its developing stage.

In a more recent paper[16] the improvements made in the French efforts at ONERA to measure solid propellant admittances using forced oscillation methods are discussed. The response of solid propellants to pressure oscillations is determined at ONERA by the technique of modulated exhaust. This technique consists in producing forced homogeneous pressure oscillations in the combustor of a small motor, by a modulation

of the nozzle throat by means of a toothed wheel. The measurement of the transfer function between the pressure oscillation and the throat modulation permits the calculation of the response of the solid propellant. The data obtained by this method were compared with those obtained by T-burner at SNPE. In some cases marked discrepancies were observed between the results obtained by two methods, and better agreements were found in some other cases.

A dynamic acoustic oscillator technique discussed in Reference 15 was developed for measuring the response of burning solid propellant surface. The experimental arrangement essentially consisted of a centrally vented cavity with propellant at one end and a phase-locked mechanical driver, which excited the cavity in a resonant mode, at the other end. An independent method for measuring the decay constant of the cavity incorporated into this system involved momentarily shorting out the drive system and observing the free decay or growth of the oscillations. Although the apparatus was designed primarily for investigation of stable or marginally stable propellant systems, it could also be used with unstable propellant systems by introducing a 180° phase shift in the drive circuit whenever the amplitude exceeds a predetermined value. It was shown in this study that the acoustic oscillator technique could be accurately used to measure the response of a cavity containing a burning propellant as a function of time, provided an accurate information on the cavity damping in the absence of the propellant was available. Since accurate cavity damping in the absence of the propellant was not easily obtainable, this study did not come out successful.

When properly planned and executed, the forced oscillation experiment can potentially offer many advantages; these include the possibility of accounting for the influence of aluminum particles in both the combustion zone and the gaseous phase; the possibility of carefully controlling the frequency and growth rate of the oscillation; and the same set-up may be used to study the response of a given solid propellant over a whole frequency range and fewer tests are needed than with any of the T-burner type experiments.

The Impedance Tube

To overcome the limitations of T-burners and previously developed forced oscillation experiments, the development of a driven burner, based on the classical impedance tube-technique,[17] has been undertaken in this study. In the classical impedance tube-technique the experimental arrangement (see Figure 2-3) consists of a tube with an acoustic driver at one end and the sample whose admittance is to be measured at the other end. During an experiment, the driver generates an incident wave of a desired frequency that propagates along the tube until it impinges upon tested sample. The interaction between the incident wave and the test sample results in a reflected wave with modified amplitude and phase. The reflected wave then combines with the incident wave to form a standing wave pattern in the tube whose structure depends, among other parameters, upon the admittance of the tested sample.[6,7] The structure of the standing wave is obtained by traversing a microphone probe along the tube. The unknown admittance is then computed using the expression for the standing wave which relates the wave structure

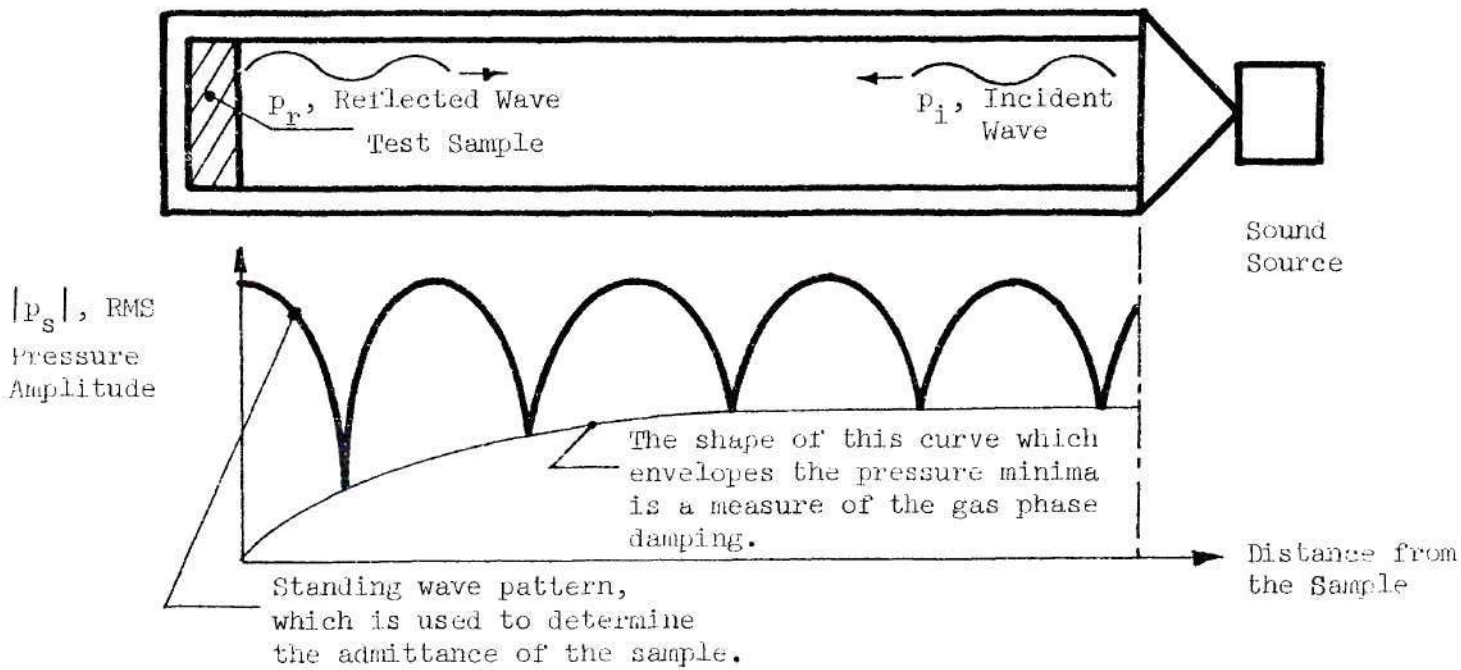

Figure 2-3. An Impedance Tube and a Typical Standing Wave Pattern

to the admittance. The tube wave behavior is described by the Helmholtz equation

$$\frac{d^2p'}{dx^2} + k^2p' = 0 \qquad (2\text{-}7)$$

The solution of Equation (2-7) can be expressed in the following form:

$$p' = A_+e^{-ikx} + A_-e^{ikx} \qquad (2\text{-}8)$$

and by using the momentum equation it can be shown that

$$\bar{\rho}\,\bar{c}\,u' = A_+e^{-ikx} - A_-e^{ikx} \qquad (2\text{-}9)$$

Using the above expressions for p' and u' the nondimensional admittance Y at x = 0 can be obtained.

The Modified Impedance Tube

The classical impedance tube method is restricted to tests with isentropic, one-dimensional oscillation and without any mean flow. This technique was recently modified to determine the response of choked rocket nozzles[18] and acoustic liners[19] under cold flow conditions. In this study, this technique is further modified in order to be used in determining the admittances of burning solid propellants.[20] In the modified experimental set-up (see Figure 2-4) the test sample is replaced by a burning solid propellant sample and a nozzle is provided at the other end for exhausting the combustion products.

During an experiment, the acoustic drivers are switched on and then the propellant sample is ignited. The drivers generate an incident

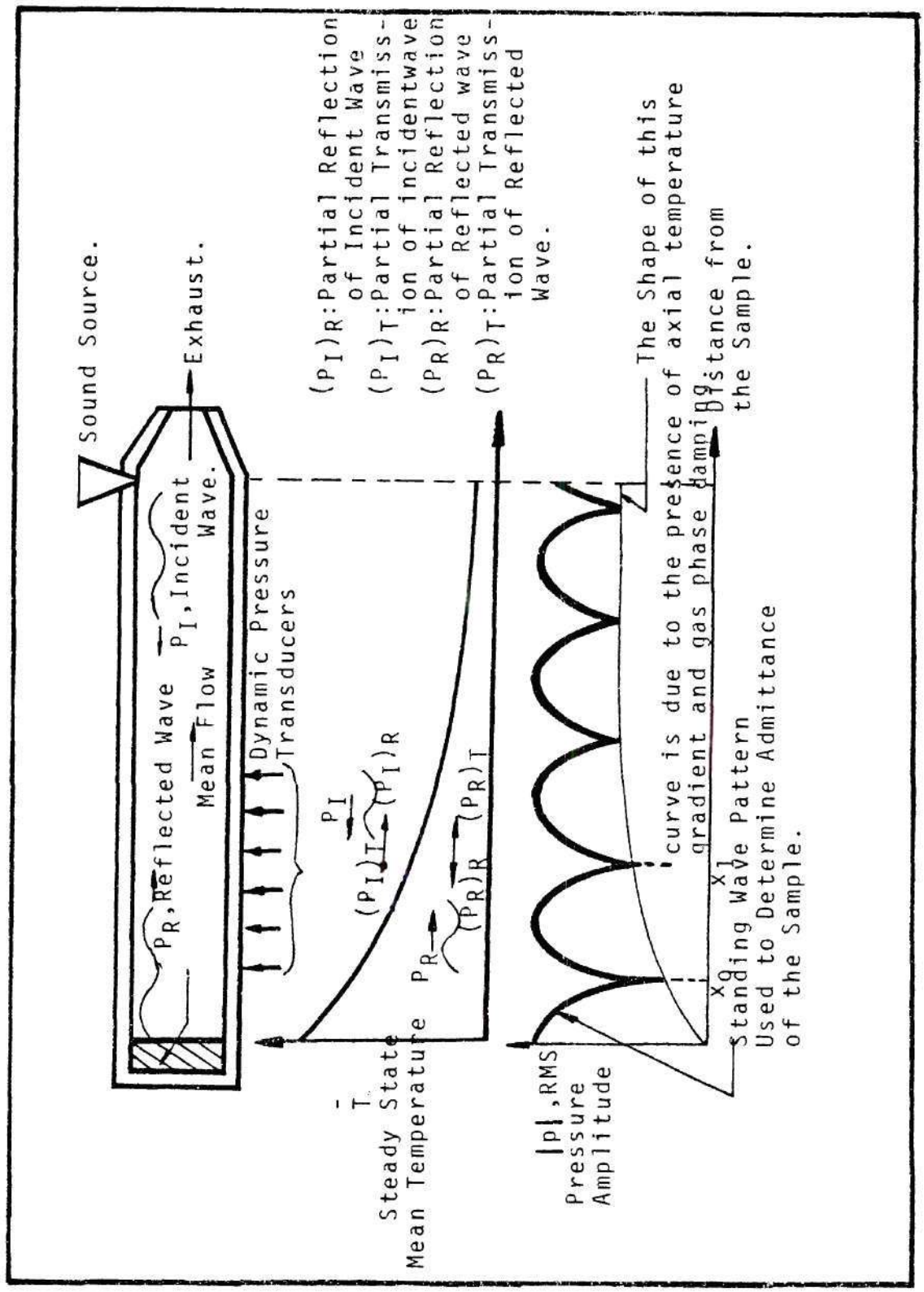

Figure 2-4. An Impedance Tube, a Typical Axial Steady State Temperature Distribution and a Typical Standing Wave Pattern.

wave, P_I of a given frequency f that propagates along the tube. The presence of an axial temperature gradient in the tube results in continuous reflection of the incident and reflected waves as they propagate along the tube. The interaction of the incident wave with the burning solid propellant surface results in a reflected wave with a modified amplitude and phase. The two systems of incident and reflected waves interact to form a standing wave pattern in the tube whose structure depends, among other parameters, upon the surface admittance of the burning propellant sample and the axial mean temperature distribution in the impedance tube.

Since due to hardware limitations the duration of each test run is very short, it is not possible to traverse a microphone in the impedance tube to measure the standing wave structure. Instead, the structure of the impedance tube standing wave is measured using several dynamic pressure transducers that are located at several pre-selected locations along the walls of the impedance tube. The measured acoustic pressure data are then used to determine the wave structure in the impedance tube and the admittance of the burning solid propellant.

In a T-burner the admittance of a propellant is determined from the observed growth and decay rates which are observable only if the propellant can drive the T-burner, whereas in an impedance tube the admittance of a propellant is determined from the structure of the standing pressure wave set-up by the acoustic driver. Therefore, the modified impedance tube should in principle be capable of determining the admittances of the damping or weakly driving propellants whose

admittances can not be determined in conventional T-burners. The admittance of a burning solid propellant is expected to depend on both the frequency and the growth rate of the gas oscillation. Therefore in comparing the driving capabilities of different solid propellants it is essential that their admittances be determined under identical conditions. In a T-burner, the relative driving capabilities of different propellants are determined by comparing their admittances at the same frequency and ignoring the different growth rates of the oscillations for which these admittances were measured. In the impedance tube set-up zero growth rate of pressure amplitude is maintained by keeping the same oscillatory flow conditions during the test. This enables the impedance tube technique to determine the driving capabilities of different propellants under the identical conditions of zero growth rate and at a fixed frequency. In the T-burner the frequency of oscillation is determined by the length of the tube, thus requiring several T-burners of different lengths to cover a certain frequency range. In contrast, in the impedance tube set-up the acoustic driver not the burning propellant is primarily responsible for maintaining the oscillation in the tube, a single tube can be used to determine the propellant admittance over a desired frequency range.

CHAPTER III

REDUCTION OF EXPERIMENTAL DATA

The modified impedance tube experimental set-up for the measurement of admittances under high temperature conditions has been discussed in the last chapter. In this chapter the analytical procedure and numerical methods that have been developed, in the course of this investigation, to determine the unknown admittance at a surface under high temperature conditions in general and of burning solid propellant samples in the impedance tube, in particular, utilizing the measured acoustic pressure data, are discussed. Specifically, the analytical procedure and numerical methods developed to utilize a discrete number of acoustic pressure measurements in the determination of the structure of the standing wave and the unknown admittance at one end of the impedance tube, accounting for the presence of an axial steady temperature gradient along the tube and gas phase losses, will be discussed.

The behavior of the standing wave in the impedance tube is considered with the following assumptions: (1) the combustion process is concentrated at the propellant surface; (2) the gas in the impedance tube is perfect and it consists of a single species; (3) the fluctuating part of the heat transfer to the wall is negligible; (4) both the steady and unsteady flows are one dimensional; (5) the ratios of the various perturbation quantities to the corresponding steady state quantities are sufficiently small so that all non-linear terms involving products of

these quantities may be neglected in the conservation equations; and (6) the acoustic losses in the flow field due to viscous dissipation and gas phase attenuation (i.e., due to presence of particles) can be accounted for in the conservation equations by introducing an overall bulk loss coefficient, which is proportional to the oscillatory velocity. Under these assumptions, the flow in the impedance tube can be described by the following system of conservation equations.[20]

Continuity:
$$\frac{\partial \rho}{\partial t} + \frac{\partial}{\partial x} (\rho u) = 0 \tag{3-1}$$

Momentum:
$$\frac{\partial}{\partial t} (\rho u) + \frac{\partial}{\partial x} (\rho u^2) = - \frac{\partial p}{\partial x} - F \tag{3-2}$$

Energy:
$$\rho T \left(\frac{\partial s}{\partial t} + u \frac{\partial s}{\partial x}\right) = C_V \frac{Q}{R} \tag{3-3}$$

State:
$$p = \rho R T \tag{3-4}$$

where:

$-F$ = Losses due to viscosity and gas phase damping and

Q = Heat transfer to the wall per unit volume.

The first law of thermodynamics:

$$ds = C_p \frac{dT}{T} - R \frac{dp}{p} \tag{3-5}$$

The remaining variables appearing in the above equations are defined in the nomenclature. Using the equations of continuity and state the momentum and energy equations can be reduced to the following forms respectively:

$$\frac{\partial u}{\partial t} + u \frac{\partial u}{\partial x} = - \frac{1}{\rho} \frac{\partial p}{\partial x} - F \tag{3-6}$$

$$\frac{\partial s}{\partial t} + u \frac{\partial s}{\partial x} = C_v \frac{Q}{p} \tag{3-7}$$

To investigate the wave behavior in the tube the dependent variables are expressed in the following form:

$$\begin{aligned} u &= \bar{u}(x) + u'(x,t) \\ p &= \bar{p}(x) + p'(x,t) \\ \rho &= \bar{\rho}(x) + \rho'(x,t) \\ T &= \bar{T}(x) + T'(x,t) \\ s &= \bar{s}(x) + s'(x,t) \\ F &= \bar{F}(x) + F'(x,t) \\ Q &= \bar{Q}(x) + Q'(x,t) \end{aligned} \tag{3-8}$$

where the barred quantities describe steady state variables and the primed quantities describe the perturbations. Substituting the expressions given in Equation (3-8) into Equations (3-1), (3-4), (3-5), (3-6) and (3-7), linearizing the resulting equations and separating them into steady and unsteady equations, yield the following set of steady state equations:

Continuity:
$$\frac{d}{dx} (\bar{\rho}\, \bar{u}) = 0 \tag{3-9}$$

Momentum:
$$\bar{u} \frac{d\bar{u}}{dx} = - \frac{1}{\bar{\rho}} \frac{d\bar{p}}{dx} - \bar{F} \tag{3-10}$$

Energy: $$\bar{u}\,\frac{d\bar{s}}{dx} = C_v\,\frac{\bar{Q}}{\bar{p}} \tag{3-11}$$

State: $$\bar{p} = \bar{\rho}R\bar{T} \tag{3-12}$$

$$d\bar{s} = C_p\,\frac{d\bar{T}}{\bar{T}} - R\,\frac{d\bar{p}}{\bar{p}}$$

$$= C_v\,\frac{d\bar{p}}{\bar{p}} - C_p\,\frac{d\bar{\rho}}{\bar{\rho}} \tag{3-13}$$

and the following system of unsteady equations.

Continuity: $$\frac{\partial\rho'}{\partial t} + \frac{\partial}{\partial x}\,(\bar{\rho}u' + \bar{u}\rho') = 0 \tag{3-14}$$

Momentum: $$\left\{\frac{\partial u'}{\partial t} + \bar{u}\,\frac{\partial u'}{\partial x} + u'\,\frac{d\bar{u}}{dx}\right\}\bar{\rho} + \bar{u}\,\frac{d\bar{u}}{dx}\,\rho' = \frac{\partial p'}{\partial x} - F' \tag{3-15}$$

Energy: $$\bar{p}\,\left(\frac{\partial s'}{\partial t} + u'\,\frac{d\bar{s}}{dx} + \bar{u}\,\frac{\partial s'}{\partial x}\right) + p'\bar{u}\,\frac{d\bar{s}}{dx} = C_v Q' \tag{3-16}$$

State: $$p' = R(\bar{\rho}T' + \bar{T}\rho') \tag{3-17}$$

$$s' = C_p\left\{\frac{p'}{\gamma\bar{p}} - \frac{\rho'}{\bar{\rho}}\right\} \tag{3-18}$$

While this study is primarily concerned with the solution of the wave equations, the latter require the solutions of the corresponding steady state equations, which are considered next. The steady state continuity equation can also be expressed in the following form:

$$\bar{\rho}\,\bar{u} = \bar{r}\,\rho_s \tag{3-19}$$

where $\bar{r}$ and ρ_s are the steady state burning rate and the density of the solid propellant, respectively. Using Equations (3-9) through (3-13) and Equation (3-19) and neglecting viscous and gas phase losses, as represented by $\bar{F}$ in Equation (3-10), the following system of ordinary differential equations is obtained:

$$\frac{d\bar{p}}{dx} = \frac{(\bar{r}\,\rho_s)^2 R\,\bar{p}}{(\bar{r}\,\rho_s)^2 R\,\bar{T} - \bar{p}^2}\,\frac{d\bar{T}}{dx} \tag{3-20}$$

$$\frac{d\bar{\rho}}{dx} = \frac{1}{R\bar{T}}\left\{\frac{d\bar{p}}{dx} - \frac{\bar{p}}{\bar{T}}\,\frac{d\bar{T}}{dx}\right\} \tag{3-21}$$

$$\frac{d\bar{u}}{dx} = -\frac{\bar{r}\rho_s}{\bar{\rho}^2}\,\frac{d\bar{\rho}}{dx}$$

$$= -\frac{\bar{r}\rho_s R\,\bar{T}}{\bar{p}}\left\{\frac{d\bar{p}}{dx} - \frac{\bar{p}}{\bar{T}}\,\frac{d\bar{T}}{dx}\right\} \tag{3-22}$$

Equation (3-20) can be solved once the mean temperature distribution $\bar{T}(x)$, the mean pressure $\bar{p}(x)$ at any one x location, the mean burning rate of the propellant $\bar{r}$, the thermodynamic properties of the gaseous products and the propellant density ρ_s are known. Equations (3-21) and (3-22) can then be solved using the solution of Equation (3-20).

Temperature measurements along the impedance tube could, in principle, be used to provide the needed axial steady temperature distribution. However, measured temperature data (i.e., see Figure A-6 in Appendix A) indicate the presence of a radial temperature gradient along the length of the tube. Therefore, the question comes up regarding the

"best" radial location to be used for the measurement of a bulk axial temperature distribution that is consistent with the one dimensional flow model. Since it is difficult to locate such a radial position in the impedance tube, a different approach for the determination of the average or bulk axial temperature distribution has been developed and it is discussed below.

Using energy conservation considerations, it is shown in Appendix A and References 21 and 22 that the axial steady state temperature distribution in the impedance tube is given by the following expression:

$$\bar{T}(x) = T_w(x) + (T_c - T_{wo})e^{-x/\Lambda} \qquad (3\text{-}23)$$

where:

$$\Lambda = C \left\{ 1 + \frac{T_w(x)}{\bar{T}(x)} \right\}^n ; \quad n = 0.68 \qquad (3\text{-}24)$$

and the unknown constant C needs to be determined from experimental data. In the present study this constant is determined from measured oscillatory pressure data, applying a non-linear regression technique; details of this procedure are described later in this chapter. The computed value of C is the one that results in the "best" fit between the measured and computed impedance tube wave structures. The mean pressure $\bar{p}(x)$ can be measured at some location $x = x_o$ in the impedance tube directly and the burning rate $\bar{r}$ is determined from the known propellant sample thickness and the observed burning time. The thermodynamic properties, the flame temperature T_c and the propellant density ρ_s are

generally known. As discussed in Appendix A, the wall temperature distribution $T_w(x)$ is obtained from measured wall temperature data. Thus, Equations (3-20) through (3-22) can be solved to determine the axial distributions of all the steady state variables. Finally, the steady state entropy distribution is obtained by integrating Equation (3-13); that is

$$\bar{s} - s_{ref} = C_p \left\{ \frac{1}{\gamma} \log \frac{\bar{p}}{p_{ref}} - \log \frac{\bar{\rho}}{\rho_{ref}} \right\} \tag{3-25}$$

Solution of Unsteady Flow Conservation Equations

The linearized partial differential Equations (3-15) through (3-17) are simplified by neglecting oscillatory heat transfer Q' (i.e., see assumption (3)). Since the oscillations in the impedance tube are periodic, the time dependence of the dependent variables can be accounted for by the following relationships:

$$\begin{aligned} p' &\alpha e^{i\omega t} \\ u' &\alpha e^{i\omega t} \\ \rho' &\alpha e^{i\omega t} \quad \text{etc.} \end{aligned} \tag{3-26}$$

Using the assumed time dependence (Equation (3-26)) and eliminating the entropy from the energy equation, the conservation equations for the oscillatory flow can be expressed in the following form:

$$i\omega\rho' + \frac{d}{dx}\left(\bar{\rho}u' + \bar{u}\rho'\right) = 0 \tag{3-27}$$

$$\{i\omega u' + \frac{d}{dx}(\bar{u}\,u')\}\,\bar{\rho} + \bar{u}\,\frac{d\bar{u}}{dx}\,\rho' = -\frac{dp'}{dx} - Gu' \tag{3-28}$$

$$i\omega p' + \frac{d\bar{p}}{dx}\,u' + \bar{u}\,\frac{dp'}{dx} = \bar{c}^2\{i\omega p' + \frac{d\bar{\rho}}{dx}\,u' +$$

$$\bar{u}\,\frac{d\rho'}{dx} + \bar{u}\,\frac{d\bar{\rho}}{dx}\,\frac{p'}{\bar{p}} - \bar{u}\,\frac{d\bar{\rho}}{dx}\,\frac{\rho'}{\bar{\rho}}\} \tag{3-29}$$

where:

$$\bar{c}^2 = \gamma\bar{p}/\bar{\rho} \quad \text{and} \tag{3-30}$$

$$G = \text{Bulk loss coefficient} = \frac{F'}{u'}$$

Solving Equations (3-27) through (3-29) for the space derivatives of the velocity, pressure and density perturbations yield the following system of differential equations:

$$\frac{dZ_i}{dx} = \sum_{j=1}^{3} A_{ij}Z_j,\ i = 1,2,3 \tag{3-31}$$

or

$$\{Z'\}_x = [A]_x\{Z\}_x \tag{3-32}$$

where Z_1, Z_2 and Z_3 respectively represent u', p' and ρ' and the coefficients A_{ij} are defined as follows:

$$A_{11} = \{\bar{u}\bar{\rho}\,\frac{d\bar{u}}{dx} - \frac{d\bar{p}}{dx} + i\omega\bar{u}\bar{\rho} + G\bar{u}\}/\bar{\rho}\,(\bar{c}^2 - \bar{u}^2) \tag{3-33}$$

$$A_{12} = \{\frac{\bar{u}\,\bar{c}^2}{\bar{p}}\frac{d\bar{\rho}}{dx} - i\omega\}/\,\bar{\rho}\,(\bar{c}^2 - \bar{u}^2) \tag{3-34}$$

$$A_{13} = -\frac{1}{\bar{\rho}}\frac{d\bar{u}}{dx} - \{\frac{\bar{c}^2\,\bar{u}}{\bar{\rho}}\frac{d\bar{\rho}}{dx}\}\,/\,\bar{\rho}\,(\bar{c}^2 - \bar{u}^2) \tag{3-35}$$

$$A_{21} = -\{i\omega\bar{\rho} + \bar{\rho}\frac{d\bar{u}}{dx} + G + (\bar{u}^2\bar{\rho}\frac{d\bar{u}}{dx} - \bar{u}\frac{d\bar{p}}{dx} + i\omega\bar{u}^2\bar{\rho})\}/(\bar{c}^2 - \bar{u}^2) \tag{3-36}$$

$$A_{22} = -\bar{u}\{\frac{\bar{c}^2\,\bar{u}}{\bar{\rho}}\frac{d\bar{\rho}}{dx} - i\omega\}/(\bar{c}^2 - \bar{u}^2) \tag{3-37}$$

$$A_{23} = \bar{u}\{\frac{\bar{c}^2\,\bar{u}}{\bar{\rho}}\frac{d\bar{\rho}}{dx}\}/(\bar{c}^2 - \bar{u}^2) \tag{3-38}$$

$$A_{31} = -\frac{1}{\bar{u}}\{\frac{d\bar{\rho}}{dx} + [\bar{u}\,\bar{\rho}\frac{d\bar{u}}{dx} - \frac{d\bar{p}}{dx} + i\omega\bar{u}\,\bar{\rho} + G\,\bar{u}]/(\bar{c}^2 - \bar{u}^2)\} \tag{3-39}$$

$$A_{32} = -\frac{1}{\bar{u}}\{\frac{\bar{u}\,\bar{c}^2}{\bar{p}}\frac{d\bar{\rho}}{dx} - i\omega\}/(\bar{c}^2 - \bar{u}^2) \tag{3-40}$$

$$A_{33} = \frac{1}{\bar{u}}[-i\omega + \{\frac{\bar{c}^2\,\bar{u}}{\bar{\rho}}\frac{d\bar{\rho}}{dx}\}/(\bar{c}^2 - \bar{u}^2)] \tag{3-41}$$

The above system of equations can be considerably simplified when the magnitude of the mean flow $\bar{u}$ is very small. For this case the oscillatory flow equations become:

$$\frac{du'}{dx} = i\omega p'/\,\bar{\rho}\,\bar{c}^2 \tag{3-42}$$

$$\frac{dp'}{dx} = -(i\omega\bar{\rho} + G)u' \tag{3-43}$$

$$\rho' = \frac{p'}{\bar{c}^2} + \frac{iu'}{\omega}\frac{d\bar{\rho}}{dx} \qquad (3\text{-}44)$$

Examination of Equations (3-42) through (3-44) shows that in this case the oscillatory density is decoupled from the system of differential equations. Therefore, Equations (3-42) and (3-43) can be solved to determine the oscillatory velocity and pressure, and these solutions together with Equation (3-44) can be used to determine the unknown density perturbation.

Since the solutions of the systems of wave equations for the cases $\bar{u} = 0$ and $\bar{u} = \bar{u}(x) \neq 0$ are similar, the method of solution for these two cases can be illustrated by discussing the general case, when $\bar{u} \neq 0$, described in Equations (3-31). To solve the Equations (3-31), the coefficients A_{ij} must be evaluated. Inspection of Equations (3-33) through (3-41) reveals that these coefficients can be evaluated once the steady state solutions of Equations (3-20) through (3-22) and the value of the bulk loss coefficient G are known. As described later, the quantities G and $\bar{T}(x)$ (which is needed to determine the steady state solutions) are determined by utilizing the measured oscillatory pressure data and a non-linear regression technique.

Equations (3-31) are a system of three linear, homogeneous coupled first order ordinary differential equations, and they could be treated as an initial value problem once the dependent variables u', p' and ρ' are known at any x location in the impedance tube. Using these initial conditions, Equations (3-31) can be integrated from the initial location toward the propellant surface, to determine the values of the dependent

variables u', p' and ρ' at that location. Once determined, these quantities can be used to determine the unknown admittance of the burning solid propellant and the entropy perturbation at the propellant surface.

Determination of the Initial Conditions

Unfortunately, accurate measurements of Z_1 and Z_3 (i.e., u' and ρ') are extremely difficult if not impossible. Hence, one must resort to the use of a different analytical technique for the solution of the Equations (3-31). Due to the linearity of the Equations (3-31) the needed initial value data on Z_1 and Z_3 can be replaced by measurements of Z_2 (i.e., p') at two additional axial locations. The mathematical technique that allows the use of measured Z_2 data in the solution of the system of equations is based on the "transmission matrix" concept.[23]

Equations (3-32) can be written in the following matrix form:

$$\{Z'\}_x = [A]_x\{Z\}_x \tag{3-45}$$

where the subscript x represents the location at which the elements of the matrix are evaluated. Introducing the backward transmission matrix [T], {Z} can be written as follows

$$\{Z\}_x = [T]_x\{Z\}_{x_o} \tag{3-46}$$

Equation (3-46) indicates that once the transmission matrix $[T]_x$ and $\{Z\}_{x_o}$ are known, $\{Z\}_x$ can be evaluated. To determine $[T]_x$ and $\{Z\}_{x_o}$, one can use Equation (3-46) to get the following expression for $\{Z\}_{x_o}$

$$\{Z\}_{x_o} = [T]_x^{-1}\{Z\}_x \tag{3-47}$$

Now, differentiating Equation (3-46) with respect to x and using Equation (3-47) yield the following expression for $\{Z'\}_x$:

$$\{Z'\}_x = [T']_x [T]_x^{-1} \{Z\}_x \tag{3-48}$$

Comparing Equations (3-45) and (3-48), one gets

$$[A]_x \{Z\}_x = [T']_x [T]_x^{-1} \{Z\}_x \tag{3-49}$$

Since $\{Z\}_x$ is an arbitrary matrix, it can be eliminated from both sides of Equation (3-49) to give

$$[T']_x = [A]_x [T]_x \tag{3-50}$$

The matrix $[T]_x$ can be determined from the integration of Equation (3-50) once $[T]_{x_o}$ is known. By letting x go to x_o in Equation (3-46) one obtains $[T]_{x_o} = I$, the identity matrix. From Equation (3-46) it follows that

$$Z_{x_1} = [T]_{x_1} \{Z\}_{x_o} \tag{3-51}$$

$$Z_{x_2} = [T]_{x_2} \{Z\}_{x_o} \tag{3-52}$$

Using Equations (3-51) and (3-52) to obtain expressions for the elements $(Z_2)_{x_1}$, $(Z_2)_{x_2}$ leads to the derivation of two algebraic equations involving $(Z_1)_{x_o}$ and $(Z_3)_{x_o}$. These algebraic equations can then be solved for $(Z_1)_{x_o}$ and $(Z_3)_{x_o}$, since Z_2 at x_o, x_1 and x_2 are known from experimental

data. Thus, making use of $\{Z\}_{x_o}$ and $[T]_x$, $\{Z\}_x$ can be evaluated from Equation (3-46).

Non-Linear Regression Technique

According to the above discussion any three pressure measurements together with a known axial temperature profile can be used to determine the unknown propellant admittance. However, errors in the experimental measurements results in errors in the computed admittance values. These errors can be minimized by increasing the number of acoustic pressure measurements and utilizing a non-linear regression technique in the data reduction.[24]

Let E_i be a quantity measured at x_i, $i = 1,2,\ldots,n$ and T_i the corresponding theoretically calculated quantity evaluated at the same location x_i. In the present problem, the experimentally measured quantity is the acoustic pressure Z_2 which is measured at various x_i locations. Nonlinear regression consists of finding values of u',p' and ρ' at $x = x_o$, (i.e., values of Z_{o1}, Z_{o2}, and Z_{o3}) which give the best fit between the theoretically predicted acoustic pressure distribution, obtained from the solution of the differential Equations (3-32), and the experimentally measured acoustic pressures. This is accomplished by computing the values of u', p' and ρ' and $x = x_o$ which minimize the root-mean-square deviation between the theoretically predicted acoustic distribution and experimental data. The calculated optimum values of u', p' and ρ' at $x = x_o$ can then be used to obtain optimum values of the propellant admittance and response factor. To find the minimum root-mean-square deviation, the following function F is minimized:

$$F = \sum_{i=1}^{n} (E_i - T_i)^2 \tag{3-53}$$

If a minimum of F exists, then the gradient of F vanishes at the minimum; that is

$$\frac{\partial F}{\partial Z_{o_1}} = \frac{\partial F}{\partial Z_{o_2}} = \frac{\partial F}{\partial Z_{o_3}} = 0$$

or

$$\frac{\partial F}{\partial Z_{o_k}} = -2 \sum_{i=1}^{n} [(E_i - T_i) \frac{\partial T_i}{\partial Z_{o_k}}] = 0; \quad k = 1,2,3 \tag{3-54}$$

Equation (3-54) represents a set of three nonlinear equations for the unknowns Z_{o_1}, Z_{o_2}, Z_{o_3} as T_i and $\partial T_i/\partial Z_{o_k}$ are both functions of Z_{o_k}. A Newton-Raphson iterative scheme is used to obtain a solution of Equation (3-54) utilizing a linearized version of this equation which involves the expansion of T_i in a first order Taylor series with respect to the parameters Z_{o_1}, Z_{o_2} and Z_{o_3}. The resulting system of linear algebraic equations can be expressed in the following form;

$$\sum_{i=1}^{n} (E_i - T_i^m)\partial T/\partial Z_{o_k}\Big|_{(i,m)} = \sum_{j=1}^{3} [(Z_{o_j}^{m+1} - Z_{o_j}^{m}) \sum_{i=1}^{n} \frac{\partial T}{\partial Z_{o_j}}\Big|_{(i,m)} \frac{\partial T}{\partial Z_{o_k}}\Big|_{(i,m)}]$$

$$k = 1,2,3 \tag{3-55}$$

where m represents the m^{th} iteration.

For compactness, Equation (3-55) will now be rewritten in matrix form; letting

$$b_k^m = \sum_{i=1}^{n} (E_i - T_i^m) \left.\frac{\partial T}{\partial Z_{o_k}}\right|_{(i,m)}$$

$$a_{kj}^m = a_{ik}^m = \sum_{i=1}^{n} \left.\frac{\partial T}{\partial Z_{o_j}}\right|_{(i,m)} \left.\frac{\partial T}{\partial Z_{o_k}}\right|_{(i,m)}$$

$$B^m \equiv \begin{Bmatrix} b_1^m \\ b_2^m \\ b_3^m \end{Bmatrix} ; \quad A_m = \begin{bmatrix} a_{11}^m & a_{12}^m & a_{13}^m \\ a_{21}^m & a_{22}^m & a_{23}^m \\ a_{31}^m & a_{32}^m & a_{33}^m \end{bmatrix} ; \quad Z_o^m = \begin{Bmatrix} Z_{o_1}^m \\ Z_{o_2}^m \\ Z_{o_3}^m \end{Bmatrix}$$

Equation (3-55) can be expressed as follows

$$A^m (Z_o^{m+1} - Z_o^m) = B^m$$

or equivalently

$$Z_o^{m+1} = Z_o^m + (A^m)^{-1} B^m \tag{3-56}$$

Equation (3-56) is a linear equation for the unknown Z_o^{m+1} and can be readily solved once the elements of A^m and B^m are computed. The computation of these elements requires the determination of the derivatives $\left.(\partial T/\partial Z_{o_k})\right|_{(i,m)}$. Since these derivatives cannot be determined analytically, numerical values for these derivatives are obtained using the following finite difference formula

$$\left.\frac{\partial T_i}{\partial Z_{o_k}}\right|_{(i,m)} \simeq \frac{T_i(Z^m_{o_1}, \ldots, Z^m_{o_k}(1+\varepsilon), \ldots) - T^m_i}{\varepsilon Z^m_{o_k}} \tag{3-57}$$

where ε is a small number. Thus, to solve for the elements of the matrices A^m and B^m of Equation (3-56), it is necessary to compute T_i four times for each iteration by solving Equations (3-32). The first solution is obtained at Z^m_o and the remaining solutions of T_i are obtained by varying each of three parameters by a small amount $\varepsilon Z^m_{o_k}$ in succession.

The nonlinear regression technique can also be used to determine the values of the heat transfer parameter C and the bulk loss coefficient G. In this case the function F in Equation (3-53) is differentiated partially with respect to C and G representing them by Z_{o_1} and Z_{o_2} respectively, and the derivatives are equated to zero. Then all the steps involved in the procedure leading from Equation (3-54) to (3-57) are repeated to evaluate the optimum values of C and G.

In the actual computational scheme, the function F in Equation (3-53) is expressed either using the real and imaginary parts (i.e., which can be computed from the amplitude and phase) of the oscillatory pressures or by oscillatory pressure amplitudes only.[25] Accordingly, the following F functions have been used.

$$F = \sum_{i=1}^{n} [(p'_{r,e} - p'_r)^2 + (p'_{i,e} - p'_i)^2] \tag{3-58}$$

$$F = \sum_{i=1}^{n} (p'_{a,e} - p'_a)^2 \tag{3-59}$$

The variables appearing in the above equations are defined in the nomenclature. Computational schemes using Equations (3-58) and (3-59) were developed for the following reasons. It was found that the magnitude of the errors in the measured phases near the pressure minima were unacceptable. This necessitated the development of a scheme to obtain values of u'_o, p'_o and ρ'_o at the propellant surface using only pressure amplitude data, which could be measured within acceptable tolerance near the pressure minima. Moreover this would provide a check on the accuracy of the admittance values determined using both oscillatory pressure amplitudes and phases. The numerical solution of Equations (3-32) gives the real and imaginary parts of the oscillatory pressures at locations in the impedance tube where these values are determined experimentally. Therefore the derivatives of these variables with respect to u'_o, p'_o and ρ'_o (i.e., $\partial p'_r/\partial Z_i$ and $\partial p'_i/\partial Z_i$) can be readily computed and used in the nonlinear regression scheme were both the amplitude and phase of the oscillatory pressures are needed to compute the admittances. In the second scheme where only the pressure amplitudes are used to compute the admittances, the derivatives $\partial p'_a/\partial Z_i$ are obtained using the $\partial p'_r/\partial Z_i$ and $\partial p'_i/\partial Z_i$ computed in the first scheme. Representing the real and imaginary parts of u'_o, p'_o and ρ'_o by Z_i, $i = 1,2,\ldots,6$ the derivatives of pressure amplitude p'_a are given by

$$\frac{\partial p'_a}{\partial Z_i} = \frac{\partial \sqrt{(p'^2_r + p'^2_i)}}{\partial Z_i} = \frac{1}{p'_a}\left(p'_r \frac{\partial p'_r}{\partial Z_i} + p'_i \frac{\partial p'_i}{\partial Z_i}\right) \qquad (3\text{-}60)$$

Once these derivatives are computed the nonlinear regression can be used to minimize the error between theoretically computed and experimentally measured pressure amplitudes.

These minimized error terms are computed in this scheme and are defined as follows:

$$E_A = \frac{1}{n}\left[\sum_{i=1}^{n}(p'_{a,e} - p'_a)^2\right]^{1/2}, \text{ DB} \qquad (3\text{-}61)$$

$$E_\phi = \frac{1}{n}\left[\sum_{i=1}^{n}(p'_{\phi,e} - p'_\phi)^2\right]^{1/2}, \text{ Degree} \qquad (3\text{-}62)$$

where E_A and E_ϕ are the root mean square deviation errors in pressure amplitude and phase respectively. The remaining variables appearing in the above equations are defined in the nomenclature. The root mean square deviation errors are termed as experimental errors in this thesis for convenience.

Computational Scheme to Minimize the Error

The nonlinear regression is used to find the values of u'_o, p'_o and ρ'_o at the propellant surface which give the best fit between the theoretically predicted acoustic pressure distribution and the corresponding experimentally measured acoustic pressures. A similar nonlinear regression procedure is also used to obtain the constants C and G. Since these two nonlinear regression operations are coupled, they must be solved together to obtain the propellant admittance. The manner in which this is being done is briefly explained in what follows:

1. Initially, arbitrary values of C and G are chosen, and, using the "Transmission Matrix" scheme a set of "initial" values for u'_o, p'_o and ρ'_o at the propellant surface is computed.

2. The nonlinear regression scheme is then used to obtain the values of u'_o, p'_o and ρ'_o which minimize the root-mean-square deviation between the theoretically predicted data and the experimentally measured data for the chosen values of C and G.

3. Then the values of C and G are recomputed while keeping (and using) the determined (in Step (2)) "optimum" values of u'_o, p'_o and ρ'_o constant.

4. Steps (2) and (3) are repeated until u'_o, p'_o, ρ'_o, C and G converge to a given set of values.

Illustrations of Computational Scheme

To check the accuracy of the data reduction schemes discussed in the last section, computations were performed for a number of hypothetical cases for which the exact values of C, G, u'_o, p'_o and ρ'_o were assumed to be known. Using these values as initial conditions, the conservation equations (i.e., Equations (3-31)) describing the oscillatory flow field in the impedance tube were solved to determine the "exact" wave structure in the hypothetical impedance tube. A number of pressure data at different axial locations along the tube were taken from the solution of the Equations (3-31) and were perturbed from the exact value. The deviations would correspond to the inherent experimental errors in the impedance tube operation. These modified pressure data were then fed into the developed data reduction programs in an effort to determine the error in

the admittance computation resulting from the experimental inaccuracies. Careful examination of the results obtained from the various investigated hypothetical cases indicates that the heat transfer parameter 'C' converges rapidly to its correct value, whereas the bulk loss coefficient 'G' converges slowly. Therefore, to obtain an accurate value of G the tolerance limit must be kept as small as possible and the errors in the input pressure data should not be too large. Two sets of such computations are presented below.

Case 1: In this case the bulk loss in the impedance tube was assumed to be zero. Then with the known values of C, u'_o, p'_o, ρ'_o the Equations (3-31) were solved and hypothetical pressure data were obtained. An arbitrarily chosen initial value of C and the modified pressure data were then used to recompute the wave structure and the desired value of C. The computed wave structures are shown in Figures 3-1 and 3-2, and Table 3-1 provides a comparison between the "exact" and the computed values of C, u'_o, p'_o, ρ'_o and the admittance.

Case 2: In this case Equations (3-31) were solved for a situation where the bulk loss was assumed to be present in the impedance tube. Thus a bulkloss coefficient G was also assumed in this case. Then using the known values of C, G, u'_o, p'_o and ρ'_o Equations (3-31) were solved and hypothetical pressure data were obtained. Then assumed arbitrary values of C and G and the modified pressure data were used to recompute the wave structure and the values of C and G. The computations were done for two different values of the real parts of the admittances, that is, +0.1 and -0.1. The computed wave structures are plotted in Figures

Table 3-1. Comparison Between Correct and Computed Values Using Nonlinear Regression

Parameters		Correct Values	Computed Values Using Amplitude and Phase	Values Using Amplitude Only	Guessed
Heat Transfer Parameter, C		0.943	0.972	0.973	2.0
Pressure	Amplitude, D.B.	145.436	145.815	145.818	
	Phase, Deg.	230.2	229.9	228.6	
Velocity	Amplitude, Ft/S	1.48	1.301	1.308	
u'_o	Phase, Deg.	-21.4	-18.17	-18.27	
Density	Amplitude, Stug/Ft^3	$.612 \times 10^{-6}$	$.6472 \times 10^{-6}$	$.6477 \times 10^{-6}$	
ρ'_o	Phase, Deg.	229.0	228.7	227.4	
Real Part of Admittance, Y_r		-0.05	-0.049757	-0.052565	

3-3 through 3-6 and the various parameters and variables computed using the developed data reduction scheme are compared with the exact values in Tables 3-2 and 3-3. In one of the two computational schemes used to compute the variables at the propellant surface, the bulk loss coefficient was kept zero. In this case (i.e., Plot B in Figures 3-3 through 3-6) the computed wave structures do not agree well, particularly at and near pressure minima with the exact wave structures, and there are considerable discrepancies between the computed and exact values of u'_o, p'_o, ρ'_o and the admittance Y. In the second case the bulk loss coefficient G was also included in the computational scheme resulting in good agreement between the wave structures (i.e., between plots A and C in Figures 3-3 through 3-6) and the variables u'_o, p'_o and ρ'_o.

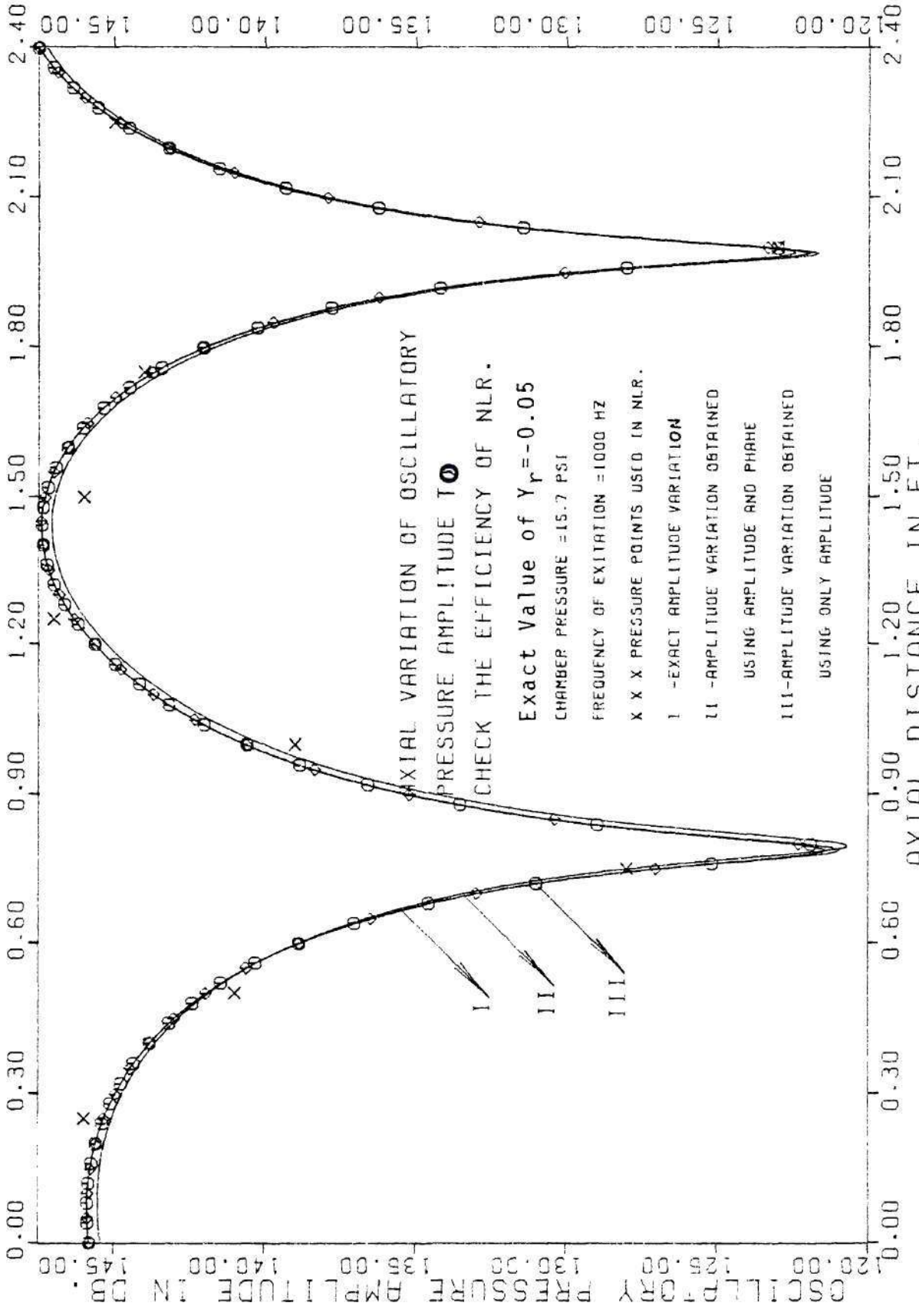

Figure 3-1. Axial Variation of Pressure Amplitude to check Non-linear Regression Technique.

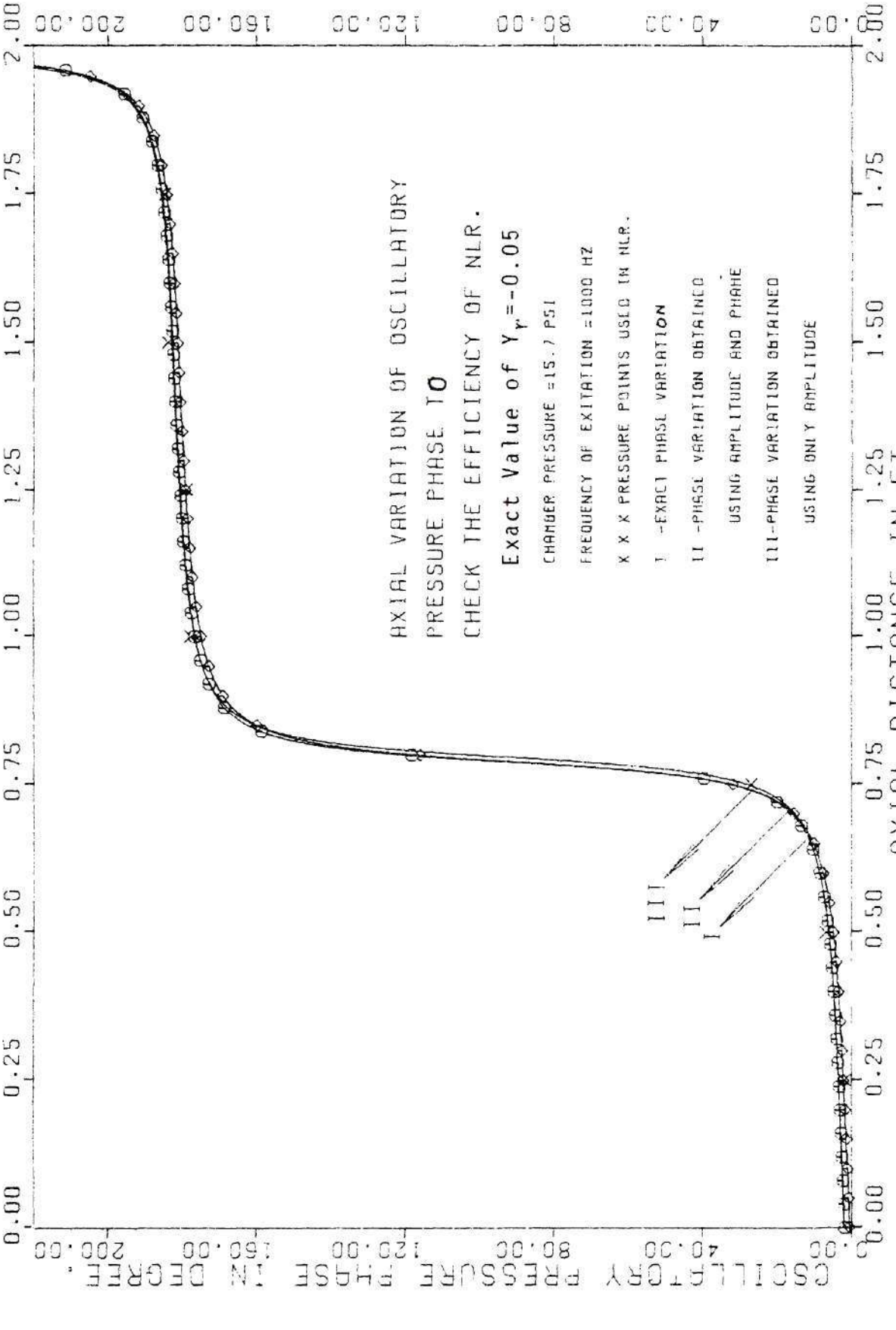

Figure 3-2. Axial Variation of Pressure Phase to check Non-linear Regression Technique.

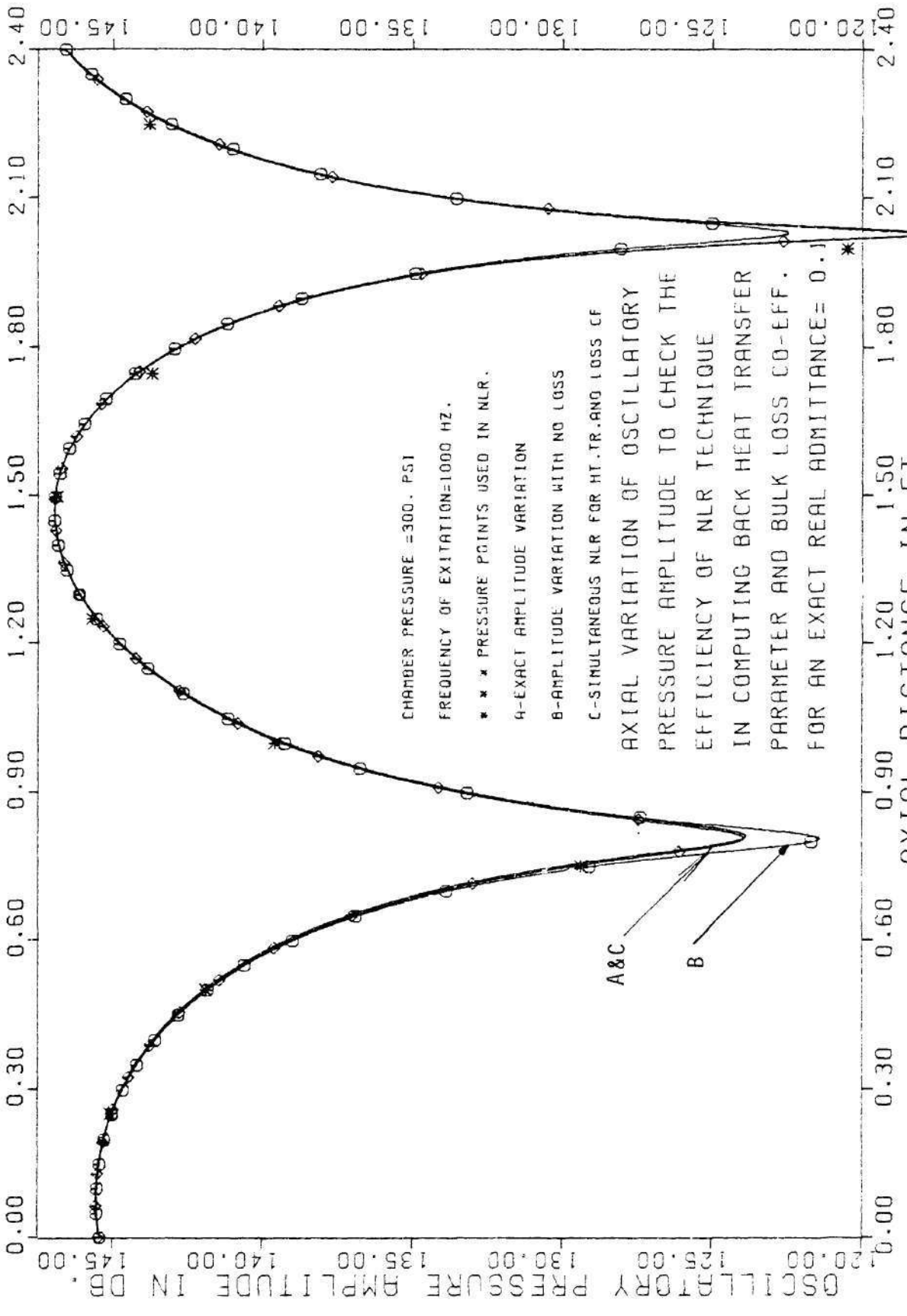

Figure 3-3. Axial Variation of Pressure Amplitude to check Non-linear Regression Technique.

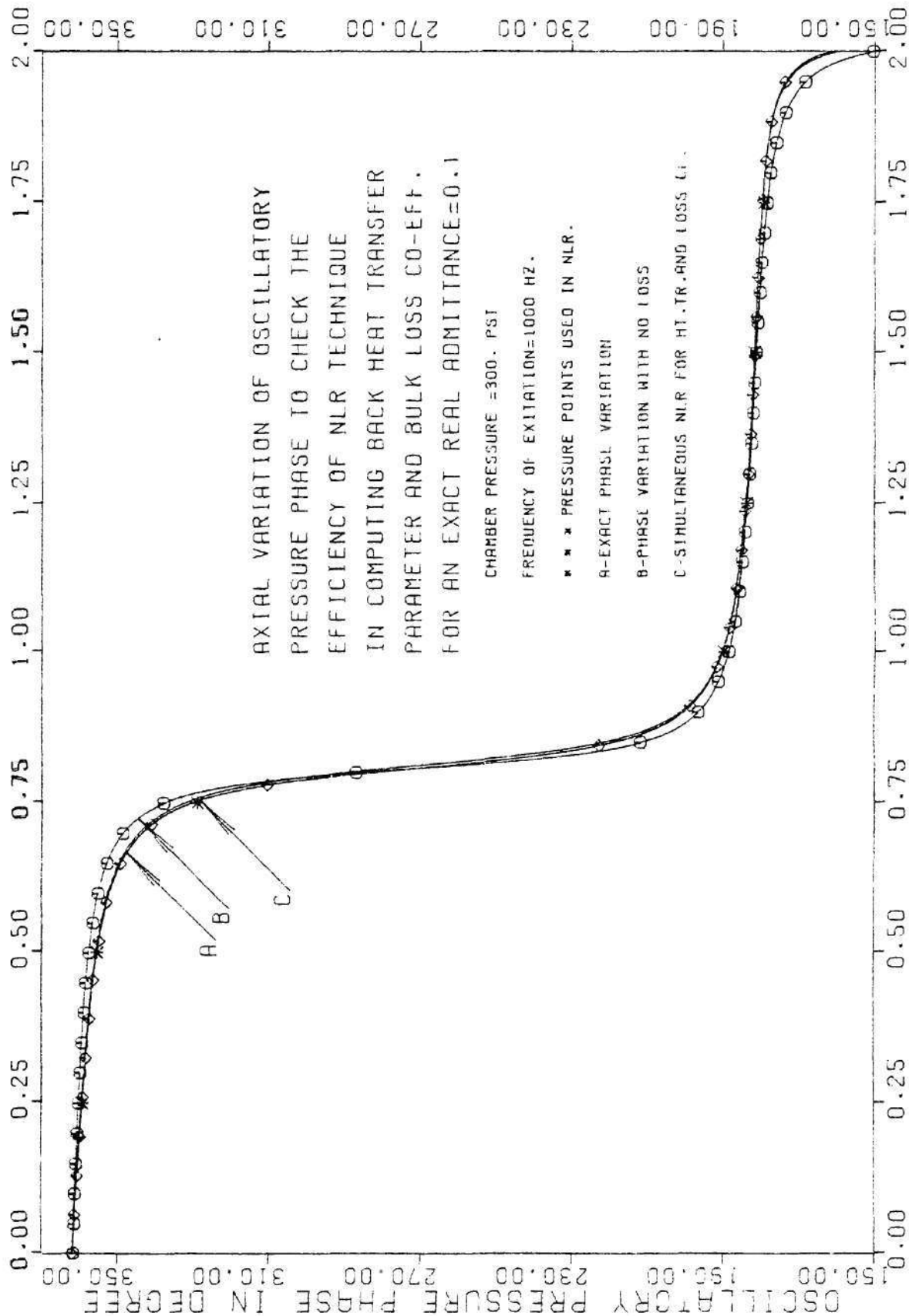

Figure 3-4. Axial Variation of Pressure Phase to check Non-linear Regression Technique.

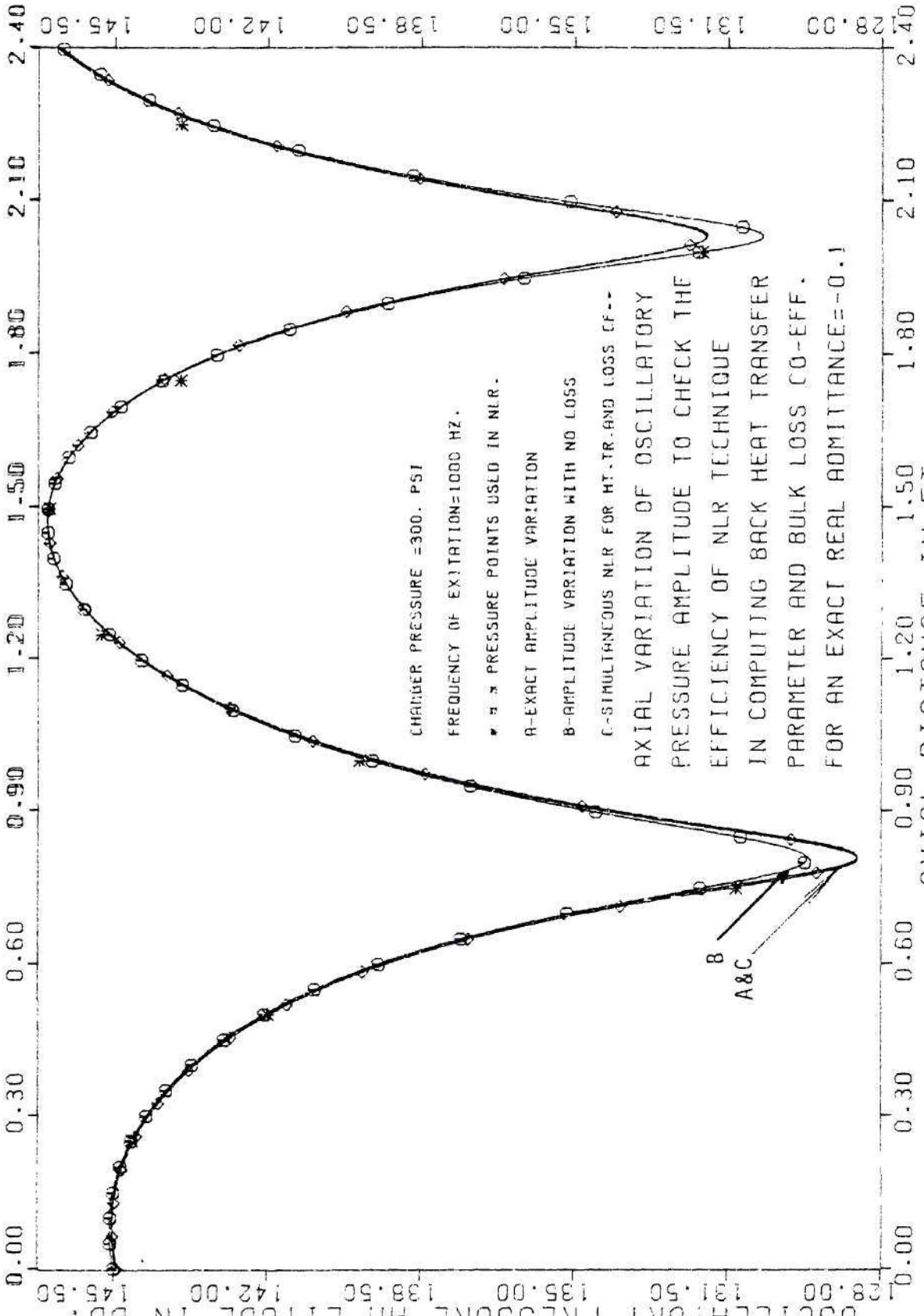

Figure 3-5. Axial Variation of Pressure Amplitude to check Non-linear Regression Technique.

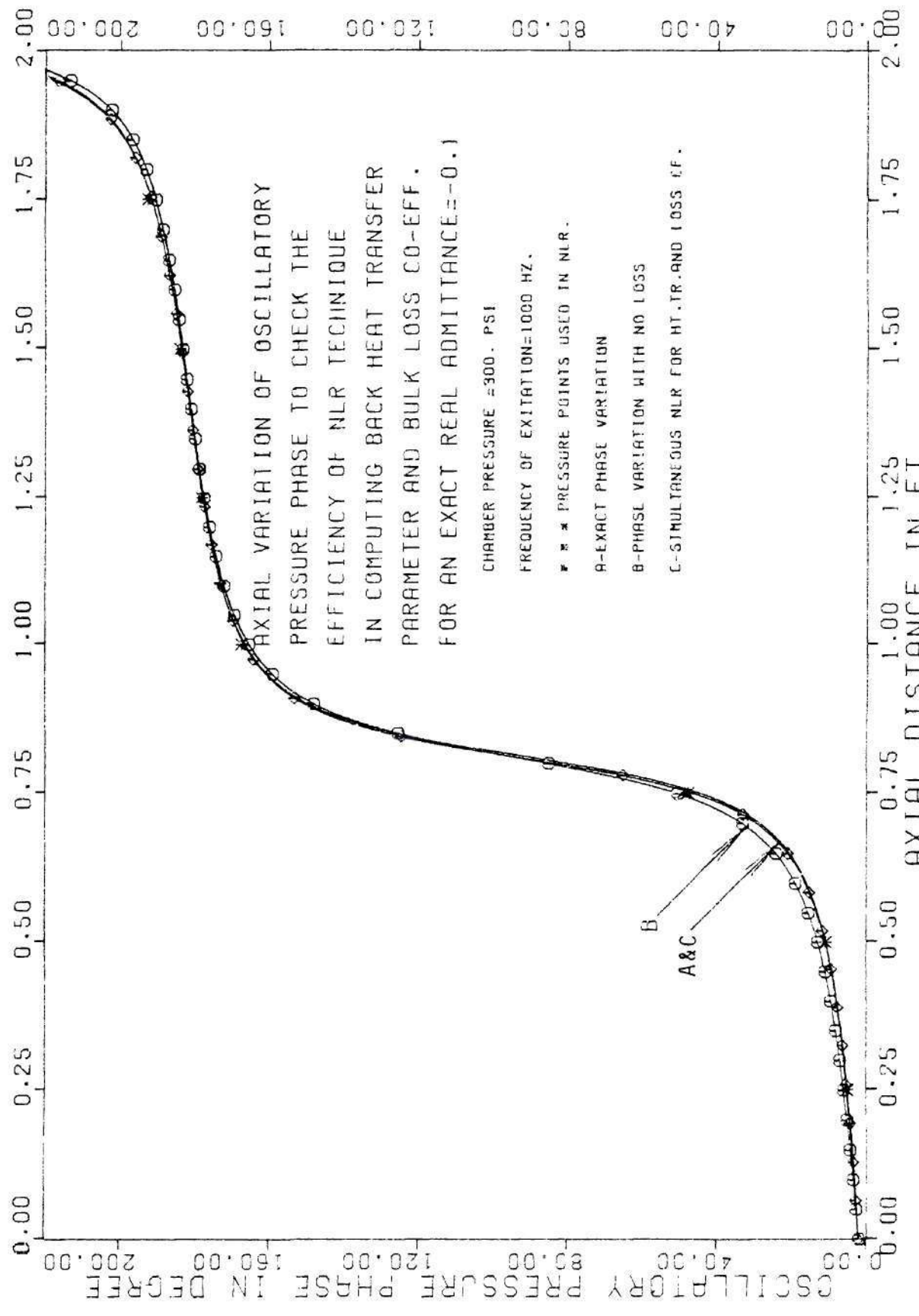

Figure 3-6. Axial Variation of Pressure Phase to check Non-linear Regression Technique.

Examination of Figures 3-1 through 3-6 and the Tables 3-1 through 3-3 indicates very good agreement between the assumed and computed values of u'_o, p'_o, $'_o$, C, G and the admittance Y. This good agreement suggests that the data reduction procedures developed as part of this research effort can be used to determine the admittance values in the impedance tube experiments without much loss of accuracy, even when small errors are present in the experimental data.

Table 3-2. Data Computed with Loss, Using Nonlinear Regression for a Positive Real Admittance

Chamber Pressure = 300 Psi
Frequency of Excitation = 1000 Hz.

Parameters	Exact Values	Computed Back Values Using NLR	
		Assuming Zero Loss	Loss Coefficient and Heat Transfer Parameter Computed Simultaneously
Y_r	0.1	0.055532	0.10147
Y_i	0.15	0.13315	0.1362
Loss CF:G	1.5	0.0	1.556
HT TRP:C	1.0	1.024	1.021
Pressure Amplitude, DB	145.4357	145.4	145.5
Pressure Phase, Deg.	230.1944	229.9	230.1
Velocity Amplitude, Ft/s	0.088204	0.07068	.08356
Velocity Phase, Deg.	-75.496	-62.76	-76.54
Density Amplitude, Stag/Ft^3	0.61433×10^{-6}	0.6197×10^{-7}	0.6219×10^{-6}
Density Phase, Deg.	232.4994	231.1	232.4

Table 3-3. Data Computed with Loss, Using Nonlinear Regression for a Negative Real Admittance

Chamber Pressure = 300 Psi
Frequency of Excitation = 1000 Hz.

Parameters	Exact Values	Computed Back Values Using NLR	
		Assuming Zero Loss	Loss Coefficient and Heat Transfer Parameter Computed Simultaneously
Real Adm: Y_r	-0.1	-0.14304	-0.10023
Imaginary Ad: Y_i	0.15	0.13624	0.13652
Loss CF: G	1.5	0.0	1.465
HT. TR. PR: C	1.0	1.021	1.025
Pressure Amplitude	145.4357	145.5	145.5
Pressure Phase	230.1944	230.0	230.3
Velocity Amplitude	.088204	.09761	0.08306
Velocity Phase	-6.115	6.445	-3.42
Density Amplitude	0.61433×10^{-6}	0.625×10^{-6}	0.6198×10^{-6}
Density Phase	227.889	226.8	228.0

CHAPTER IV

ACOUSTIC BEHAVIOR OF IMPEDANCE TUBE

The acoustic behavior of the impedance tube is investigated extensively in this chapter to provide data that could be used as a guide in the interpretation of the experimental data. The results reported in this chapter will also describe the behavior of the oscillatory velocity, density, temperature and entropy in the impedance tube, as these variables are normally difficult to measure. These results are obtained for various boundary conditions.

1. Dependence of the Impedance Tube Wave Structure Upon the Propellant Surface Boundary Conditions

An extensive study of the dependence of the impedance tube wave structures upon the boundary conditions at the propellant surface has been conducted to obtain a better understanding of the acoustic characteristics of the impedance tube which will be needed in the interpretation of the experimental data. The investigated variables include the pressure, velocity, density, temperature and entropy waves. The boundary conditions at the propellant surface may be described by the admittance Y, the oscillatory pressure p' and the oscillatory density ρ'. The oscillatory velocity u' at the propellant surface is then obtained from the known values of Y and p'. Equations (3-31) can then be solved, using the specified values of u', p' and ρ' at the propellant surface to obtain the wave structures in the impedance tube. In this investigation,

the wave structures in the impedance tube have been determined for both positive and negative values of the real part of the admittance. A positive real admittance at the propellant surface implies a condition which results in wave energy addition from the burning propellant to the gas phase[26] (i.e., the propellant is amplifying the waves). On the other hand, the oscillation in the impedance tube is attenuated (or damped) by the boundary if the real part of the admittance at the propellant surface is negative.

The mean flow variables (i.e., $\bar{u}(x)$, $\bar{T}(s)$, $\bar{\rho}(x)$ etc.) used in this investigation are computed from the steady conservation equations using the mean temperature distribution given by Equation (3-23). The various flow properties and the axial distribution of the mean flow parameters in the impedance tube, which are used in this analysis, are presented in the following table, (i.e., Table 4-1) and in Figure 4-1, respectively.

Table 4-1. Data Used to Compute Impedance Tube Wave Structure

Flame temperature, T_c		:	3780°R
Wall temperature constants		:	A = 530, B = 634, B = -0.285 (see Eq.A-11)
Specific heat ratio	γ	:	1.28
Specific heat at constant pressure, C_p		:	0.45 BTU/lbm °R
Density of the Propellant, ρ_s		:	100 lbs/ft^3
Gas constant	R	:	2480 ft lbf/slug °R

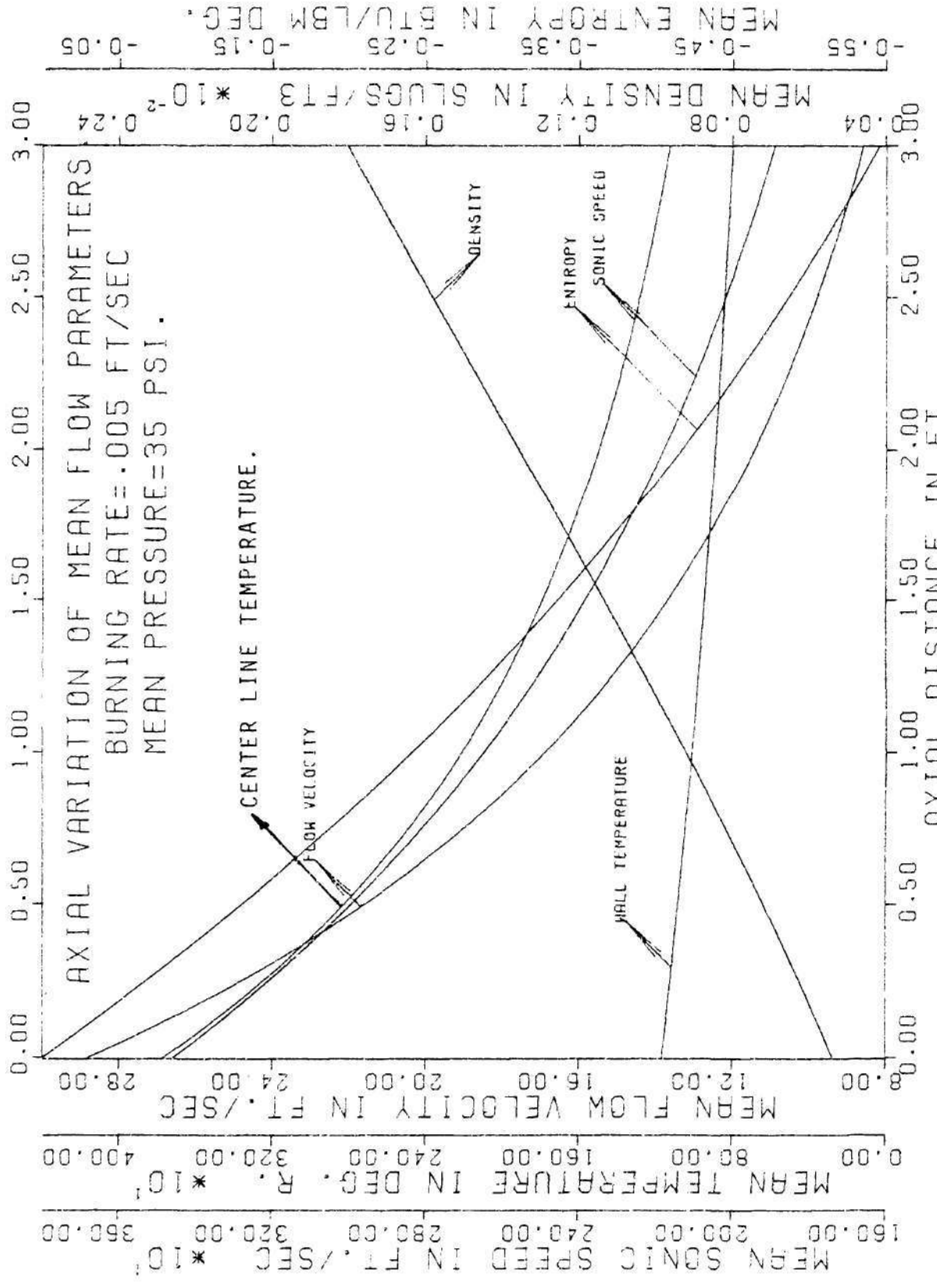

Figure 4-1. Axial Variation of Mean Flow Parameters.

The relationship between the sign of the real part of the propellant admittance and the characteristics of the pressure phase distribution had been investigated and the results obtained were used in the experimental phase of this program. Since the phase-distance relationship will be used to determine the behavior of the propellant (i.e., driving or damping) it would be desirable if one could obtain an analytical relationship between the real part of admittance and the derivative of phase with respect to axial distance. It is difficult to obtain such a relationship when the acoustic waves are described by solutions of a system of differential equations. Therefore, in this section, an analytical relationship between real part of the admittance and the spatial distribution of pressure phase is obtained for an isentropic flow condition only.

The isentropic wave equation for the no flow case is given by:

$$\frac{d^2p'}{dx^2} + k^2p' = 0 \qquad (4\text{-}1)$$

The solution of Equation (4-1) can be expressed as follows:

$$p' = -iA \sinh[\pi\alpha - i(\pi\beta + kx)] \qquad (4\text{-}2)$$

and by using the momentum equation it can be shown that

$$u' = \frac{-iA}{\bar{\rho}\,\bar{c}} \{\cosh[\pi\alpha - i(\pi\beta + kx)]\} \qquad (4\text{-}3)$$

using Equations (4-2) and (4-3), the admittance of the surface at $x = 0$ can be written as

$$Y = \bar{\rho}\,\bar{c}\,\frac{u'}{p'}\Big|_{x=0} = \text{Coth}\ \pi(\alpha - i\beta) \tag{4-4}$$

where:

$$Y_r = \frac{\tanh(\pi\alpha)\cdot \text{Sec}^2(\pi\beta)}{\tanh^2(\pi\alpha) + \tan^2(\pi\beta)} \tag{4-5}$$

and

$$Y_i = \frac{\tan(\pi\beta)\cdot \text{Sec h}^2(\pi\alpha)}{\tanh^2(\pi\alpha) + \tan^2(\pi\beta)} \tag{4-6}$$

Expressing p' as $p' = |p'|e^{i(\phi+\omega t)}$, the pressure amplitude $|p'|$ and the phase ϕ can be obtained from Equation (4-2) and they are given by

$$|p'| = A[\cosh^2(\pi\alpha) - \cos^2(\pi\beta + kx)]^{1/2} \tag{4-7}$$

$$\phi = \text{Arc tan}[\tanh(\pi\alpha)\cdot\text{Cot}(\pi\beta + kx)] \tag{4-8}$$

Differentiating Equation (4-8) with respect to x, the slope of the phase is obtained:

$$\frac{d\phi}{dx} = -\frac{\tanh(\pi\alpha)\cdot \text{Sec}^2(\pi\beta + kx)}{\tanh^2(\pi\alpha) + \tan^2(\pi\beta + kx)} \cdot k \tag{4-9}$$

Using Equation (4-5), Equation (4-9) can be expressed as follows:

$$\frac{d\phi}{dx} = -Y_r\left[k\frac{(\tanh^2(\pi\alpha) + \tan^2(\pi\beta))\cdot \text{Sec}^2(\pi\beta+kx)}{\text{Sec}^2(\pi\beta)(\tanh^2(\pi\alpha) + \tan^2(\pi\beta+kx))}\right] \tag{4-10}$$

The term inside the square bracket in Equation (4-10) is always positive. Therefore the slope of the axial pressure phase distribution depends on the sign of Y_r. If Y_r is positive, the slope becomes negative

and vice versa.

During an actual test, when a solid propellant sample is ignited inside the impedance tube, the flow does not remain isentropic. In this situation the flow field is described by Equations (3-31) and the relationship between the real part of the admittance and the pressure phase distribution in the impedance tube is obtained numerically. The axial variation of the acoustic pressure amplitude and phase, obtained by numerical computations are presented in Figures 4-2 through 4-5. Figures 4-2 and 4-3 contain pressure amplitude and pressure phase plots for different values of real admittance at the propellant surface, respectively, obtained when the mean flow velocity $\bar{u}$ is neglected. Figures 4-4 and 4-5 correspond to Figures 4-2 and 4-3 respectively and are obtained when a mean flow velocity is incorporated in the computations. An examination of these figures indicates that for negligible mean flow, the pressure amplitude depends only on the magnitude of the real part of the admittances and for a positive real admittance at the propellant surface the slope of the pressure phase-distance curve is negative, and vice-versa. Also, a near zero slope is observed when the real part of the surface admittance is a very small number. When the mean flow velocity $\bar{u}$ is included, the above mentioned symmetry is lost (see Figure 4-5). These results show that the presence of a mean flow velocity tends to make the slope of the phase-distance curve more negative, with the result, that for zero and small negative values of the real part of the propellant admittance the slope of the phase-distance curve still remains negative. An examination of the pressure amplitude data (Figures 4-2

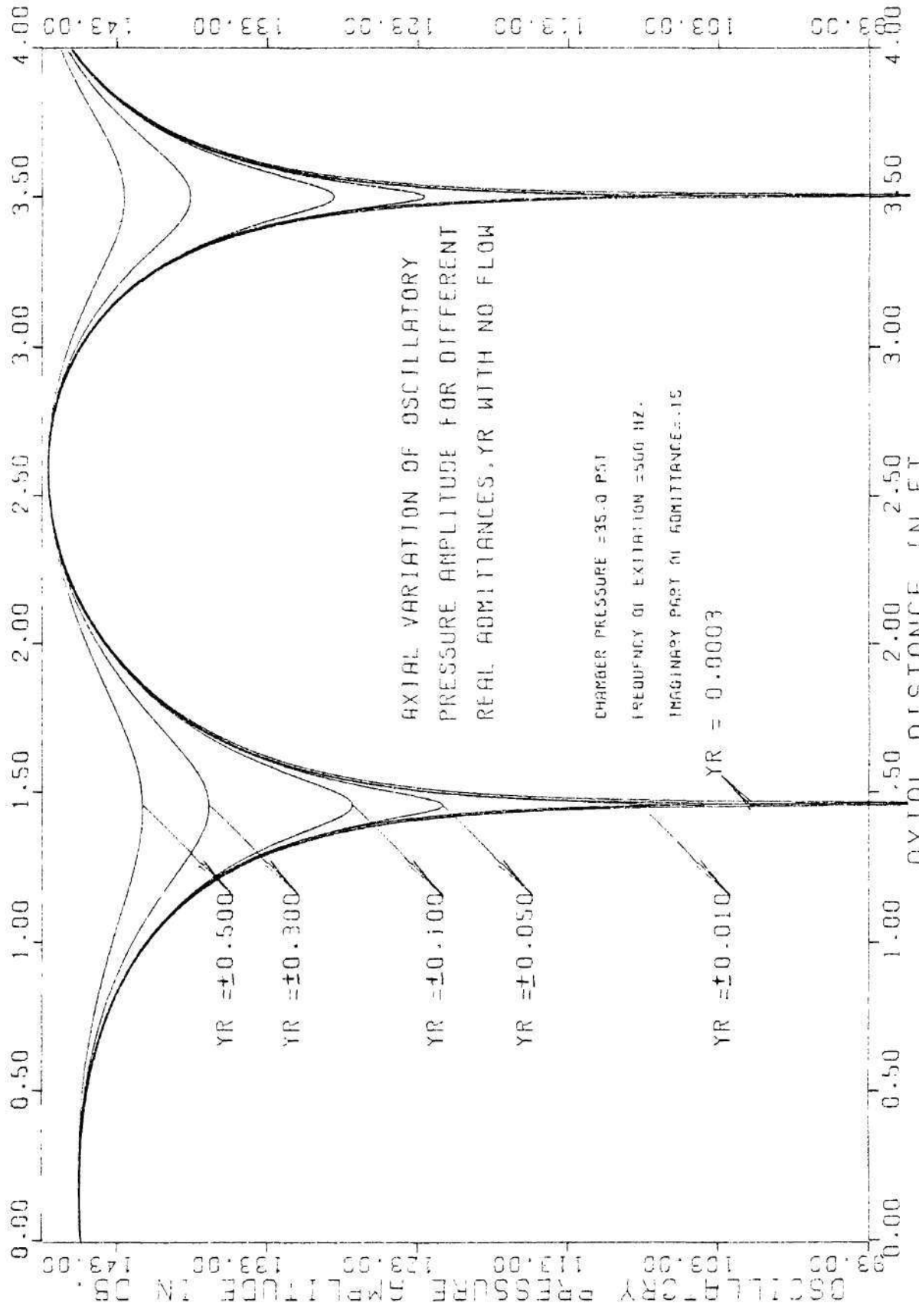

Figure 4-2. Axial Variation of Pressure Amplitude with No Flow.

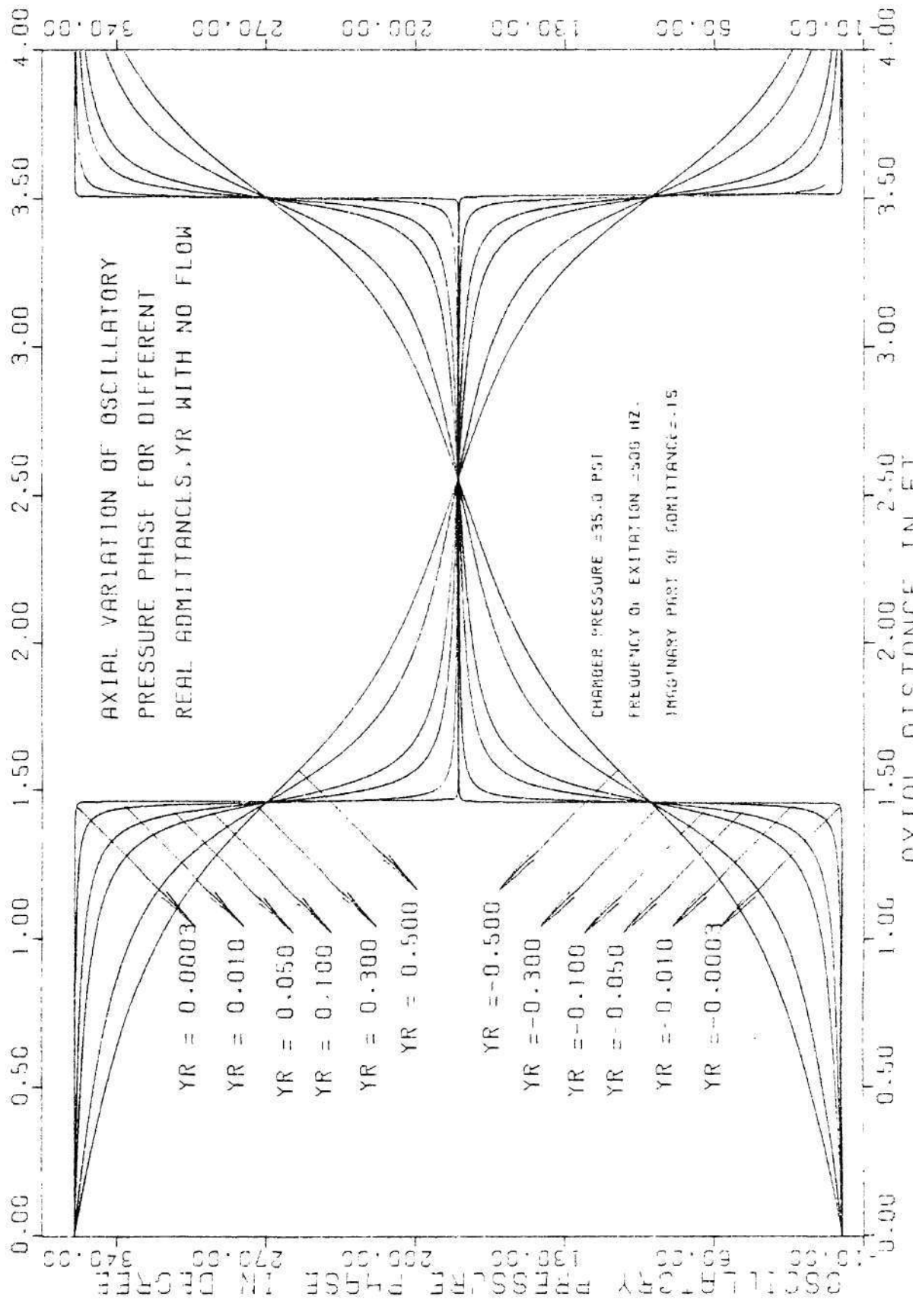

Figure 4-3. Axial Variation of Pressure Phase with No Flow.

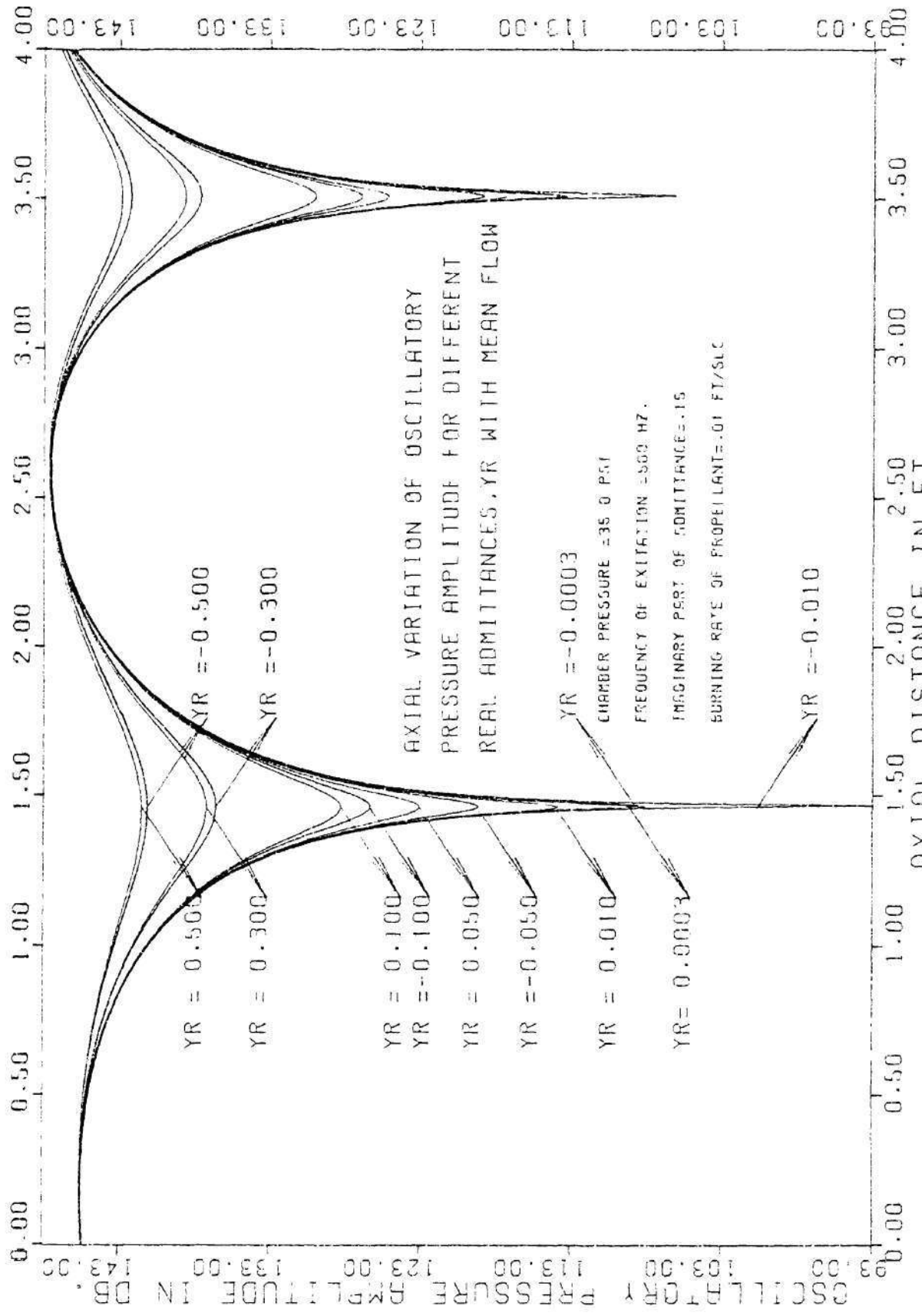

Figure 4-4.Axial Variation of Pressure Amplitude with Mean Flow.

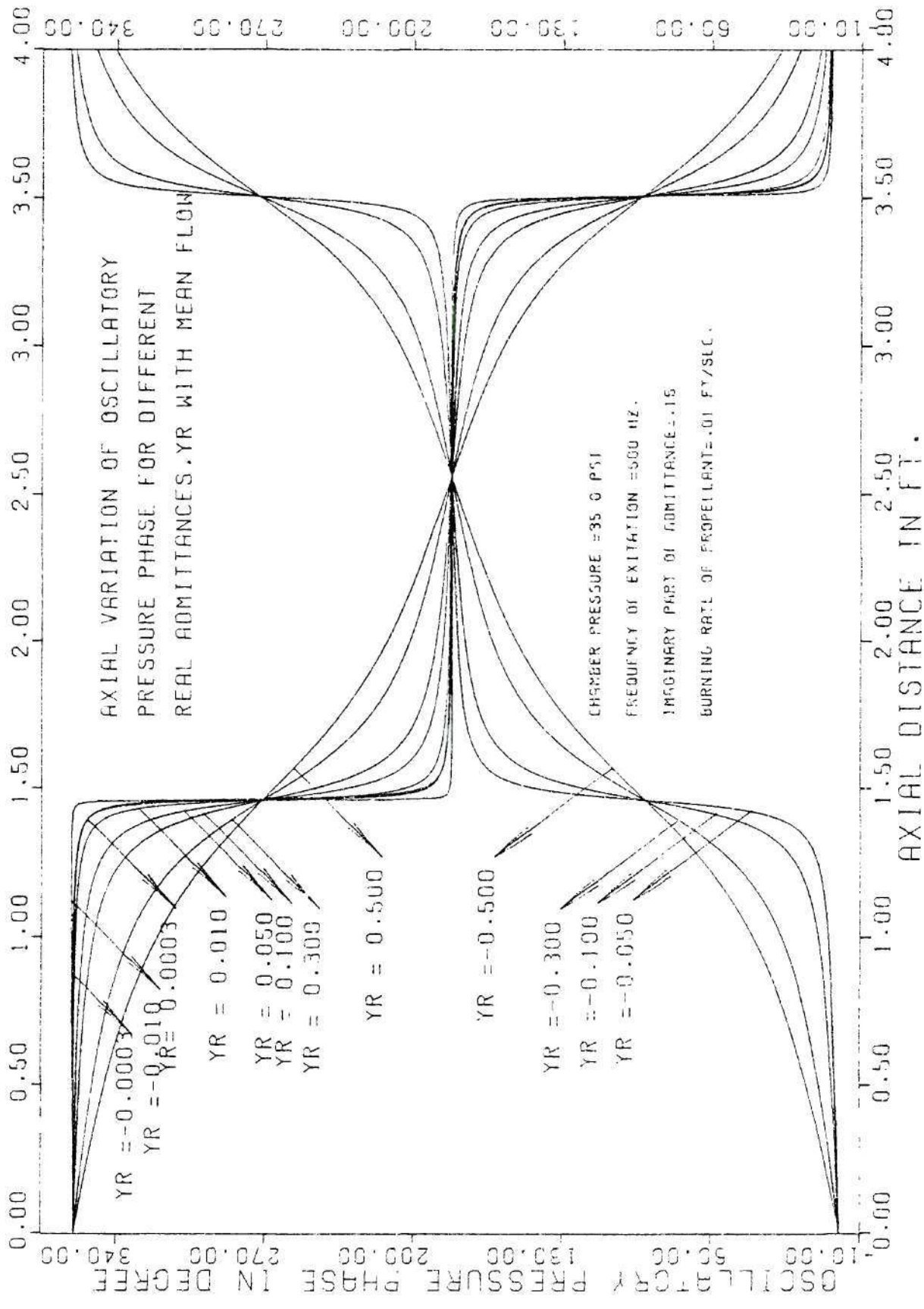

Figure 4-5. Axial Variation of Pressure Phase with Mean Flow.

and 4-4) indicates that the amplitudes of the acoustic pressure at successive nodes and antinodes increase with increasing distance from the propellant boundary. Also, the pressure amplitude at a given antinode increases with increasing magnitude of the real part of admittance at the propellant surface.

Additional parametric studies were conducted to illustrate the spatial dependence of pressure amplitude and phase. Figures 4-6 and 4-7 respectively describe pressure amplitude and phase distribution for different imaginary parts of the propellant surface admittances, keeping the real value of the admittance fixed. These figures clearly show that the pressure amplitude magnitudes and pressure phase slopes do not change with the imaginary part of the admittance. The location of the pressure minimum shifts away from the propellant surface with increasing value of the imaginary part of the admittance. Figures 4-8 and 4-9 describe the spatial dependence of the pressure amplitude and phase for different propellant burning rates (or propellant surface Mach numbers) while the admittances are kept fixed. These figures show that the magnitude of pressure amplitudes at the pressure minima goes on increasing and the slope of the phase-distance curve decreases with the increasing value of burning rate. Therefore, for a higher burning rate or surface Mach number the apparent real admittance looks higher compared to that at negligible Mach number.

Figures 4-10 through 4-13 are the plots of oscillatory velocity amplitudes and phases for cases with and without mean flow velocity. The behavior of the velocity amplitudes and phases appear to be similar

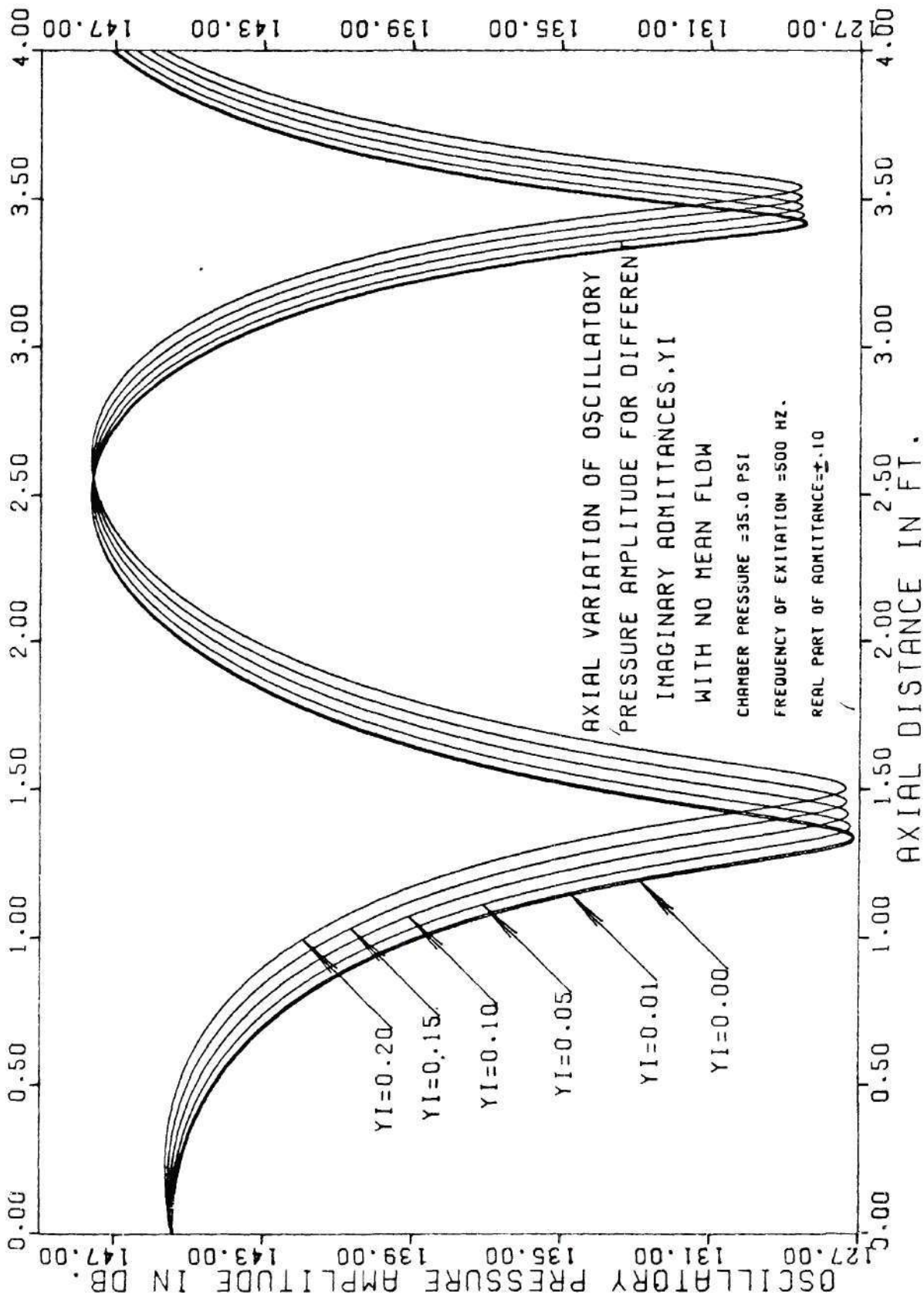

Figure 4-6. Axial Variation of Pressure Amplitude with No Flow.

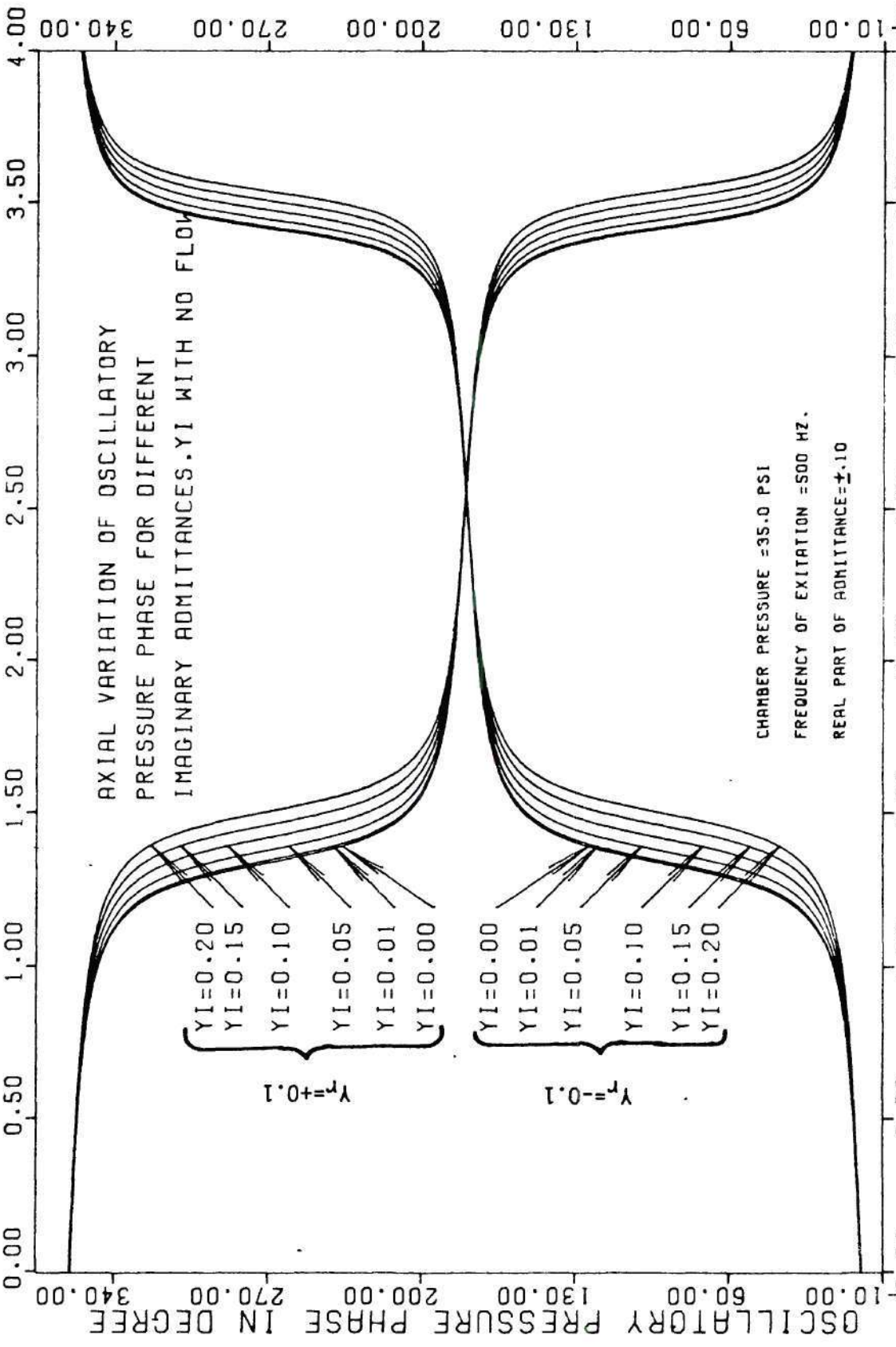

Figure 4-7. Axial Variation of Pressure Phase with No Flow.

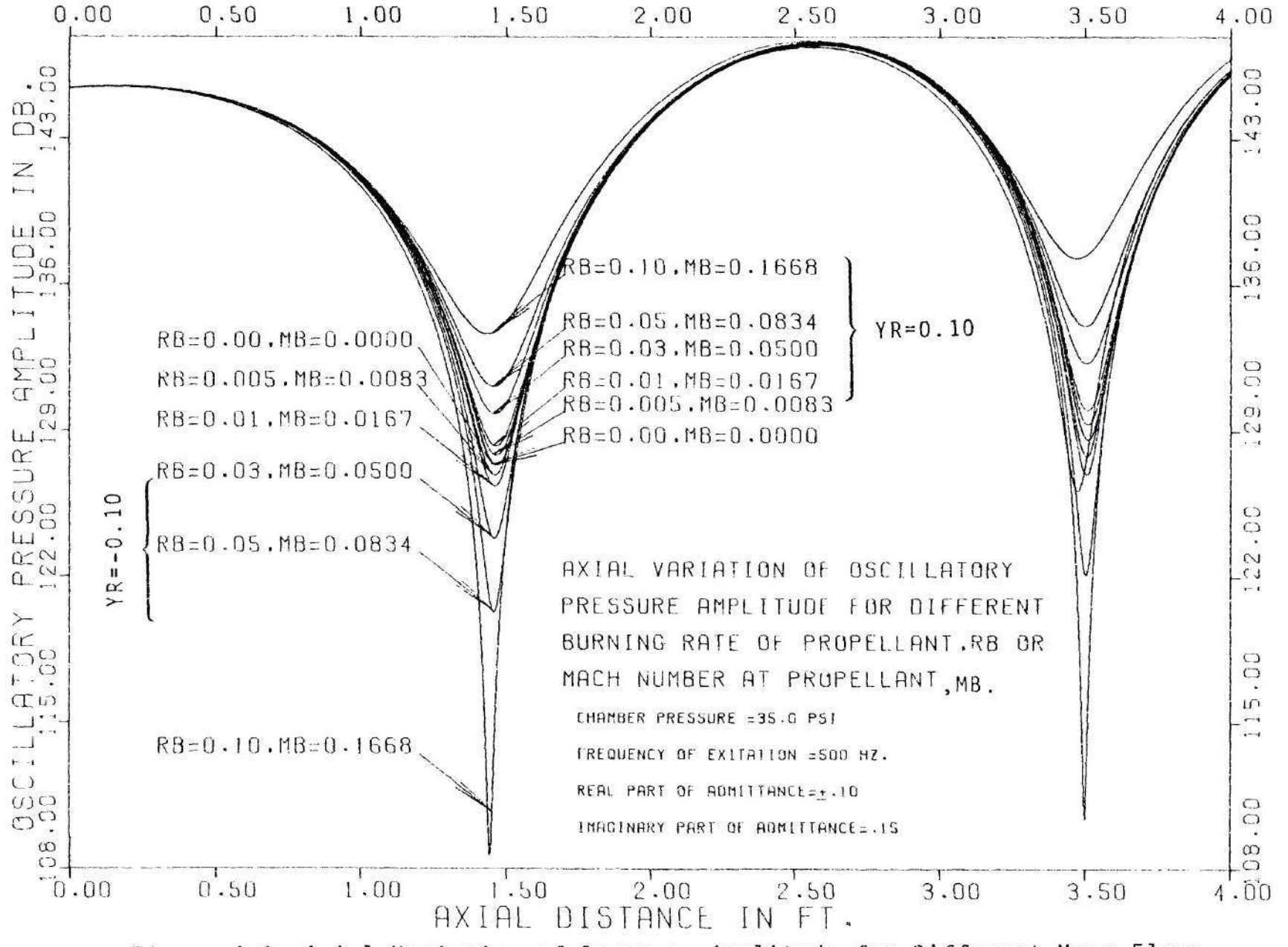

Figure 4-8. Axial Variation of Pressure Amplitude for Different Mean Flows.

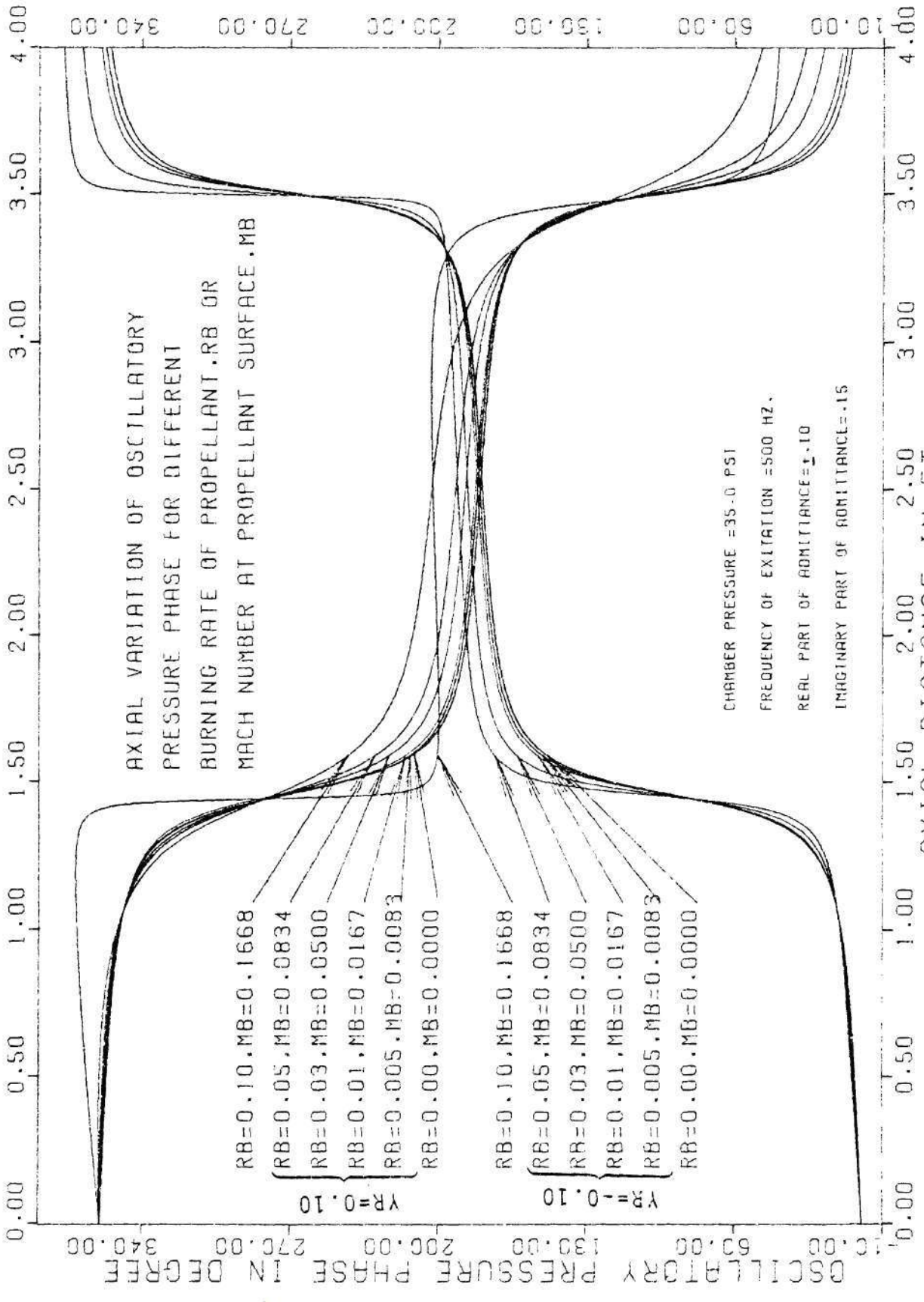

Figure 4-9. Axial Variation of Pressure Phase for Different Mean Flows.

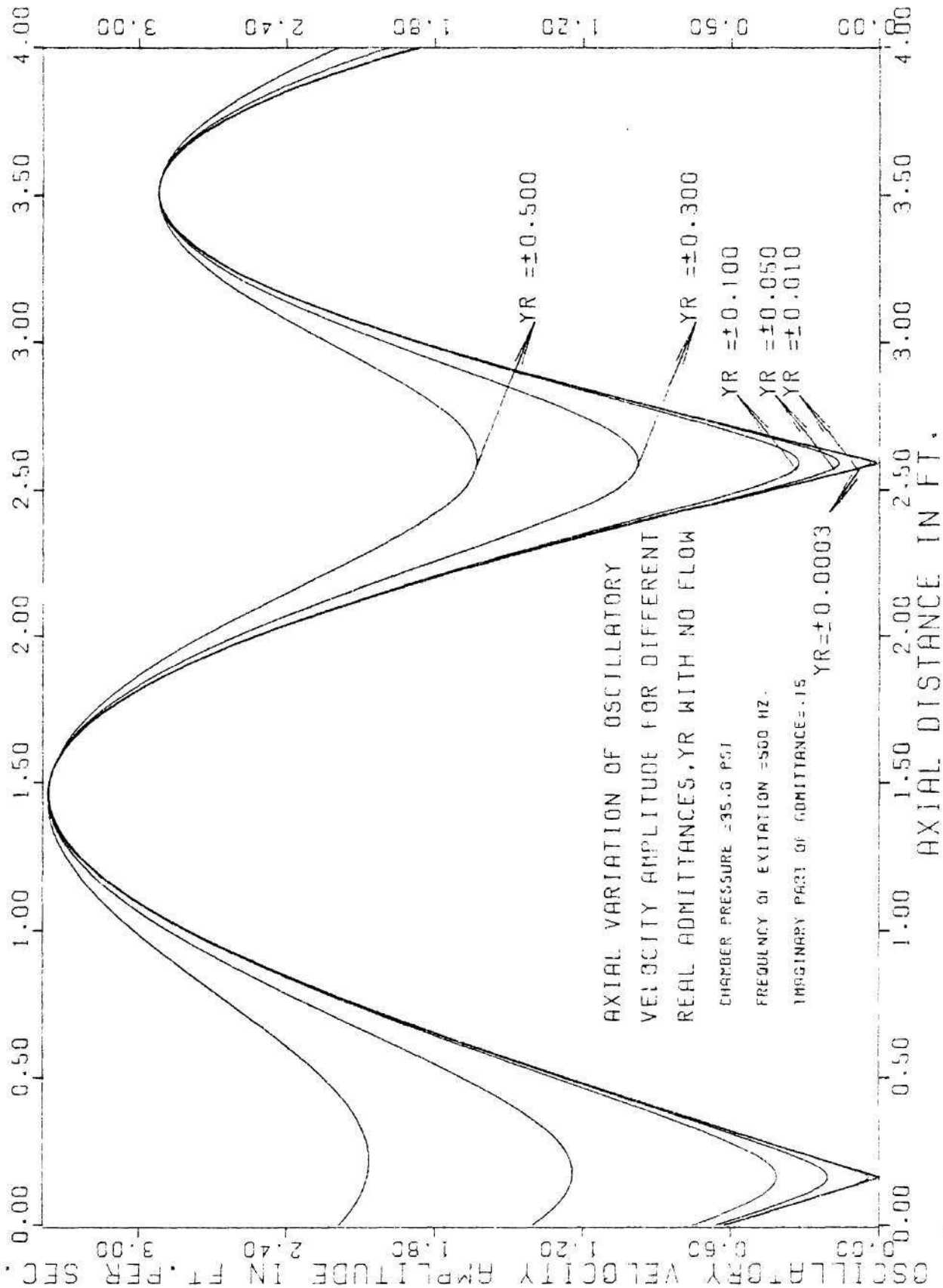

Figure 4-10. Axial Variation of Velocity Amplitude with No Flow.

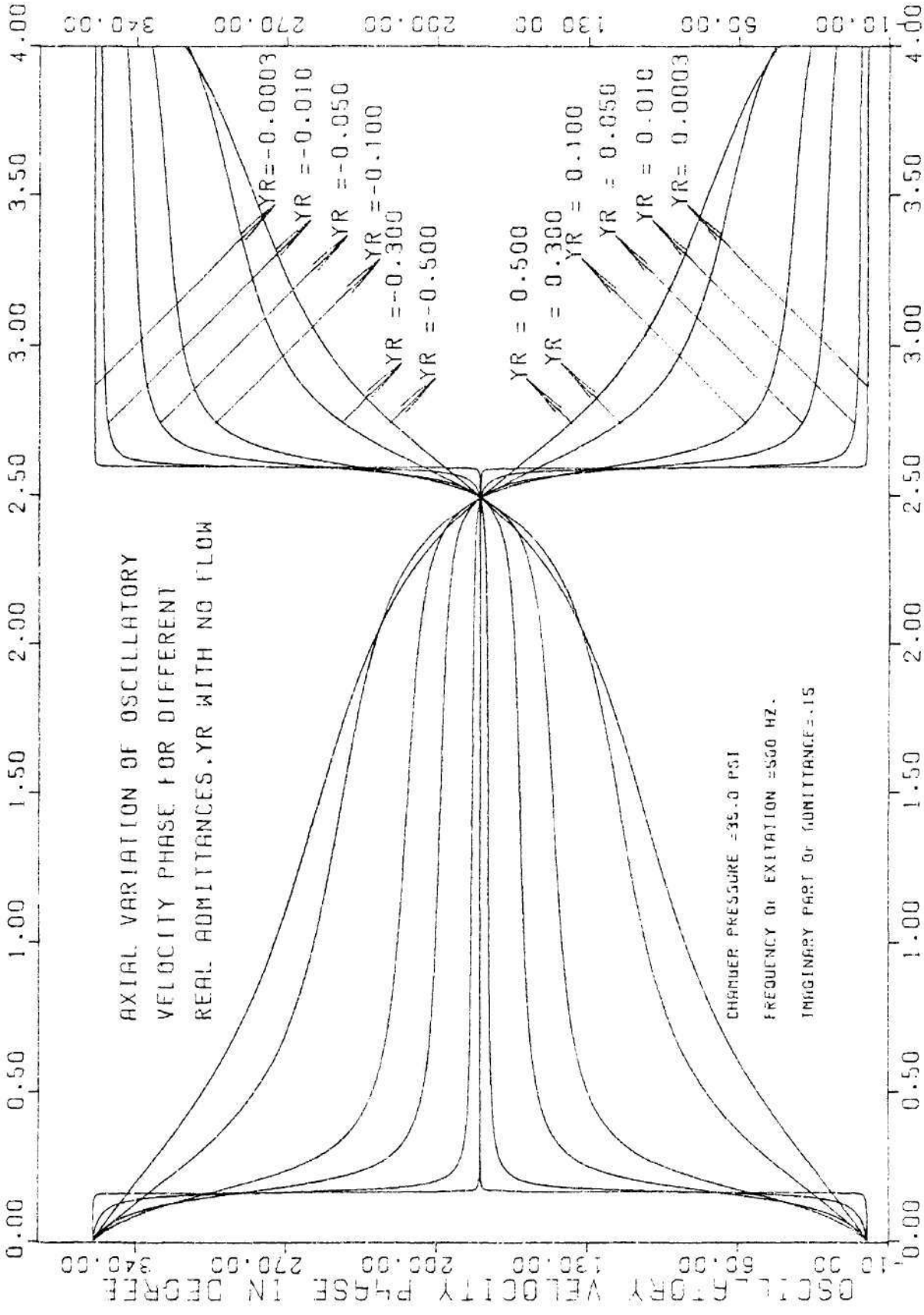

Figure 4-11. Axial Variation of Velocity Phase with No Flow.

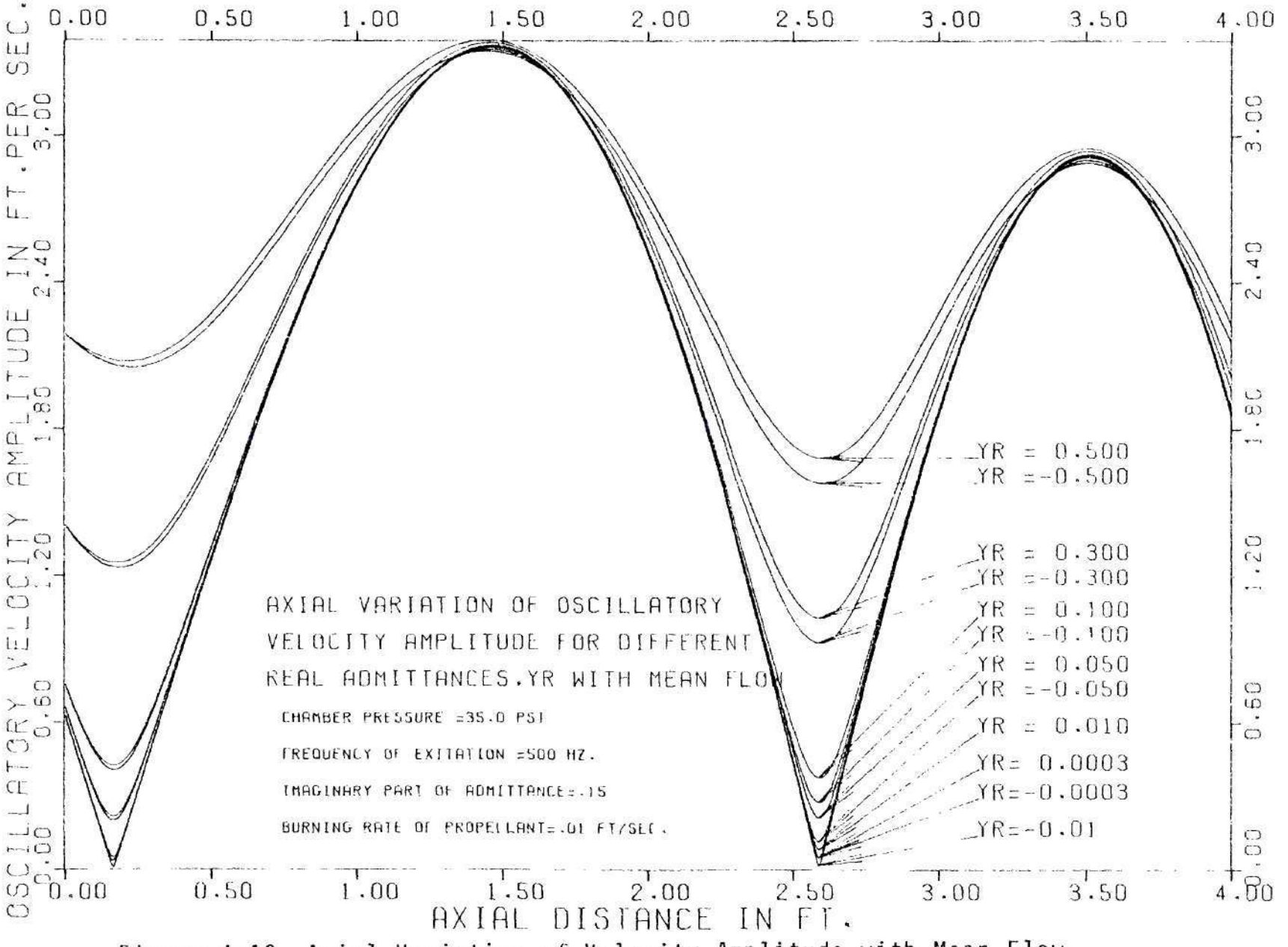

Figure 4-12. Axial Variation of Velocity Amplitude with Mean Flow.

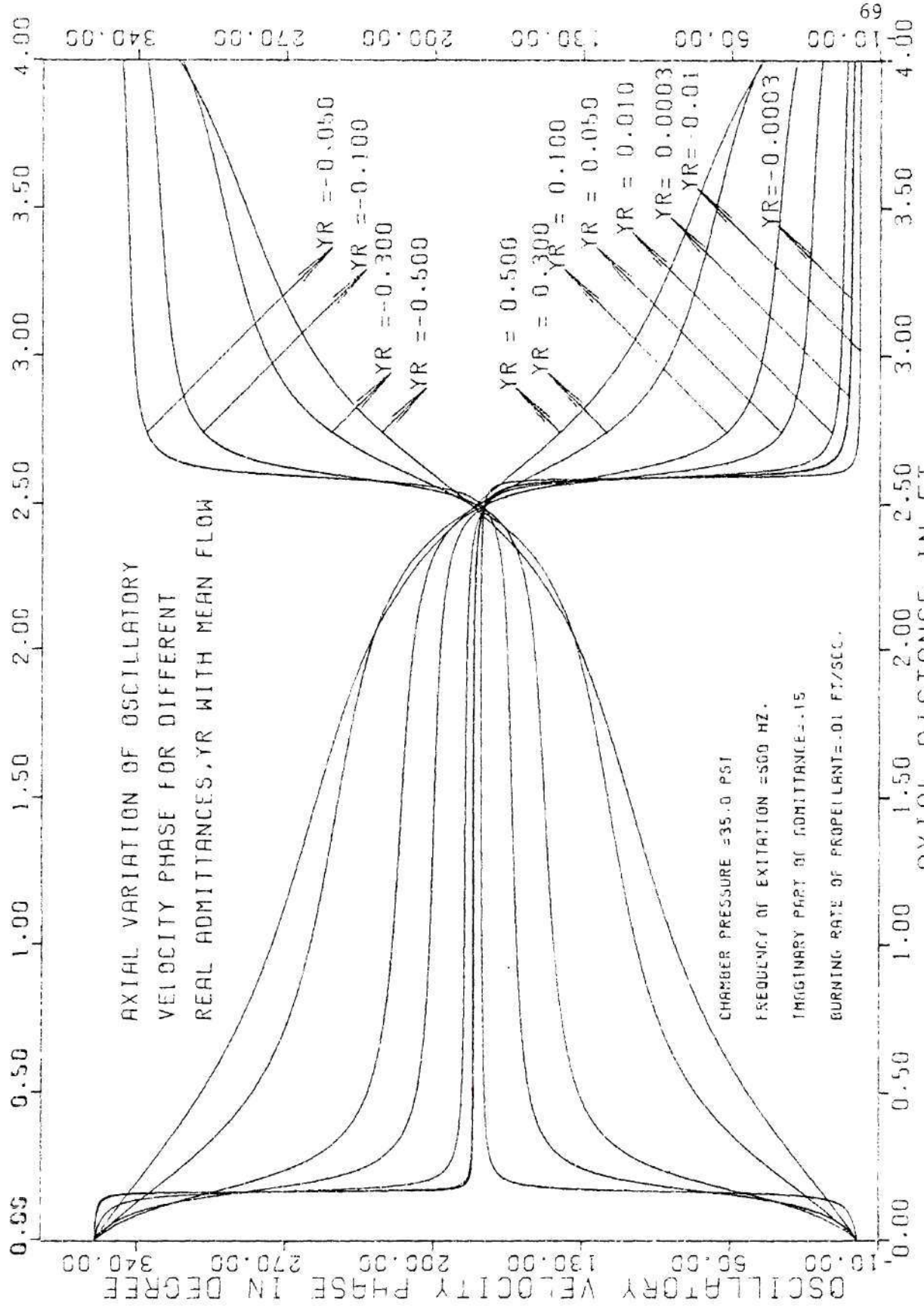

Figure 4-13. Axial Variation of Velocity Phase with Mean Flow.

to those of the oscillatory pressure amplitudes and phases. However, a difference is observed in velocity amplitude plots (i.e., Figures 4-10 and 4-12) compared to the pressure amplitude plots (i.e., Figures 4-2 and 4-4), in that the amplitude of the oscillatory velocity at successive nodes decrease with increasing distance from the propellant surface. Figures 4-14 and 4-15 show the axial variation of oscillatory velocity amplitude and velocity phase respectively for different burning rates of the propellant. The variation of velocity amplitudes and phases with respect to the axial distance are similar to the behavior observed in the pressure amplitude, and phase plots, for different burning rate of propellant (see Figures 4-8 and 4-9).

Mean chamber pressure does not affect the oscillatory pressure amplitude, pressure phase and velocity phase. But the oscillatory velocity amplitude decreases rapidly with the increase of mean chamber pressure (i.e., see Figure 4-16).

The oscillatory density phases for zero mean flow case are quite similar to those of oscillatory pressures (see Figure 4-3). The oscillatory density amplitudes for zero mean flow are plotted in Figure 4-17 for different real admittance values at the propellant surface. These plots closely resemble the oscillatory pressure amplitude plots (i.e., see Figure 4-2) except that the density amplitude increases much more rapidly at successive density antinodes as compared to the growth of pressure amplitudes.

When a mean flow velocity is introduced, the density amplitudes and phases show the superposition of high frequency periodic oscillations

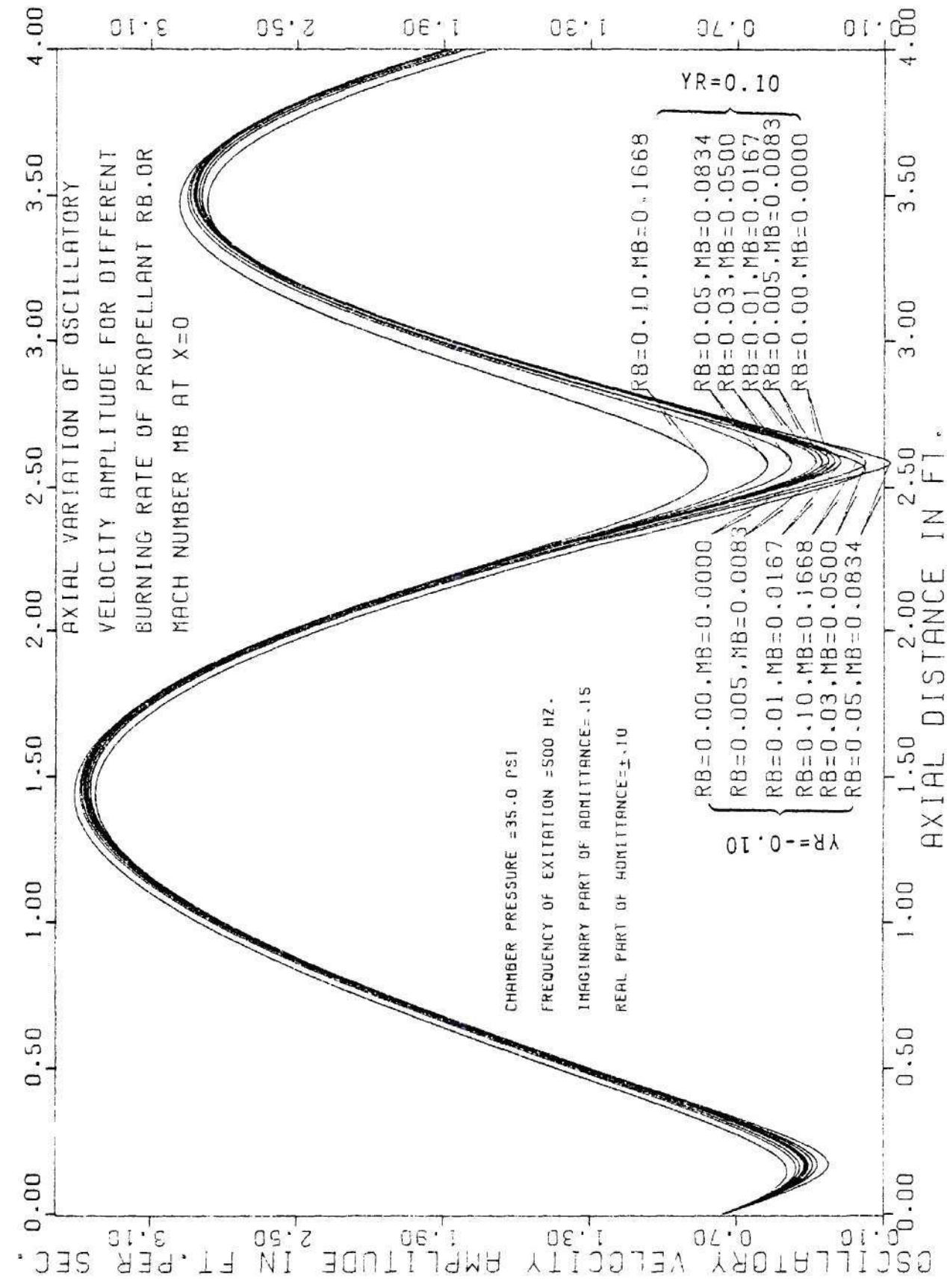

Figure 4-14. Axial Variation of Velocity Amplitude for Different Mean Flows.

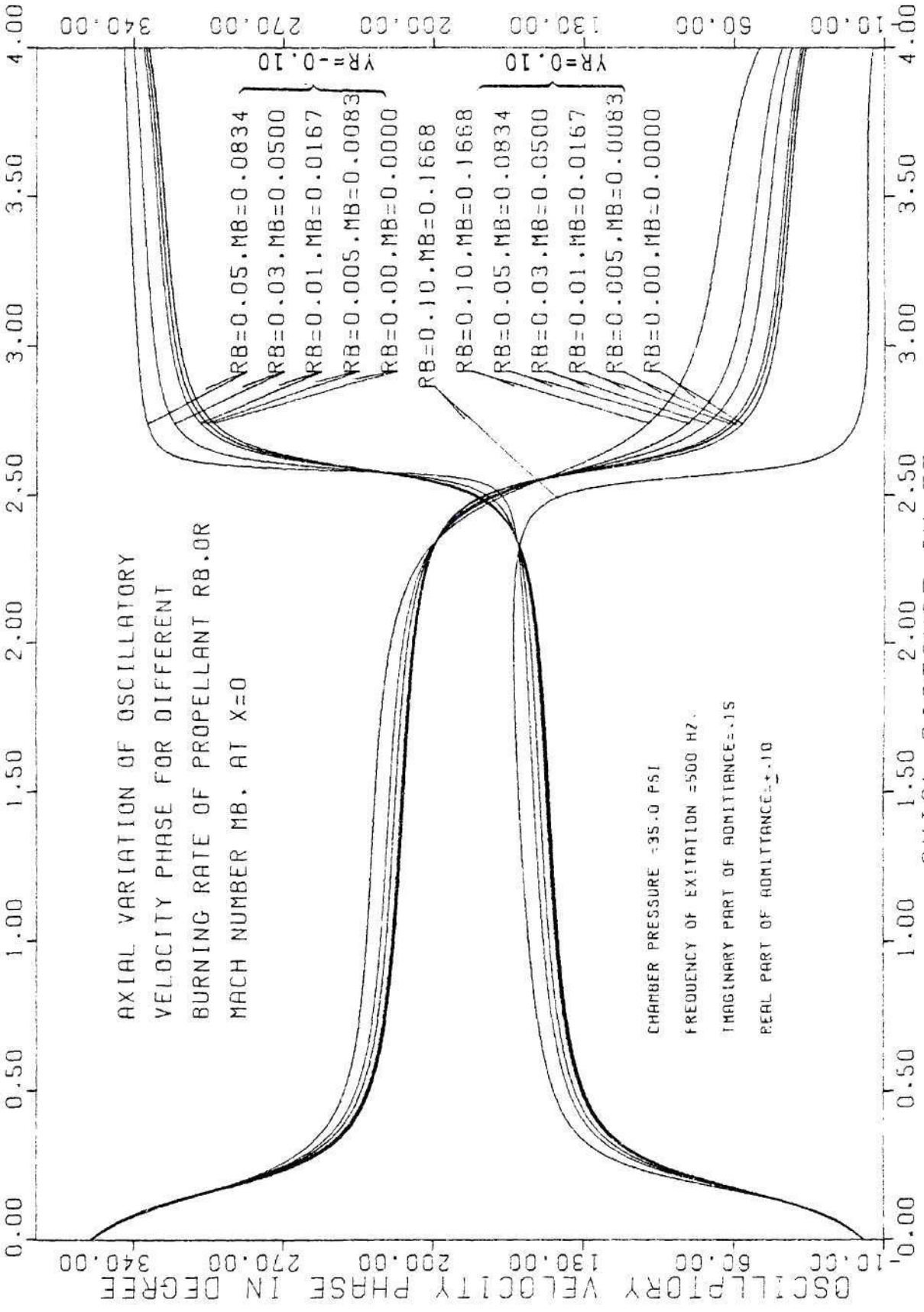

Figure 4-15. Axial Variation of Velocity Phase for Different Mean Flows.

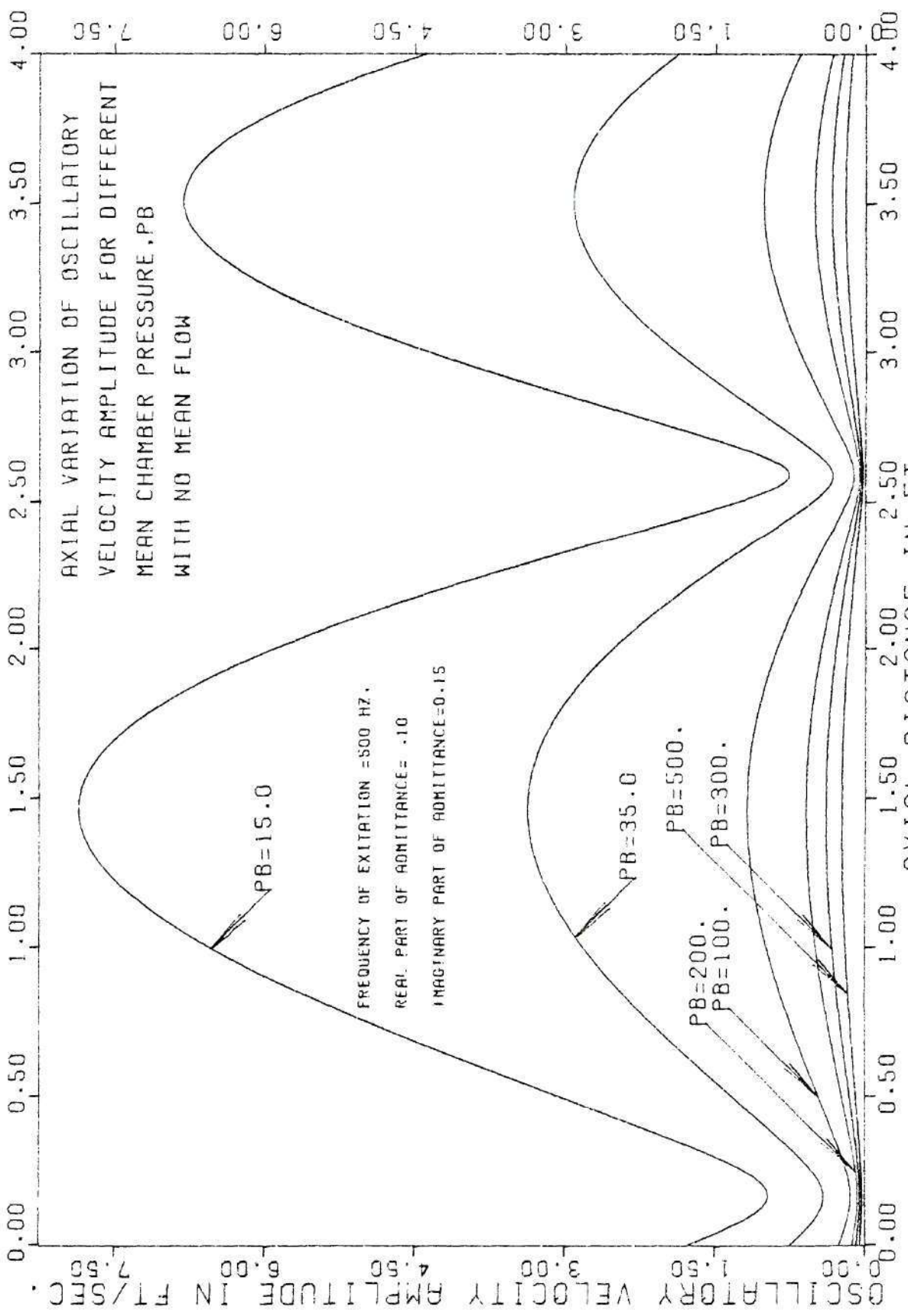

Figure 4-16. Axial Variation of Velocity Amplitude for Different Mean Pressures.

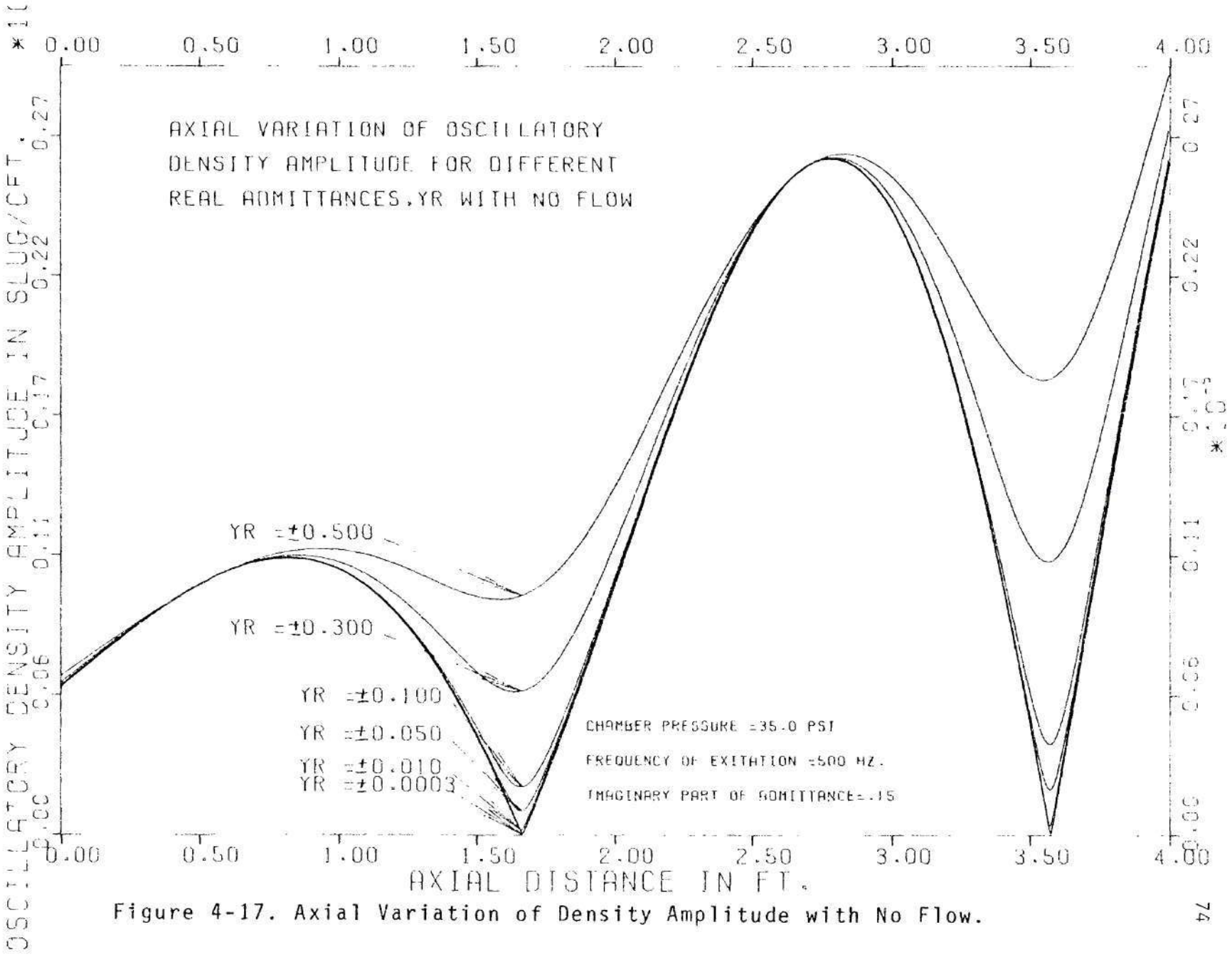

Figure 4-17. Axial Variation of Density Amplitude with No Flow.

(i.e., density waves) on the top of the accustic waves observed in Figures 4-18 and 4-19. This happens due to the presence of entropy waves, propagating with the mean flow speed. The magnitude of these entropy waves increases with increasing magnitude of the real part of the admittances.

Figure 4-20 shows the axial variation of the oscillatory temperature amplitudes for different real admittances when there is no mean flow in the impedance tube. The behavior of these plots are quite similar to those of the oscillatory density (shown in Figure 4-17), with the exception that subsequent temperature maxima decrease with axial distance. Figures 4-21 and 4-22 describe the oscillatory temperature amplitude variation for two different real admittances when a mean velocity is included in the computation. One observes a pattern similar to that seen in the density amplitude behavior; that is, a periodic oscillation is superimposed over the no flow amplitude distribution. The magnitude of these oscillations increase rapidly with the real admittances (i.e., see Figure 4-22). Figures 4-23 shows the axial variation of the oscillatory temperature phase for different real admittances with mean flow. When compared to the oscillatory density phase distributions shown in Figure 4-19, the temperature phase distributions (i.e., Figure 4-23) show a rapidly growing oscillation nearer to the propellant surface, which rapidly dies out with increasing axial distance.

Figures 4-24 and 4-25 show the axial variation of acoustic entropy amplitude and phase respectively for different real parts of the admittances, when there is no mean flow in the impedance tube.

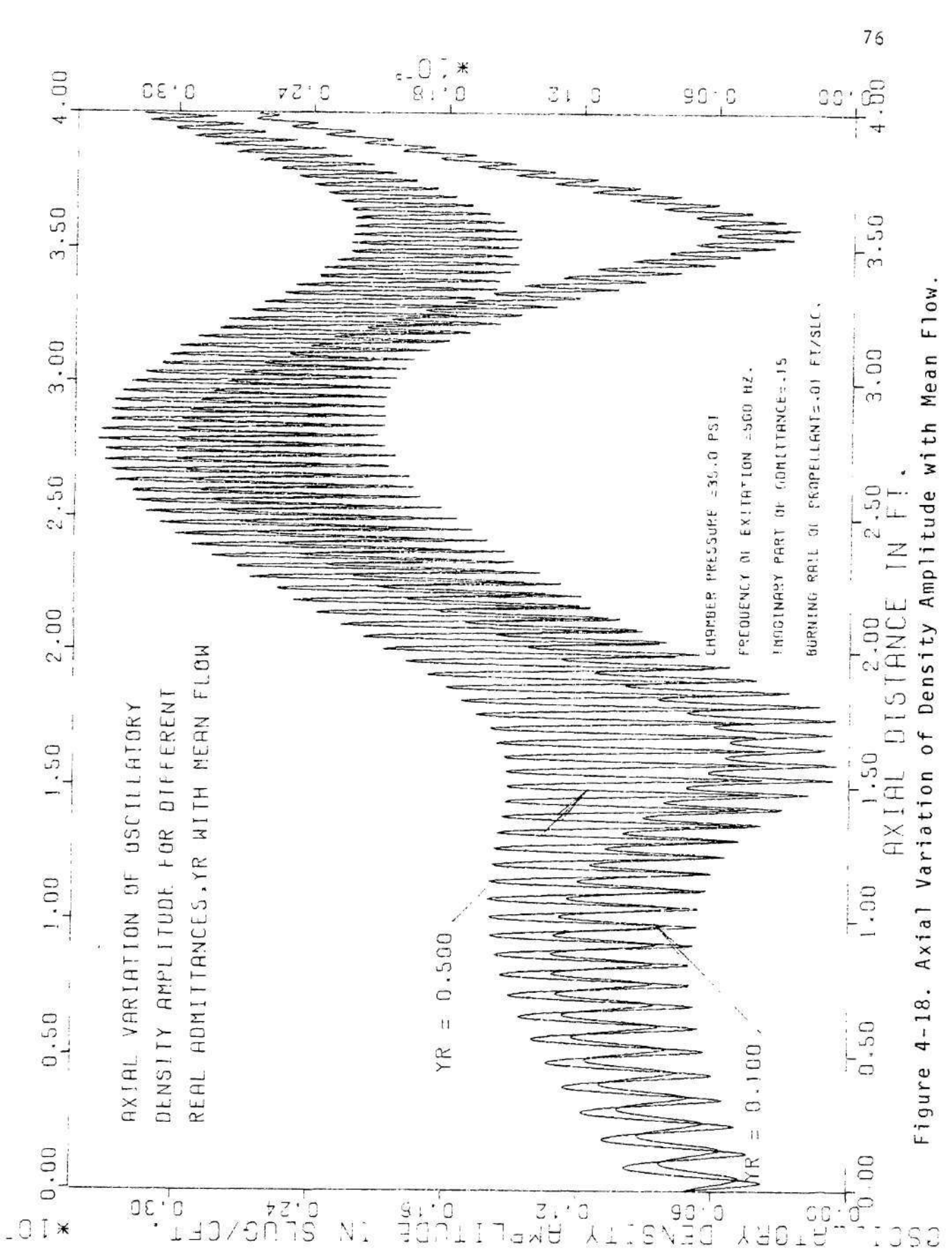

Figure 4-18. Axial Variation of Density Amplitude with Mean Flow.

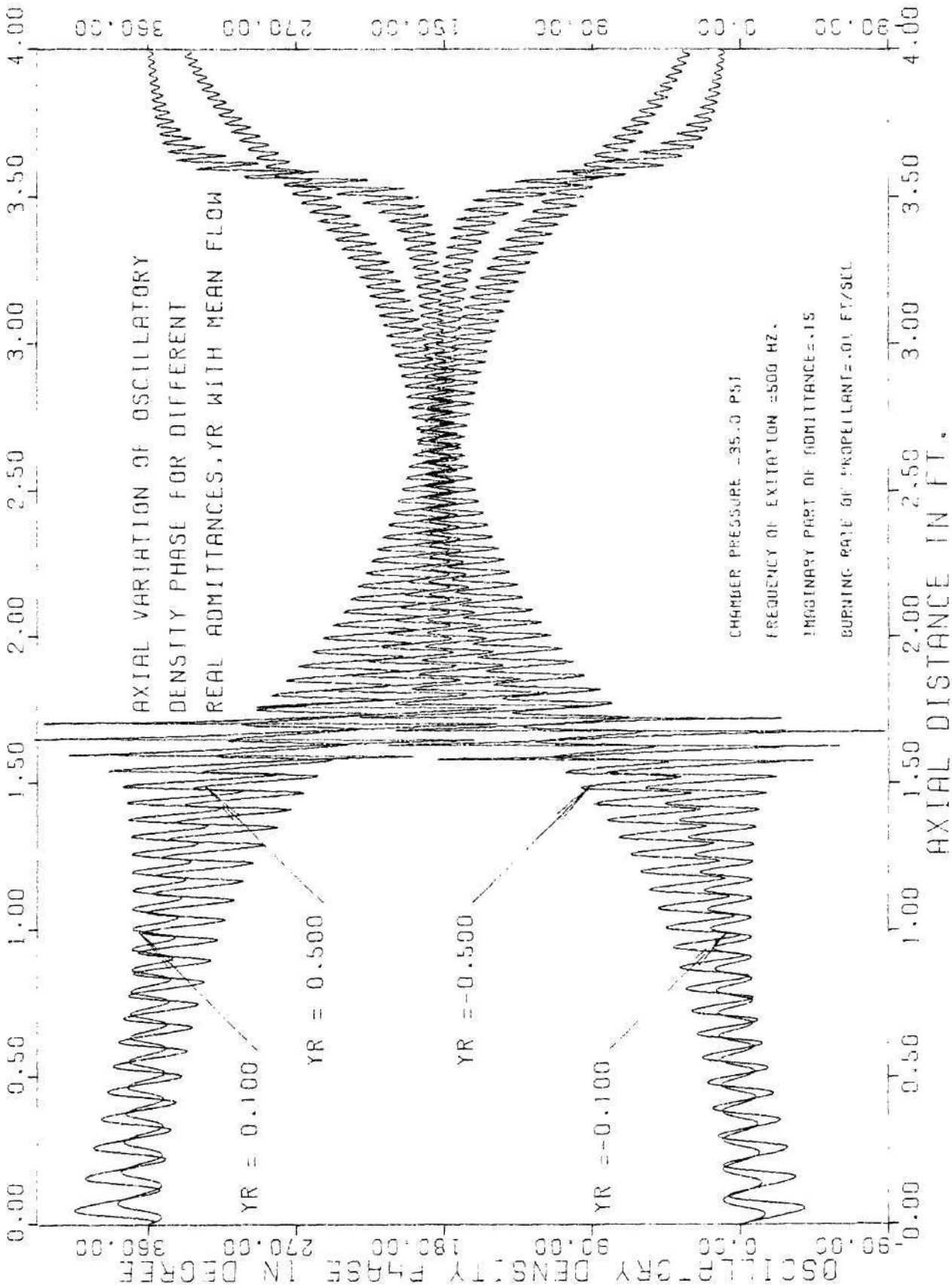

Figure 4-19. Axial Variation of Density Phase with Mean Flow.

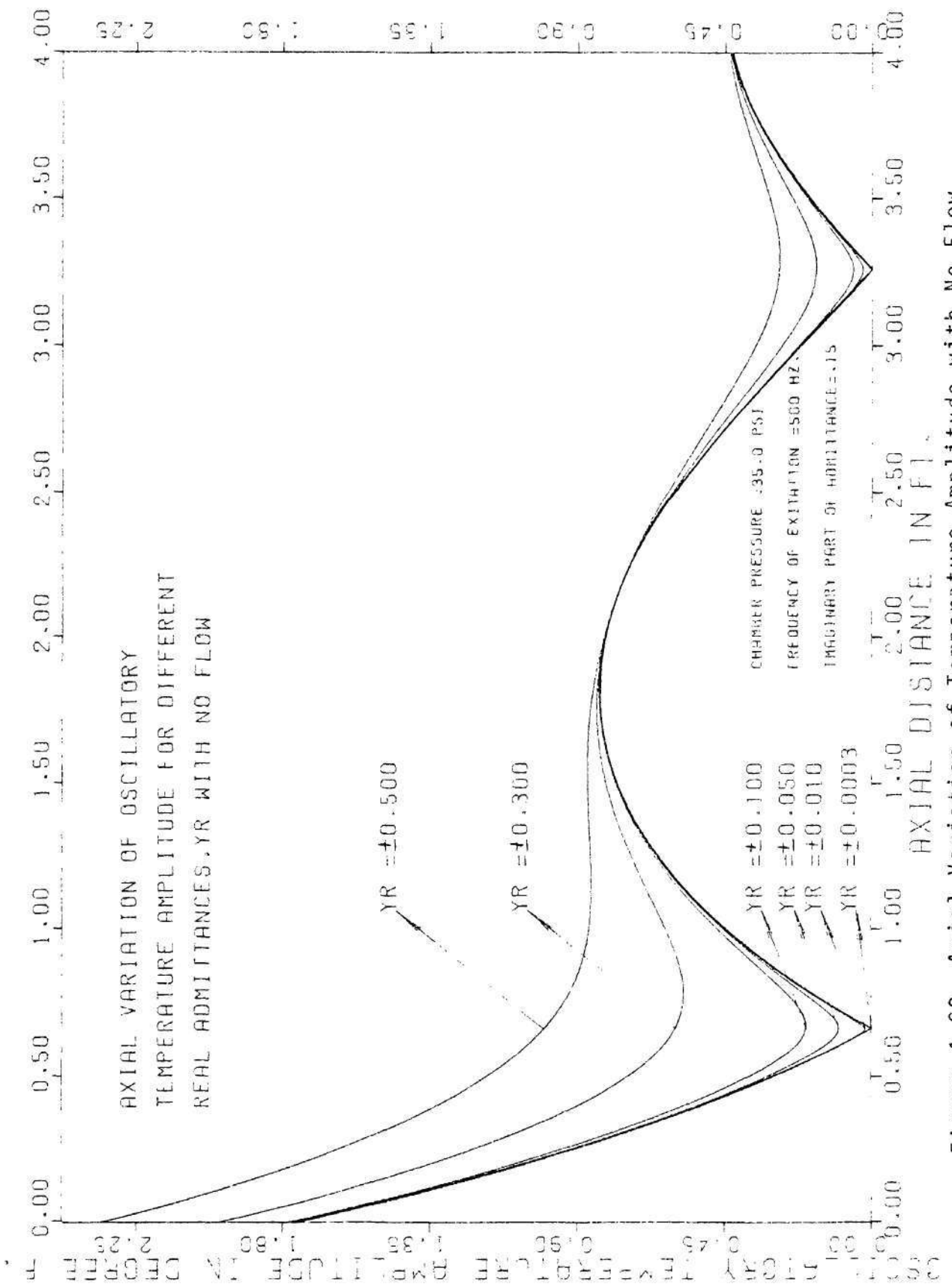

Figure 4-20. Axial Variation of Temperature Amplitude with No Flow.

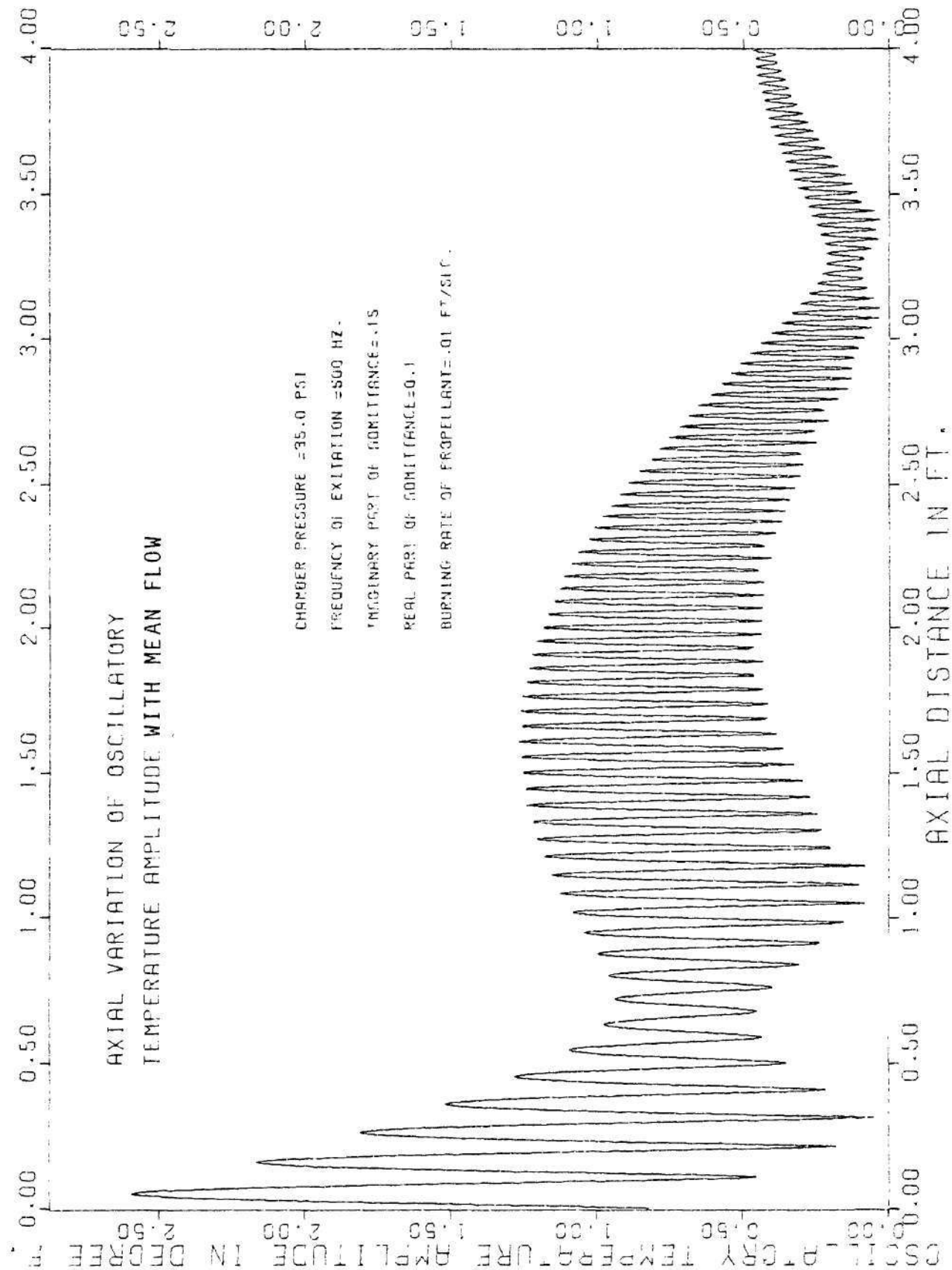

Figure 4-21. Axial Variation of Temperature Amplitude with Mean Flow.

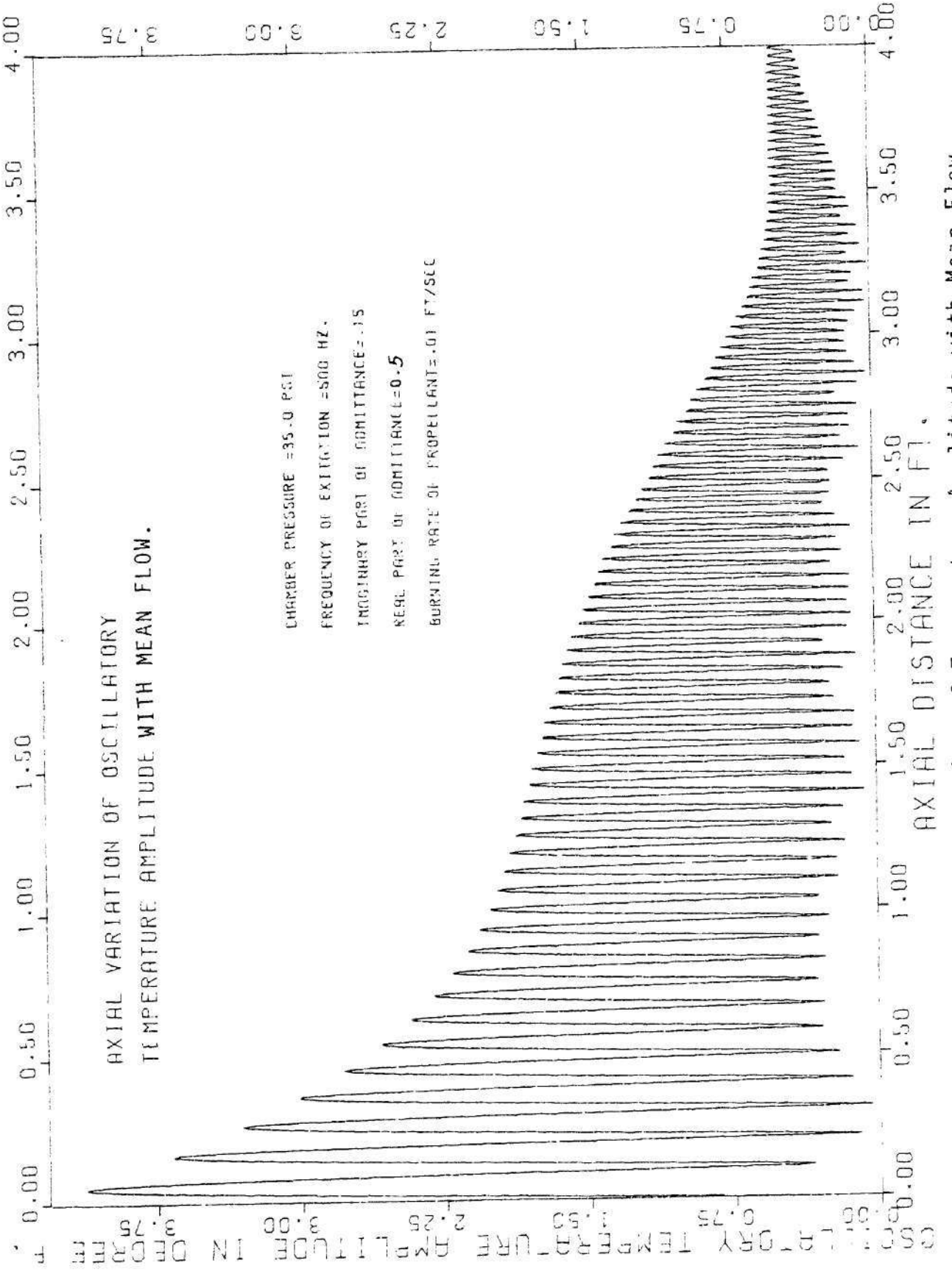

Figure 4-22. Axial Variation of Temperature Amplitude with Mean Flow.

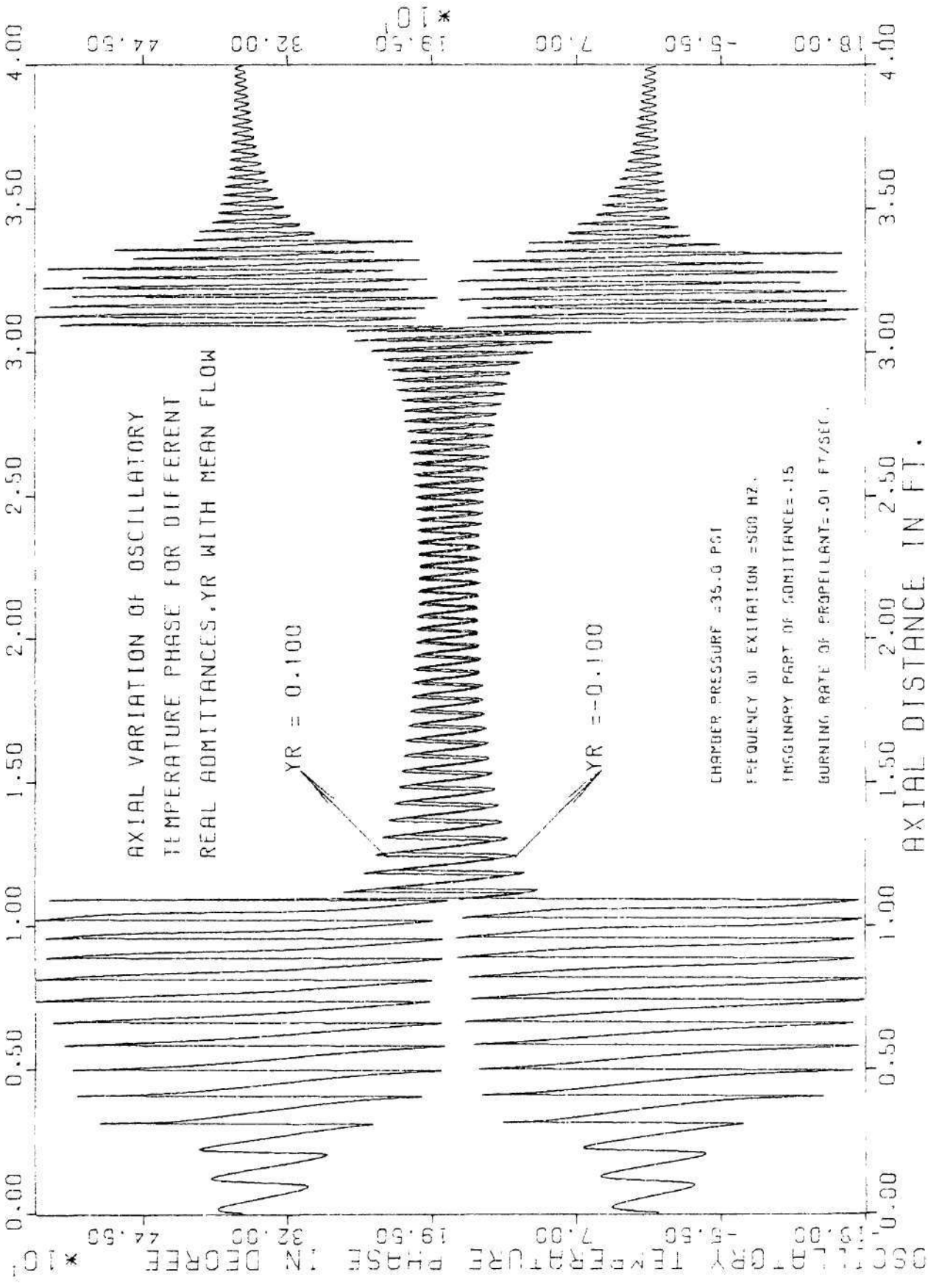

Figure 4-23. Axial Variation of Temperature Phase with Mean Flow.

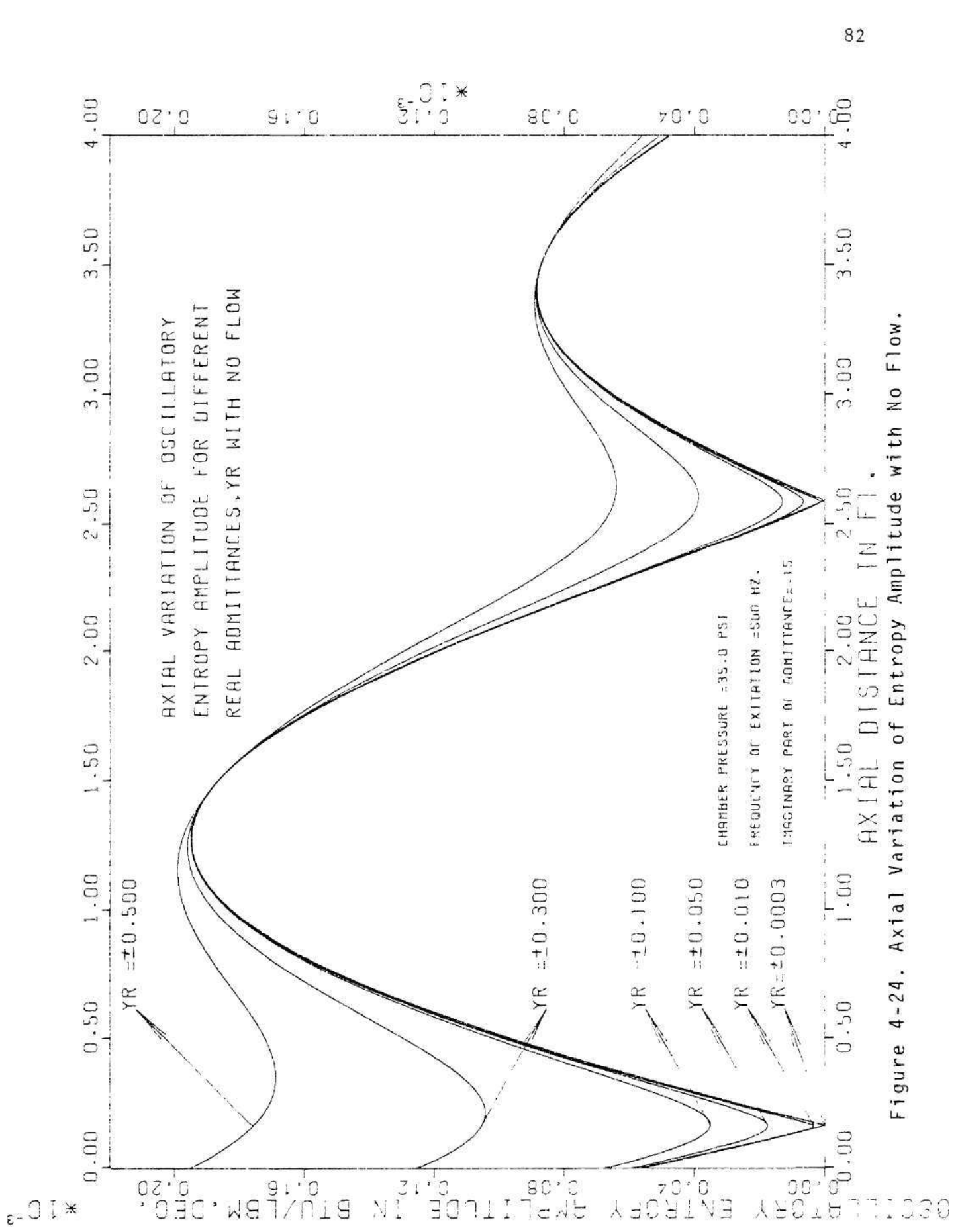

Figure 4-24. Axial Variation of Entropy Amplitude with No Flow.

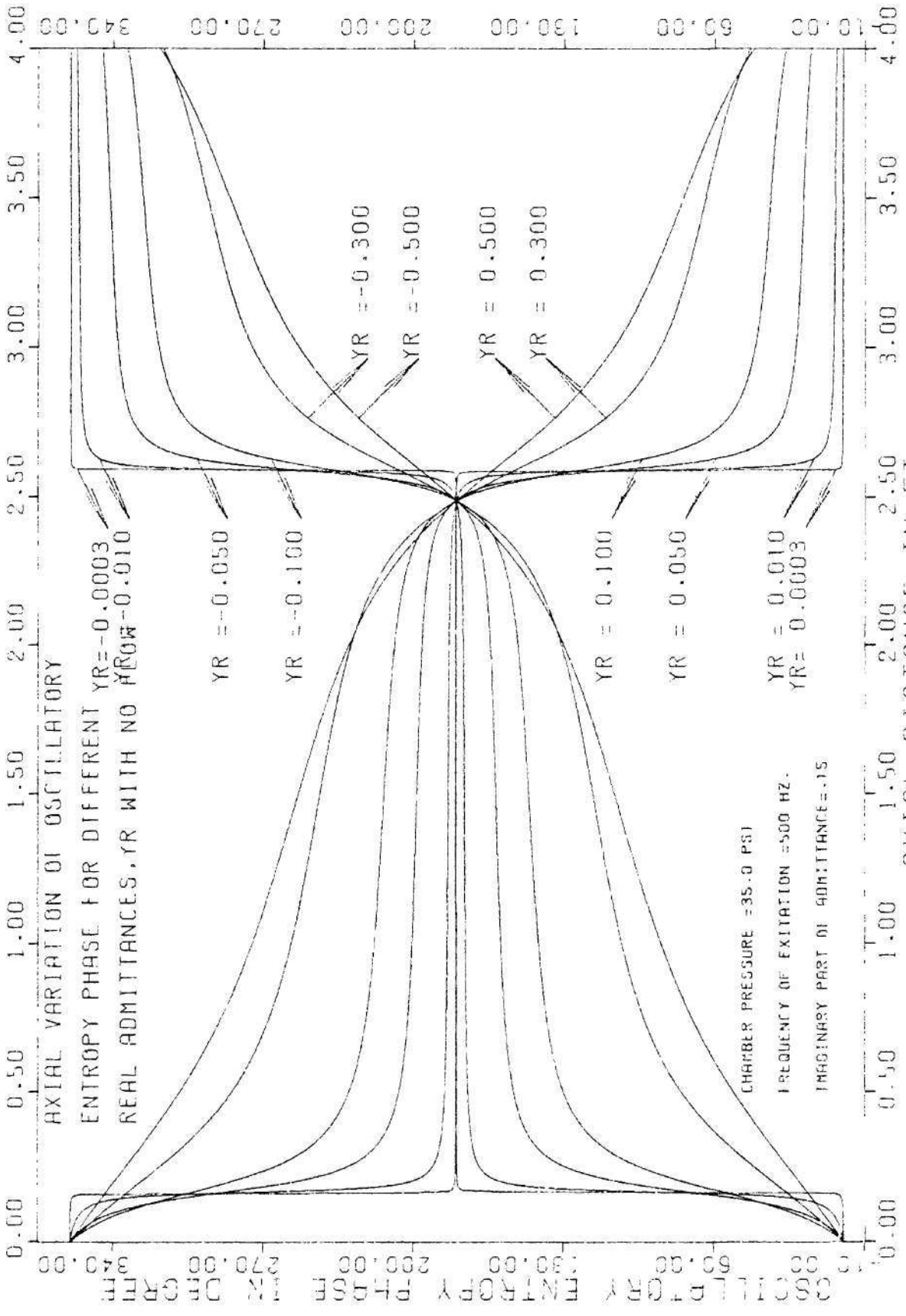

Figure 4-25. Axial Variation of Entropy Phase with No Flow.

The distribution pattern observed in these figures are qualitatively similar to those observed in the plots of the oscillatory temperature amplitude and phase distribution. Figure 4-26 describes the axial distributions of entropy wave when there is a mean flow in the impedance tube. As expected, the presence of a mean flow results in a periodic oscillation that is superimposed upon the "no flow" entropy wave pattern. The amplitudes of the oscillations in Figure 4-26 are very large compared to those observed in the no mean flow case.

Figures 4-27 and 4-28 respectively describe the axial variation of real and imaginary parts of the admittances in the impedance tube for different values of the real part of admittance at the surface of the propellant (i.e., at $x = 0$). Figure 4-27 shows a symmetric variation of real admittance about the x co-ordinate, whereas Figure 4-28 shows the identical distribution of imaginary part of the admittance for the same value of positive and negative real admittances at $x = 0$. The axial variation of the real part of the admittance (i.e., see Figure 4-27) also shows a gradual change along the impedance tube with the exception of the vicinity of the pressure nodes where high peaks are observed. The axial variation of the imaginary part of the admittance (i.e., see Figure 4-28) shows more rapid changes with distance and at pressure nodes the peak moves from a high negative value to a high positive value.

The usefulness of the spatial distributions presented in Figures 4-2 through 4-28 for the pressure, velocity, density, temperature, entropy and the real and imaginary parts of the admittances in the impedance tube can be summarized briefly as follows. (1) The spatial distributions of acoustic pressures in the impedance tube shown in

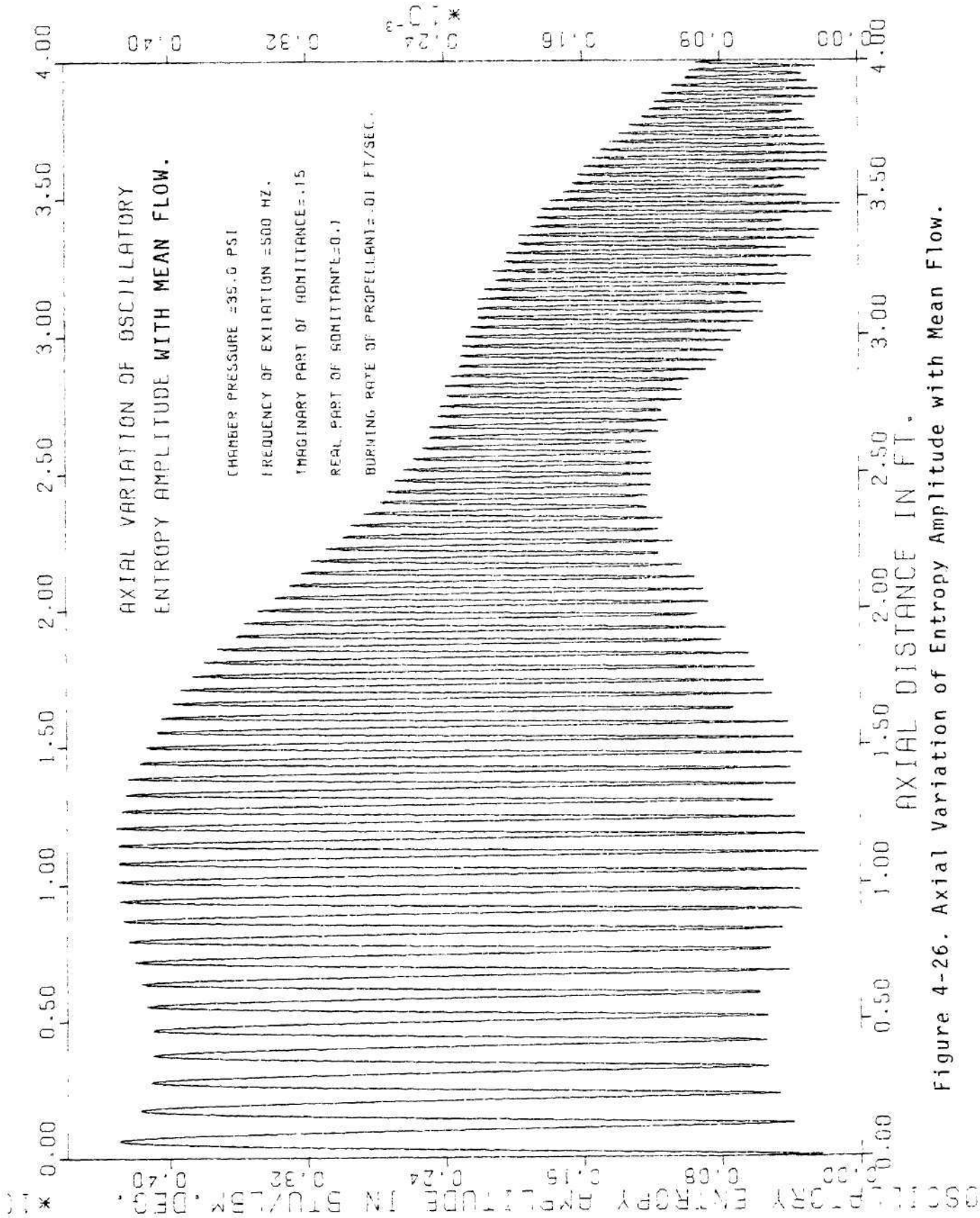

Figure 4-26. Axial Variation of Entropy Amplitude with Mean Flow.

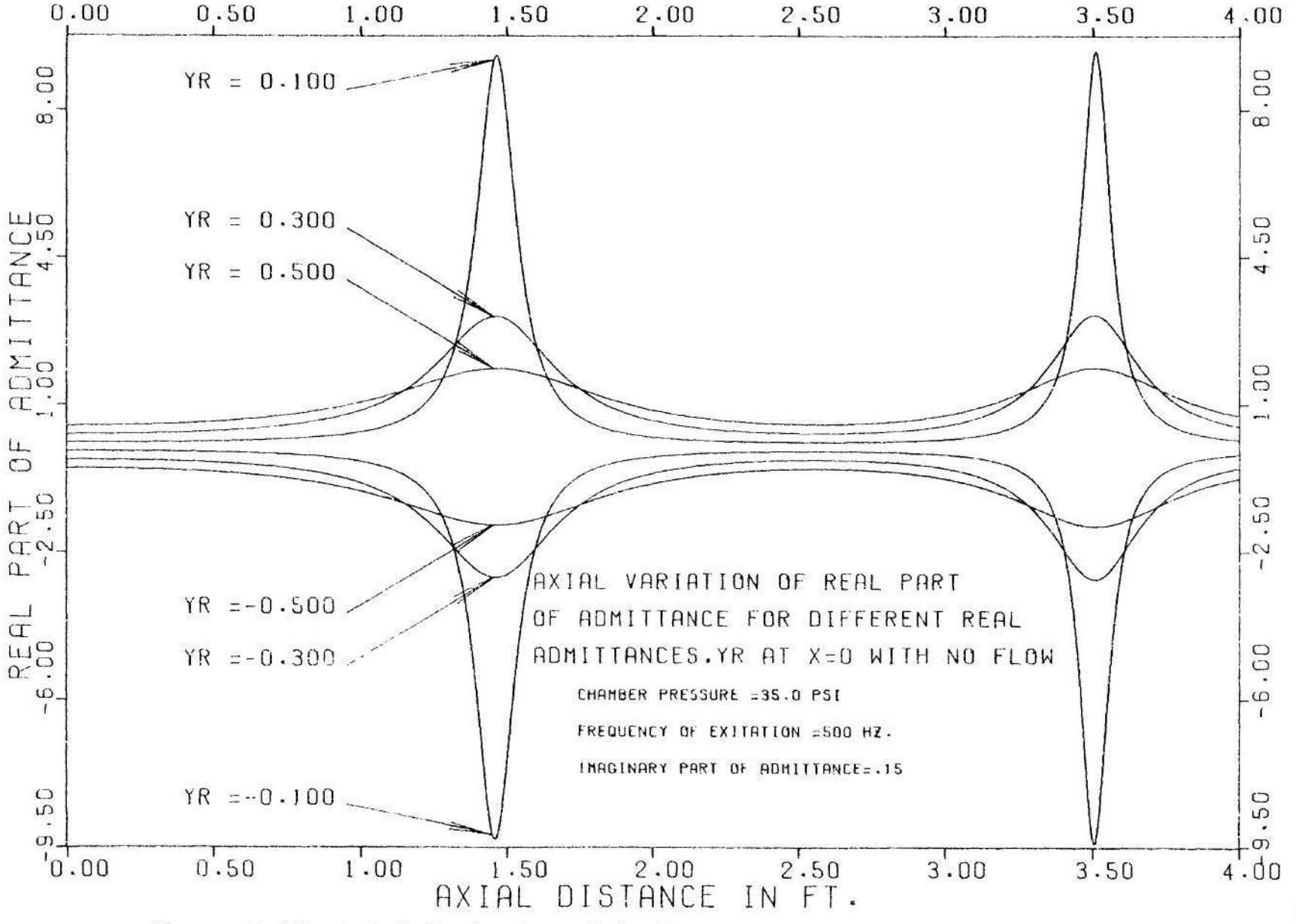

Figure 4-27. Axial Variation of Real Part of Admittance with No Flow.

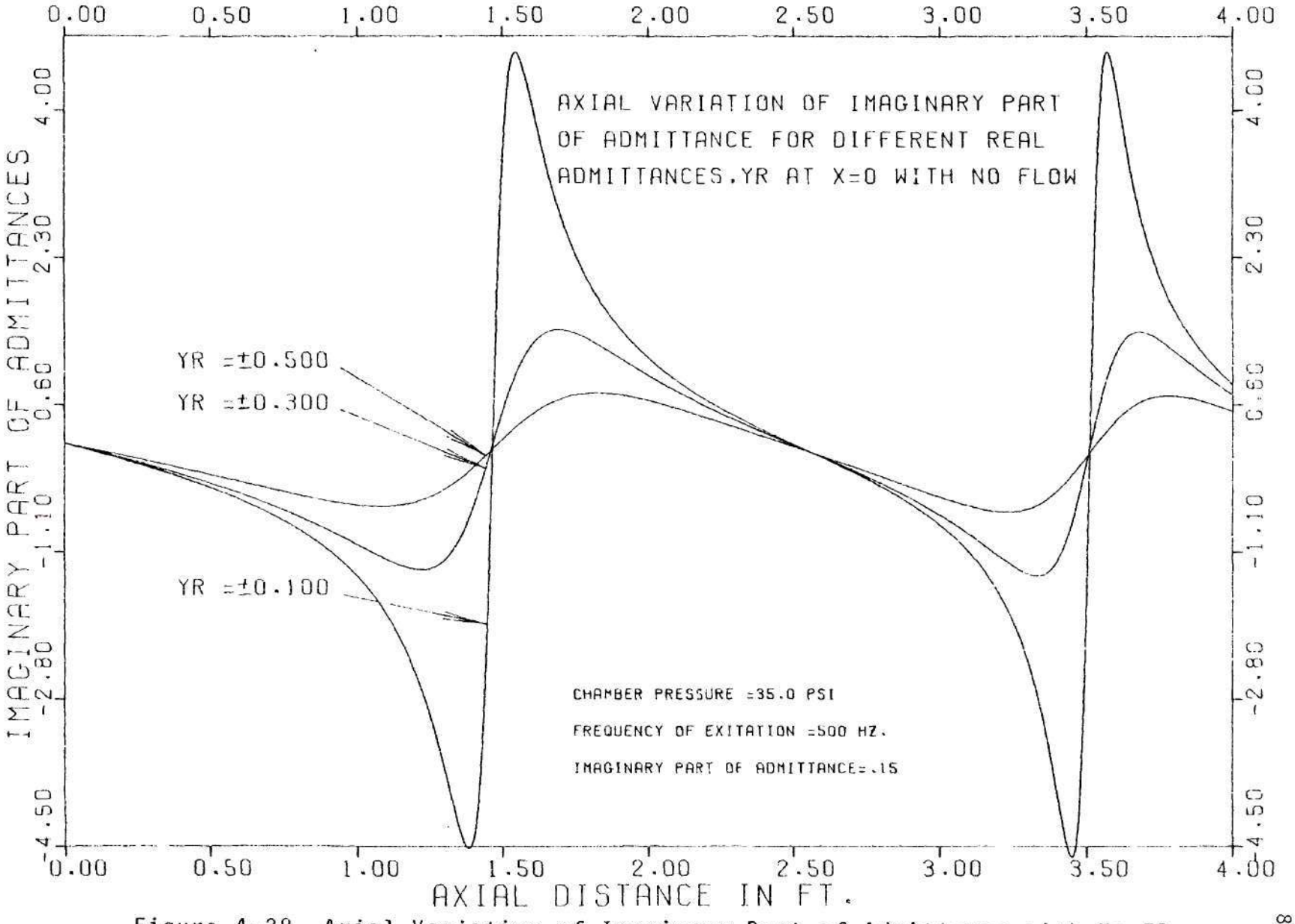

Figure 4-28. Axial Variation of Imaginary Part of Admittance with No Flow.

Figures 4-2 through 4-9 are used to interpret the experimental data to determine the driving capability of a propellant. Figures 4-6 and 4-7 indicate that a change in the imaginary part of the impedance does not alter the driving capability of the propellant. (2) The spatial distributions of oscillatory velocity shown in Figures 4-10 through 4-16 can also be used to interpret the experimental data if the oscillatory velocity distribution is measured in an experiment instead of acoustic pressures. (3) Although the variations of oscillatory density, temperature and entropy, in the impedance tube, shown in Figures 4-17 through 4-26, do not have any direct bearing on the measurement of the admittance, they are obtained in this investigation for academic interest, for a situation, at which the oscillatory pressure or velocity distributions are available from an experiment. (4) Figures 4-27 and 4-28 show the spatial distributions of real and imaginary parts of the admittance. It is observed from these figures that the real part of the admittance becomes maximum at pressure nodes, indicating that an admittance measurement around this location might be more accurate, since its relative magnitude is high. Thus the admittance value at the propellant surface can be determined more accurately from the admittance value at its maximum location.

2. Particulate Matter - Acoustic Wave Interaction

This section presents the results of an investigation carried out to determine the influence of particulate matter upon acoustic behavior of the impedance tube. This analysis has been performed in an effort to understand some of the trends exhibited by the experimental data,

which will be discussed later. The theory of particulate attenuation and dispersion of sound is formulated in a manner that explicitly shows the relaxation character of the problem.[27,28] The analysis presented herein is based on the following assumptions: (1) the gas is thermally and calorically perfect; (2) the density of the particles is much greater than the density of the surrounding gas; (3) mass transfer between particles and gas is absent (i.e., evaporation, condensation and chemical reaction are excluded); (4) the total heat-transfer and drag force between the particulate and gas phases is the sum of the effects due to each particle. This assumption implies that the particle diameter is much smaller than the distance between the particles and it restricts the theory to low particle-volume concentrations; (5) the fluctuations of pressure, density, and temperature produced by the acoustic waves are assumed to be sufficiently small as compared with their mean values so that their products can be neglected. Similarly, the fluid velocity is assumed to be much smaller than the speed of sound.

Using the above assumptions, one-dimensional wave motion through a stationary gas phase containing spherical particles in suspension is investigated by solving the following system of linearized conservation equations:[28]

Gas Phase Continuity:
$$\frac{\partial \rho'}{\partial t} + u' \frac{d\bar{\rho}}{dx} + \bar{\rho} \frac{\partial u'}{\partial x} = 0 \qquad (4\text{-}11)$$

Gas Phase Momentum:
$$\bar{\rho} \frac{\partial u'}{\partial t} + \frac{\partial p'}{\partial x} = \bar{n} F_p \qquad (4\text{-}12)$$

Gas Phase Energy: $$\frac{C_v}{R}\{\frac{\partial p'}{\partial t} - \bar{c}^2(\frac{\partial \rho'}{\partial t} + u'\frac{d\bar{\rho}}{dx})\} = \bar{n}Q_p + \bar{n}F_p(u_p' - u') \quad (4\text{-}13)$$

Particulate Continuity: $$\frac{\partial \rho_p'}{\partial t} + \bar{n}m_p\frac{\partial u_p'}{\partial x} = 0 \quad (4\text{-}14)$$

Particulate Momentum: $$m_p\frac{\partial u_p'}{\partial t} = -F_p \quad (4\text{-}15)$$

Particulate Energy: $$m_p C_p'[\frac{\partial T_p'}{\partial t} + u_p'\frac{d\bar{T}}{dx}] = -Q_p \quad (4\text{-}16)$$

Equation of State: $$p' = \bar{R}(\rho'\bar{T} + \bar{\rho}T') \quad (4\text{-}17)$$

Assuming a low Reynolds number flow, the drag of the particles can be expressed by Stokes' law for the motion of a sphere in a viscous fluid and the heat transfer coefficient h can be taken to equal k/r, where k is the coefficient of thermal conductivity of the gas and r is the particle radius. Thus,[28]

$$F_p = \frac{6\pi\mu r}{g}(u_p' - u') \quad (4\text{-}18)$$

and

$$Q_p = 4\pi rk(T_p' - T') \quad (4\text{-}19)$$

The dynamic relaxation time of the particle can be expressed as

$$\tau_d = 2r^2\bar{\rho}_p/9\mu \quad (4\text{-}20)$$

where the thermal relaxation time of the particle is given by[28]

$$\tau_t = P_r C_p' r^2 \bar{\rho}_p/3\mu C_p$$

or

$$\tau_t = \frac{3}{2}\left(\frac{C'_p}{C_p}\right) P_r \, \tau_d \tag{4-21}$$

Using the above expressions, the momentum and energy equations for the particles can be rewritten as:

$$\frac{\partial u'_p}{\partial t} = - (u'_p - u')/\tau_d \tag{4-22}$$

and

$$\frac{\partial T'_p}{\partial t} + u'_p \frac{d\bar{T}}{dx} = - (T'_p - T')\tau_t \tag{4-23}$$

Assuming periodic time behavior of u'_p and T'_p (e.g., $u' \alpha e^{i\omega t}$), Equations (4-22) and (4-23) can be used to obtain the following results.

$$u'_p = u'/(1 + i\omega\tau_d) \tag{4-24}$$

$$T'_p = (T' - \tau_t \, u'_p \frac{d\bar{T}}{dx})/(1 + i\omega\tau_t) \tag{4-25}$$

Rewriting Equation (4-19) in the form

$$T' = \frac{1}{R\bar{\rho}} \, p' - \frac{\bar{p}}{\bar{\rho}} \rho' \tag{4-26}$$

and using Equations (4-24) through (4-26), F_p and Q_p can be expressed as

$$F_p = - \frac{6\pi\mu r}{g} \{i\omega\tau_d/(1 + i\omega\tau_d)\} u' \tag{4-27}$$

$$Q_p = -4\pi rk\{\frac{\tau_t}{(1+i\omega\tau_t)}\,[\,\frac{i\omega}{R\bar{\rho}}\,(p' - \frac{\bar{p}}{\bar{\rho}}\,\rho') + \frac{u'}{(1+i\omega\tau_d)}\,\frac{d\bar{T}}{dx}\,]\} \qquad (4\text{-}28)$$

Neglecting $\bar{n}\,F_p\,(u_p' - u')$ in Equation (4-13) and assuming periodic time behavior of u', p' and ρ', Equations (4-11) through (4-13) can be rewritten as follows:

Continuity:
$$i\omega\rho' + \frac{d\bar{\rho}}{dx}\,u' + \bar{\rho}\,\frac{du'}{dx} = 0 \qquad (4\text{-}29)$$

Momentum:
$$i\omega\bar{\rho}u' + \frac{dp'}{dx} = \bar{n}F_p \qquad (4\text{-}30)$$

Energy:
$$i\omega\rho' - \bar{c}^{-2}(i\omega p' + \frac{d\bar{\rho}}{dx}\,u') = \frac{R\bar{n}}{C_v}\,Q_p \qquad (4\text{-}31)$$

Solving Equations (4-29) through (4-31) for $\frac{dp'}{dx}$ and $\frac{du'}{dx}$ yields

$$\frac{dp'}{dx} = A_{11}\,p' + A_{12}\,u' \qquad (4\text{-}32)$$

$$\frac{du'}{dx} = A_{21}\,p' + A_{22}\,u' \qquad (4\text{-}33)$$

where

$$A_{11} = 0$$

$$A_{12} = -\frac{6\pi\mu r\bar{n}}{g}\,\frac{i\omega\tau_d}{1 + i\omega\tau_d} - i\omega\bar{\rho}$$

$$A_{21} = -\frac{i\omega}{\bar{\rho}\,\bar{c}^{-2}}\,\frac{1 + C_o}{1 + C_o/\nu} \qquad (4\text{-}34)$$

$$A_{22} = \frac{RC_o}{\bar{c}^{-2}}\,\frac{d\bar{T}}{dx}\,\frac{i\omega\tau_d}{(1 + i\omega\tau_d)(1 + C_o/\nu)}$$

and $$C_o = \frac{4\pi r \bar{kn}}{C_v \bar{\rho}} \frac{\tau_t}{1 + i\omega\tau_t}$$

To investigate the effect of the particulate matter upon the wave structure in the impedance tube, Equations (4-32) and (4-33) are solved for different boundary conditions at x = 0 and different particle loadings in the gas phase. In the present investigation the particle diameter is taken as 1 micron and the particle properties are chosen to be close to those of carbon particles; the chosen particles and gas phase properties are listed in Table 4-2.

Table 4-2. Properties Associated with Two Phase Flow

C'_p	specific heat of the particle = 0.17 BTU/lb. °F
$\bar{\rho}_p$	density of the particle = 160 lb./ft.^{3}
γ	specific heat ratio of the gas = 1.28
C_p	specific heat of the gas at constant pressure = 0.45 BTU/lb. °F
P_r	Prandtl No. = 0.8
μ	coefficient of viscosity of the gas = $5.925 \times 10^{-4}(T°R/6273)^{.66}$ lbm/ft.sec.
k	thermal conductivity = $C_p \mu/P_r$ BTU/sec./ft.^{2}(°F/ft.)
$\bar{n}$	particle density = $\bar{\rho}_g / \bar{\rho}_p V_p$
R	gas constant = 2480 ft. lb_f/slug °R

The computed wave structures are plotted in Figures 4-29 through 4-32. In Figure 4-29 the dependence of the acoustic pressure phases are plotted for an assumed admittance value of .0002 + i 0.15 at the burning propellant surface (i.e., x = 0) for various particle loadings. For zero particle loading, the phase plot indicates wave energy addition (i.e., driving) at the propellant surface as discussed earlier in this thesis when the real part of propellant surface admittance is positive. With a small particle loading, the slope of the phase-distance curve starts changing, beginning at the propellant surface where the slope remains the same as long as the propellant surface remains unchanged. The change in slope as one moves away from the propellant is due to the wave energy dissipation by the particle-wave motion interaction. Further increase in the particle loading results in a complete reversal of the slope of the phase-distance curve from partially negative values to completely positive values. It should be emphasized, however, that in all of these cases, the slope of phase-distance curves does not change at the propellant surface, indicating the same wave energy addition. Figure 4-30 shows a plot similar to the one presented in Figure 4-29 but for higher positive value of the real part of the surface admittance. A comparison of the two indicates that with an increase in the value of the real part of the propellant admittance, wave energy is transmitted from left to right for all the investigated particle loadings. Figure 4-31 describes the dependence of the phase-distance curve upon the real part of the propellant surface admittance. Trends similar to those observed in the previous figures

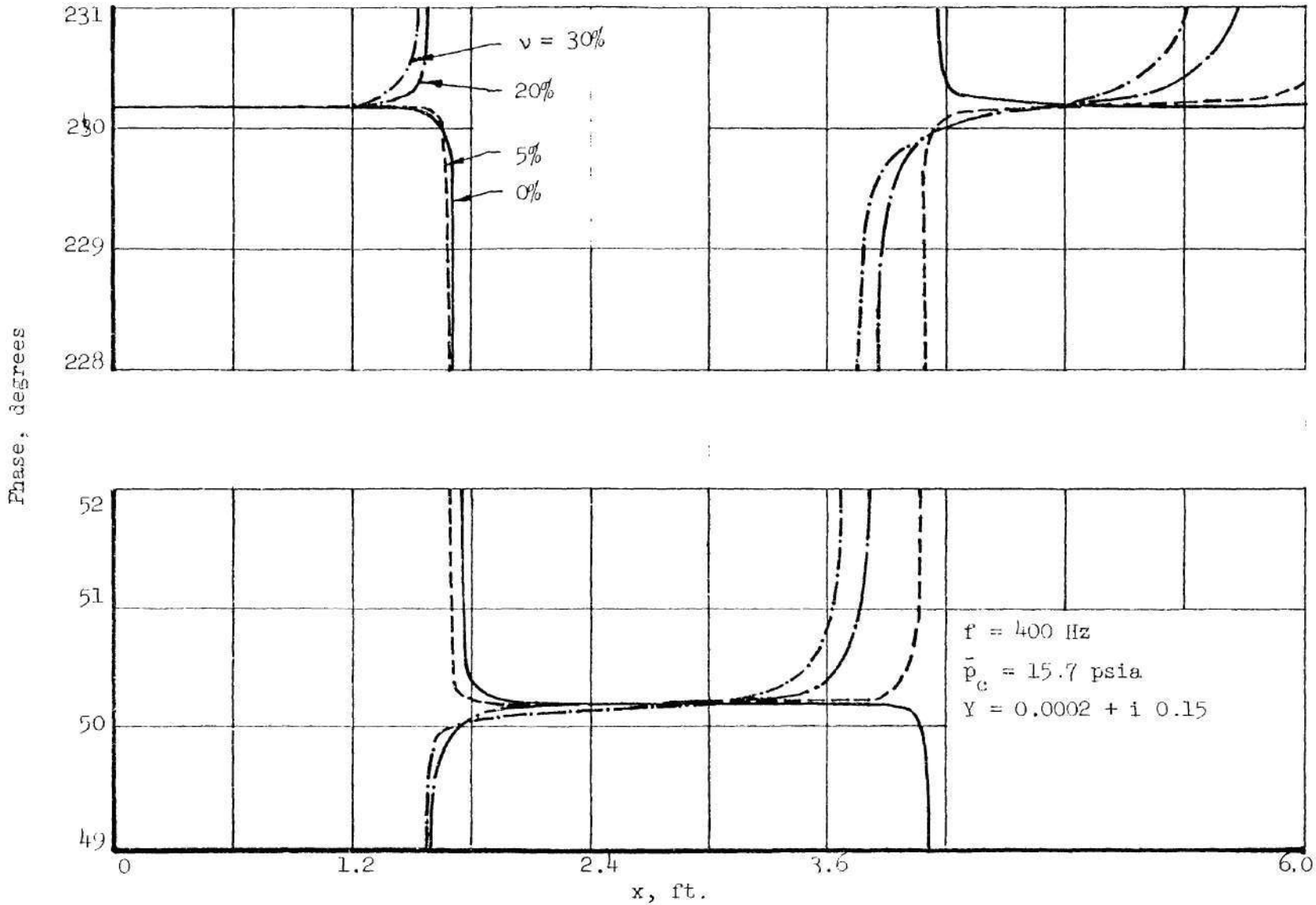

Figure 4-29. Dependence of Pressure Phase Distribution Upon Particulate Attenuation For a Given Y

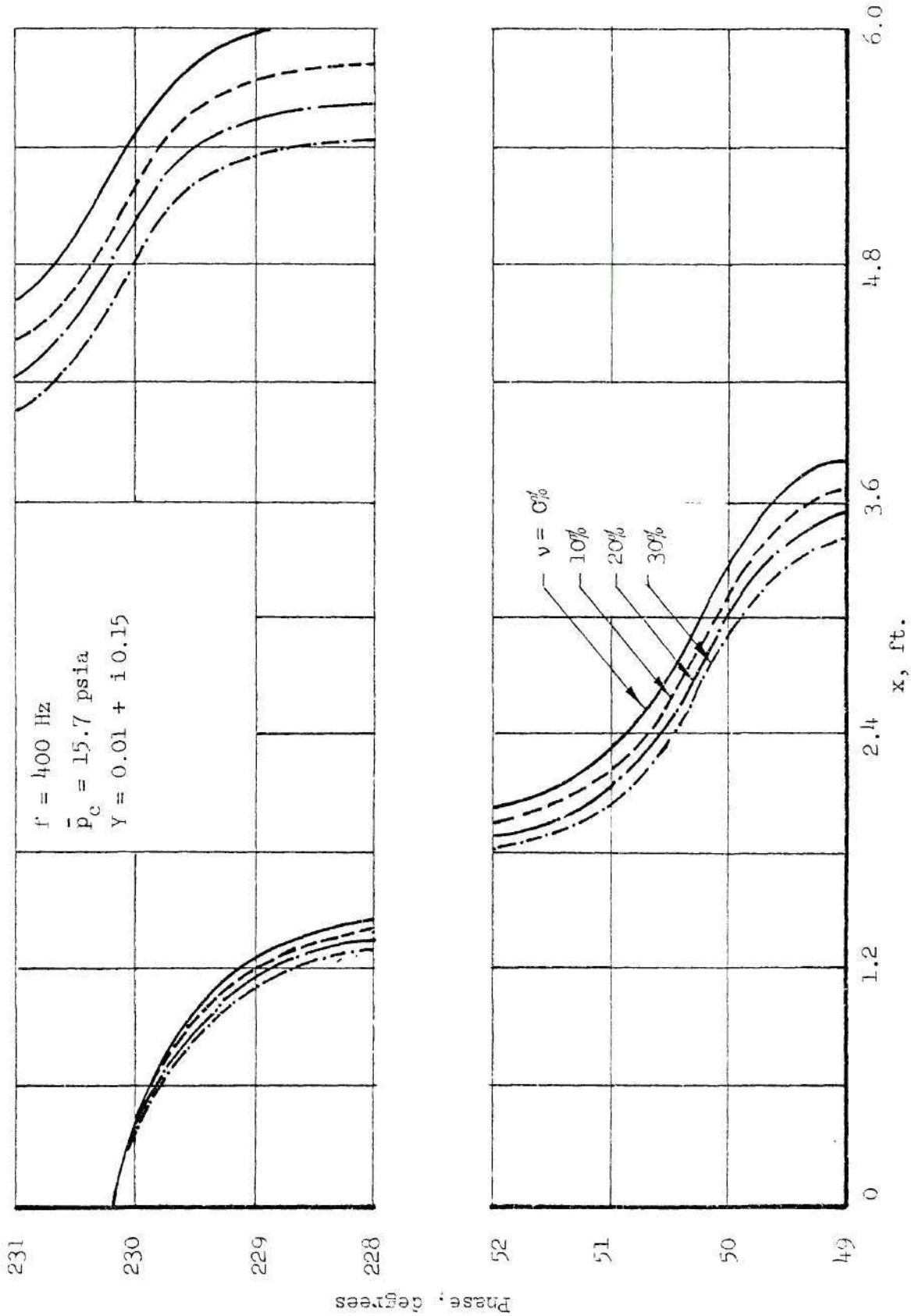

Figure 4-30 Dependence of Pressure Phase Distribution Upon Particle Attenuation for a Given Y

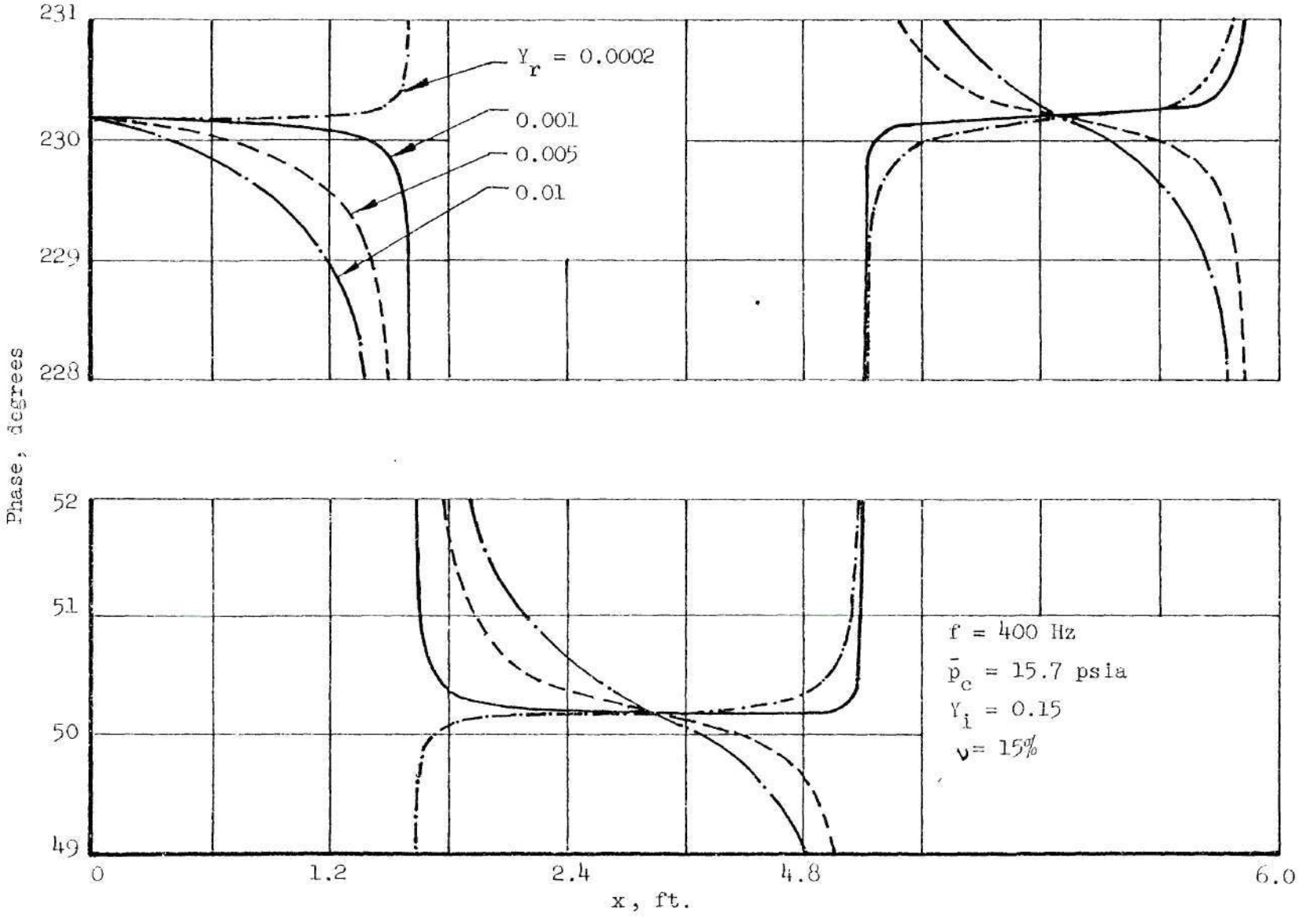

Figure 4-31. Dependence of Axial Pressure Phase Distribution Upon Y_r, for A Given ν

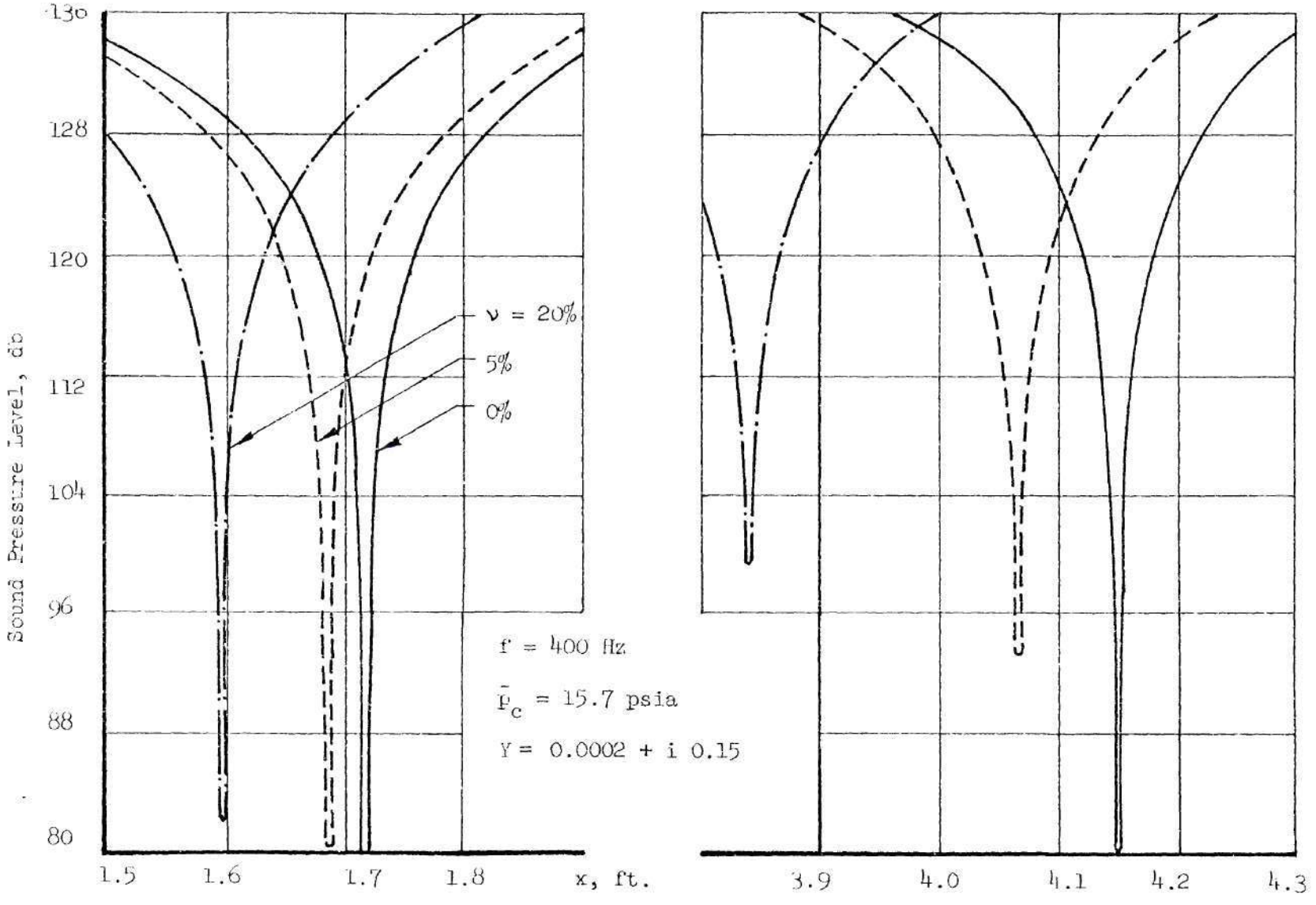

Figure 4-32 Dependence of Pressure Amplitude Distribution Upon ν

may also be noted in this figure. Figure 4-32 presents a plot of the standing wave amplitude for different particle loadings. Examination of this figure shows that a higher value of the particle loading reduces the wave length and increases the pressure amplitude at the nodal points.

Though the particulate attenuation analysis explains some of the trends exhibited by the experimental data, it is not possible to account for these losses in the data reduction scheme as the informations regarding the particles (i.e., particle density, particle size, etc.) present in the flow are not evaluated in the present experimental study. However, the acoustic losses in the flow field due to viscous dissipation and gas phase attenuation (i.e., due to presence of particles) can be accounted for in the conservation equations by introducing an overall bulk loss coefficient, which is proportional to the oscillatory velocity (see Equations (3-27) through (3-30)). The values of loss coefficients are evaluated from the pressure data which are measured experimentally in this study, as discussed in Chapter III.

To investigate the effect of the bulk loss coefficient upon the wave structure in the impedance tube, Equations (3-27) through (3-29) are solved for different boundary conditions at $x = 0$ and different bulk loss coefficients. The computed wave structures are plotted in Figures 4-33 through 4-36. The dependence of the acoustic pressure amplitudes and phases are plotted in Figures 4-33 and 4-34 respectively for an assumed admittance value of $0.05 + i\ 0.15$ at the burning propellant surface for various loss coefficients, G. Examination of Figure 4-33

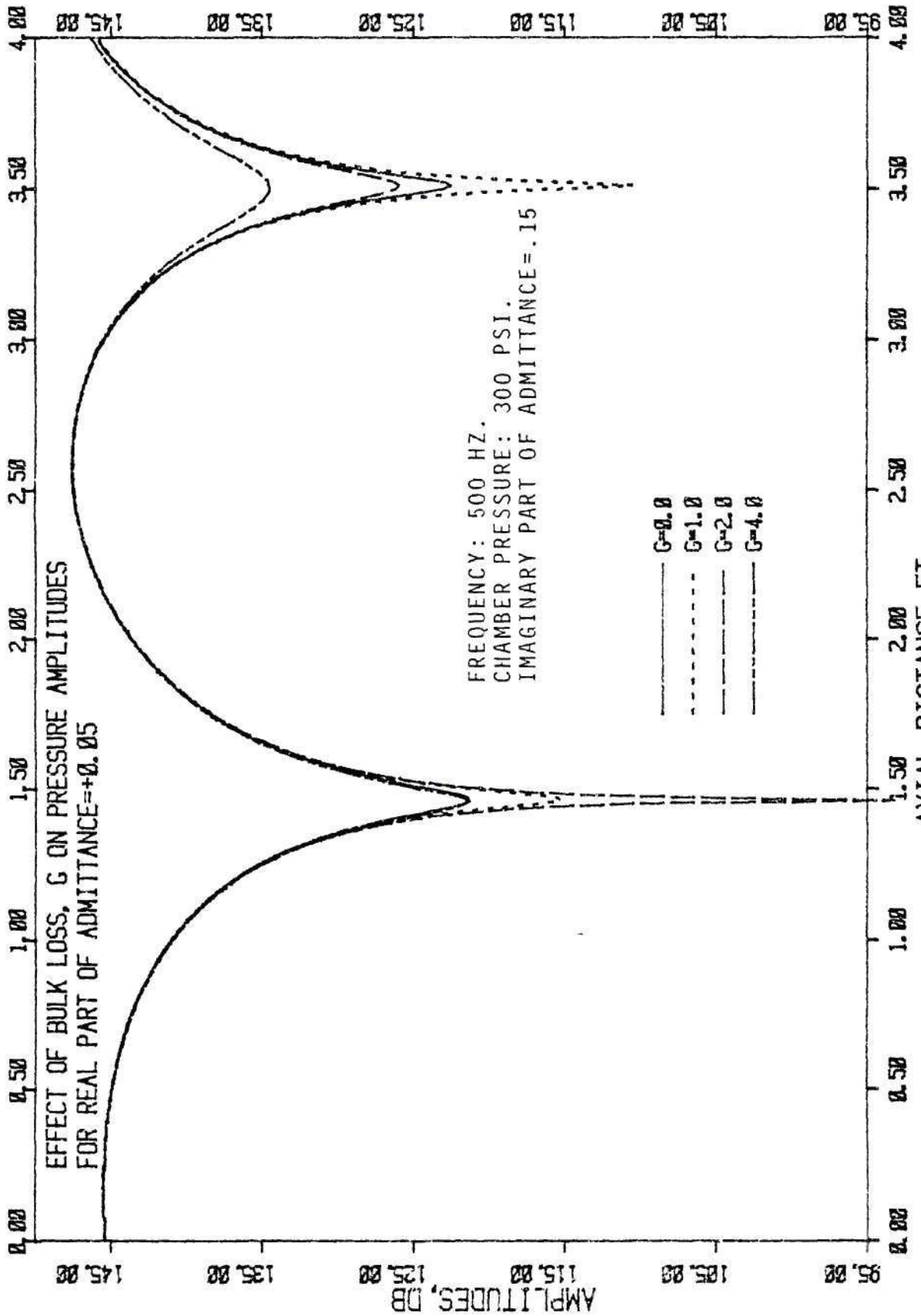

Figure 4-33. Axial Variation of Pressure Amplitude with No Flow.

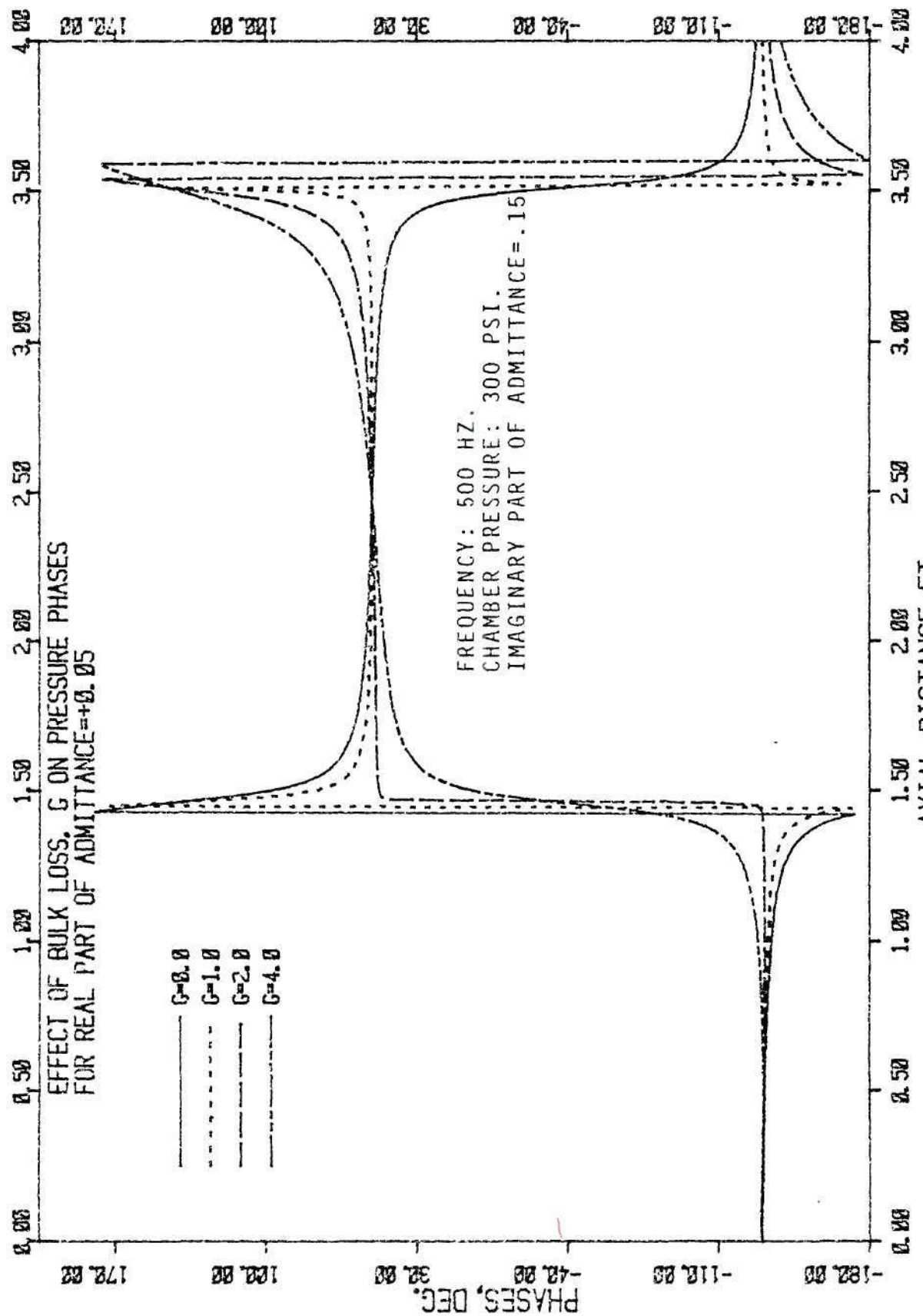

Figure 4-34. Axial Variation of Pressure Phase with No Flow.

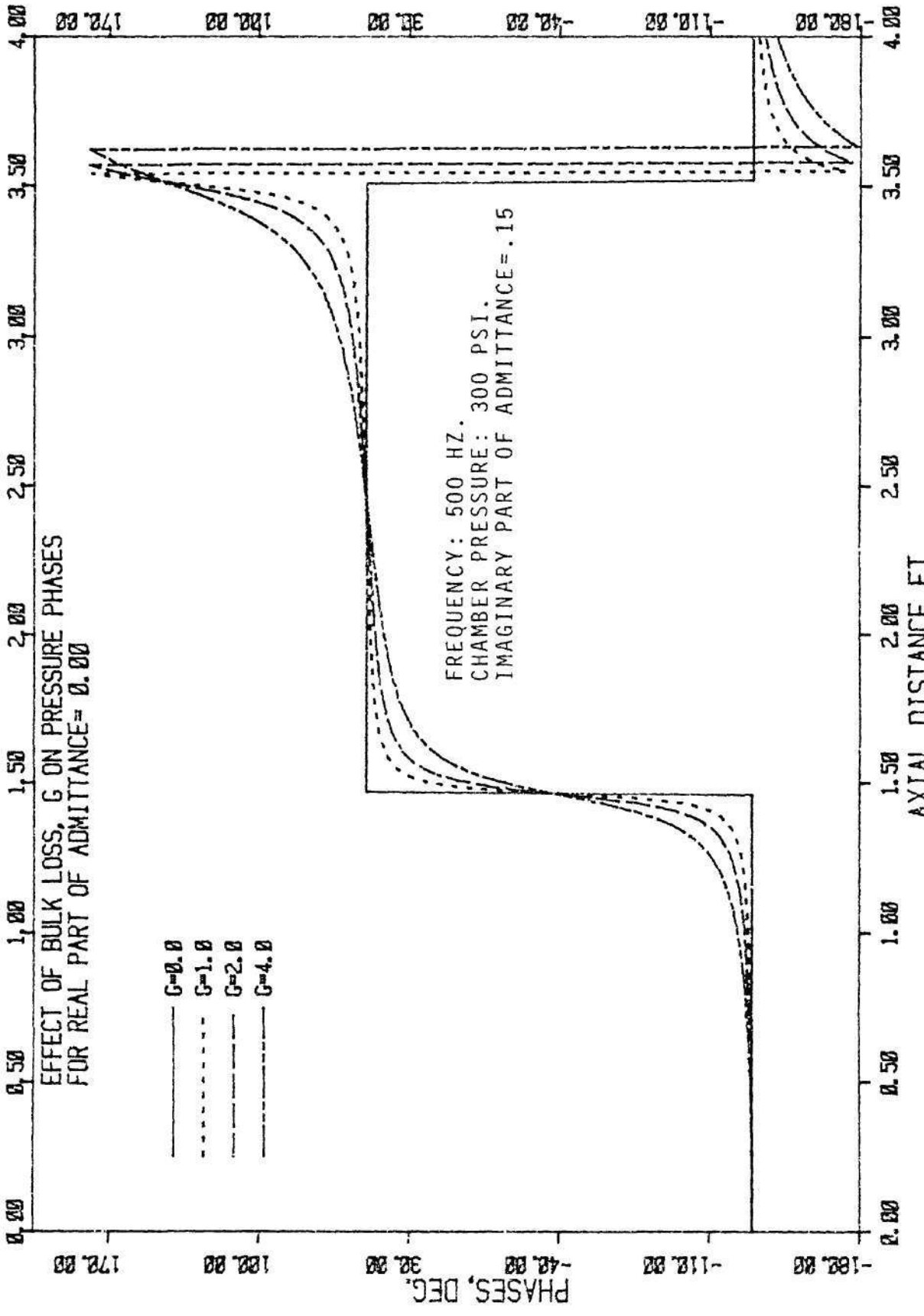

Figure 4-35. Axial Variation of Pressure Phase with No Flow.

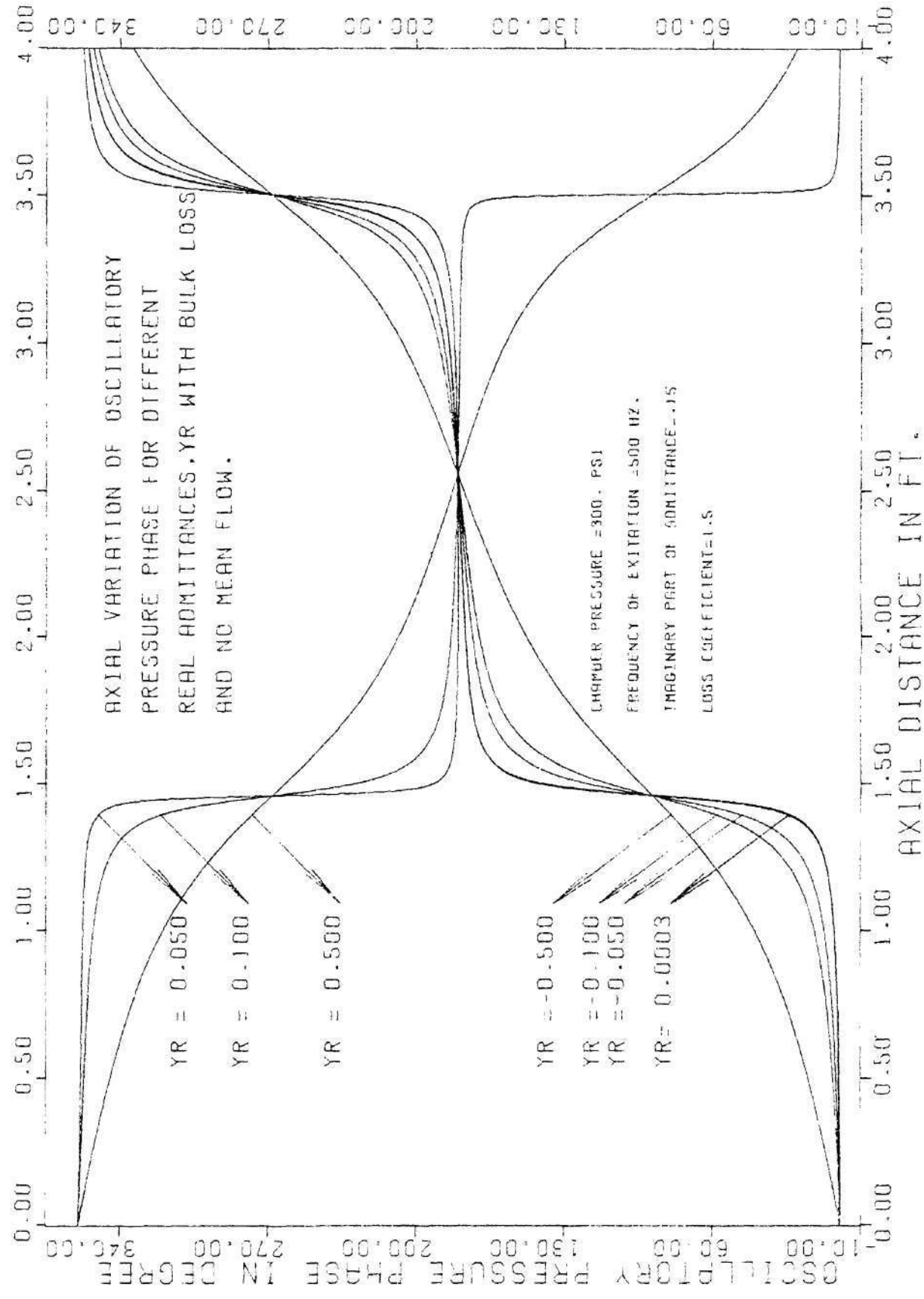

Figure 4-36. Axial Variation of Pressure Phase with No Flow.

shows that for loss coefficient G = 1, the pressure amplitude at first node goes down, since the effective value of the real part of admittance becomes smaller. For higher values of G the effective real part of admittances become negative but their magnitudes are higher. So the pressure amplitudes at the first nodal point start increasing compared to that at G = 1. Figure 4-35 shows a plot similar to the one presented in Figure 4-34 but with a zero value of the real part of admittance. In this case a square type phase-distance distribution is obtained for zero loss coefficient and for any other value of loss coefficient the shape of phase-distance curve becomes positive (i.e., damping). Figure 4-36 describes the dependence of the phase-distance curve upon the real part of the propellant surface admittance for a fixed loss coefficient.

3. Dependence of the Impedance Tube Wave Structure Upon the Propellant Self-Noise

The study described in this section has been conducted in an effort to explain some of the unexpected results which were obtained during an experimental phase of this program that was conducted at atmospheric pressure. Briefly, experiments conducted with two different exhaust conditions downstream of the acoustic drivers produced different wave structures in front of the propellant surface. This result was completely unexpected and it could not be explained by the commonly used propellant surface boundary condition; that is

$$\frac{dp'}{dx} + ikYp' = 0 \qquad (4-35)$$

where Y is the propellant surface admittance.

It has been shown,[29] that when the propellant responds to the pressure oscillation at its surface and, in addition, produces its own velocity oscillation which is independent of the local pressure oscillation, the boundary condition at the propellant surface can be expressed in the following form:

$$\frac{dp'}{dx} + ikYp' = -i\omega\bar{\rho}u \tag{4-36}$$

where the second term describes the propellant (or boundary) response to the local pressure oscillation and the inhomogeneous part describes the pressure independent velocity perturbation, which will be referred to as the propellant self-noise.

To investigate the effect of the inhomogeneous part of the propellant boundary condition upon the burner tube wave structure, the wave structure in a simple tube whose acoustic behavior is described by the one-dimensional Helmholtz equation.

$$\frac{d^2p'}{dx^2} + k^2 p' = 0 \tag{4-37}$$

and whose solutions must satisfy the following inhomogeneous boundary conditions:

$$\frac{dp'}{dx} + ikY_1p' = -i\omega\bar{\rho}u_1 \quad \text{at} \quad x = 0 \tag{4-38}$$

and

$$\frac{dp'}{dx} - ikY_2p' = i\omega\bar{\rho}u_2 \quad \text{at} \quad x = L \tag{4-39}$$

is analyzed in this section. The change in signs between these boundary conditions is due to changes in the direction of the inward unit normal vector at the two boundaries. The solution of Equation (4-37) is

$$p' = C \sin kx + D \cos kx \tag{4-40}$$

where

$$C = -\frac{i}{k}\{\omega\bar{\rho}u_1 + kY_1D\} \tag{4-41}$$

and

$$D = -\frac{\omega\bar{\rho}}{k}\frac{(u_2 + u_1 \cos kL)i + Y_2u_1 \sin kL}{(Y_1Y_2+1)\sin kL + i(Y_1+Y_2)\cos kL} \tag{4-42}$$

The above solution was used to investigate the tube's wave structure for four different cases and the results are presented in Figures 4-37 through 4-40. In the cases investigated, all of the parameters of the problem with the exception of $(Y_r)_2$ were kept constant in order to determine the dependence of the phase-distance curve upon $(Y_r)_2$. An examination of Figure 4-37 shows that even though the real part of the admittance at the left boundary is positive (i.e., $(Y_r)_1 = .001$), the slope of the phase-distance curve is positive for positive values of $(Y_r)_2$, indicating wave energy transmission from right to left. This unexpected result may be explained if one recognizes that the direction of movement of acoustic energy at a given point depends upon the sign of the real part of the local <u>effective</u> admittance which can be expressed (using the linearized momentum equation and Equation (4-38)) in the

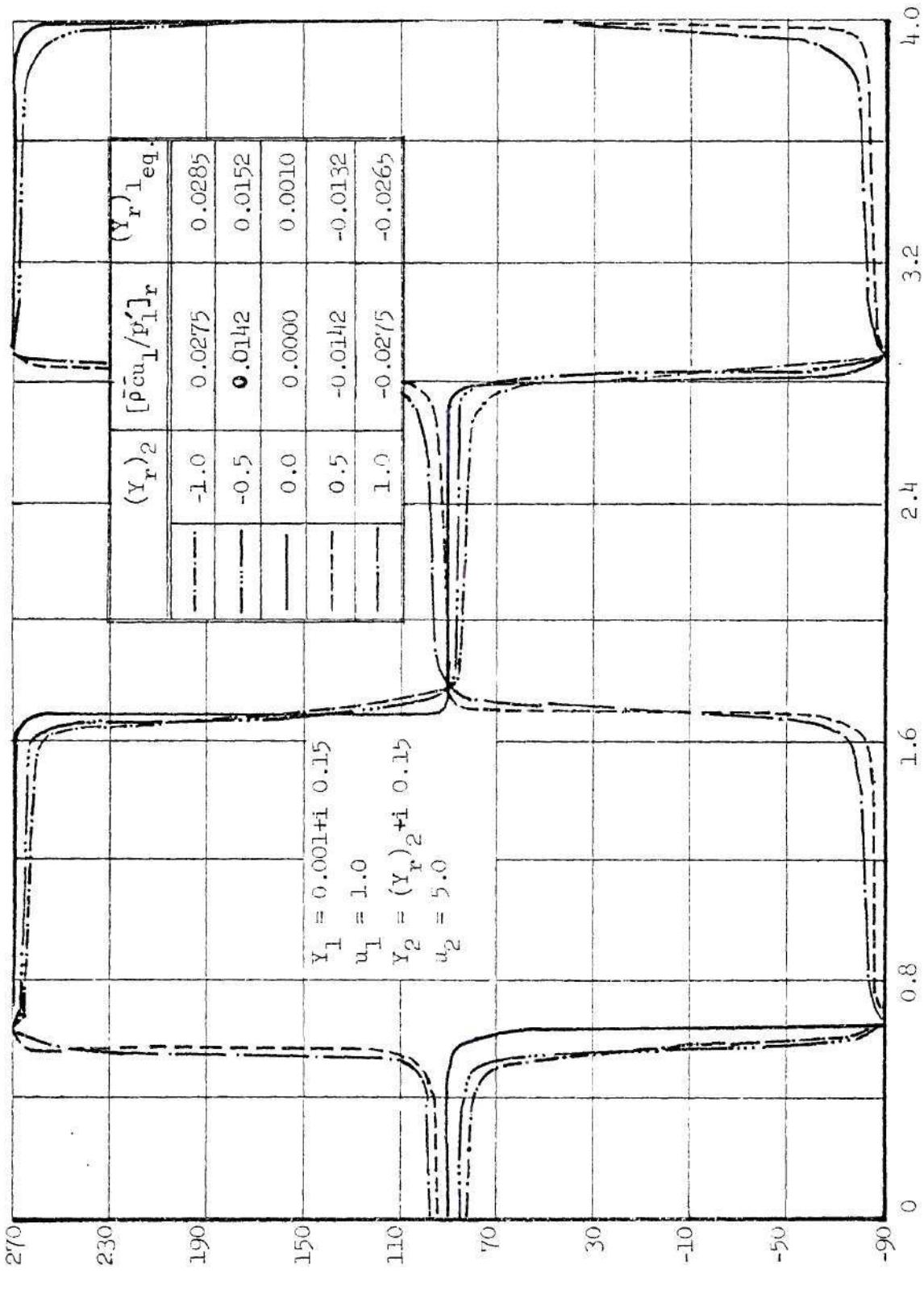

Figure 4-37. Dependence of Pressure Phase Distribution Upon $(Y_r)_2$.

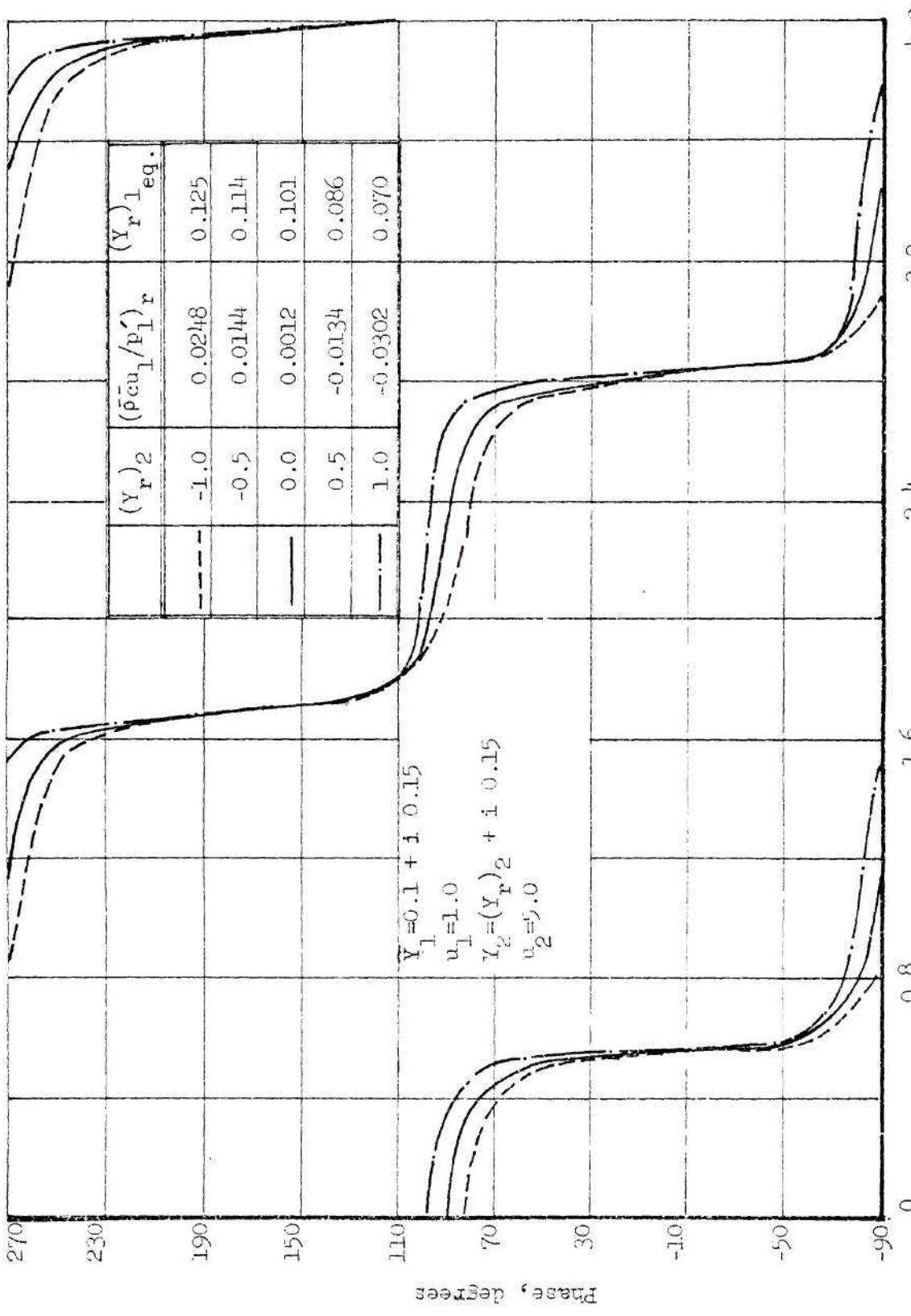

Figure 4-38. Dependence of Pressure Phase Distribution Upon $(Y_r)_2$.

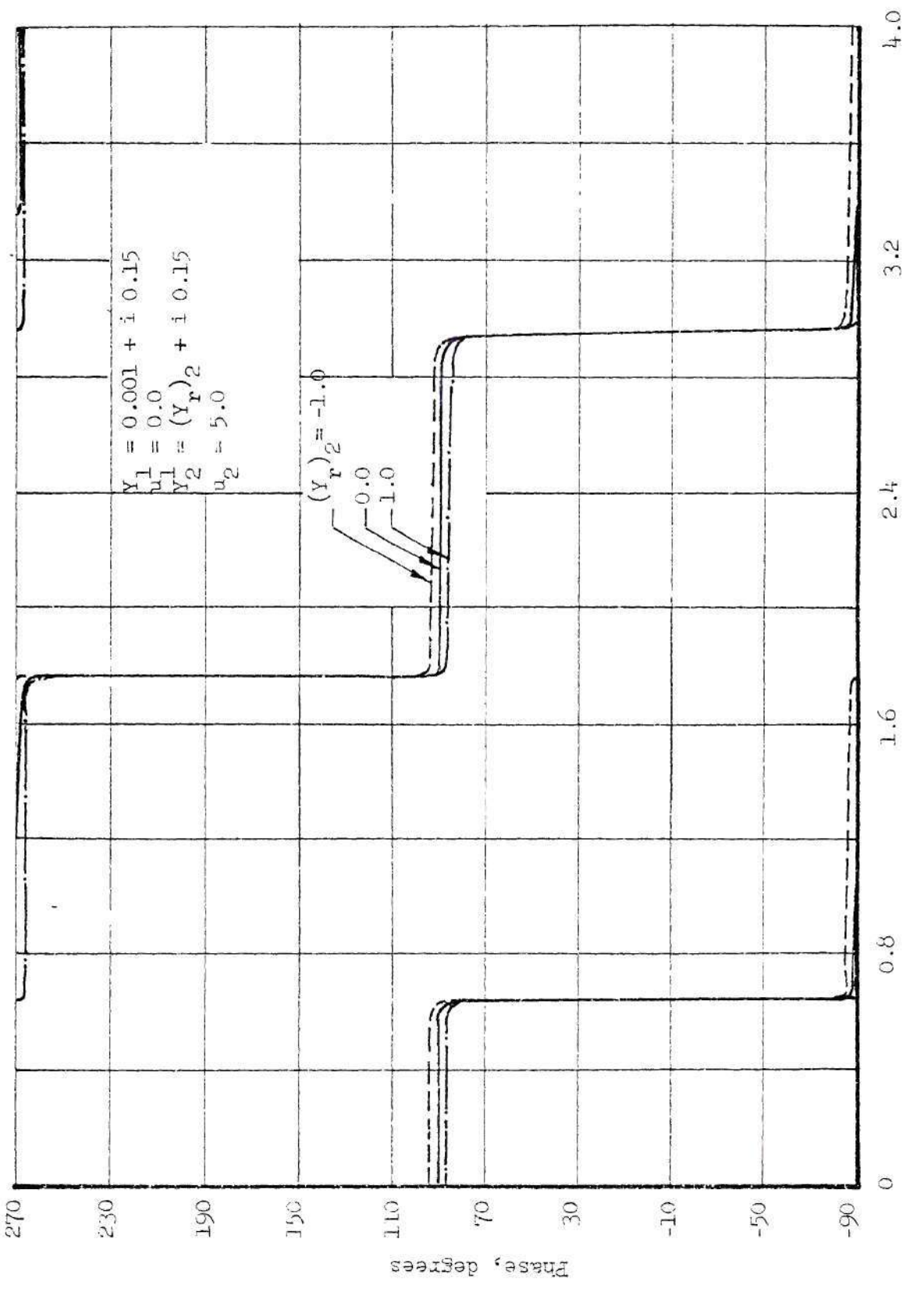

Figure 4-39. Dependence of Pressure Phase Distribution Upon $(Y_r)_2$.

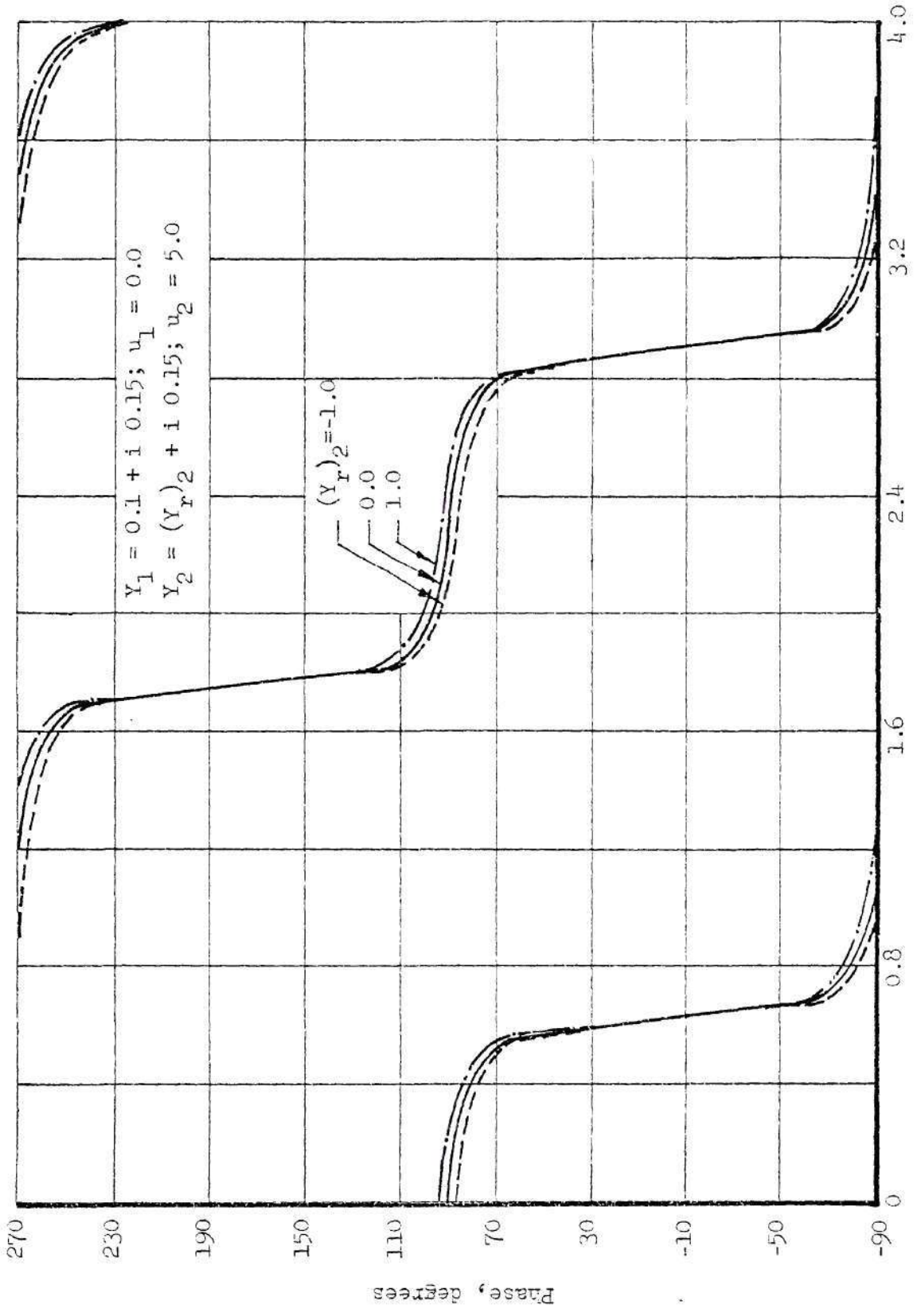

Figure 4-40. Dependence of Pressure Phase Distribution Upon $(Y_r)_2$.

following form at the x = 0 location

$$(Y_r)_{1_{eq.}} = \left\{Y_1 + \bar{\rho}\,\bar{c}\,\frac{u_1}{p_1'}\right\}_r \qquad (4\text{-}43)$$

Since Y_1 is fixed, the sign of $(Y_r)_{1_{eq.}}$ depends upon $(\bar{\rho}\,\bar{c}\,u_1/p_1')_r$ which in turn, depends upon the solution for p'.

Examination of the data in Figure 4-37 reveals that the characteristics of the wave structure in front of the left boundary may be changed by merely changing $(Y_r)_2$. This suggests that the presence of an inhomogeneous part (i.e., self-noise) in the propellant boundary condition makes the effective admittance value a dependent on the exhaust end boundary condition.

Figure 4-37 also contains a table with the computed values of $(Y_r)_{1_{eq.}}$ for different values of $(Y_r)_2$. Examination of this table shows that as $(Y_r)_2$ increases in value, $(Y_r)_{1_{eq.}}$ decreases in value allowing more wave-energy to be absorbed at the left hand boundary. It is of particular interest to note that $(Y_r)_{1_{eq.}}$ approaches $(Y_r)_1$ when $(Y_r)_2 = 0$.

Figure 4-38 has been prepared to show the effect of changing $(Y_r)_1$ upon the trends presented in Figure 4-37. In going from Figure 4-37 to Figure 4-38 the value of $(Y_r)_1$ increased from .001 to .1. Examination of Figure 4-38 shwos that under the new condition the slope of the phase-distance curve is always negative indicating wave energy movement from left to right. Once again, the value of $(Y_r)_{1_{eq.}}$ approaches the value of $(Y_r)_1$ when $(Y_r)_2 = 0$.

In Figure 4-39 the value of u_1 was set equal to zero while all the remaining parameters are the same as those used in Figure 4-37. Examination of this figure shows that in this case changes in $(Y_r)_2$ do not affect the wave structure in front of the left boundary. A comparison of the data presented in Figures 4-37 and 4-39 provides additional support to the argument that the presence of u_1 in the boundary condition may be responsible for the trends observed in the experimental data. In Figure 4-40 data similar to that of Figure 4-39 are presented with the exception that now the value of $(Y_r)_1$ is alrger than the one used in Figure 4-39.

From the above results it becomes evident that if a self driving term (i.e., u_1) is present at x = 0, the observed admittance $(Y_r)_{1_{eq.}}$ will not represent the actual admittance of the surface. However, if the real part of the admittance at x = L is kept zero, the observed real admittance at x = 0 (i.e., $(Y_r)_{1_{eq.}}$) would approach the actual real admittance $(Y_r)_1$. Also, if $(Y_r)_1$ is large, then the effect of $(\bar{\rho}\,\bar{c}\,u_1/p'_1)_r$ is negligible and the value of $(Y_r)_{1_{eq.}}$ remains close to that of $(Y_r)_1$.

CHAPTER V

EXPERIMENTAL MEASUREMENTS

To date, the impedance tube technique developed under this program has been applied in the measurement of the surface admittances of burning solid propellants and the admittances of the combustion process that is associated with rocket injectors utilizing gaseous propellants. The development of the experimental set-up for the above-mentioned solid propellant study, which represents a major portion of this work is described in this chapter. The experimental set-up developed for the gaseous rocket injector study is discussed in Chapter VI.

The experimental measurements made to determine the admittances of burning solid propellants using the impedance tube technique were carried out in two phases. In the first phase, all the measurements were made at low chamber pressures which were below 50 Psig. Separate experimental facilities were fabricated for each phase of this experimental program. The experimental set-ups and the measurement techniques are discussed in detail in the remainder of this chapter.

The experimental set-up (i.e., see Figures 5-1 and 5-2) developed for measuring the admittance of burning solid propellant at pressures below 50 Psig., consists of a circular tube, the propellant sample and its holder, the acoustic drivers and a pressure regulating valve. The impedance tube has an inside diameter of 1.5 inches and is approximately 4.5 feet long. The tube has provisions for the attachment of pressure

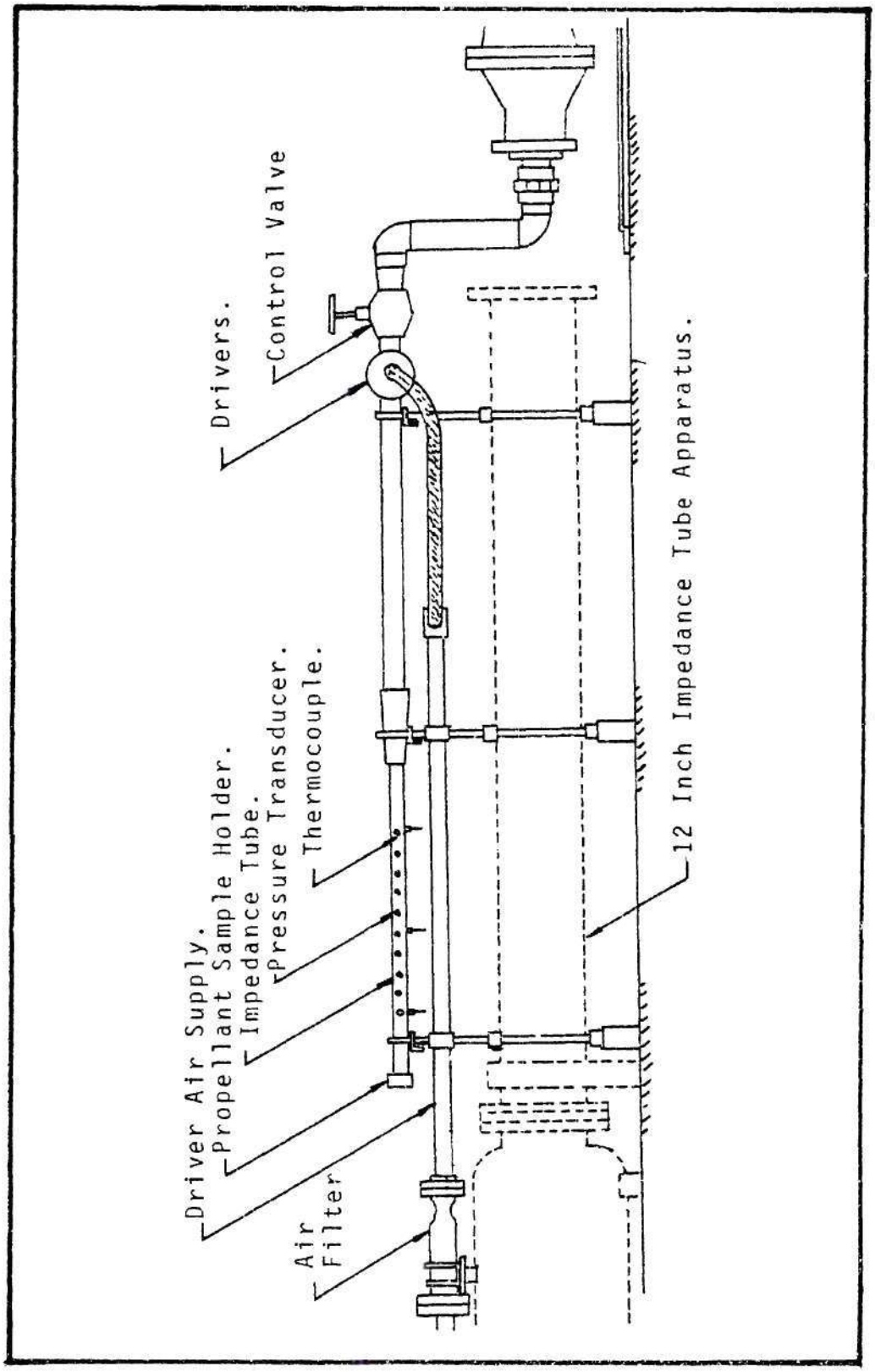

Figure 5-1. Sketch of The General Arrangement of the Unpressurized Impedance Tube Experiment.

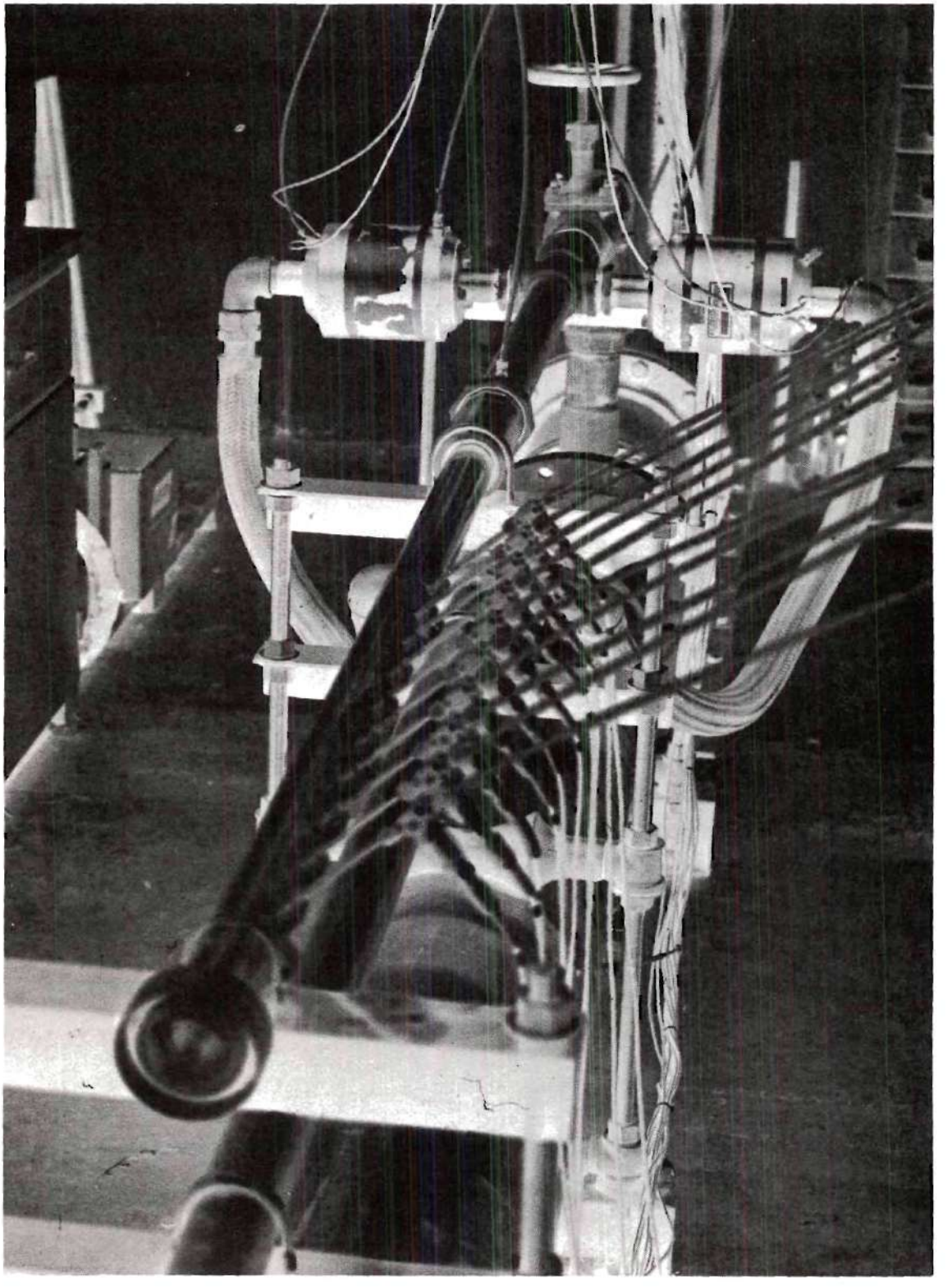

Figure 5-2. Reproduction of a Photograph of the Impedance Tube Experiment.

transducers and thermocouples at numerous locations along its wall. The distribution of the pressure transducers and thermocouples along the impedance tube wall, during each experiment, is determined by the frequency of the test.

Two line EPT-94B electro-pneumatic drivers, each capable of developing 4,000 watts of acoustic power, are close-coupled to the tube wall a short distance upstream of the exhaust valve. The frequency and wave form output of the acoustic drivers are controlled by a spectral Dynamic oscillator, Model SD 104A-5. For this investigation, the wave form of the oscillations were sinusoidal and the frequency of the oscillation was maintained constant during a test.

Measuring the admittance of a burning solid propellant using the impedance tube technique imposes stringent requirements on the instrumentation. The pressure measurement at high temperature poses the problem of protecting the highly sensitive transducers from direct exposure to the hot gases in the tube. Various ways for protecting the transducers were tested. Satisfactory results were obtained using the semi-infinite tube technique. In this technique, the long tube shown in Figure 5-3 was attached in the impedance tube's wall while the pressure transducer was attached to the side of the long tube several inches away from the impedance tube wall. The need to measure the high temperature of the hot gas in the tube called for the use of special thermocouples. In this study, platinum/platinum 13% rhodium thermocouples were used. These thermocouples are capable of measuring temperatures up to 3090°F (3550°R).

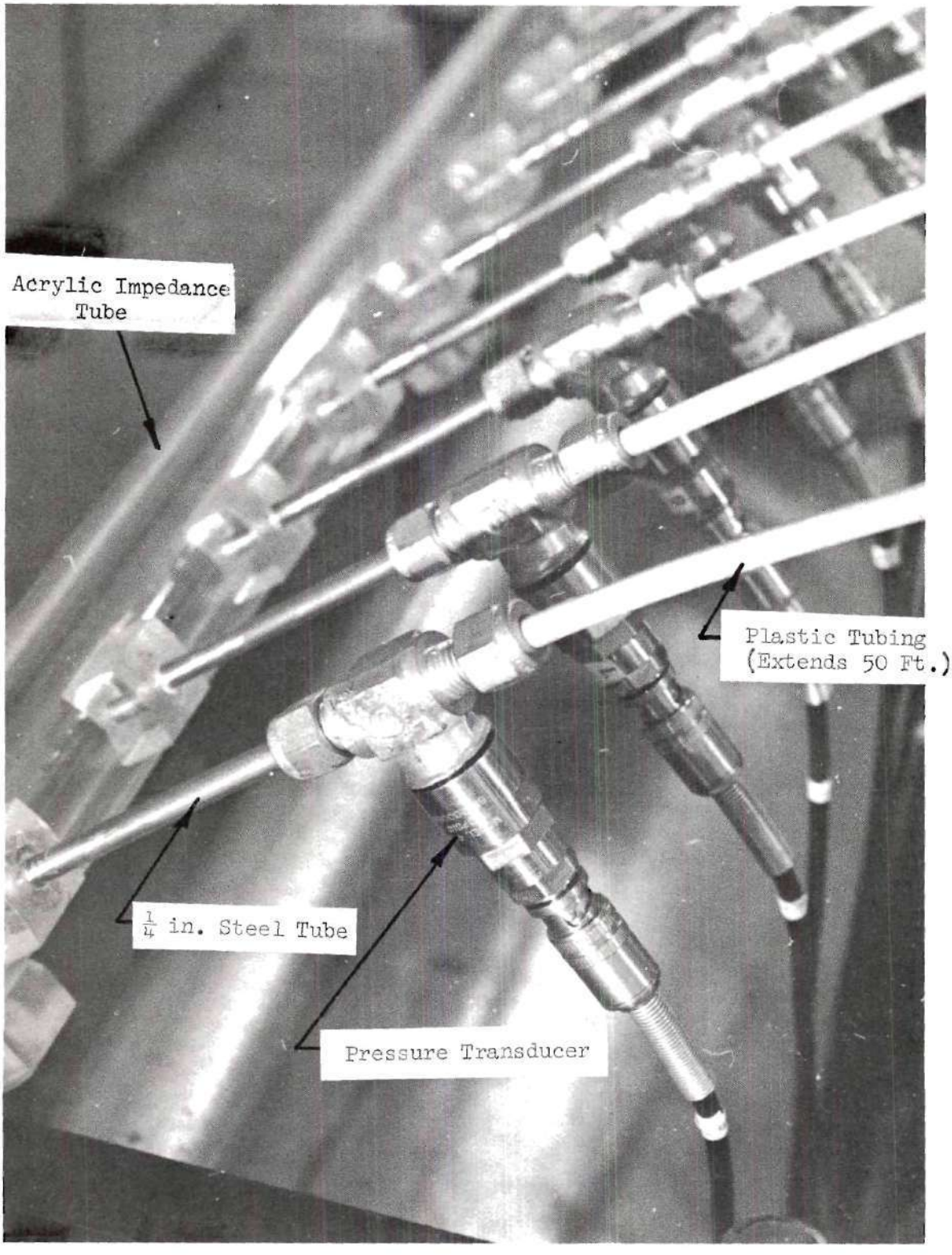

Figure 5-3. Infinite Tube Arrangement in the Impedance Tube Experiment

In order to achieve a uniform combustion of the tested samples, it is of utmost importance that all parts of the sample surface be ignited simultaneously. After considerable experimentation, best results were obtained with a nichrome wire glued to the sample surface in a "Z" shape. The surface of the sample was then coated with an X-225 pyrotechnic mixture (potassium percholate (72.4%); titanium (14.8%); boron powder (6.9%); and polyisobutylene binder (6.0%) dissolved in toulene). The nichrome wires were attached to copper wire leads which were connected to a power supply. Uniform ignition was obtained when the power supply was turned on.

The experimental set-up described above was limited to chamber pressure less than 50 Psig. However, the main objective of this investigation was to develop a facility which would be capable of determining the admittances of burning solid propellant samples at the pressure range of 300-500 Psig simulating actual rocket motor operating conditions. The low pressure facility could not be used for this purpose without modification because the acoustic drivers used were not capable of operating at high pressures and the pressure transducers were not capable of withstanding pressures of up to 500 Psig. Therefore, the low pressure facility needed a few modifications to operate at pressures up to 500 Psig., with the same acoustic drivers and pressure transducers.

A photograph of the facility and a corresponding schematic are shown in Figures 5-4 and 5-5, respectively. The driven tube with the propellant sample holder, the pressure transducers, and the acoustic

Figure 5-4. Photograph of Pressurized Impedance Tube Facility.

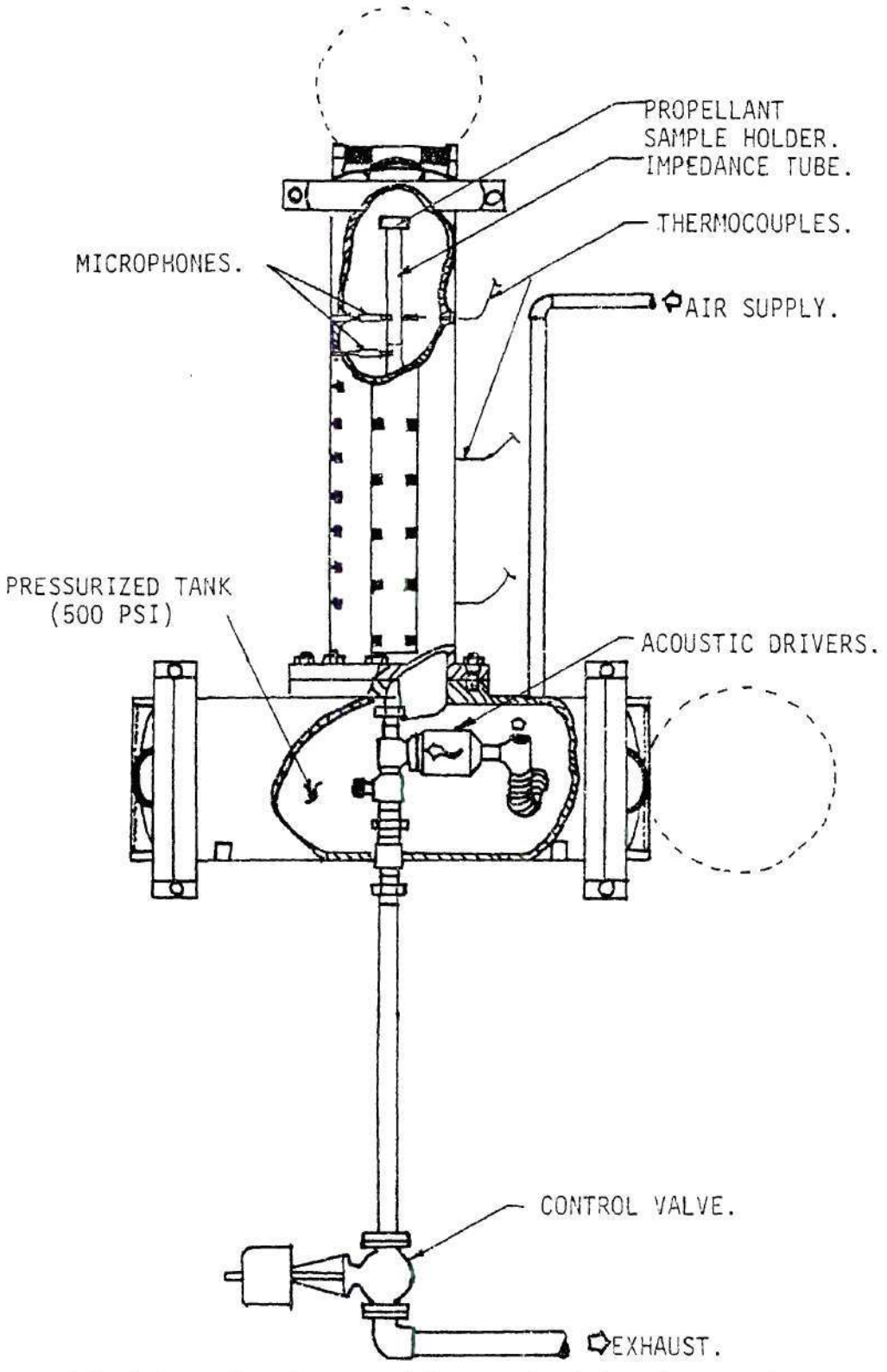

Figure 5-5. Schematic Diagram of Pressurized Impedance Tube Facility.

drivers are all contained within the 0 to 500 Psig. pressurization tank which is equipped with high pressure hinged ports to allow easy access for sample changes, impedance tube removal, and maintenance. By enclosing the impedance tube in a pressurized tank a relatively low pressure differential could be maintained across the pressure transducers mounted on the side walls of the impedance tube and the acoustic drivers closed-coupled to the tube. This permits the use of the available acoustic drivers and low pressure, high resolution transducers to provide more accurate data.

Air supply for tank pressurization and the flow requirements of the electro-pneumatic driver is provided by a 3000 Psig, 500 cu. ft. blow-down facility. The tank pressure and driver airflow are maintained by a pressure control valve in the exhaust line of the system as shown in the schematic of the flow system in Figure 5-6.

The components of the high pressure impedance tube facility and the principles of its operation are basically unchanged from the low pressure facility previously in operation. The impedance tube contained in the high pressure tank was fabricated from a stainless steel pipe of two inch inside diameter and six feet length. Provisions for instrumentation had been included along the length of the tube wall. The semi-infinite tube technique previously used to protect the transducers from the high temperature gases has proven unsatisfactory for high pressure operation. Under high pressure conditions, the pressure amplitude and phase measured with the semi-infinite tube technique, showed an oscillatory behavior with time, due to low frequency resonance in the

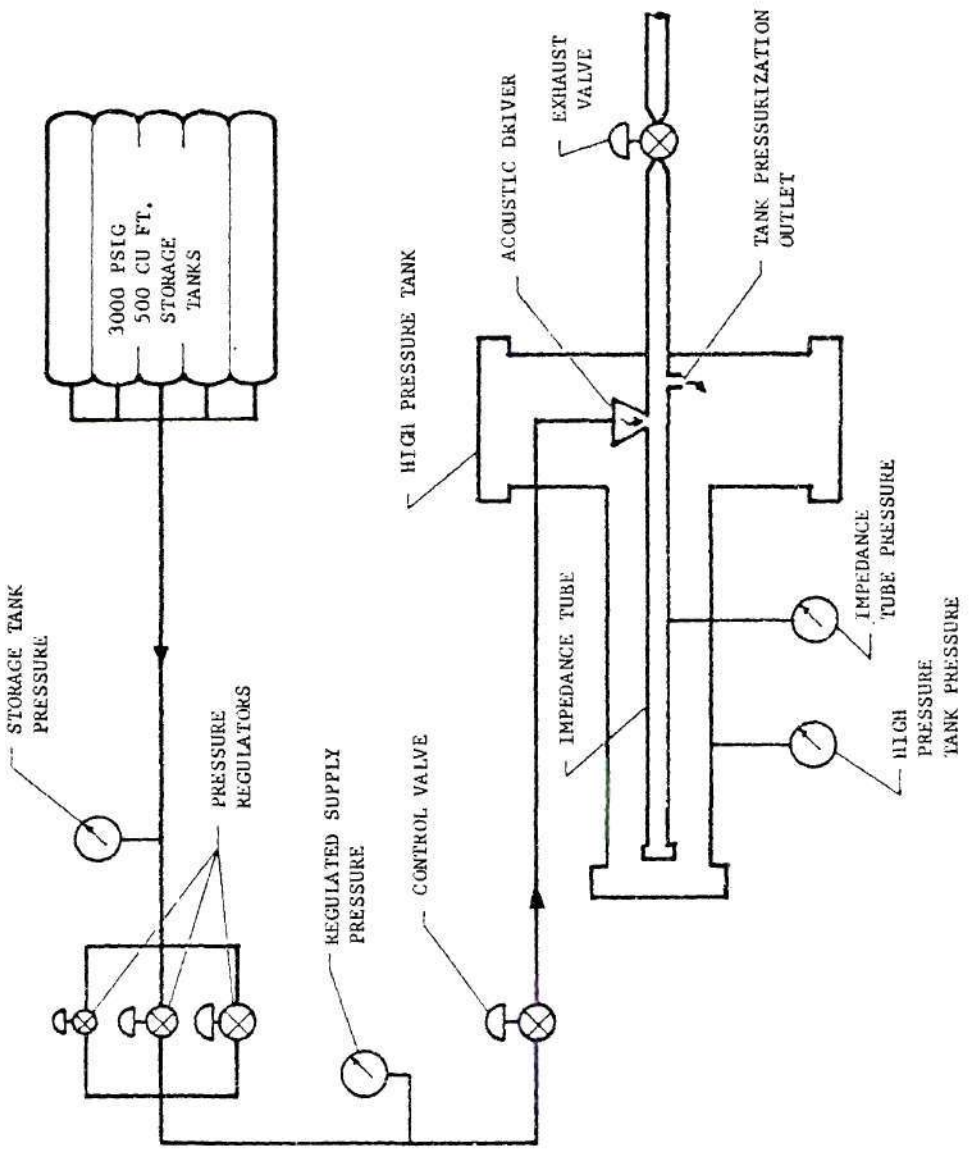

Figure 5-6. Schematic of Flow system Facility.

semi-infinite tube. Therefore, an alternate pressure transducer installation utilizing a short adapter had been developed for the high pressure operation[30] to overcome the low frequency resonance. The pressure transducers with the short adapter installation gave a flat response up to 1300 Hz., which was above the frequency range (i.e., 100 to 1000 Hz.) investigated in this study.

The data acquisition system and the equipment to establish and monitor test conditions for high pressure testing were located in a laboratory area adjacent to the room housing the high pressure impedance tube experiment. A photograph of the control area for the experiment is presented in Figure 5-7. Test conditions were established by slowly pressurizing the high pressure tank housing and the impedance tube to the desired operating pressure. The pressurization tank pressure and driver airflow requirements were maintained by the tank pressurization control valve in the exhaust line. With tank pressure stabilized and a standing waveform of a desired frequency established a test run was initiated.

The data acquisition period of a test includes four phases; a brief pre-ignition test period with the acoustic drivers on and test conditions established in the burner tube, ignition of the propellant sample, the propellant "quasi-steady" burning period and the propellant extinguishment phase. The data acquisition period was normally about two to three seconds. For each test run the dynamic pressure and temperature data were recorded on a 14 channel analog magnetic tape recorder. These data were then played back at reduced speed and automatically plotted providing a time history of the sound pressure levels,

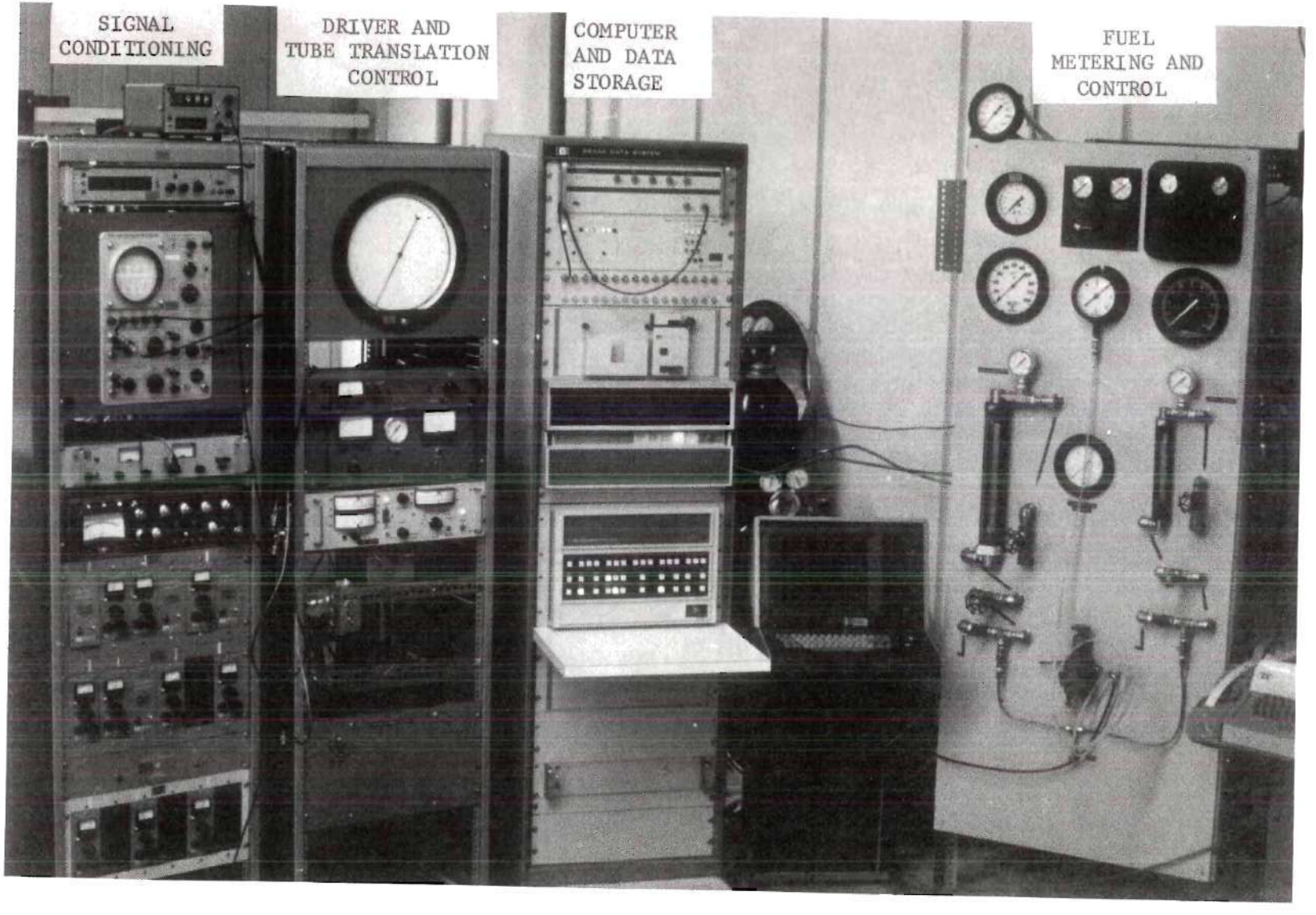

Figure 5-7. Experiment Control Area.

phase relationship of the pressure, and the temperatures of the hot gases at several locations inside the tube.

At a later date, during this investigation, a mini-computer based data acquisition system was incorporated in the program instead of recording the data on a tape recorder. This system shown in Figure 5-7 processes the data in three stages.

(1) Data Sampling: During a test the analog signal from the transducer and thermocouple channels were sampled, digitized and stored at a controlled rate. This system was capable of sampling up to 12 channels of input data and had a range of ±2.56 volts with a resolution of 20 mv. To obtain maximum signal resolution, the input from the transducer and thermocouple channels were amplified so that the maximum anticipated amplitude for the test was as close to ±2.56 volts as possible. The sampling rate depends upon the frequency of the driven oscillations. The samples were taken rapidly enough to obtain a sufficient number of data points per cycle period for a good signal definition. The sampling interval was determined by the test conditions. In this study, the ignition and burnout transients produced large variations in pressure amplitude and phase. The sampling interval must be small enough to detect these variations so that they can be distinguished from the nearly constant amplitudes which occurred during the period of quasi-steady burning. On the other hand the sampling interval must be long enough to ensure the digital filtering interval was sufficient. During a test, data were taken at up to 80 sampling intervals of from 10 to 50 milliseconds, and the time between intervals

was from 15 to 30 milliseconds. The duration of the run was from two to three seconds for the 3/8"-thick propellant samples used and from 20 to 40 data points were obtained during steady burning. After the digitized data points taken during one sampling interval had been stored, they were then written onto a disc so that room could be made in the buffer to receive the data from the next sampling interval. These steps are depicted in Figure 5-8.

(2) Data Processing: During the data processing phase, the disc, computer and a Tektronix 4012 graphics display terminal were used. The steps involved are shown in Figure 4-9. During this process the digitized data taken over one time interval was read form the disc into the computer. The digitized signals from the pressure transducers and thermocouple channels, were then used to obtain average pressure amplitudes, phases and temperatures over the sampled time interval. A similar process was repeated for each successive time interval. Then the resulting pressure amplitude, and phase data were plotted against non-dimensional time (i.e., record) on the terminal. These data were used to check that proper test conditions were established during the run. In addition to being displayed on the terminal, the amplitude, phase and temperature data were also stored on the disc for later use.

(3) Data Presentation: Finally, pressure amplitude, phase and temperature data were printed out versus distance for various time intervals. The data could be plotted against non-dimensional time. From these plots the time interval at which steady state burning was achieved could be ascertained. At some selected points during the steady state

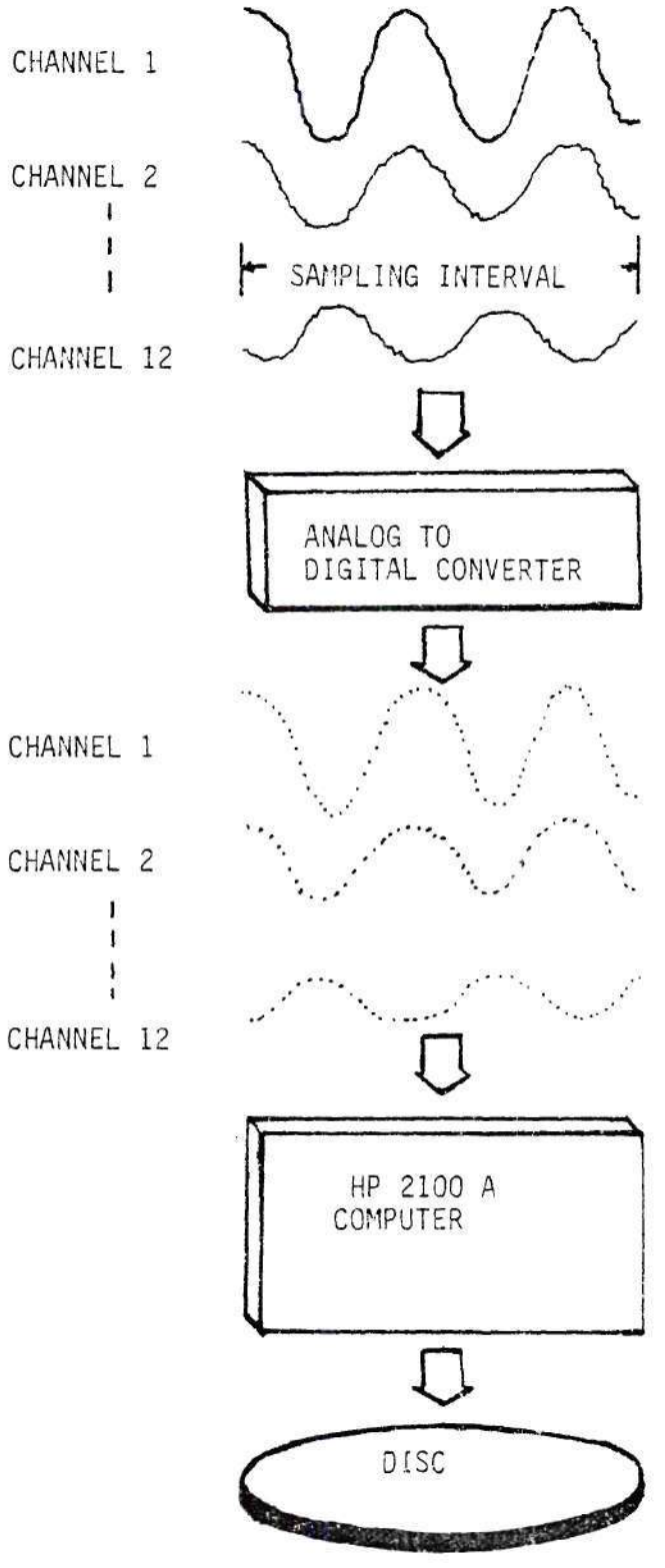

Figure 5-8. Signal Processing During Data Sampling Phase.

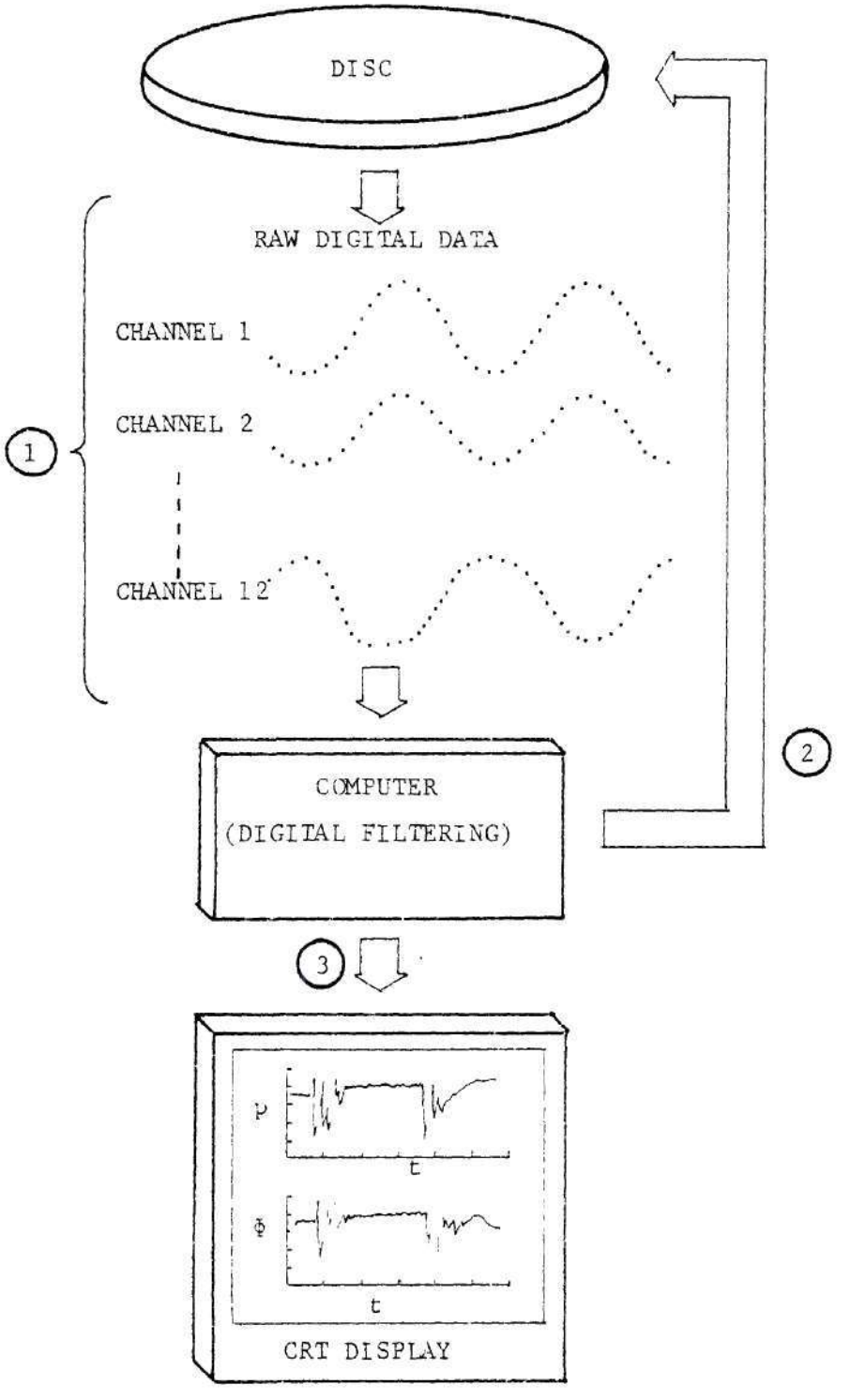

Figure 5-9. Data Processing Schematic

burning, the amplitude, phase and temperature data could then be plotted versus distance. These data were then used in the data reduction scheme described in Chapter III to obtain the admittance values.

CHAPTER VI

EXPERIMENTAL RESULTS AND CONCLUSION

In this chapter the experimental data obtained from both the solid propellant and the reactive gaseous rocket injector studies are presented and discussed. Most of the data presented here are, however, for the solid propellant case, as the experimental phase of this program was primarily concerned with determining the admittances of burning solid propellants.

During the initial stages of this study, a uniform burning of the solid propellant sample in the impedance tube throughout the test run was anticipated. Such uniform burning would have established a steady state condition in the impedance tube, during which all the flow properties would have remained constant, enabling an accurate measurement of the pressure data required for determining the admittance values of the burning solid propellants. Unfortunately, a uniform burning was seldom achieved during any test run. Also, the propellant samples used in a test run could burn only for a short duration (i.e., about 2 to 3 seconds). In an effort to increase the burning time, the burning characteristics of thicker propellant samples were tested. However, with the thicker propellant samples though the burning time was increased, the burning characteristics become more uneven. Therefore, optimum size propellant samples were used, which could last for 2 to 3 seconds with relatively even burning.

The total burning time of 2 to 3 seconds of the propellant sample was not adequate to establish a steady state condition in the impedance tube during a test run. Also, due to the presence of higher modes of the excited frequency and flow noise in the impedance tube, the pressure oscillations observed at different transducer locations during a test run were not exactly sinusoidal. The magnitude of admittance values for burning solid propellants were expected to be very small[9] (i.e., of the order of 0.03). For such low values of admittance the pressure amplitudes at and near pressure minimum become very small compared to the maximum pressure amplitude of the standing wave. Often those low pressure values fall below the magnitude which cannot be measured accurately by the transducers. This led to an inaccurate measurement of pressures at and near the pressure minima. Furthermore, whenever the oscillations in the impedance tube were not sinusoidal, the data acquisition systems were prone to introduce errors in the measured data.

Two different data acquisition systems were used to acquire the analog data measured in the impedance tube. One of them was a 14 channel magnetic tape recorder and the other one was an analog to digital converter. The tape recorder recorded the oscillatory pressure data at a speed of 30 inches per second and these tapes were played back at 1 7/8" per second for data reduction. This slower playback speed resulted in a proportionately diminished apparent frequency of the input signal to the tracking filter, phase meter and log converter, the components associated with the data reduction system, causing inaccuracies in the output

data. These inaccuracies were especially predominant at lower frequencies.

The analog to digital converter was used in this program to acquire most of the high pressure data. Whenever the oscillatory signals in the impedance tube were not sinusoidal, the analog to digital converter needed more samples per data point (i.e., higher sampling rate) as discussed in Chapter V, to filter out the higher modes, nonlinearities and random noise present in the signal. However, owing to the short test duration, the sampling rate could not be increased, resulting in some errors in the digitized data.

In summary, due to uneven burning of the propellant, short duration of the tests and the experimental difficulties discussed above, significant scatter is observed in the measured admittance values. In contrast, in the reactive gaseous rocket injector study,[2] where these short-comings were overcome with a steady burning and a longer test duration, the admittance values obtained show very little scatter and they agree well with an available theory. In this study a fixed flow rate of the gaseous fuel and the oxidizer mixture was maintained into the impedance tube throughout a test run. Due to the fixed flow rate of fuel-oxidizer mixture a uniform burning was achieved for a longer time, (i.e., about 5 minutes) during which a steady state condition was established. Since the duration of the burning was long, the excitation frequency was selected after a steady state condition was established in the impedance tube, by monitoring the output signal of a transducer. In this process an excitation frequency could be chosen such that a good

sinusoidal oscillation could be maintained in the impedance tube. Moreover, in this case the analog to digital converter used for data acquisition could get a sufficient number of samples per data point to produce accurate digitized data. Thus, to demonstrate the applicability of the impedance tube technique, some of the results obtained in the gaseous rocket injector study are also discussed in this chapter.

1. Admittances of Burning Solid Propellants

The experimental efforts conducted under this study include the development of the experimental facilities and techniques for the determination of the admittances of a number of solid propellants under near atmospheric and high pressure conditions over the frequency range of 100 to 1000 Hz, that is of interest in solid propellant combustion instability. The data obtained in this study are presented and discussed in this chapter. Furthermore, these data are compared with corresponding T-burner results.

The admittances of four different propellants have been investigated in more than two hundred tests. The tested propellants included a T-13 propellant, an undesignated propellant white in color, supplied by Thiokol, an A-13 propellant and an A-15 propellant.

A series of experiments were conducted at low pressures to determine the flow conditions inside the impedance tube during the combustion of solid propellant samples. Specifically, the steady state temperature gradients inside the tube were measured in several tests by using thermocouples. The results are presented in Figure 6-1. The data presented in Figure 6-1 are crossplotted to deduce radial temperature

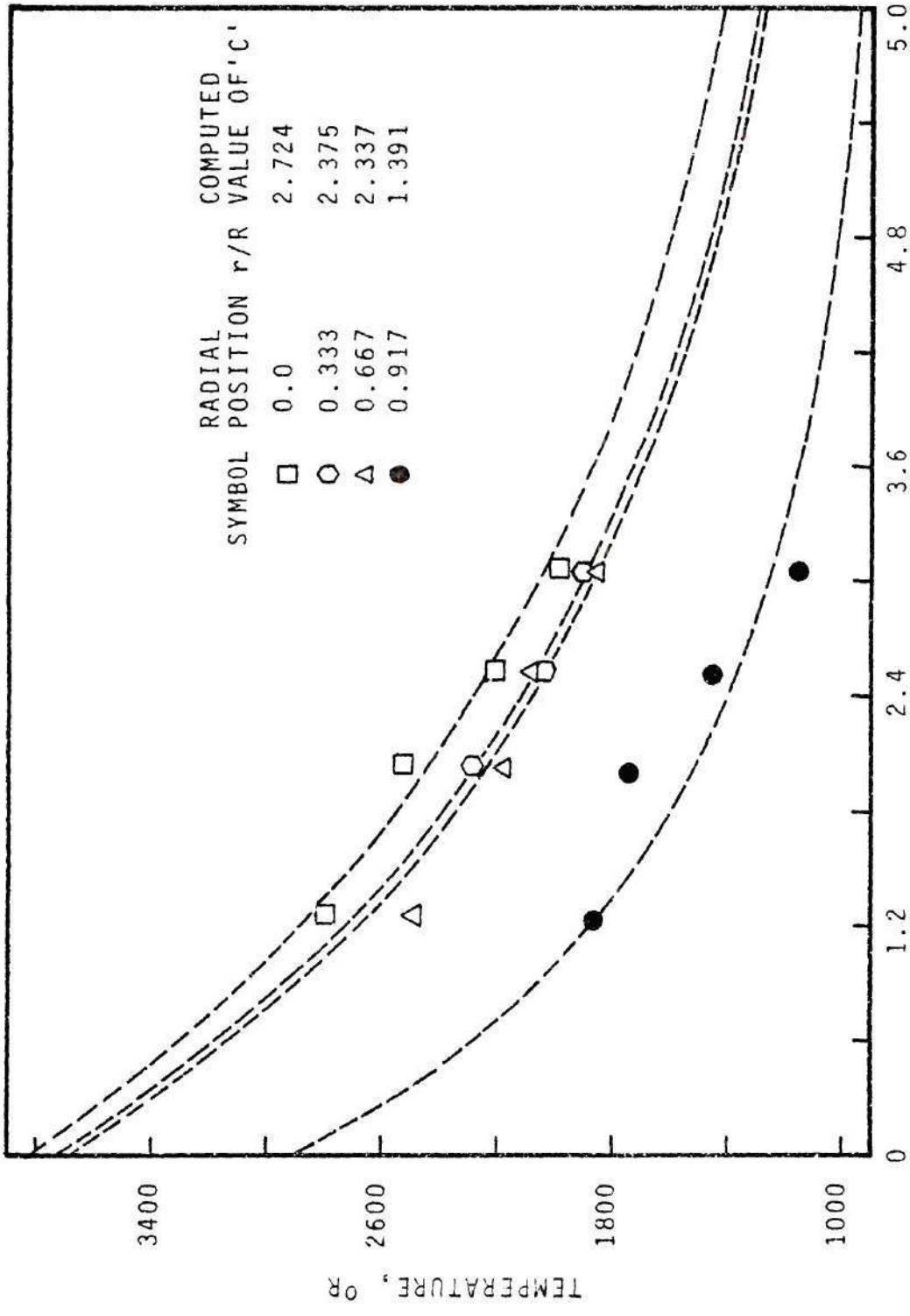

Figure 6-1. Axial Variation of Mean Temperature.

profiles at various axial locations and the results are presented in Figure 6-2. The inescapable conclusion reached from this temperature data is that both axial and radial temperature gradients exist in the impedance tube during a test. The experimental data describing the variation of the temperature along the tube at various radial locations are fitted with the analytical expressions given in Equations (3-23) and (3-24), the heat transfer parameter "C" being different for different radial locations and the results are shown as solid lines in Figure 6-1.

The next set of experiments was conducted with the objective of determining the wave structure and the admittance of burning solid propellants at low pressures. Tests at a number of frequencies were conducted using a number of different propellant samples and the measured pressures were recorded on a tape recorder. These data were later reduced and the time histories of the pressures and temperatures were obtained. The data obtained with a T-13 propellant (supplied by the Naval Weapon Center, China Lake, California) at 467 Hz. are presented in Figures 6-3 through 6-11. Examination of Figure 6-3 clearly indicates the transient temperature rise in the tube following the ignition of the propellant, the quasi-steady period of burning and the temperature drop upon completion of burning. Figures 6-4 through 6-10 describe the corresponding time histories of the pressure amplitudes and phases. Cross plotting the amplitude and phase data at a given instant in Figures 6-4 through 6-10, yields the instantaneous amplitude and phase patterns shown in Figure 6-11. Figures 6-3 through 6-10 are

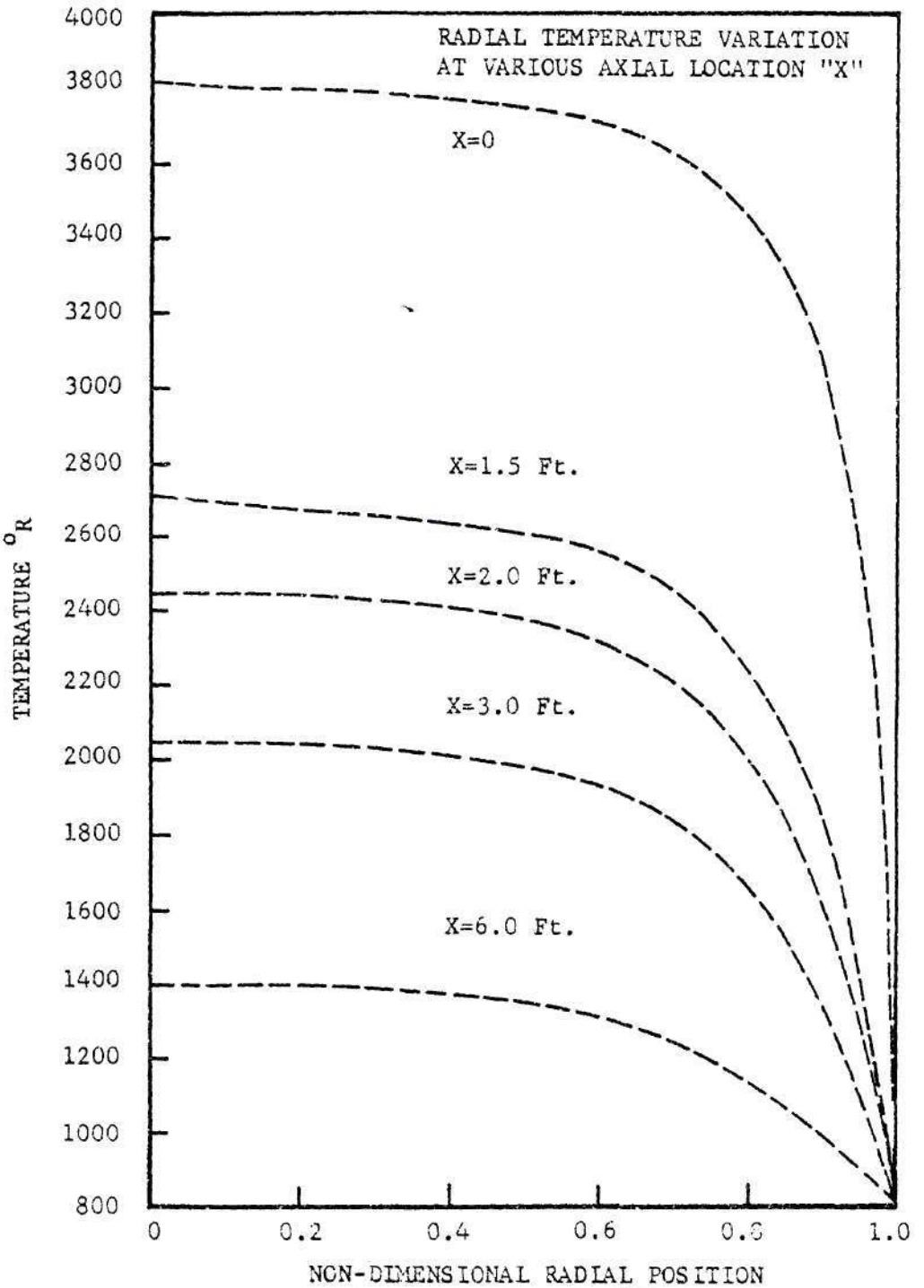

Figure 6-2. Radial Variation of Mean Temperature.

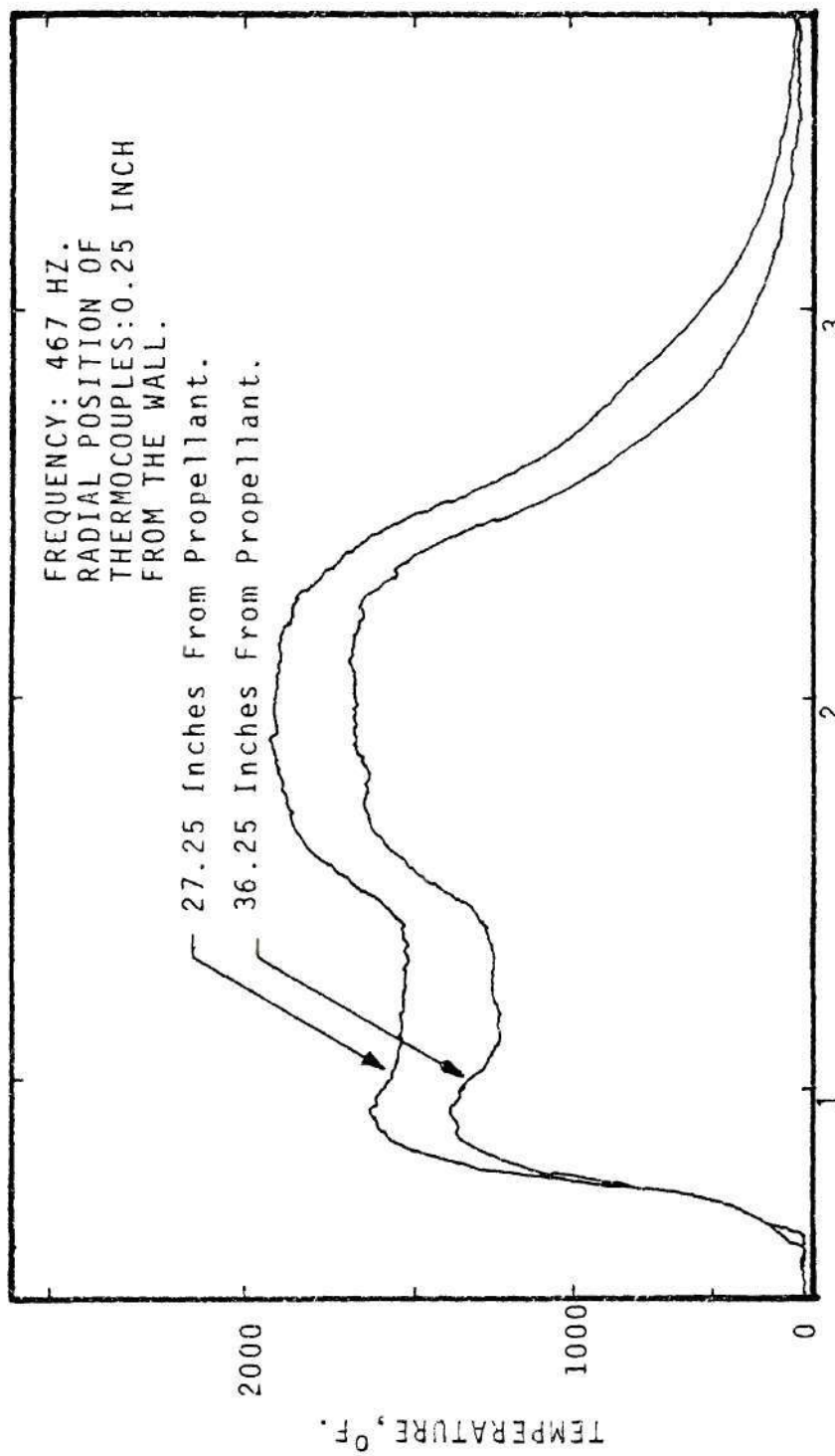

Figure 6-3. Variation of Mean Temperature with respect to Time.

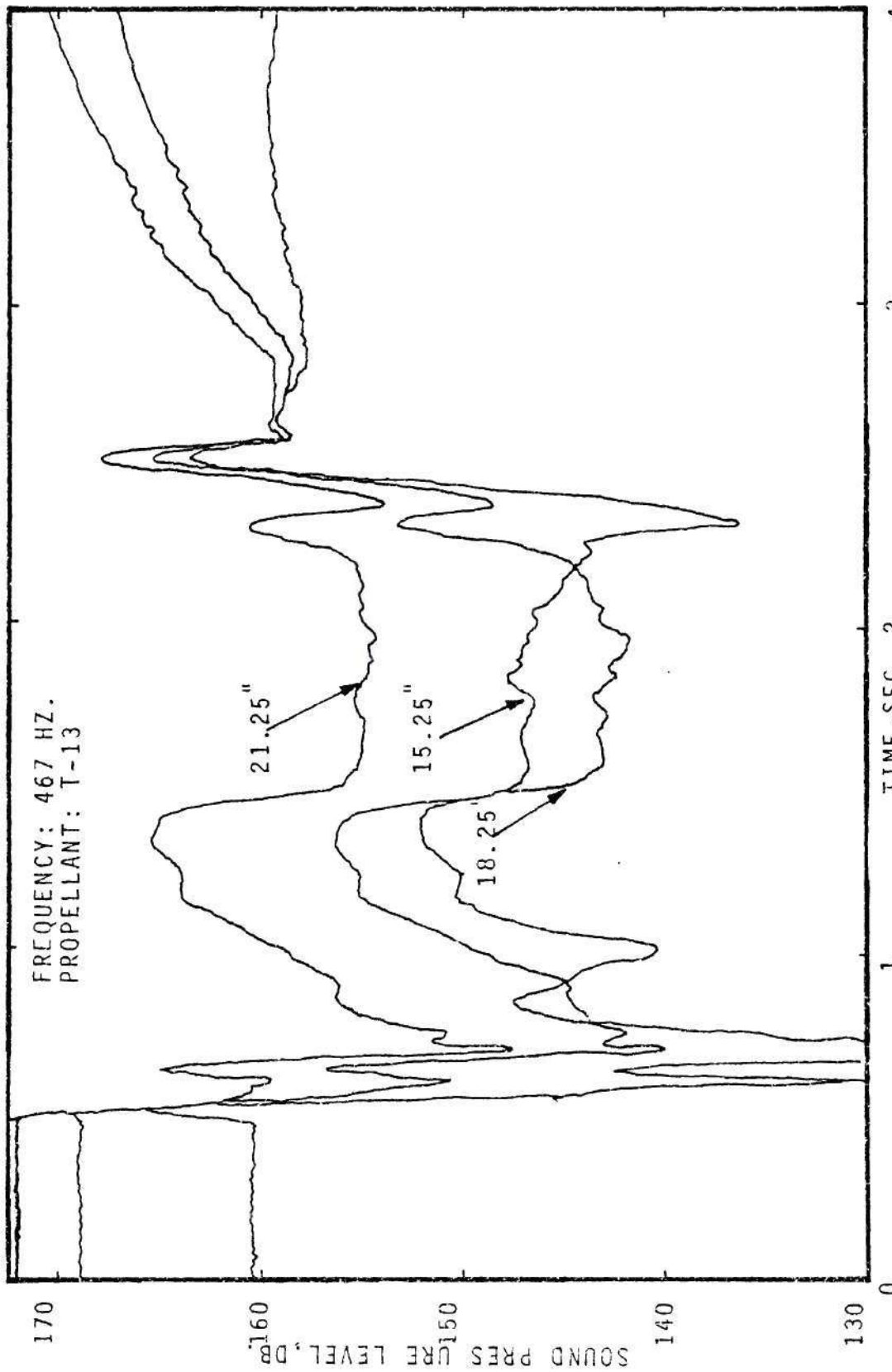

Figure 6-4. Variation of Pressure Amplitude with respect to Time.

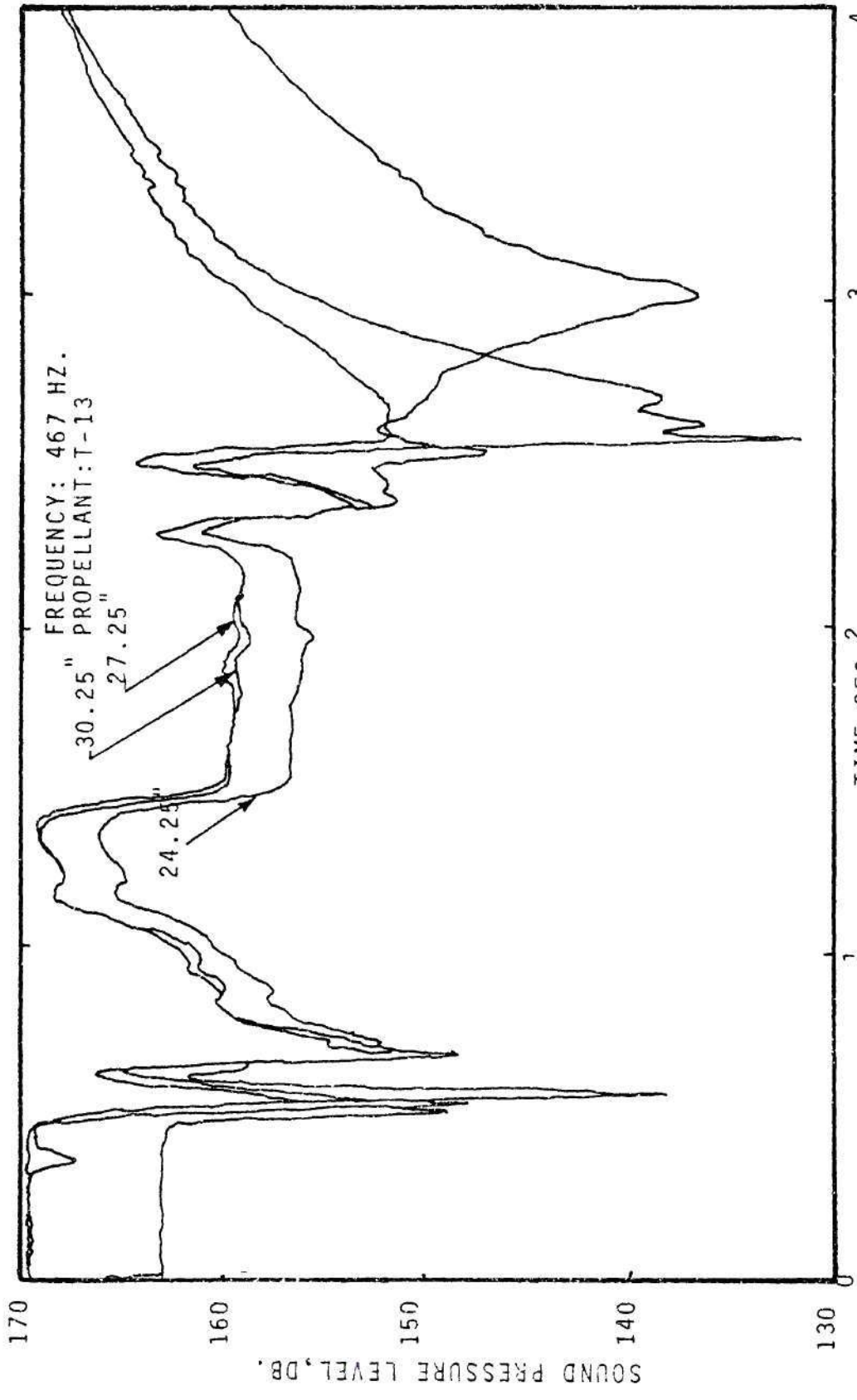

Figure 6-5. Variation of Pressure Amplitude with respect to Time.

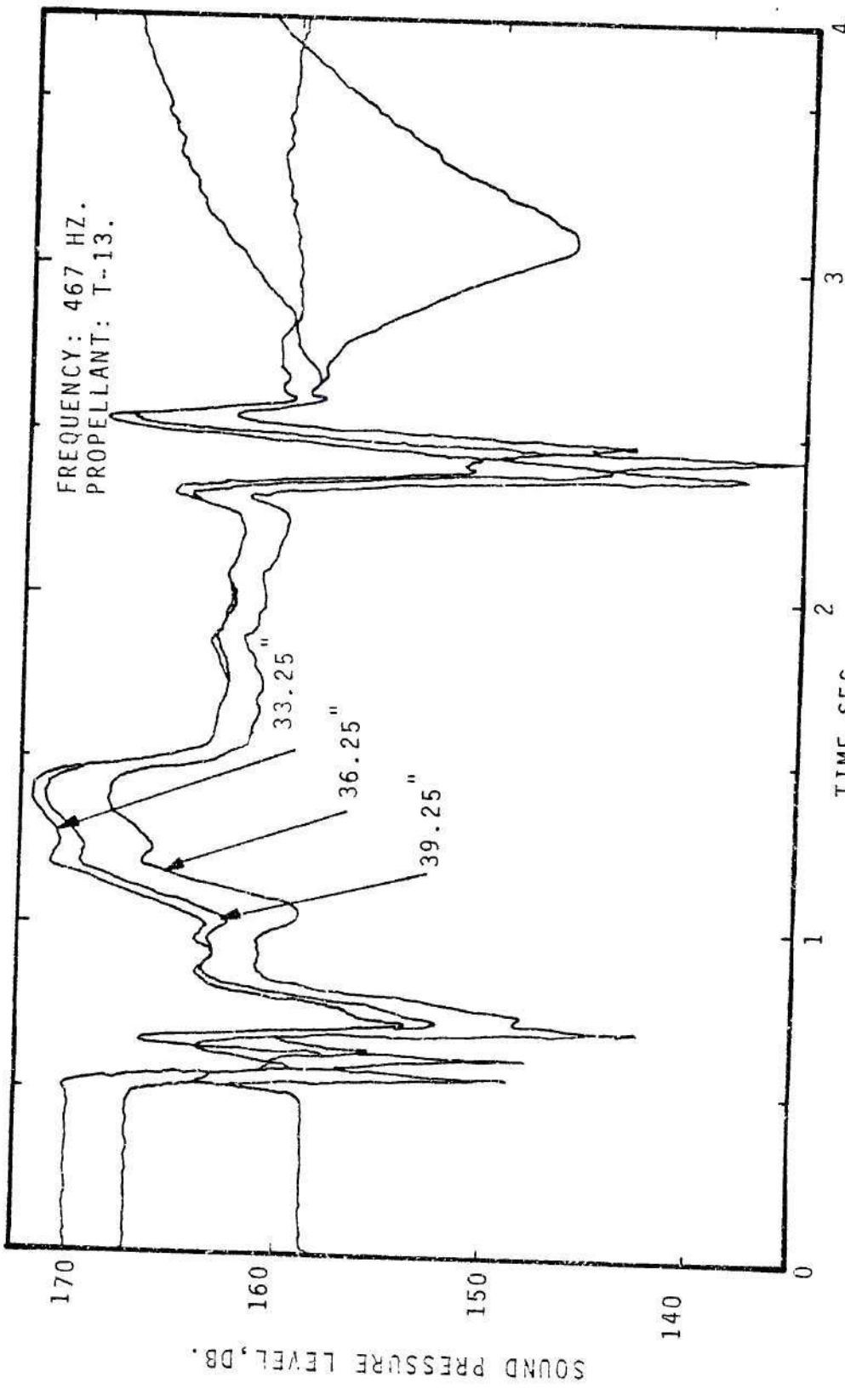

Figure 6-6. Variation of Pressure Amplitude with respect to Time.

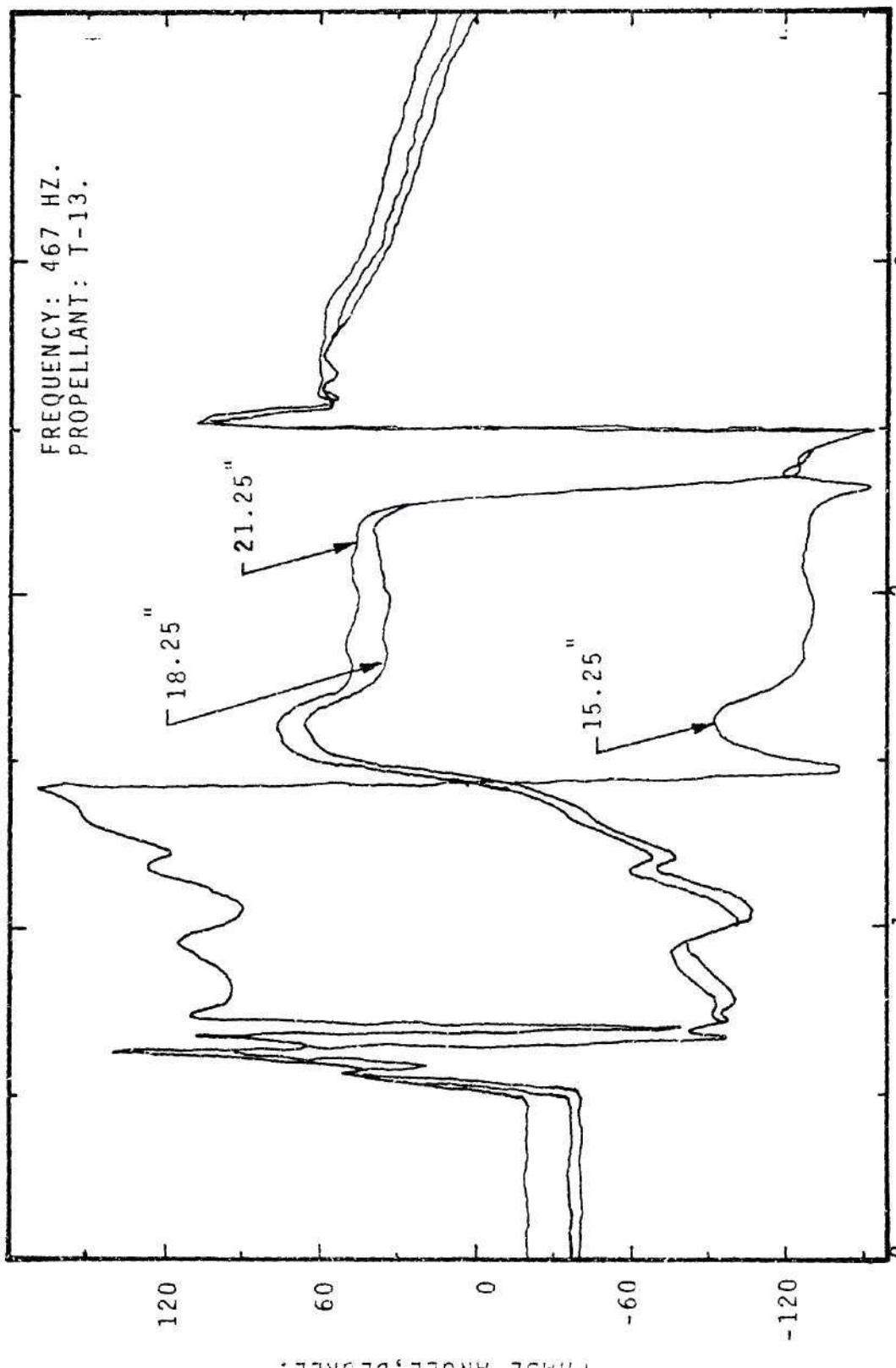

Figure 6-7. Variation of Pressure Phase with respect to Time.

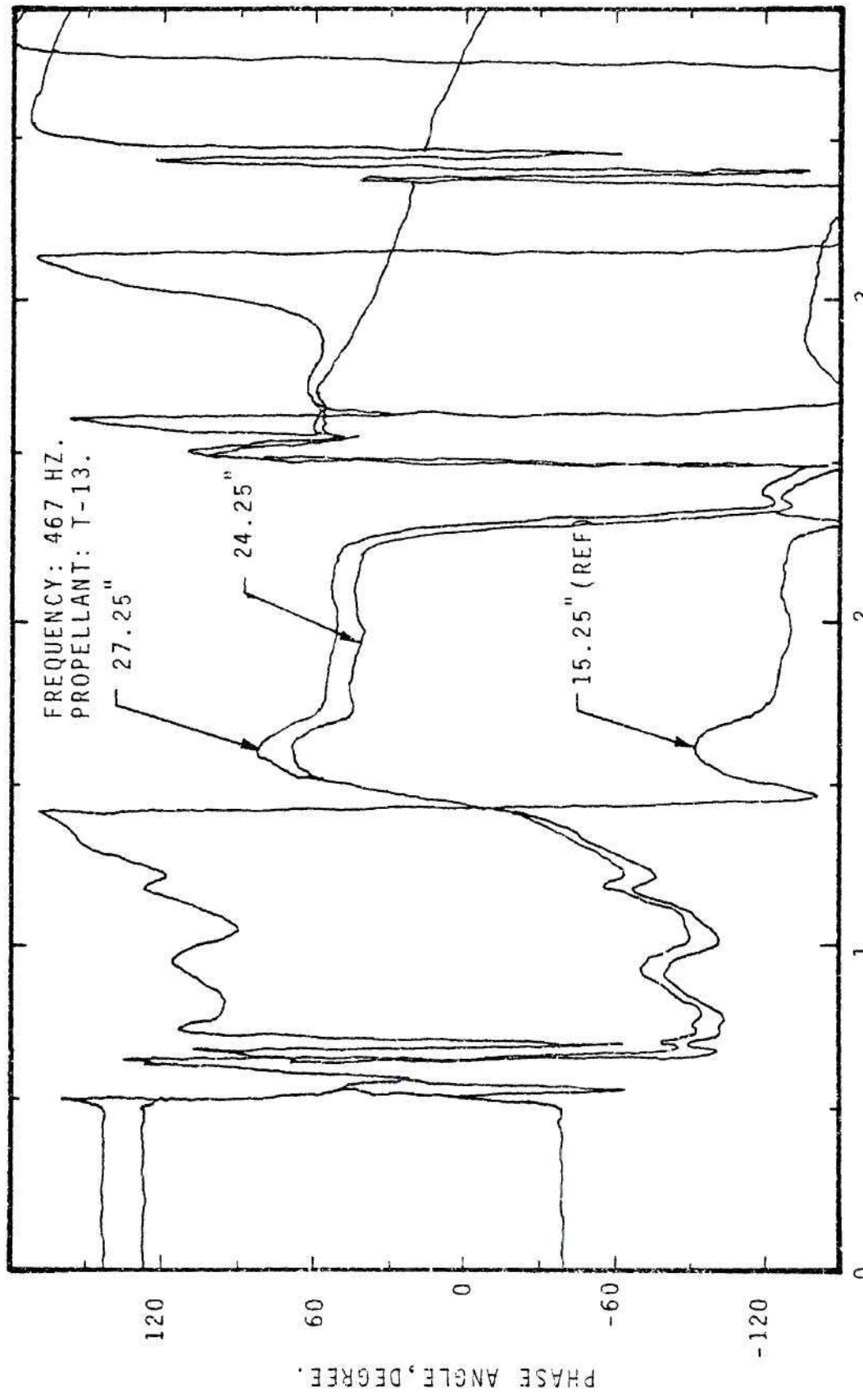

Figure 6-8. Variation of Pressure Phases with respect to Time.

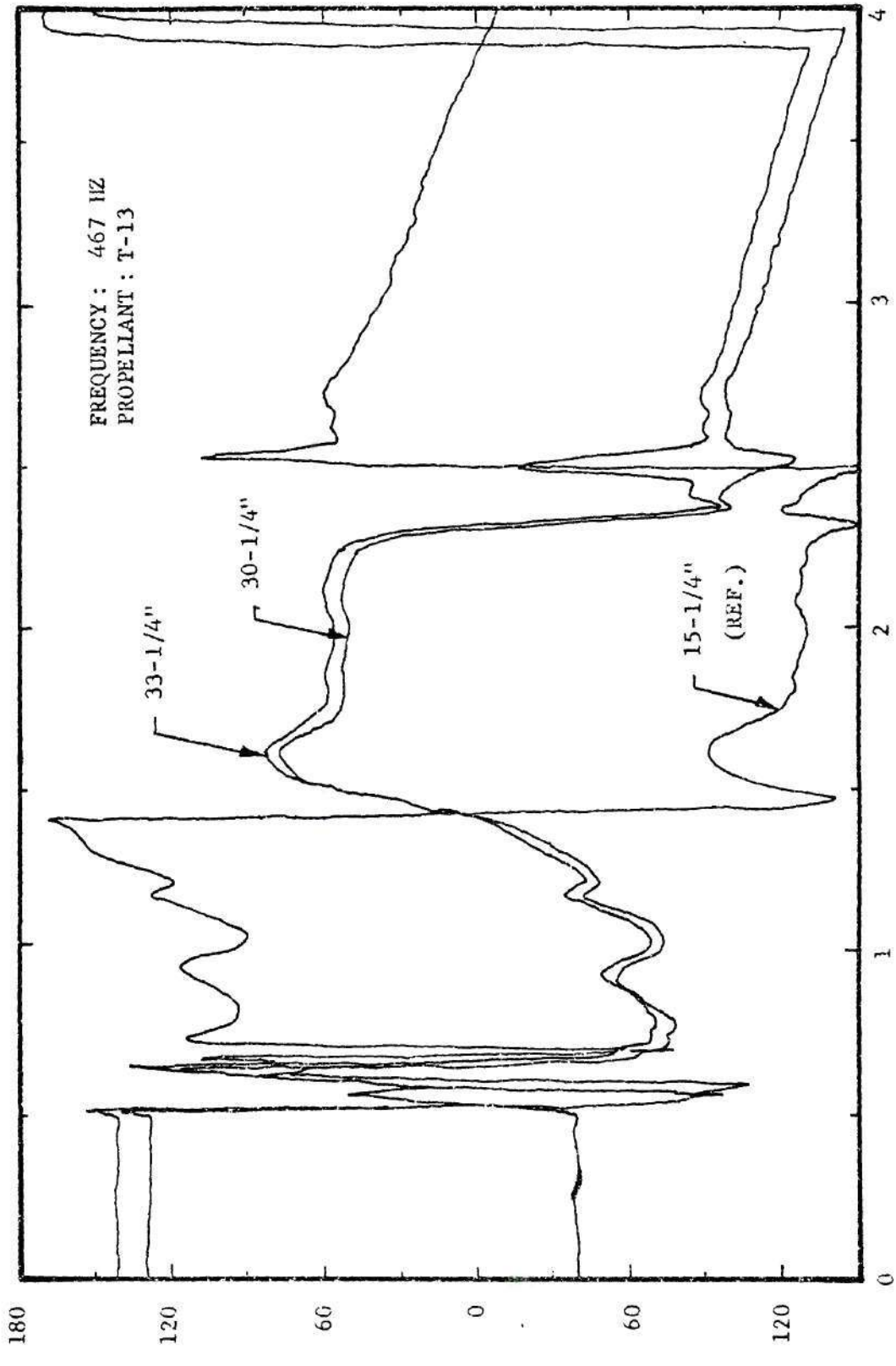

FIGURE 6-9 Variation of Pressure Phases with Respect to Time

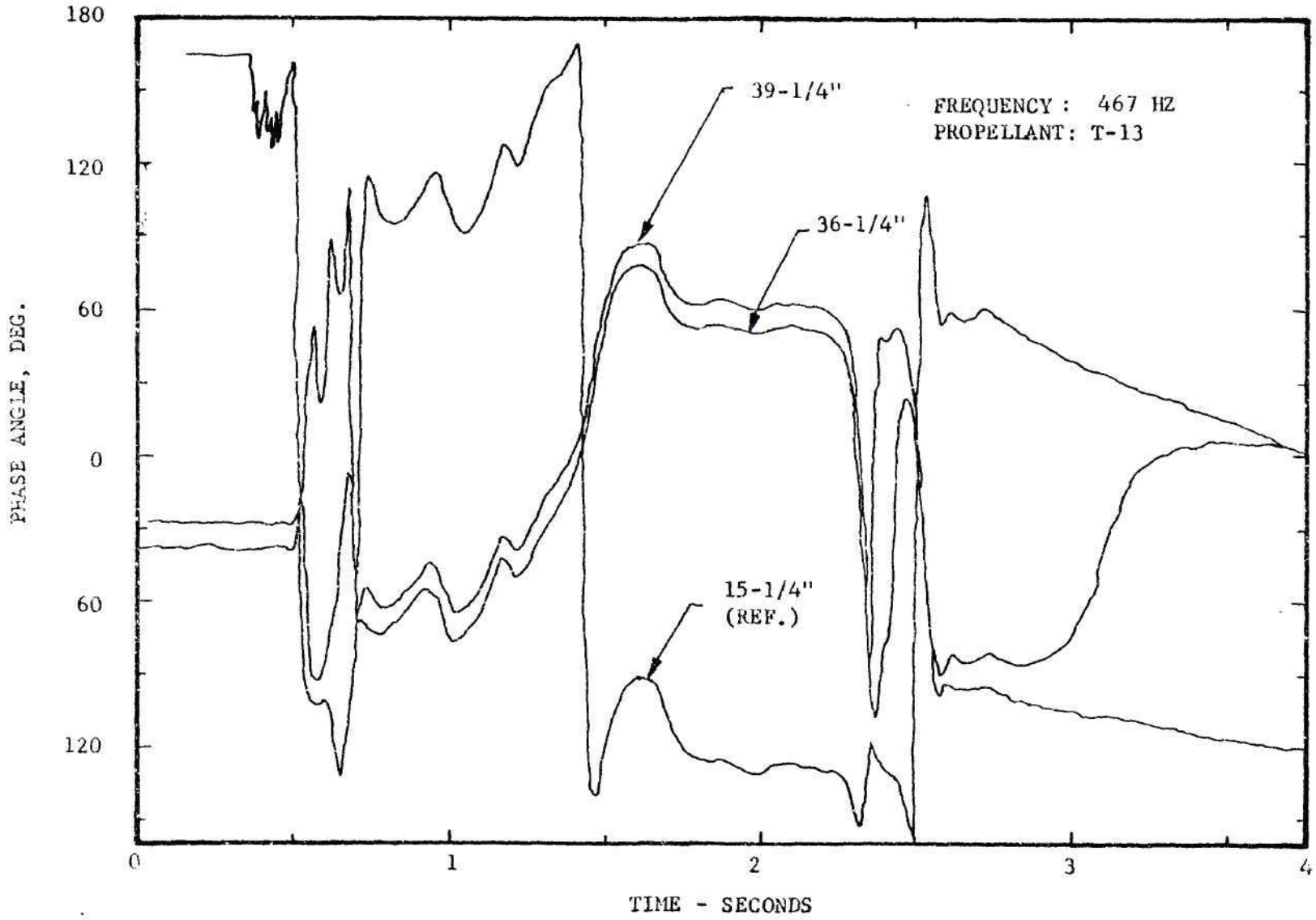

Figure 6-10 Variation of Pressure Phases with Respect to Time

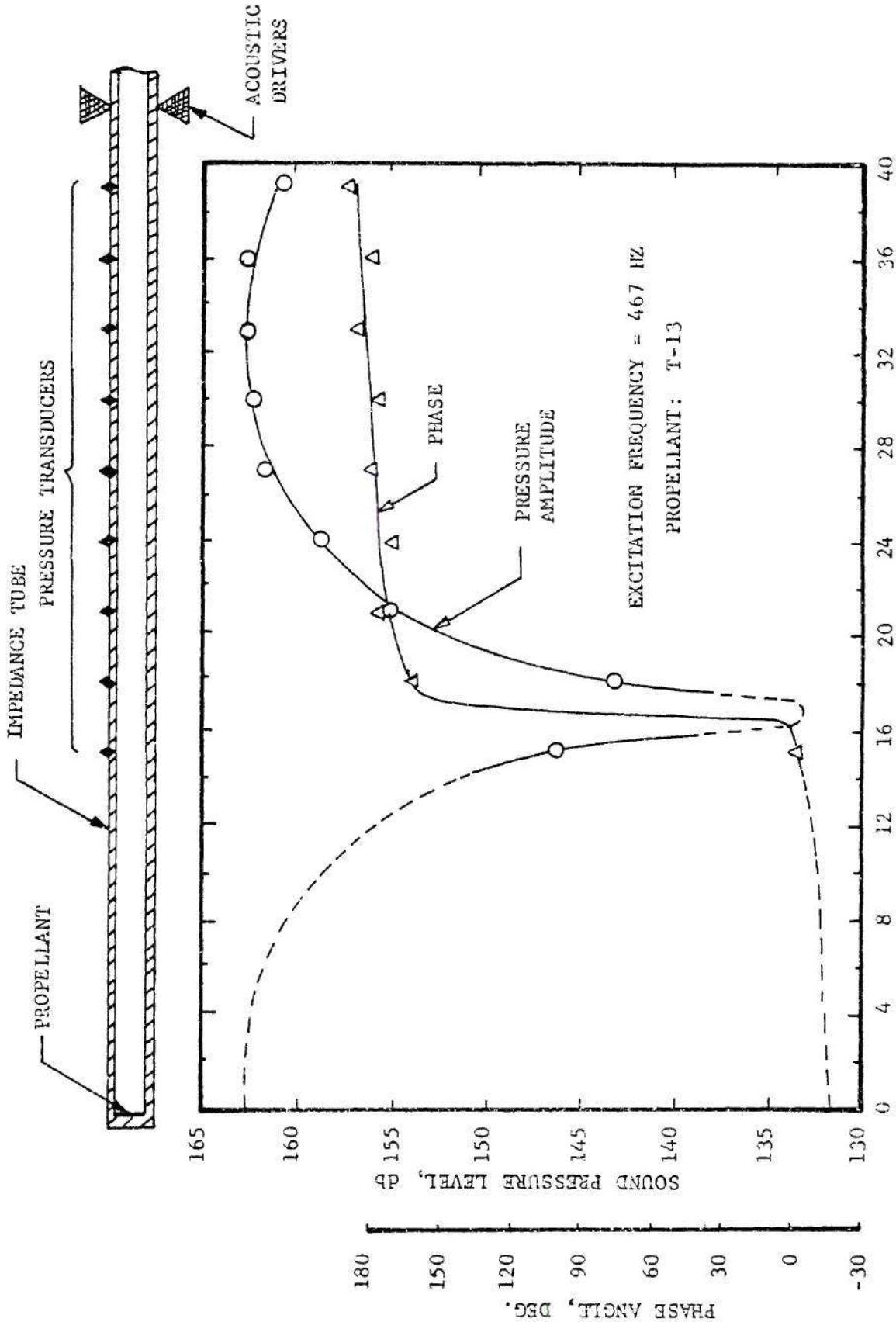

Figure 6-11. Axial Variation of Pressure Amplitude and Phase in the Impedance Tube.

also used to obtain the total burning time of the tested samples, which is used together with the sample thickness to obtain the burning rate of the propellant.

The data reduction procedures, discussed in Chapter III, were used to compute the admittances of burning solid propellants, assuming negligible gas phase losses. These data plotted in Figures 6-12 and 6-13. These figures describe the frequency dependence of the real and imaginary parts of the admittances of A-13, T-13 and the unidentified perchlorate based white propellant, respectively. Figures 6-12 shwos that all the three propellants have damping admittances throughout the frequency range at atmospheric pressure. Based on later studies, it is now believed that the admittance values presented in Figures 6-12 and 6-13 would have been different had the gas phase damping been taken into account. The computed admittances and other parameters such as the response factors, heat transfer parameters and the experimental errors are listed in Table 6-1.

The low pressure tests also showed that the characteristics of the measured data depend upon the location of the exhaust valve. Most of the test runs were conducted with the exhaust valve located immediately downstream of the acoustic drivers (i.e., the valve position number 1 in Figure 6-14), while a few runs using an A-13 propellant were conducted with the exhaust valve located at position number 2, which was situated forty feet downstream of the acoustic drivers. Some tests conducted with the exhaust valve located at position number 2, showed a different spatial pressure-phase distribution, compared to

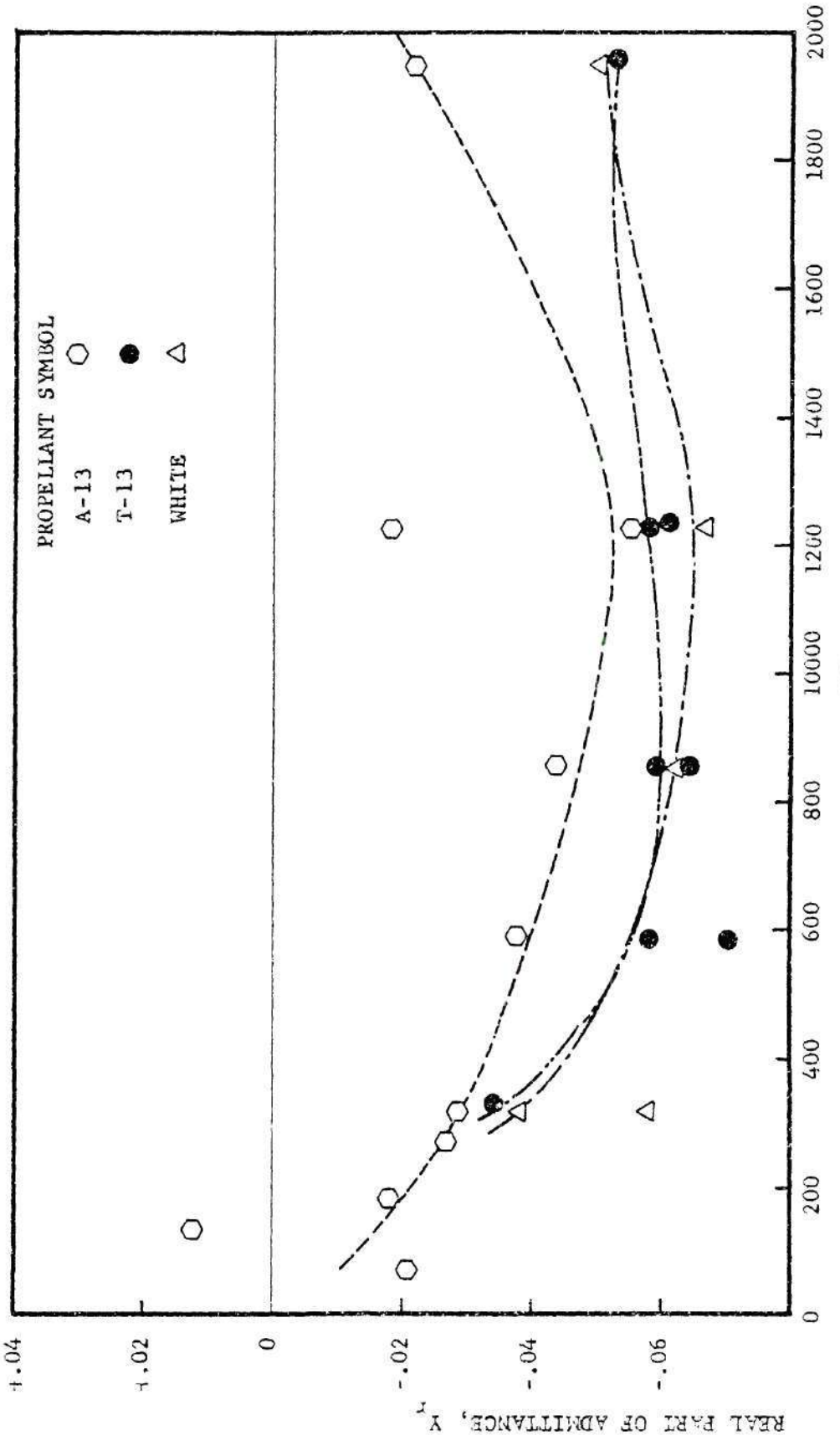

Figure 6-12. Frequency Dependence of Real Part of Admittance for Three Different Propellants at Atmospheric Pressure.

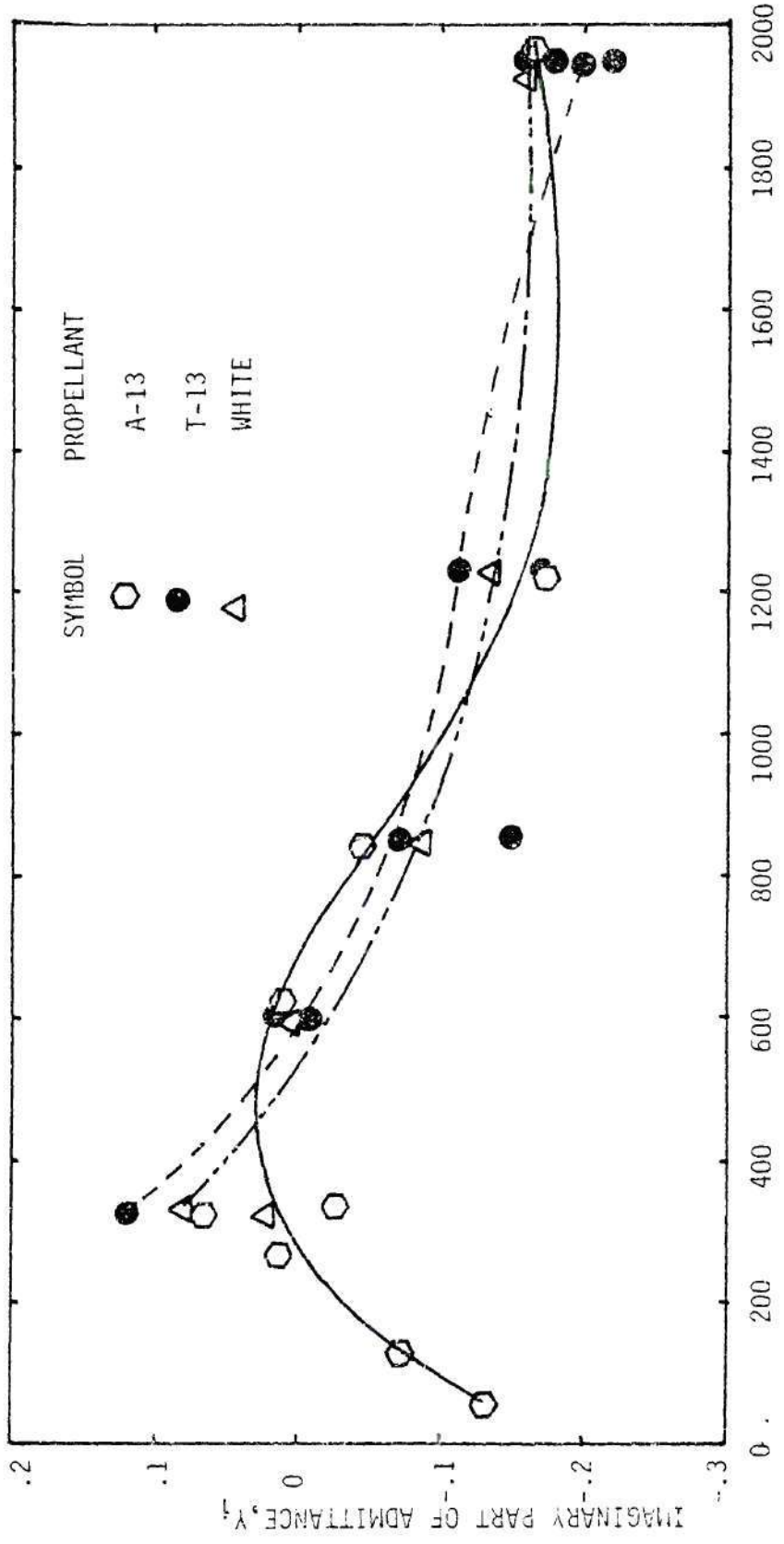

Figure 6-13. Frequency Dependence of Imaginary part of Admittance for three Different Propellants at Atmospheric Pressure.

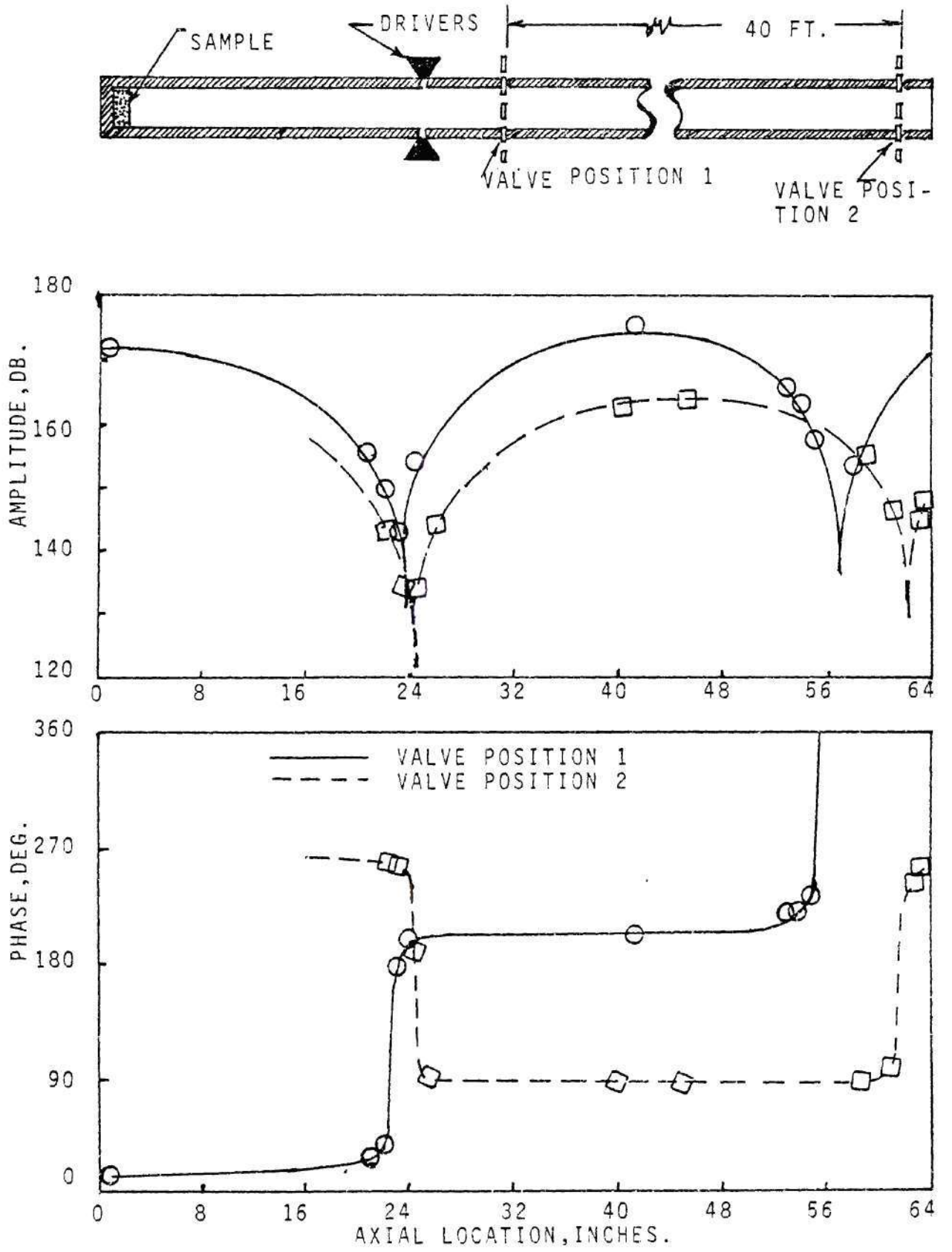

Figure 6-14. Effect of Valve Position on Pressure Amplitude and Phase.

Table 6-1. Low Pressure Data for Propellant A-13

Expt. No.	Frequency, Hz.	Pressure PSI	Y_r	Y_i	R_r	R_i	Burning Rate Ft/Sec.	Heat Transfer Parameter, C	Amp. Error DB	Phase Error, Deg.
633-66	1950.00	15.70	-.21716E-01	-.10662E+00	-.52310E+00	-.64519E+01	.004	1.431	.649E+00	.636E+00
633-73	1225.00	15.70	-.17770E-01	-.62421E-01	-.27928E+00	-.37802E+01	.004	.864	.206E+01	.103E+00
633-74	1225.00	15.70	-.58752E-01	-.74544E-01	-.27570E+01	-.45220E+01	.004	.938	.133E+01	.952E-01
633-75	850.00	15.70	-.44182E-01	-.11181E-01	-.18876E+01	-.69153E+00	.004	.839	.958E+00	.136E+00
633-76	598.00	15.70	-.38379E-01	.38087E-01	-.15646E+01	.22797E+01	.004	.647	.118E+01	.106E+00
633-79	69.00	15.70	-.21218E-01	-.25798E+00	.41882E+00	-.15682E+02	.004	.995	.103E+01	.218E-01
633-80	129.00	15.70	.12342E-01	-.20540E+00	.18036E+01	-.12409E+02	.004	1.416	.125E+01	.262E+00
633-82	270.00	39.70	-.10857E-01	-.54628E-01	-.23701E+00	-.53796E+01	.006	1.013	.491E+00	.947E-01
633-83	270.00	34.70	-.19404E-02	-.17129E-01	.62895E+00	-.15055E+01	.006	.863	.159E+01	.243E+00
633-84	270.00	34.70	-.90373E-02	.62966E-01	-.95838E-01	.55146E+01	.006	.682	.181E+01	.325E+00
633-86	598.00	34.70	-.83688E-01	.19182E+00	-.68508E+01	.16711E+02	.006	.274	.274E+01	.184E+00
633-87	598.00	34.70	-.44708E-01	.37638E-01	-.31784E+01	-.32615E+01	.006	.435	.164E+01	.445E+00
633-88	598.00	34.70	-.13952E+00	.78675E-02	-.11473E+02	-.54228E+00	.006	.386	.311E+00	.360E-01
633-89	129.00	34.70	-.98811E-03	-.18441E-01	.73515E+00	-.16208E+01	.006	.862	.218E+00	.134E-01
633-91	69.00	34.70	.96959E-02	.83540E-01	.23673E+00	.74945E+01	.006	.213	.261E+00	.316E-01
633-92	129.00	34.70	.19133E-01	.10242E-01	-.87735E+00	-.93781E+00	.006	.936	.261E+00	.251E-01
633-93	598.00	34.70	-.35779E-01	.53451E-01	-.24193E+01	.46513E+01	.006	.364	.157E+01	.181E+00
633-90	69.00	34.70	.40704E-01	.42988E-01	.37793E+01	.43173E+01	.006	.266	.487E+00	.804E-02

those obtained with the valve located at position number 1 (i.e., see Figure 6-14), indicating that the pressure-phase-distance behavior is dependent upon the valve position. The phase distance curves for the test runs with the valve located at position number 1 have a positive slope indicating that acoustic energy is moving from right to left along the impedance tube, while the slope of the phase distance curve for tests conducted with the exhaust valve located at position number 2 changes from negative to positive values as one moves away from the propellant surface.

An attempt was made to explain the observed experimental trends by correlating them with the predictions of the analytical studies of Chapter IV. First, the change in the sign of the slope of the phase-distance curve was considered. A similar behavior was predicted in Chapter IV, Section 2 where particle wave attenuation was considered. It was shown in that section (i.e., see Figure 4-31) that for a proper combination of values of the propellant surface admittance and gas phase damping the above-mentioned phase-distance behavior is indeed possible. This qualitative agreement between the analytical and experimental trends suggests that the observed experimental behavior may indeed have been caused by wave attenuation in the gas phase.

Next, the change in the slope of the phase-distance curve, at the propellant surface, with change in the exhaust valve position is considered. It was shown in Section 3 of Chapter IV that such a change in slope may be accomplished when the boundary condition describing the propellant surface behavior is inhomogeneous; that is, when there is

"self-noise" present at the propellant surface. While the presence of self-noise may offer one possible explanation to the observed experimental behavior, it still remains to be explained why and how wave energy was "absorbed" by the burning propellant when the valve was located at position number 1, and why and how wave energy is "supplied" by the propellant surface when the valve was located at position number 2.

The above explanation implies that the self-noise of the propellant may be sufficiently significant as to affect the observed experimental trends. This implication is in contrast with the results obtained in a study[31] in which the noise generated by burning solid propellant strands was measured independently. In this investigation combustion noise from composite solid propellants were measured in roughly, two distinct frequency regimes. One broad band region was between 40 and 2000 Hz. and another was between 2000 Hz and 10 KHz. Insignificant amount of sound power was generated and most of it occurred in the high frequency band. Therefore the "self-noise" of the propellant may not be a plausible explanation for such behavior when the admittance value of the propellant is high. However, such behavior is possible at low chamber pressures, due to the presence of a little amount of "self-noise," when the propellant has a very small driving admittance.

The next set of the tests were conducted at high chamber pressure (i.e., 300 Psig.) using the high pressure experimental facility discussed in Chapter V. In these tests, most of the measured data were sampled, digitized, and stored in a disc using the mini computer based data

acquisition system instead of the tape recorder. Later on, the stored data were plotted and printed out. Figures 6-15 through 6-18 represent the time histories of pressure amplitudes and phases obtained from a test conducted at a frequency of 280 Hz., using an A-13 propellant sample at 300 Psig. chamber pressure. Figures 6-19 and 6-20 are the cross plots of amplitudes and phases at a record point of 36 obtained from the plotter attached to the mini computer.

An examination of Figures 6-15 through 6-18 reveals that steady state burning occurs in the time interval between records 33 and 46. Admittance values for all these record points were computed using several different data reduction schemes and the real part of the admittances were plotted against record points in Figures 6-21 and 6-22. The admittances plotted in Figures 6-21 and 6-22 were computed neglecting gas phase bulk losses. The computed admittances and other quantities such as the response factors, heat transfer parameters and computed experimental errors are listed in Tables 6-2 through 6-6. Results obtained using both pressure amplitudes and phases with constant wall temperature with and without mean flow, are presented in Tables 6-2 and 6-3, respectively. A comparison of real part of admittance values computed with and without mean flow are shown in Figure 6-21. The admittance values are relatively smaller when computed with mean flow. Also, the admittances, the response factors, heat transfer parameter and the experimental errors in amplitude and phase, computed with and without mean flow for the record point of 33 are compared in Table 6-4. It is observed that the errors with mean flow are relatively smaller compared to those computed without mean flow. Therefore, the results

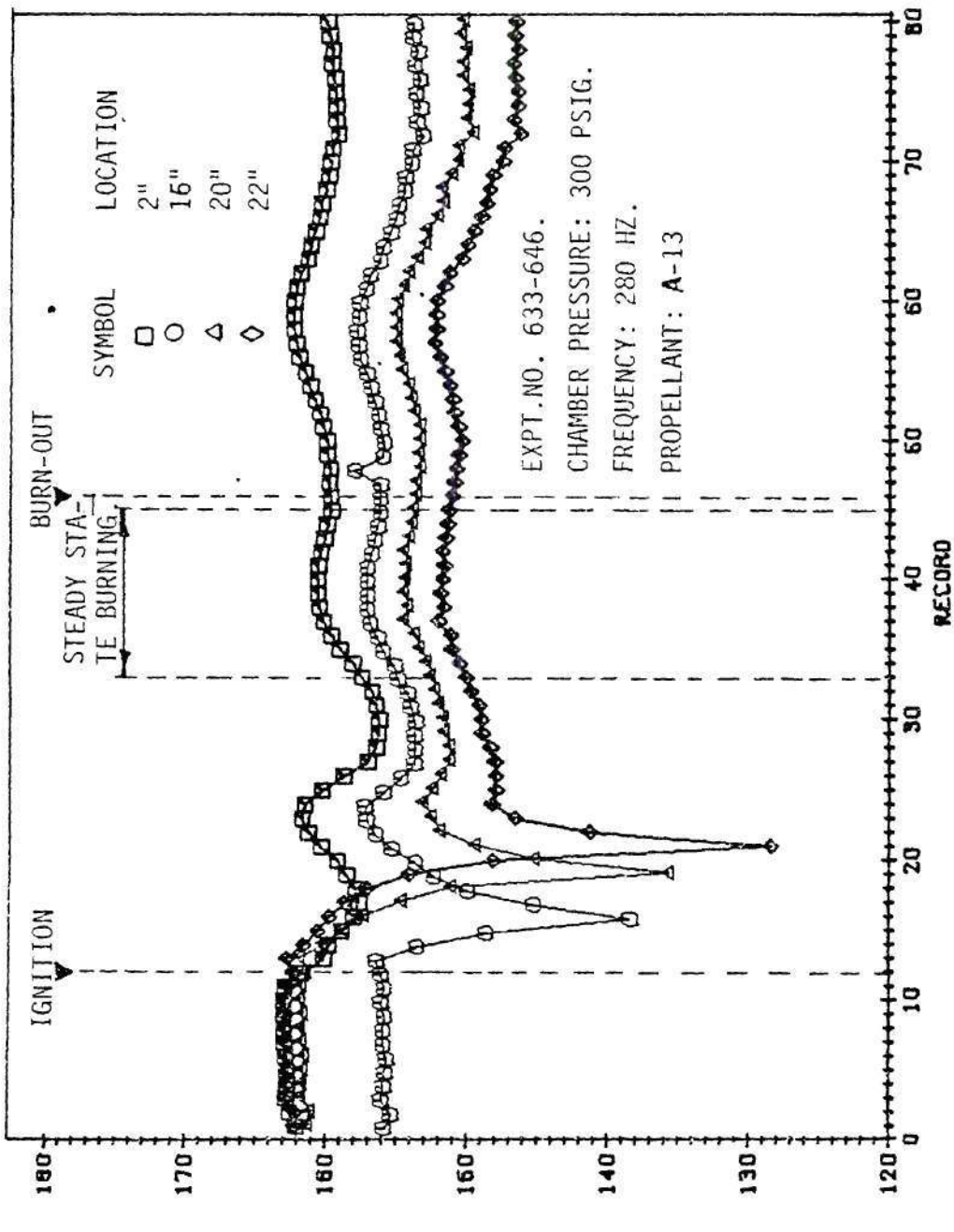

Figure 6-15. Variation of Pressure Amplitude with Respect to Time.

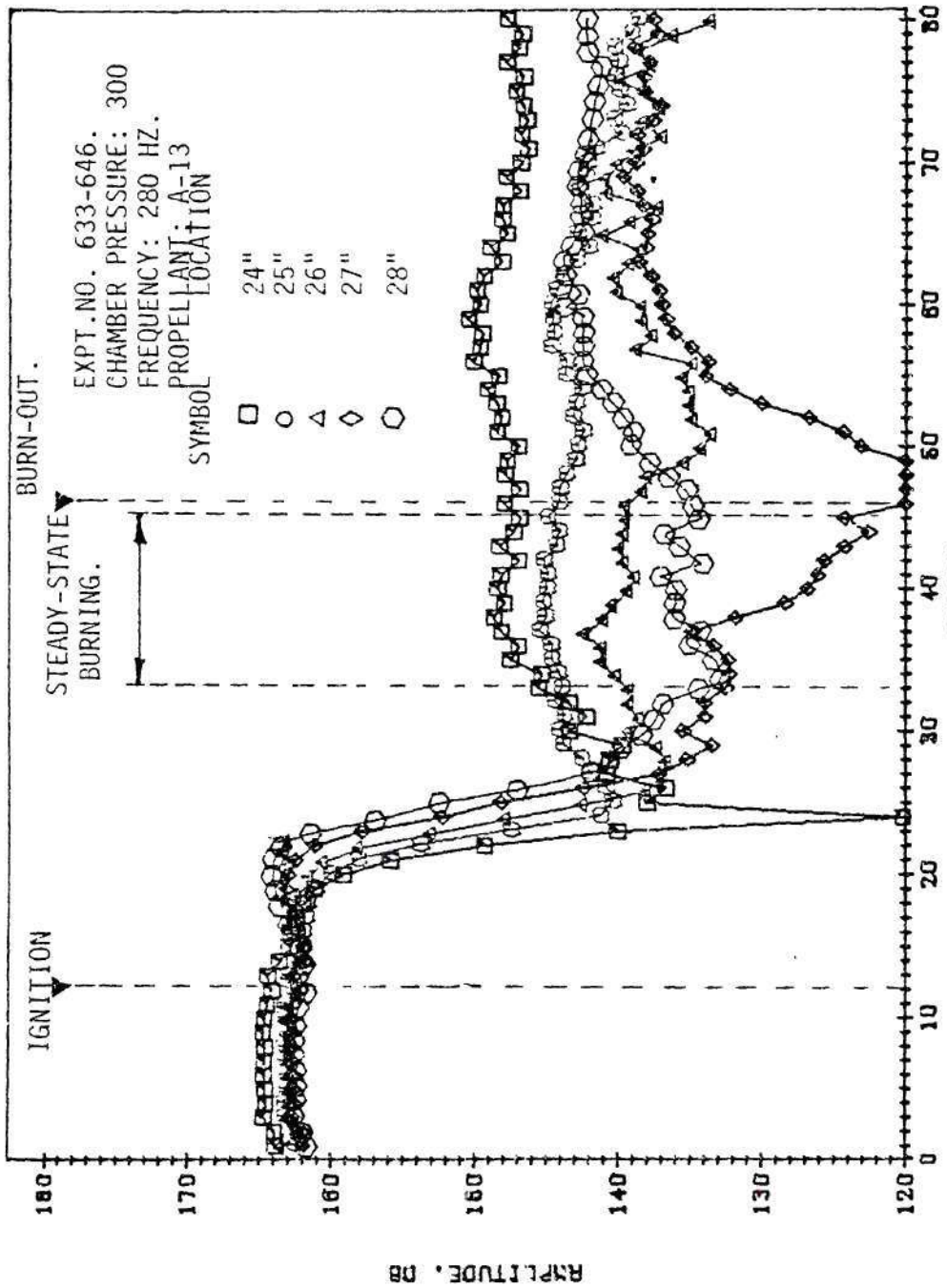

Figure 6-16. Variation of Pressure Amplitude with Respect to Time.

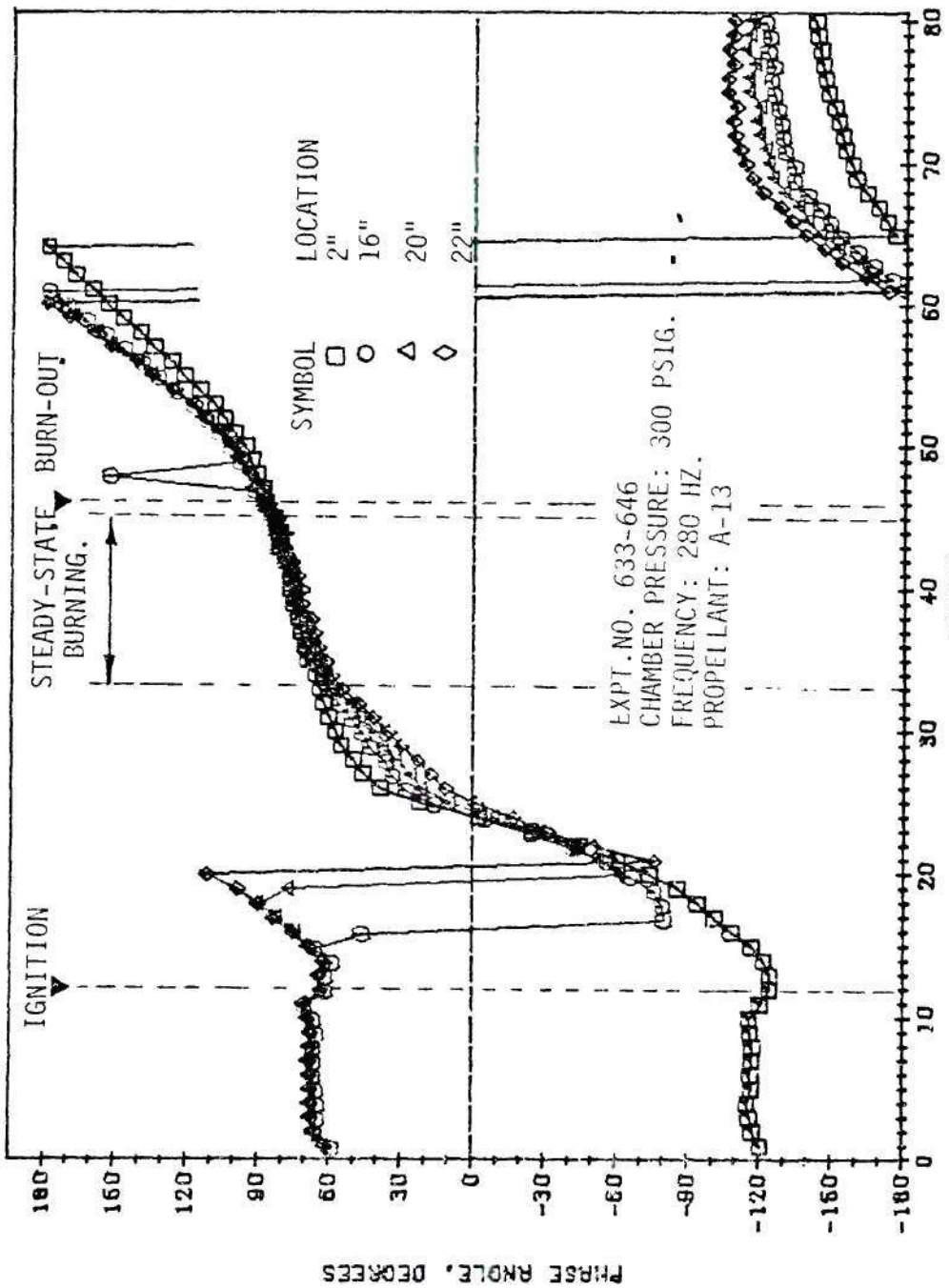

Figure 6-17. Variation of Pressure Phase with Respect to Time.

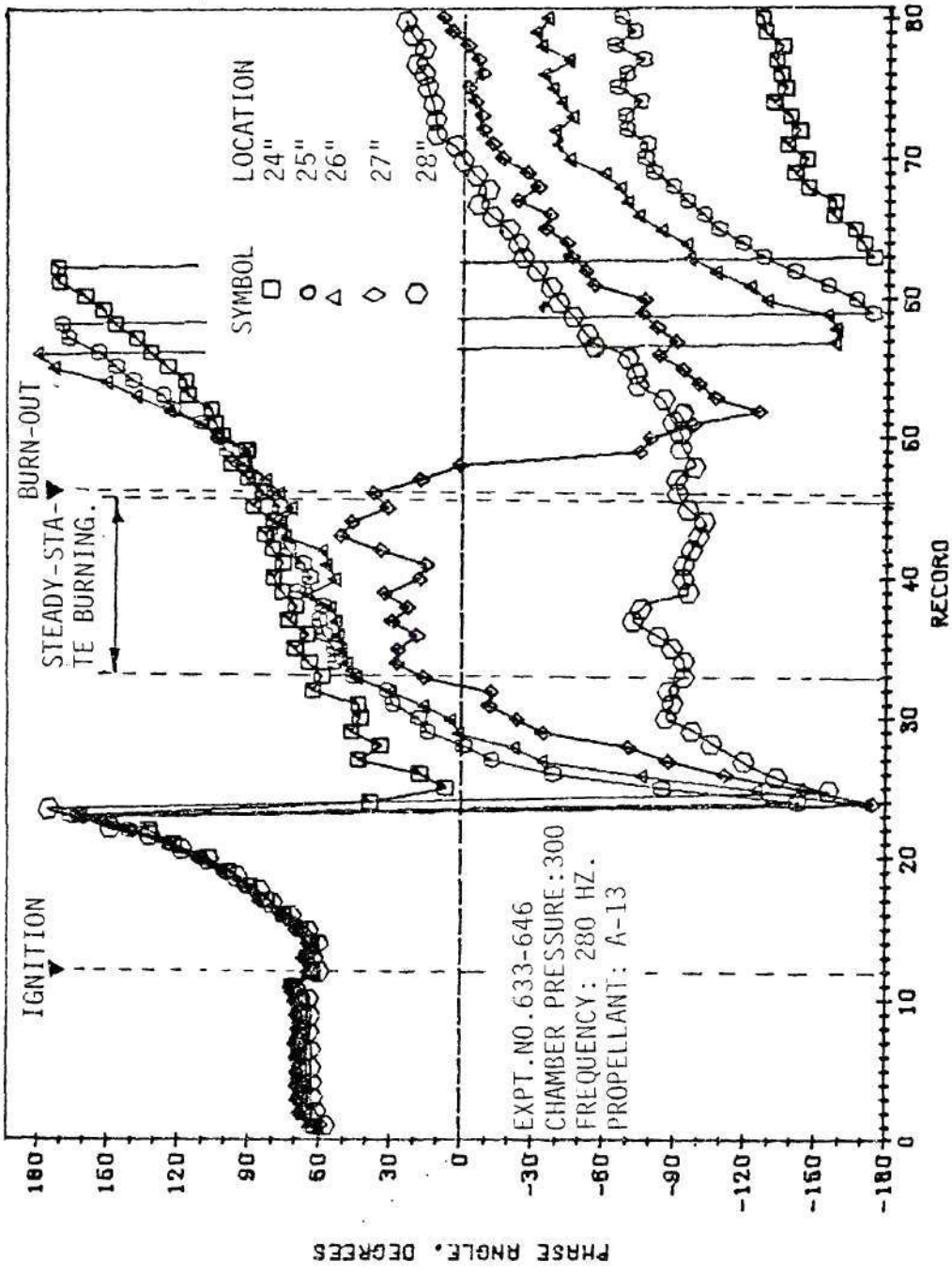

Figure 6-18. Variation of Pressure Phase with Respect to Time.

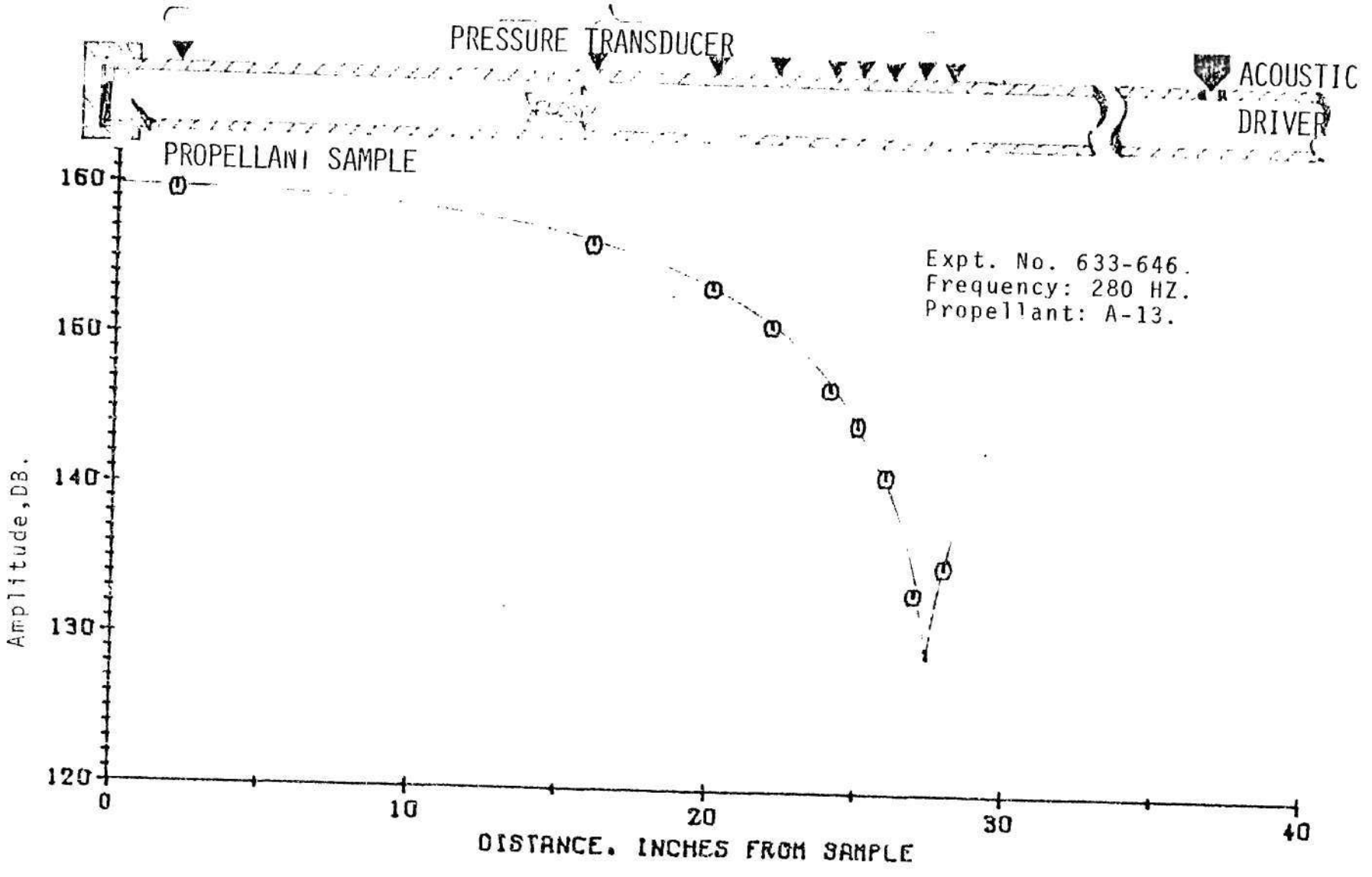

Figure 6-19. Axial Variation of Pressure Amplitude in Impedance Tube.

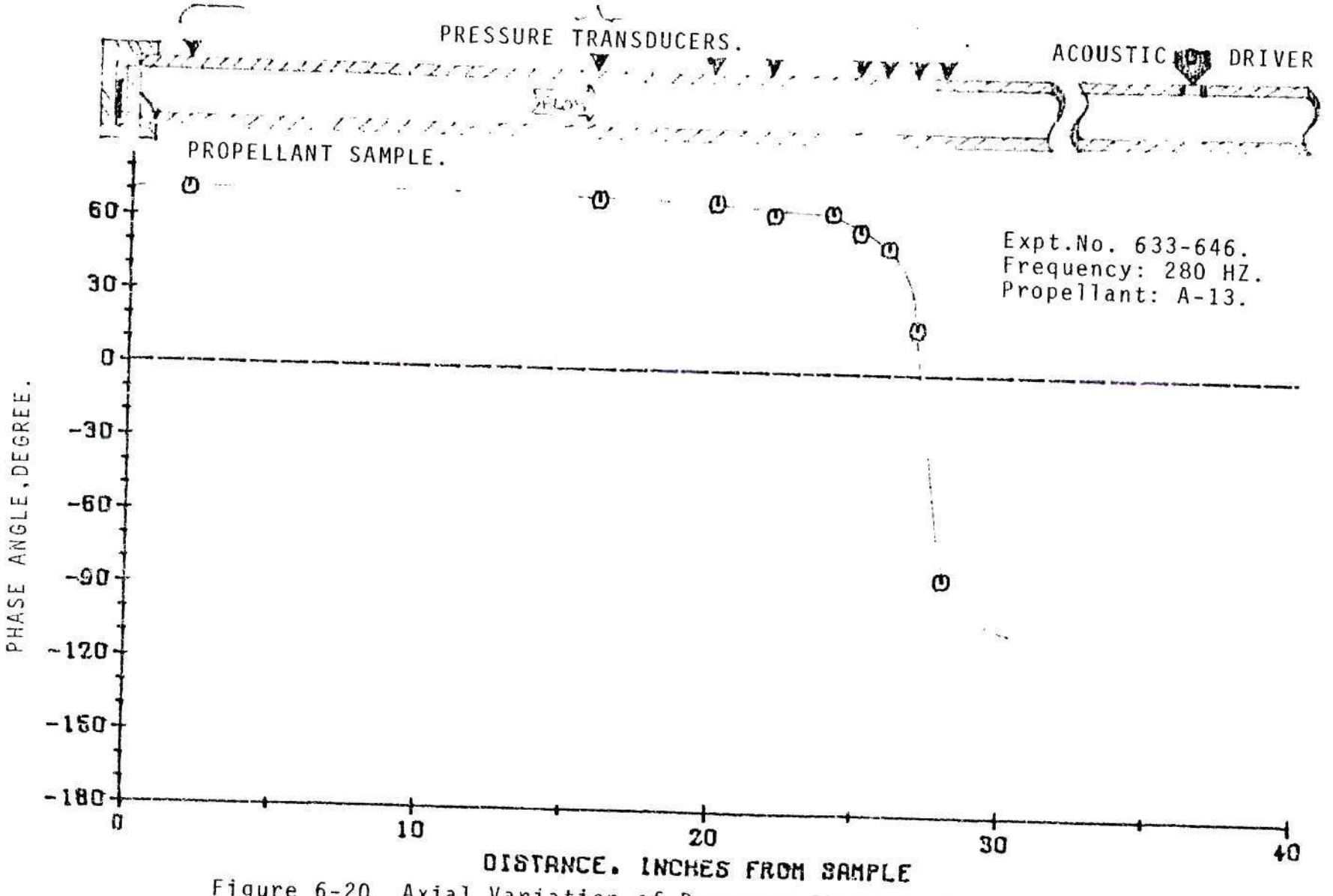

Figure 6-20. Axial Variation of Pressure Phase in Impedance Tube.

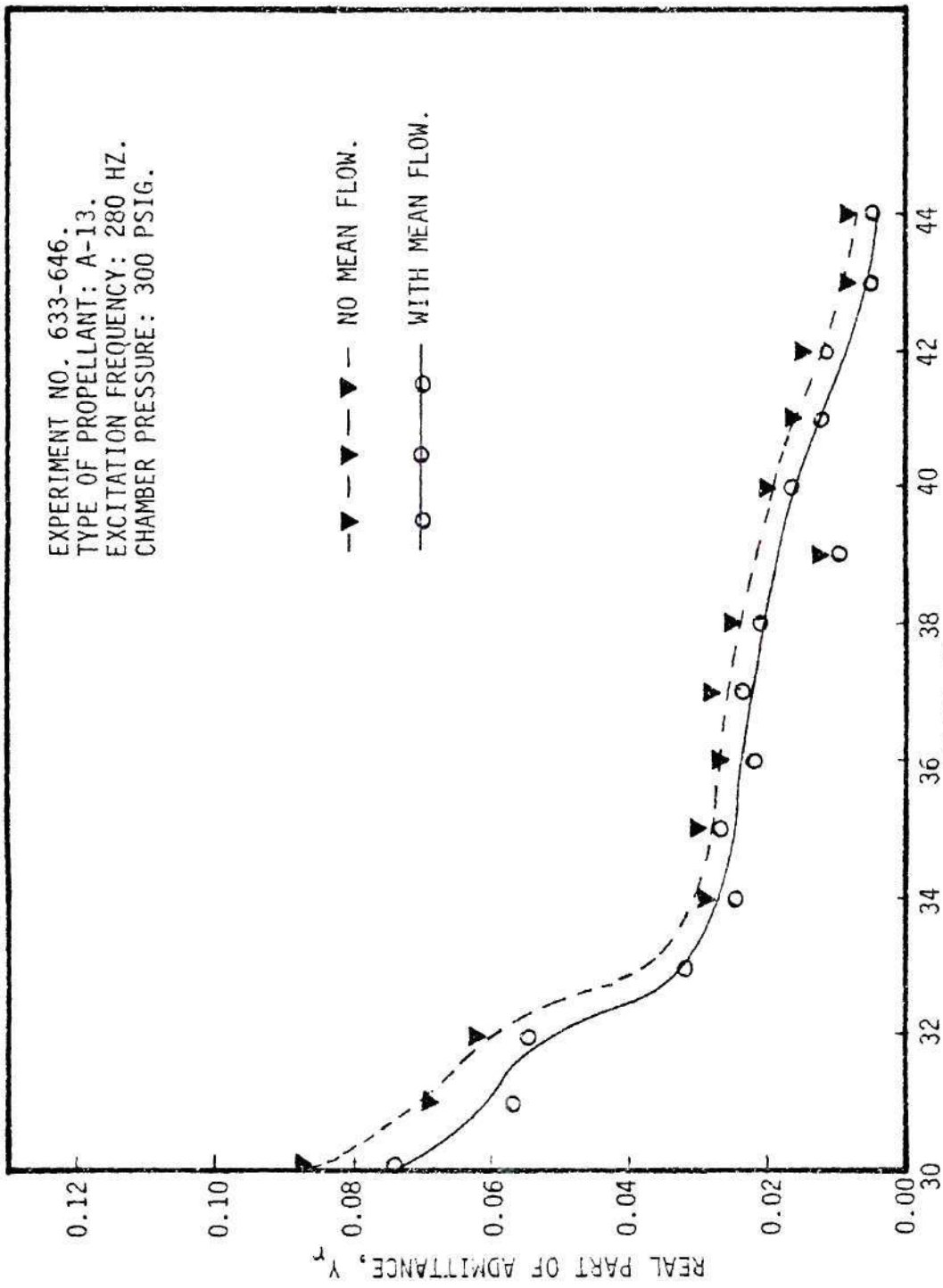

Figure. 6-21. Variation of Real Part of Admittace With Respect to Record Numbers, With and Without Mean Flow.

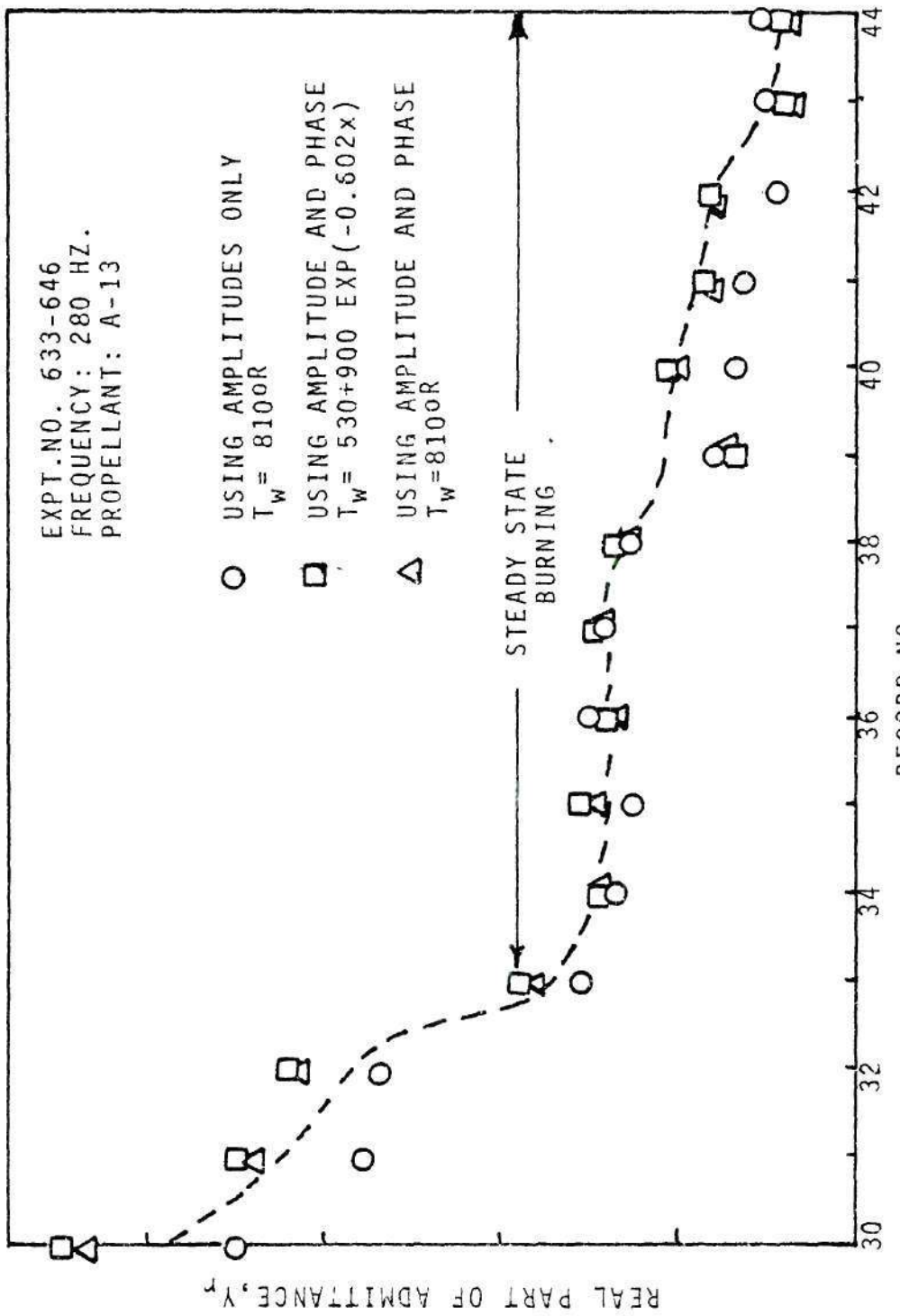

Figure 6-22. Time Dependence of Real Part of Admittance.

Table 6-2. High Pressure Data for A-13 Propellant at 280 Hz. with Mean Flow

Experiment No. E-16-633-646
Type of Propellant: A-13
Burning Rate: 0.0139 Ft/sec.
Chamber Pressure: 300 Psig.
Frequency of Excitation: 280 Hz.

Flame Temperature: 3780 °R
Wall Temperature: 810 °R
Method of Computation: Amplitude and Phase were used. With Mean Flow

Record No.	Real Admittance Y_r	Imaginary Admittance Y_i	Real Response Factor R_r	Imaginary Response Factor R_i	Heat Transfer Parameter C	Error in Amp. DB	Error in Phase Deg.
30	.74665E-01	.10197E+00	.22168E+02	.29436E+02	1.000	.609E+00	.568E-01
31	.56829E-01	.10069E+00	.17036E+02	.29046E+02	1.007	.724E+00	.674E-01
32	.54208E-01	.10690E+00	.16276E+02	.30831E+02	1.016	.674E+00	.730E-01
33	.31523E-01	.11823E+00	.97384E+01	.34069E+02	1.019	.215E+00	.515E-01
34	.24131E-01	.19798E+00	.97384E+01	.57039E+02	.774	.362E+00	.444E-01
35	.25748E-01	.20176E+00	.79150E+01	.58119E+02	.759	.253E+00	.573E-01
36	.21643E-01	.19575E+00	.67391E+01	.56383E+02	.751	.333E+00	.326E-01
37	.23837E-01	.20647E+00	.73531E+01	.59472E+02	.746	.264E+00	.370E-01
38	.20816E-01	.19636E+00	.64958E+01	.56559E+02	.740	.396E+00	.411E-01
39	.92532E-02	.19537E+00	.31673E+01	.56257E+02	.735	.148E+00	.344E+00
40	.16022E-01	.19340E+00	.51166E+01	.55700E+02	.731	.628E+00	.361E+00
41	.12193E-01	.19219E+00	.40149E+01	.55700E+02	.727	.439E+00	.364E+00
42	.11967E-01	.19724E+00	.39413E+01	.56799E+02	.724	.739E+00	.360E+00
43	.45008E-02	.20071E+00	.17862E+01	.57788E+02	.721	.571E+00	.347E+00
44	.49463E-02	.19788E+00	.19176E+01	.56974E+02	.719	.403E+00	.479E-01

Table 6-3. High Pressure Data for A-13 Propellant at 280 Hz. Without Mean Flow

Experiment No. E-16-633-646
Type of Propellant: A-13
Burning Rate: 0.0139 Ft/sec.
Chamber Pressure: 300 Psig.
Frequency of Excitation: 280 Hz.

Flame Temperature: 3780 °R
Wall Temperature: 810 °R
Method of Computation: Amplitude and Phase were used.

Record No.	Real Admittance Y_r	Imaginary Admittance Y_i	Real Response Factor R_r	Imaginary Response Factor R_i	Heat Transfer Parameter C	Error in Amp. DB	Error in Phase
30	.87548E-01	.12705E+00	.25835E+02	.36663E+02	.940	.964E+00	.933E-01
31	.68330E-01	.12786E+00	.2303E+02	.36874E+02	.940	.961E+00	.104E+00
32	.63041E-01	.13524E+00	.18772E+02	.38994E+02	.940	.862E+00	.102E+00
33	.37299E-01	.1428E+00	.11355E+02	.41145E+02	.943	.396E+00	.744E-01
34	.27879E-01	.14043E+00	.86478E+01	.40446E+02	.947	.585E+00	.620E-01
35	.29825E-01	.13867E+00	.92102E+01	.39943E+02	.949	.518E+00	.743E-01
36	.26054E-01	.12888E+00	.81360E+01	.37122E+02	.951	.845E+00	.463E-01
37	.28528E-01	.13871E+00	.88370E+01	.39953E+02	.951	.695E+00	.334E-01
38	.25668E-01	.12210E+00	.80343E+01	.35169E+02	.962	.650E+00	.755E-01
39	.12582E-01	.12251E+00	.42659E+01	.35274E+02	.952	.863E+00	.747E-01
40	.19962E-01	.11890E+00	.63940E+01	.34242E+02	.951	.878E+00	.414E+00
41	.15876E-01	.11626E+00	.52209E+01	.33478E+02	.951	.671E+00	.430E+00
42	.15311E-01	.12080E+00	.50534E+01	.34785E+02	.952	.962E+00	.422E+00
43	.71432E-02	.12789E+00	.26993E+01	.35632E+02	.951	.822E+00	.712E-01
44	.72737E-02	.11986E+00	.27412E+01	.34503E+02	.951	.734E+00	.116E+00

Table 6-4. Comparison of High Pressure Data for Propellant A-13 With and Without Mean Flow

Experiment No. E-16-633-646, Record No.: 33
Type of Propellant: A-13
Burning Rate: 0.0139 Ft/Sec.
Chamber Pressure: 300 Psig.
Frequency of Excitation: 280 Hz.
Flame Temperature: 3780 °R
Wall Temperature: 810 °R
Method of Computation: Using Amplitude and Phase

Parameters	With Mean Flow	Without Mean Flow
Real Part of Admittance: Y_r	0.0315	0.0373
Imaginary Part of Admittance: Y_i	0.118	0.143
Real Part of Response: R_r	9.736	11.355
Imaginary Part of Response: R_i	34.07	41.145
Heat Transfer Parameter: "C"	1.019	0.943
Error in Amplitude, DB	0.215	0.396
Error in Phase, Deg.	0.0515	0.0744

Table 6-5. High Pressure Data for A-13 Propellant at 280 Hz, with a Variable Wall Temperature

Experiment No. E-16-633-646
Type of Propellant: A-13
Burning Rate: 0.0139 Ft/Sec.
Chamber Pressure: 300 Psig.
Frequency of Excitation: 280 Hz.

Flame Temperature: 3870 °R
Wall Temperature 530. + 900 EXP (-.602x)
Method of Computation: Amp. and Phase were used. No Mean Flow

Record No.	Real Admittance Y_r	Imaginary Admittance Y_i	Real Response Factor R_r	Imaginary Response Factor R_i	Heat Transfer Parameter C	Error in Amp. DB	Error in Phase
30	.90028E-01	.13526E+00	.26614E+02	.38979E+02	.946	.101E+01	.980E-01
31	.70208E-01	.13588E+00	.20910E+02	.39147E+02	.946	.101E+01	.110E+00
32	.64792E-01	.14354E+00	.19347E+02	.41350E+02	.946	.938E+00	.106E+00
33	.38366E-01	.15125E+00	.11737E+02	.43552E+02	.949	.527E+00	.793E-01
34	.28961E-01	.13575E+00	.90425E+01	.39085E+02	.995	.876#+00	.685E-01
35	.31324E-01	.11140E+00	.97402E+01	.32078E+02	1.072	619E+00	.776E-01
36	.27986E-01	.66807E-01	.88057E+01	.19240E+02	1.202	.855E+00	.462E-01
37	.30472E-01	.85842E-01	.95115E+01	.24720E+02	1.168	.792E+00	.374E-01
38	.27839E-01	.37348E-01	.87779E+01	.10760E+02	1.311	.548E+00	.661E-01
39	.13554E-01	.50714E-01	.46599E+01	.14601E+02	1.240	.814E+00	.702E-01
40	.21418E-01	.51123E-01	.69228E+01	.14723E+02	1.223	.847E+00	.416E+00
41	.17071E-01	.43917E-01	.55047E+01	.12646E+02	1.219	.644E+00	.431E+00
42	.16478E-01	.43917E-01	.55047E+01	.12646E+02	1.261	.939E+00	.416E+00
43	.76239E-02	.60239E-01	.29484E+01	.17340E+02	1.207	.857E+00	.739E-01
44	.76925E-02	.61594E-01	.29670E+01	.17730E+02	1.184	.775E+00	.128E+00

Table 6-6. High Pressure Data for Propellant A-13 at 280 Hz.Using Pressure Amplitudes Only

Experiment No. E-16-633-646
Type of Propellant: A-13
Burning Rate: 0.0139 Ft/Sec.
Chamber Pressure: 300 Psig.
Frequency of Excitation: 280 Hz.

Flame Temperature: 3870 °R
Wall Temperature: 810 °R
Method of Computation: Amp. was used.
No Mean Flow.

Record No.	Real Admittance Y_r	Imaginary Admittance Y_i	Real Response Factor R_r	Imaginary Response Factor R_i	Heat Transfer Parameter C	Error in Amp. DB
30	.70114E-01	.13918E+00	.20803E+02	.40137E+02	.94063	.62468E+00
31	.55799E-01	.13327E+00	.16690E+00	.38419E+02	.93800	.75362E+00
32	.53363E-01	.14256E+00	.15979E+02	.41089E+02	.94021	.71406E+00
33	.31315E-01	.14447E+00	.96316E+01	.41615E+02	.94359	.19872E+00
34	.27318E-01	.13946E+00	.84878E+01	.40168E+02	.94849	.60368E+00
35	.25163E-01	.13900E+00	.78684E+01	.40032E+02	.95102	.44564E+00
36	.30571E-01	.11943E+00	.94498E+01	.34405E+02	.97382	.77459E+00
37	.28973E-01	.13399E+00	.89723E+01	.38594E+02	.96255	.70168E+00
38	.25056E-01	.90031E-01	.79031E+01	.25936E+02	1.06682	.61431E+00
39	.15964E-01	.11101E+00	.52563E+01	.31966E+02	.98393	.68010E+00
40	.12611E-01	.10932E+00	.42932E+01	.31478E+02	.98421	.75024E+00
41	.12415E-01	.11177E+00	.42312E+01	.32182E+02	.96271	.68782E+00
42	.92841E-02	.10789E+00	.33385E+01	.31060E+02	.99595	.10611E+01
43	.98168E-02	.11965E+00	.34749E+01	.34446E+02	.96239	.64258E+00
44	.10342E-01	.11793E+00	.36265E+01	.33951E+02	.95251	.49501E+00

computed with mean flow are more accurate. However, it is also observed that the effect of mean flow on computed admittance values are quite small. Since the computation time, when a mean flow was considered, was considerably higher, all the subsequent computations were done neglecting the mean flow velocity.

Results obtained using both pressure amplitudes and phases with constant wall temperature are presented in Table 6-3 and those obtained assuming a variable wall temperature are presented in Table 6-5. Results presented in Table 6-6 pertain to the case where the wall temperature was kept constant and only pressure amplitudes were used in the data reduction. Results presented in Tables 6-3, 6-5 and 6-6 and in Figure 6-22 were computed with zero mean flow. Examination of Figure 6-22 and Tables 6-3, 6-5 and 6-6 indicates a very good agreement between the results obtained using the different computational schemes. Figures 6-23 and 6-24 contain plots of the real and imaginary parts of admittances, respectively, with respect to record points of the test run discussed above. In these figures comparison is made between the admittances computed with and without bulk losses in the flow. The various parameters computed assuming the presence of bulk loss in the flow are listed in Table 6-7. Examination of the data shows the magnitude of Y_r decreases rapidly between record points 30 and 33, which are just prior to the attainment of a quasi-steady burning condition. The measured admittance values presented in Figure 6-22 change gradually even during the quasi-steady burning period. In contrast, the admittance data presented in Figure 6-23, which was obtained assuming the presence of bulk loss in the flow field are relatively higher in

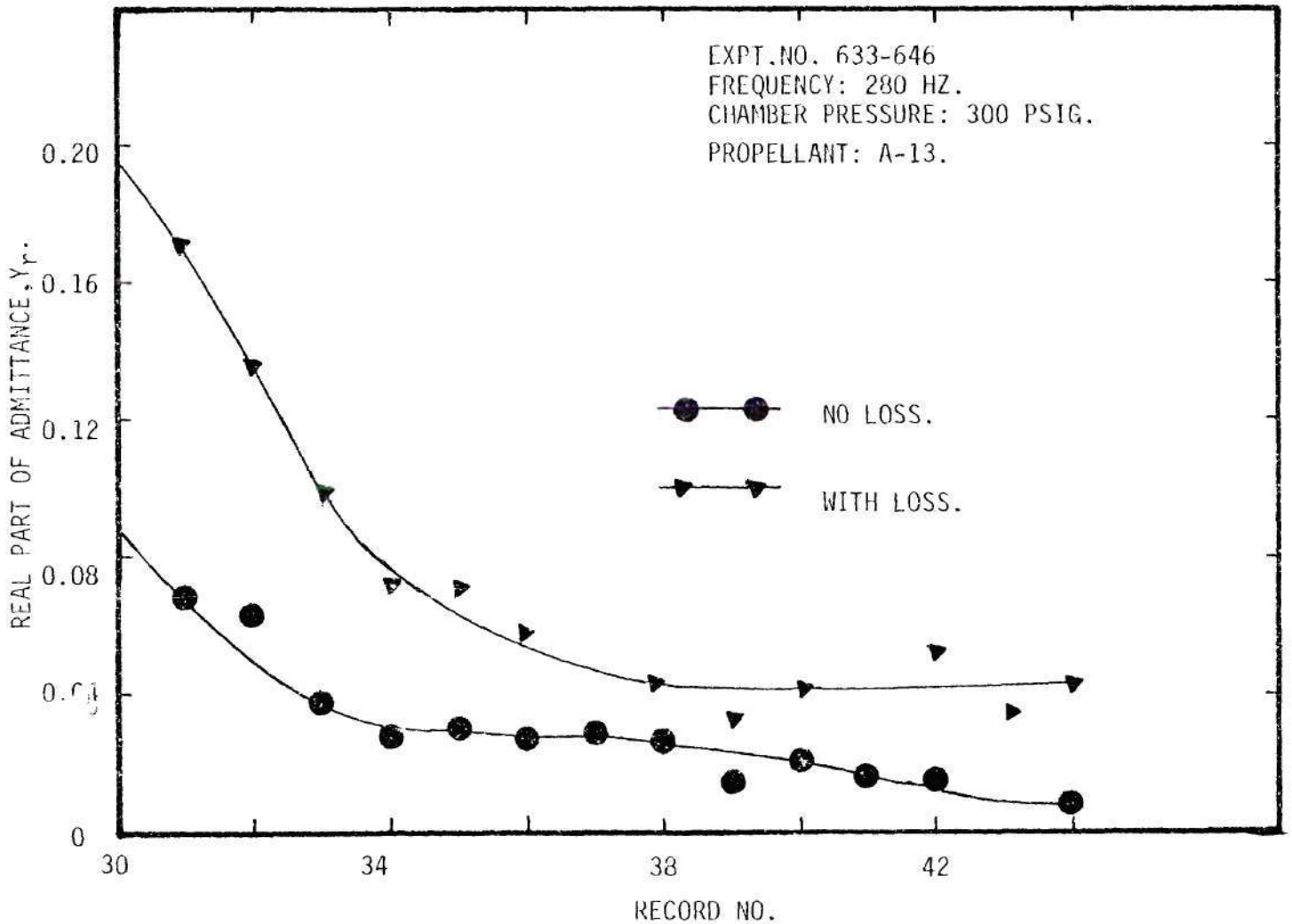

Figure 6-23. Real Part of Admittance with respect to Records with and without Loss.

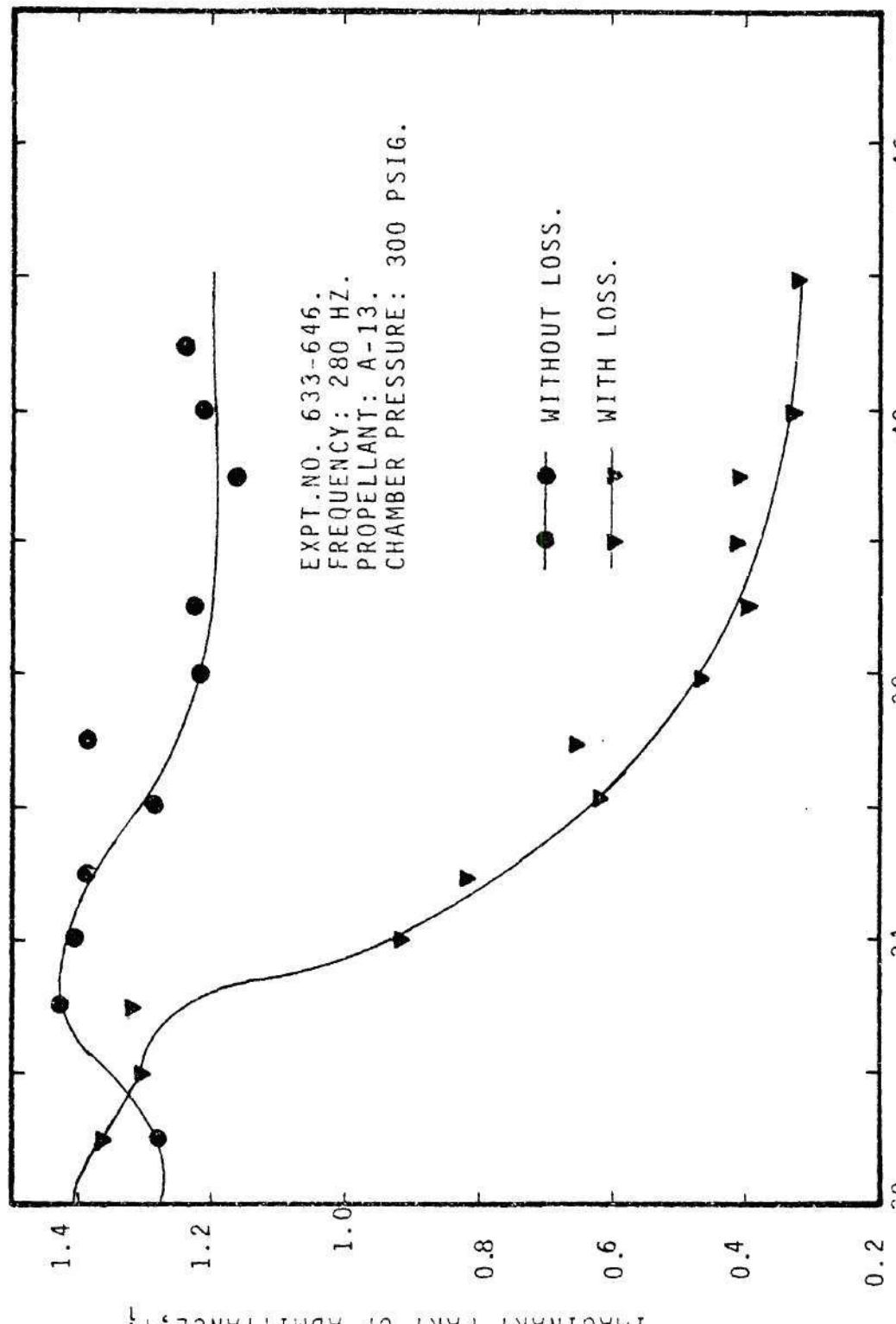

Figure 6-24. Imaginary Part of Admittance with respect to Record No.

Table 6-7. High Pressure Data for Propellant A-13 at 280 Hz. with Bulk Loss

Experiment No. E-16-633-646
Type of Propellant: A-13
Burning Rate: 0.0139 Ft/Sec.
Chamber Pressure: 300 Psig.
Frequency of Excitation: 280 Hz.

Flame Temperature: 3780 °R
Wall Temperature: 810 °R
Method of Computation: Amplitude and Phase were used. No Mean Flow

Record No.	Real Admittance Y_r	Imaginary Admittance Y_i	Real Response Factor R_r	Imaginary Response Factor R_i	Heat Transfer Parameter C	Loss Coeff. G	Error in Amp. DB	Error in Phase
30	.19588E+00	.12350E+00	.57031E+02	.35741E+02	1.056	3.857	.900E+00	.792E-01
31	.17232E+00	.13646E+00	.50231E+02	.39456E+02	.998	3.875	.858E+00	.882E-01
32	.13686E+00	.12955E+00	.40035E+02	.37429E+02	1.005	2.649	.790E+00	.905E-01
33	.98106E-01	.13241E+00	.28877E+02	.38212E+02	1.005	2.163	.294E+00	.610E-01
34	.73389E-01	.91228E-01	.21818E+02	.26324E+02	1.139	1.418	.329E+00	.510E-01
35	.72620E-01	.81702E-01	.21607E+02	.23580E+02	1.170	1.293	.327E+00	.635E-01
36	.58118E-01	.61420E-01	.17454E+02	.17728E+02	1.208	.923	.427E+00	.304E-01
37	.47608E-01	.65609E-01	.14426E+02	.18924E+02	.1227	.528	.296E+00	.341E-01
38	.41415E-01	.47001E-01	.12661E+02	.13562E+02	1.247	.421	.385E+00	.362E-01
39	.34551E-01	.39418E-01	.10692E+02	.11373E+02	1.268	.605	.191E+00	.351E+00
40	.42265E-01	.41959E-01	.12909E+02	.12112E+02	1.241	.614	.645E+00	.368E+00
41	.41317E-01	.40841E-01	.12637E+02	.11790E+02	1.235	.712	.386E+00	.375E+00
42	.52361E-01	.32130E-01	.15825E+02	.92897E+01	1.301	1.006	.765E+00	.363E+00
43	.34854E-01	.31700E-01	.10787E+02	.91515E+01	1.311	.755	.570E+00	.355E+00
44	.46417E-01	.32812E-01	.14113E+02	.94814E+01	1.292	1.081	.461E+00	.346E+00

magnitudes and their relative changes during the quasi-steady period are much smaller. The observed changes in admittance values during the quasi-steady period might be due to an uneven burning or propellant during the test. The real parts of the admittance values for a test conducted at 350 Hz., for the quasi-steady period only are computed with and without bulkloss and they are plotted in Figure 6-25 with respect to the record points. A similar trend is observed in both the cases during the quasi-steady period of burning. The various quantities, such as, response factors, heat transfer parameter, experimental error, etc., computed with and without the assumed bulk losses in the flow, for the test run conducted at 350 Hz., are presented in Tables 6-8 and 6-9, respectively. It is to be noted that the computed errors in pressure amplitudes and phases are relatively smaller when a bulkloss is assumed to be present in the flow compared to those without any assumed bulklosses (i.e., compare Tables 6-3 and 6-7; and Tables 6-8 and 6-9). These results, thus, strongly suggest that the presence of gas phase losses be included in the developed data reduction scheme, especially when the investigated admittances are small.

Figures 6-26 and 6-27 describe the frequency dependence of both the real and imaginary parts of the admittances of an A-13 propellant at low and high pressures. It is observed from Figure 6-26 that the propellant has negative real admittances at low chamber pressures (i.e., both at 1 and 20 Psig.), indicating that the propellant is damping under these conditions, whereas it shows "driving" behavior at a chamber pressure of 300 Psig., as the real part of the admittance becomes positive

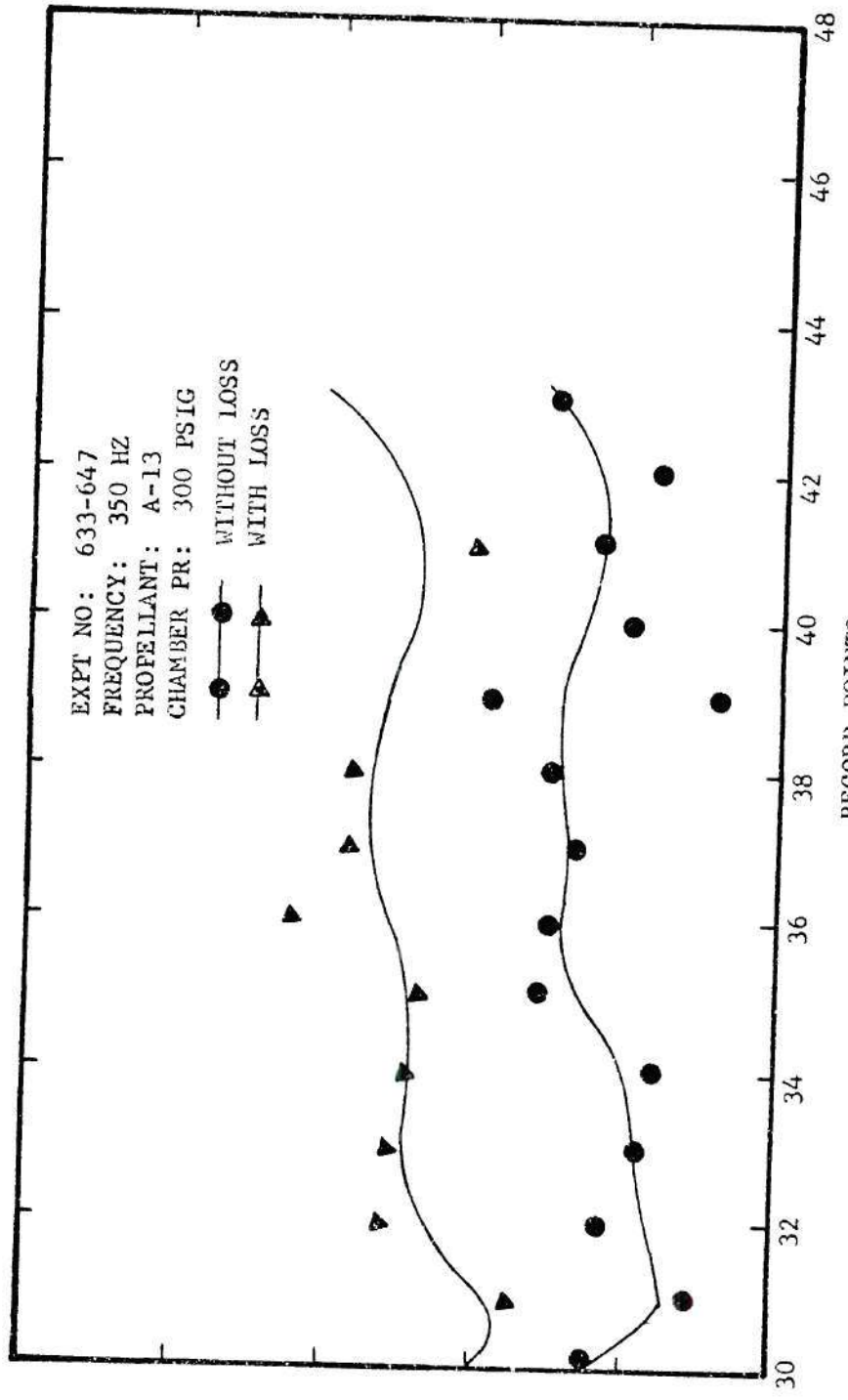

Figure 6-25. Real Part of Admittance with Respect to Records with and without Loss.

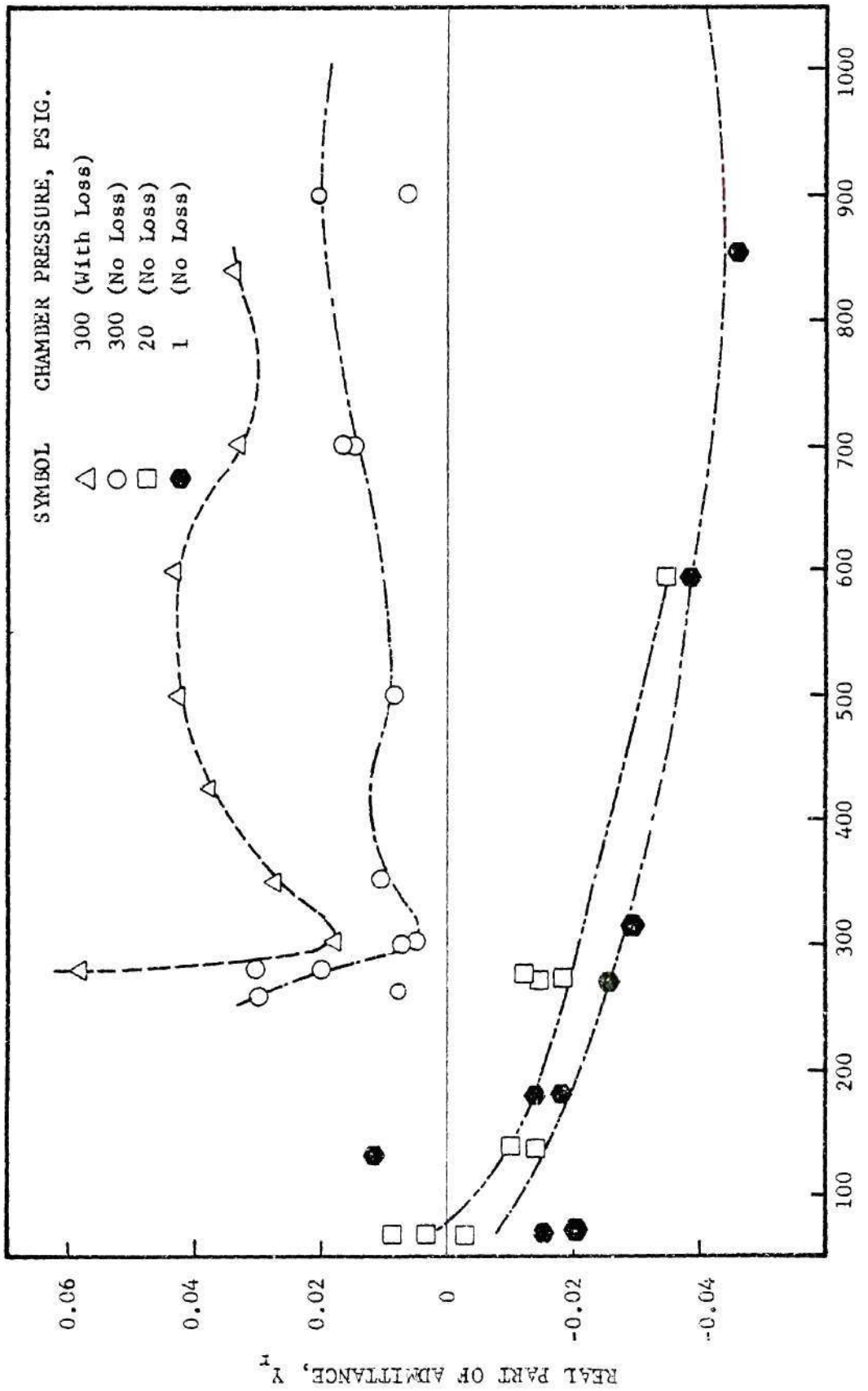

Figure 6-26. Frequency Dependence of Real Part of Admittance of A-13 Propellant.

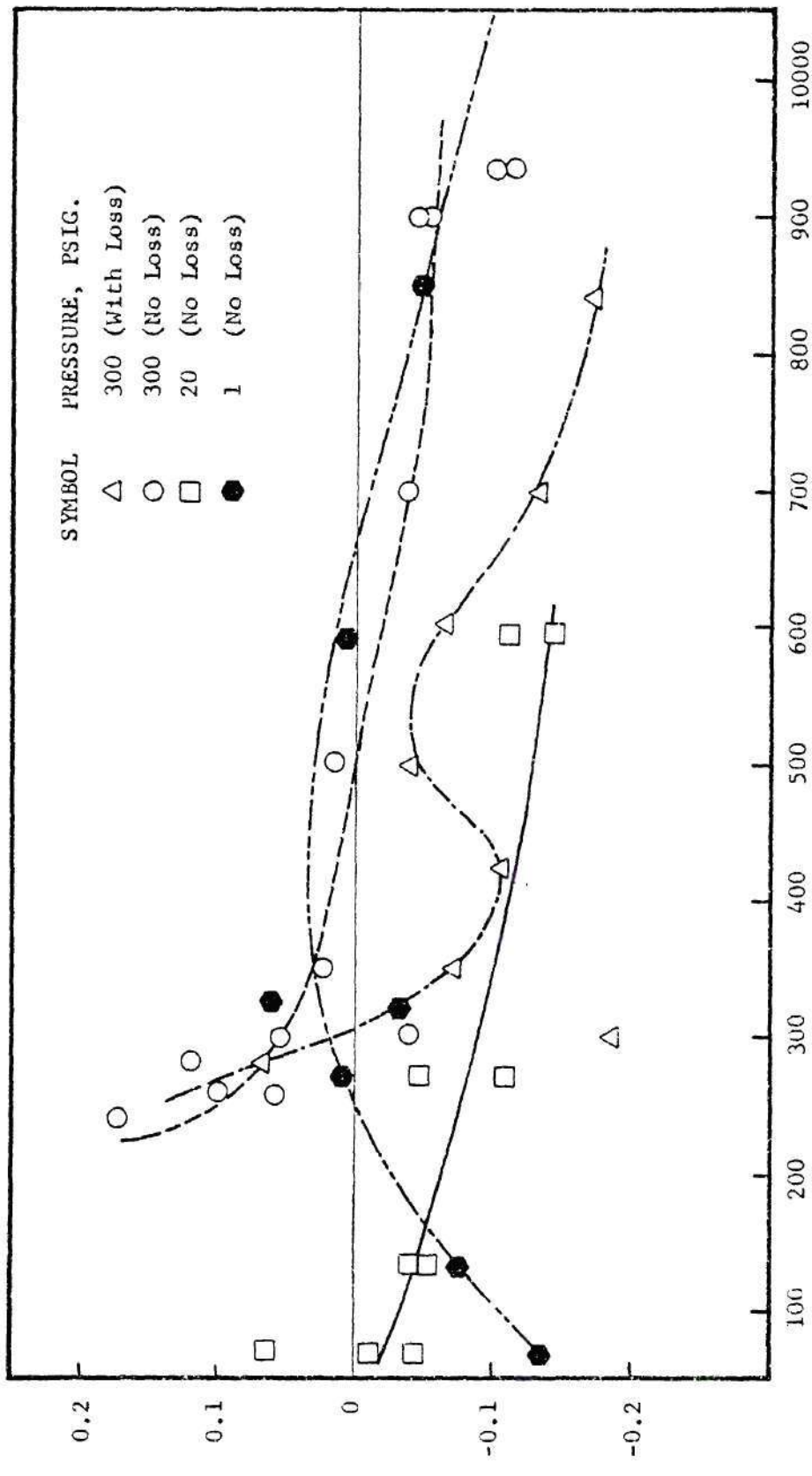

Figure 6-27. Frequency Dependence of Imaginary Part of Admittance of A-13 Propellant.

Table 6-8. High Pressure Data for Propellant A-13 at 350 Hz. with Bulk Loss

Experiment No. E-16-633-647
Type of Propellant: A-13
Burning Rate: 0.0139 Ft/Sec.
Chamber Pressure: 300 Psig.
Frequency of Excitation: 350 Hz.

Flame Temperature: 3780 °R
Wall Temperature: 810 °R
Method of Computation: Amplitude and Phase were used. No Mean Flow.

Record No.	Real Admittance Y_r	Imaginary Admittance Y_i	Real Response Factor R_r	Imaginary Response Factor R_i	Heat Transfer Parameter C	Loss Coeff. G	Error in Amp. DB	Error in Phase
30	.21908E-01	-.13155E+00	.71363E+01	-.37851E+02	2.237	.366	.230E+00	.119E-01
31	.14291E-01	-.11830E+00	.49453E+01	-.34041E+02	1.961	.542	.166E+00	.111E-01
32	.32654E-01	-.10020E+00	.10229E+02	-.28822E+02	1.718	.709	.225E+00	.810E-02
33	.31050E-01	-.11319E+00	.97750#+01	-.32561E+02	1.674	.766	.216E+00	.185E-01
34	.28933E-01	-.96447E-01	.91553E+01	-.27744E+02	1.741	.812	.185E+00	.727E-02
35	.27153E-01	-.74037E-01	.86364E+01	-.21293E+02	1.558	.379	.171E+00	.695E-02
36	.43886E-01	-.91742E-01	.13461E+02	-.26380E+02	1.590	.798	.125E+00	.179E-01
37	.37292E-01	-.91526E-01	.11562E+02	-.26322E+02	1.607	.738	.167E+00	.245E-01
38	.36801E-01	-.10597E+00	.11427E+02	-.30480E+02	1.647	.623	.130E+00	.285E-01
39	.18546E-01	-.88465E-01	.61669E+01	-.25450E+02	1.562	.820	.203E+00	.129E-01
40	.28161E-01	-.60438E-01	.89209E+01	-.17378E+02	1.473	.746	.137E+00	.353E+00
41	.20685#-01	-.83763E-01	.67800E+01	-.24096E+02	1.558	.395	.206E+00	.149E-01
43	.40696E-01	-.11963E+00	.12553E+02	-.34410E+02	1.711	.685	.284E+00	.360E+00

Table 6-9. High Pressure Data for Propellant A-13 at 350 Hz. Without Bulk Loss

Experiment No. E-16-633-647
Type of Propellant: A-13
Burning Rate: 0.0139 Ft/Sec.
Chamber Pressure: 300 Psig.
Frequency of Excitation: 350 Hz.

Flame Temperature: 3780 °R
Wall Temperature: 810 °R
Method of Computation: Amplitude and Phase were used. No Mean Flow.

Record No.	Real Admittance Y_r	Imaginary Admittance Y_i	Real Response Factor R_r	Imaginary Response Factor R_i	Heat Transfer Parameter C	Error in Amp. DB	Error in Phase
30	.48303E-02	.95534E-02	.21645E+01	.27530E+01	1.169	.392E+00	.142E-01
31	-.84879E-02	-.15184E-01	-.16512E+01	-.43758E+01	1.236	.384E+00	.888E-02
32	.37062E-02	-.24545E-01	.18647E+01	-.70616E+01	1.236	.517E+00	.637E-02
33	-.18874E-03	-.41487E-01	.75547E+00	-.11940E+02	1.232	.618E+00	.165E-01
34	-.37379E-02	.23137E-01	-.31317E+00	.66558E+01	1.052	.444E+00	.138E-01
35	.11948E-01	.22366E-01	.42018E+01	.64465E+01	1.052	.444E+00	.138E-01
36	.11966E-01	-.11272E-01	.42336E+01	-.32353E+01	1.134	.484E+00	.285E-01
37	.76451E-02	.20644E-01	.29643E+01	.59479E+01	1.017	.475E+00	.331E-01
38	.10962E-01	-.13018E-01	.39461E+01	-.37383E+01	1.119	.512E+00	.404E-01
39	-.12322E-01	.17987E-01	-.27799E+01	.51665E+01	1.016	.658E+00	.212E-01
40	.71498E-03	.22339E-01	.96904E+00	.64299E+01	1.052	.445E+00	.352E+00
41	.51613E-02	.16500E-01	.22532E+01	.47530E+01	1.039	.525E+00	.192E-01
42	-.32152E-02	-.96253E-02	-.13689E+00	-.27726E+01	1.133	.501E+00	.342E+00
43	.11649E-01	-.21394E-01	.41497E+01	-.61485E+01	1.133	.642E+00	.361E+00

at this chamber pressure. However, when the presence of acoustic bulk loss is included in the data reduction the computed admittance values are increased considerably. Figures 6-28 and 6-29 describe the frequency dependence of both the real and imaginary parts of the admittances of A-13 and A-15 propellants, when the presence of acoustic bulk loss in the flow is included in the data reduction. Figure 6-30 describes the frequency dependence of the real parts of response factors of propellants A-13 and A-15. The parameters computed for propellants A-13 and A-15, at different frequencies and at record points where the computed error in phases were below a certain specified minimum value are listed in Tables 6-10 and 6-11, respectively. Examination of Figure 6-28 shows that propellant A-13 is a better driver than propellant A-15 in the frequency range below 700 Hz.; this trend seems to reverse itself at higher frequencies. Figure 6-29 indicates that the imaginary part of the admittance of propellant A-15 is higher than that of A-13 and they both follow the same trend with respect to frequency. Figure 6-30, in which the real part of the response factor of propellants A-13 and A-15 are plotted shows that the A-13 propellant has higher response factors than propellant A-15 throughout the frequency range.

The accuracy of the data presented so far is open to question due to the observed scatter in the shown admittance values. The significant contribution to the observed scatter in the admittance values is possibly due to the inability of the instrumentation system to accurately measure the pressure amplitudes and phases at and near the pressure amplitude minima. From available T-burner data[9] it is known

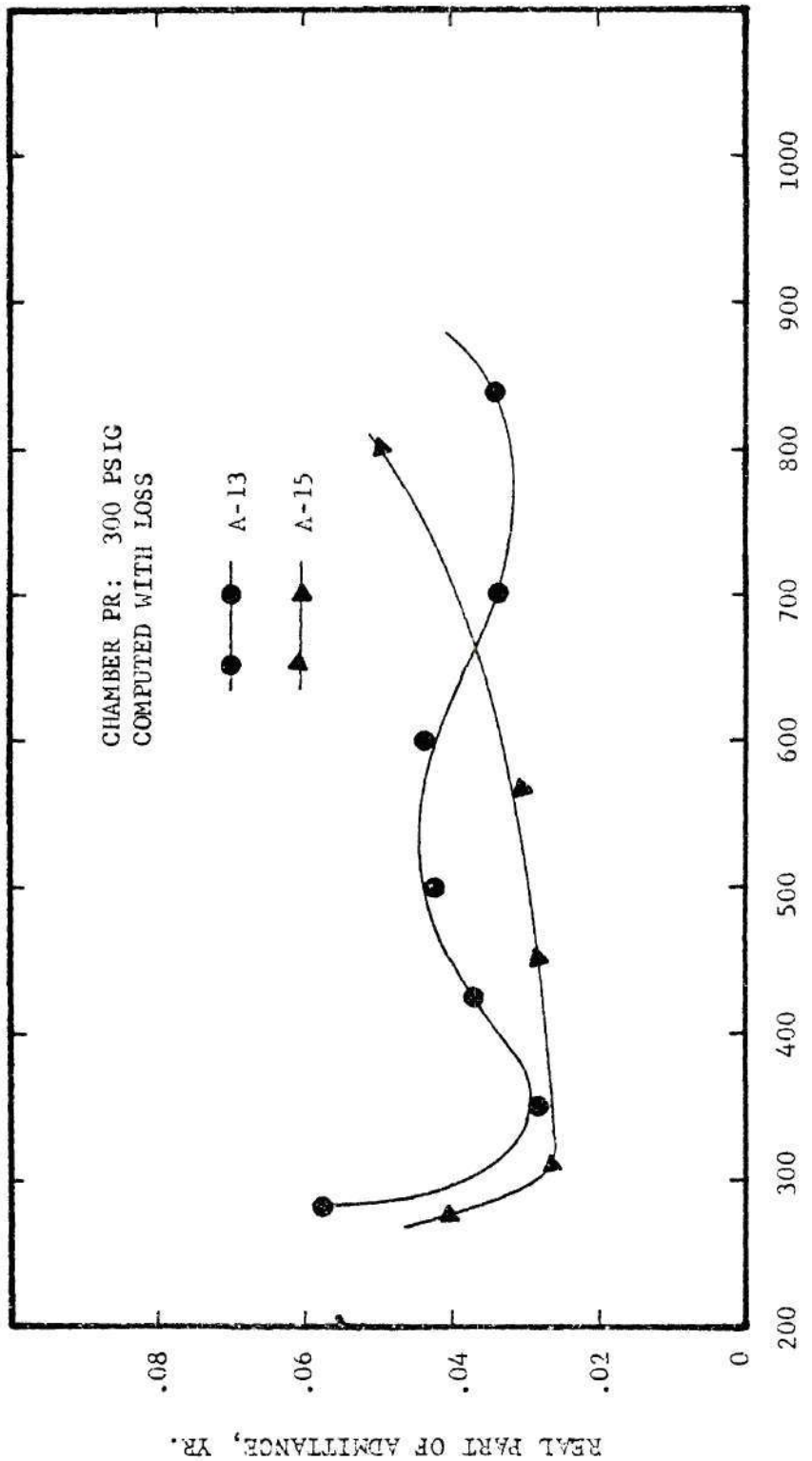

Figure 6-28. Frequency Dependence of Real Part of Admittance for Two Different Propellants.

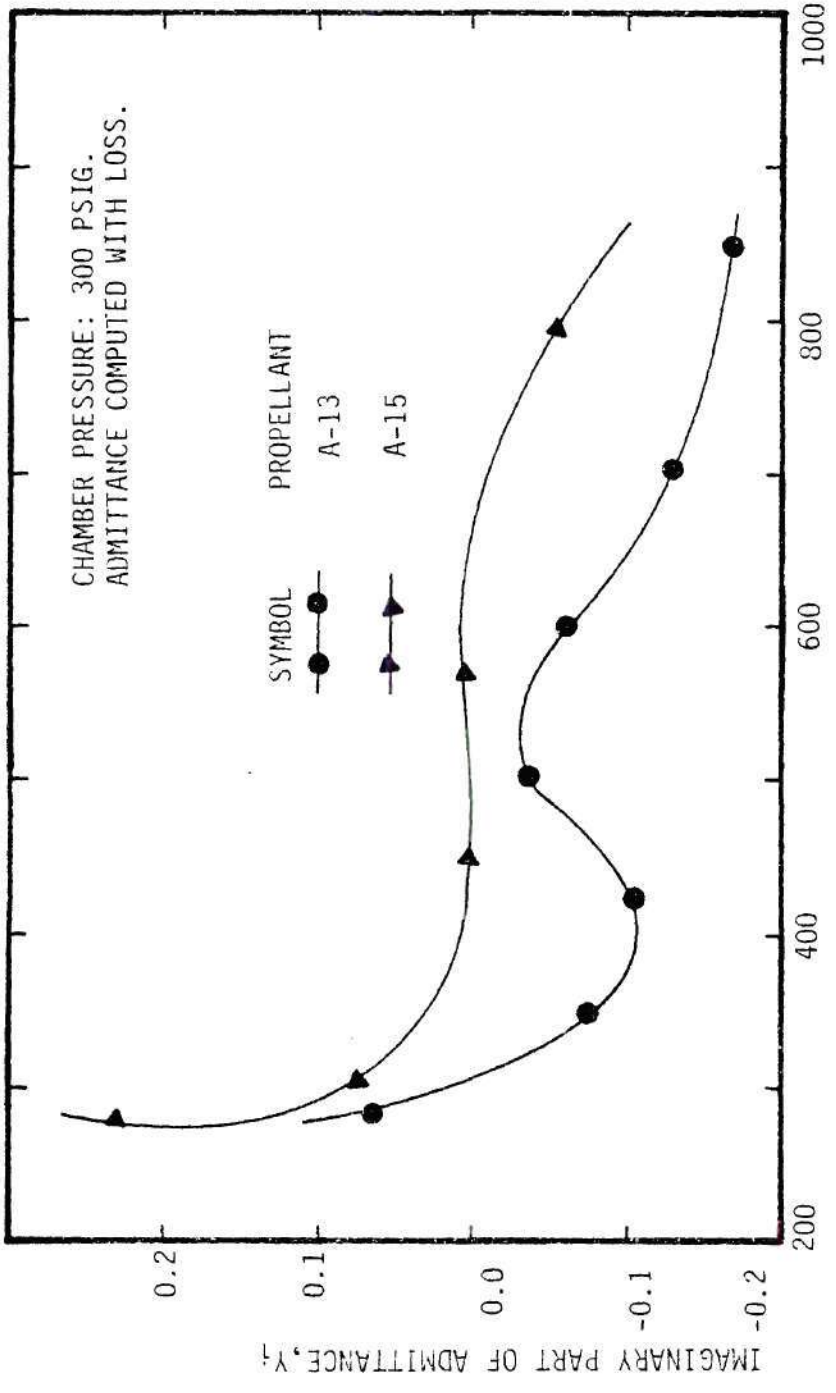

Figure 6-29. Frequency Dependence of Imaginary part of Admittance for two Different Propellants.

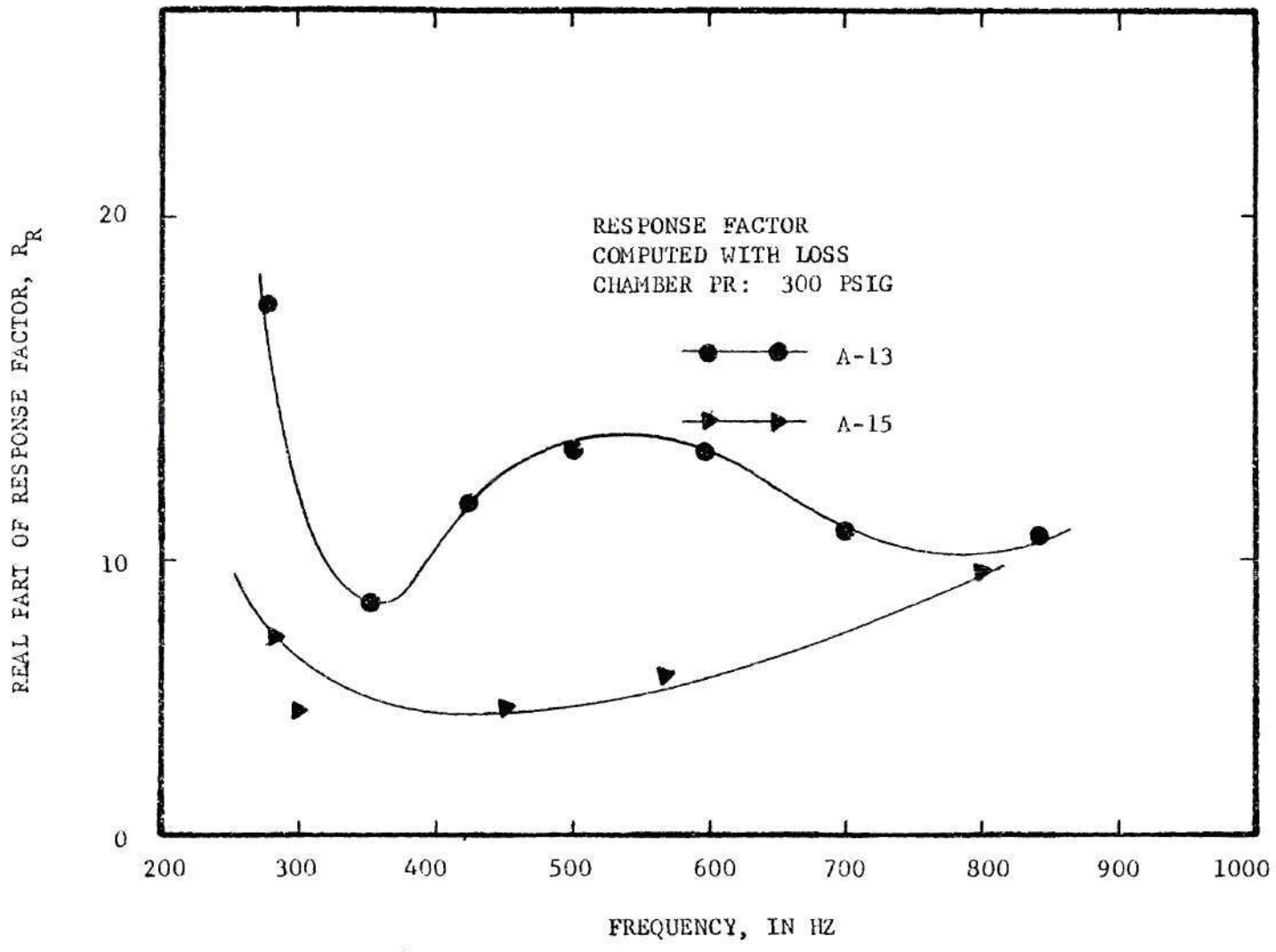

Figure 6-30. Frequency Dependence of Real Part of Response Factor for two Different Propellants.

Table 6-10. High Pressure Data for Propellant A-13 at Various Frequencies Computed, Allowing for Bulk Loss in the Flow

Propellant Type: A-13
Chamber Pressure: 300 Psig.
Burning Rate 0.0139'/Sec.

Expt. No. and Record No.	Frequency	Y_r Real Admittance	Y_i Imaginary Admittance	R_r Real Response	R_i Imaginary Admittance	C Heat Transfer Parameter	G Loss Coeff.	Error in Amp. DB	Error in Pha Deg.
646-36	280	.0581	.0614	17.454	17.728	1.208	0.923	.427	.0304
634-23	300	.0176	-.1942	5.903	-55.878	2.871	0.245	1.69	.738
647-35	350	.0272	-.074	8.636	-21.293	1.558	0.379	0.171	.0069
663-33	425	.0378	-.1063	11.684	-30.581	2.031	0.842	0.518	.0096
635-25	500	.0428	-.034	13.13	-9.8	1.183	1.503	.388	.073
662-27	600	.0435	-.0589	13.342	-16.92	.988	1.502	.430	.0180
636-15	700	.0335	-.1291	10.465	-37.153	1.427	0.716	0.669	0.381
660-40	840	.0344	-.1695	10.736	-48.770	1.153	1.160	0.449	.0394
702-34	300	.0274	.0099	8.654	28.658	1.075	.844	1.52	.0324

Table 6-11 High Pressure Data for Propellant A-15 at Various Frequencies Computed, Allowing for Bulk Loss in the Flow

Following Computations are made considering "bulk loss" in the flow

Propellant Type: A-15
Chamber Pressure: 300 Psig
Burning Rate: 0.025'/Sec.

Expt. No. and Record No.	Frequency	Y_r Real Admittance	Y_i Imaginary Admittance	R_r Real Response	R_i Imaginary Admittance	C Heat Transfer Parameter	G Loss Coeff.	Error in Amp. DB	Error in Pha Deg
649-29	280	.0407	.231	7.794	41.279	.960	1.048	.503	.0665
650-36	300	.0269	.0703	5.523	12.58	1.185	1.127	1.65	.0399
651-64	450	.0286	.00294	5.885	0.538	1.43	1.241	.265	.00788
652-44	567	.033	.0082	6.681	1.48	1.287	1.369	.822	.0263
653-17	796	.05	-.0501	9.733	-8.929	1.07	2.177	.184	.0203

that the magnitudes of real parts of the admittances of various unstable propellants are very small (i.e., of the order of 0.03). For such low values of Y_r the pressure amplitude at the pressure minimum becomes very low compared to the maximum pressure amplitude (i.e., see Figure 4-2). Also, the spatial pressure-phase plot for $Y_r = 0.003$ shown in Figure 4-3 closely resembles a square-type behavior with a change of 180° in the phase value near the pressure minimum. To obtain accurate admittance values, it is necessary to accurately measure both the pressure amplitude and the phase variation near the pressure minimum. In the instrumentation system, the analog to digital converter is more likely to introduce errors in the experimental data, specifically at and near the pressure minima. Due to the presence of higher modes of the excitation frequency and flow noise in the impedance tube, the pressure oscillations observed at different transducer locations were not exactly sinusoidal. At and near low pressure amplitude locations, the higher modes and flow noise were comparable in magnitude to the amplitude of excited standing wave. The presence of such significant flow noise was observed during a few test runs in which the sound pressure levels in the impedance tube were measured without using any external excitation. The digital filtering done by the analog to digital converter needs more samples per data point (i.e., sampling rate) as discussed in Chapter V, to filter out the higher modes and flow noise associated with the output of the transducers, specifically at and near the low amplitude locations. The sampling rate could be increased by increasing the duration of a test run. In principle, the duration of a test run could be increased by using a thicker propellant

sample. However, significant uneven burning was observed when a thicker sample was burnt. Therefore to avoid severe uneven burning, an optimum size sample was used, which could burn only about 2 to 3 seconds. This imposed a limit on the number of samples taken by the A to D converter to give a sufficient number of data points (i.e., records) during that period of burning. This limitation could introduce errors in both the phase and amplitude data measured during a test run, mainly at and near the pressure minima. As discussed in Chapter V, only a limited number of discrete pressure measurements (i.e., about 10) were possible along the impedance tube during a test and these data were used in the data reduction scheme (as described in Chapter III) to describe the standing wave in the impedance tube and to minimize the experimental errors in the measured pressure data. The fewer pressure measurements used in the data reduction scheme were inadequate to accurately describe the standing wave in the impedance tube. Therefore, the errors present in the measured pressure data were not completely eliminated and these errors showed up in the computed admittance values. The experimental difficulties discussed above are believed to be responsible for the observed scatter in the computed admittance values. Similar scatter of admittance values were also observed in the results obtained in T-burner experiments.[9,32]

A comparison of the real parts of admittance values of an A-13 propellant obtained in T-burner experiments[9] and those obtained in the present investigation is presented in Figure 6-31. The T-burner data presented in the form of growth and decay rate coefficients in Reference

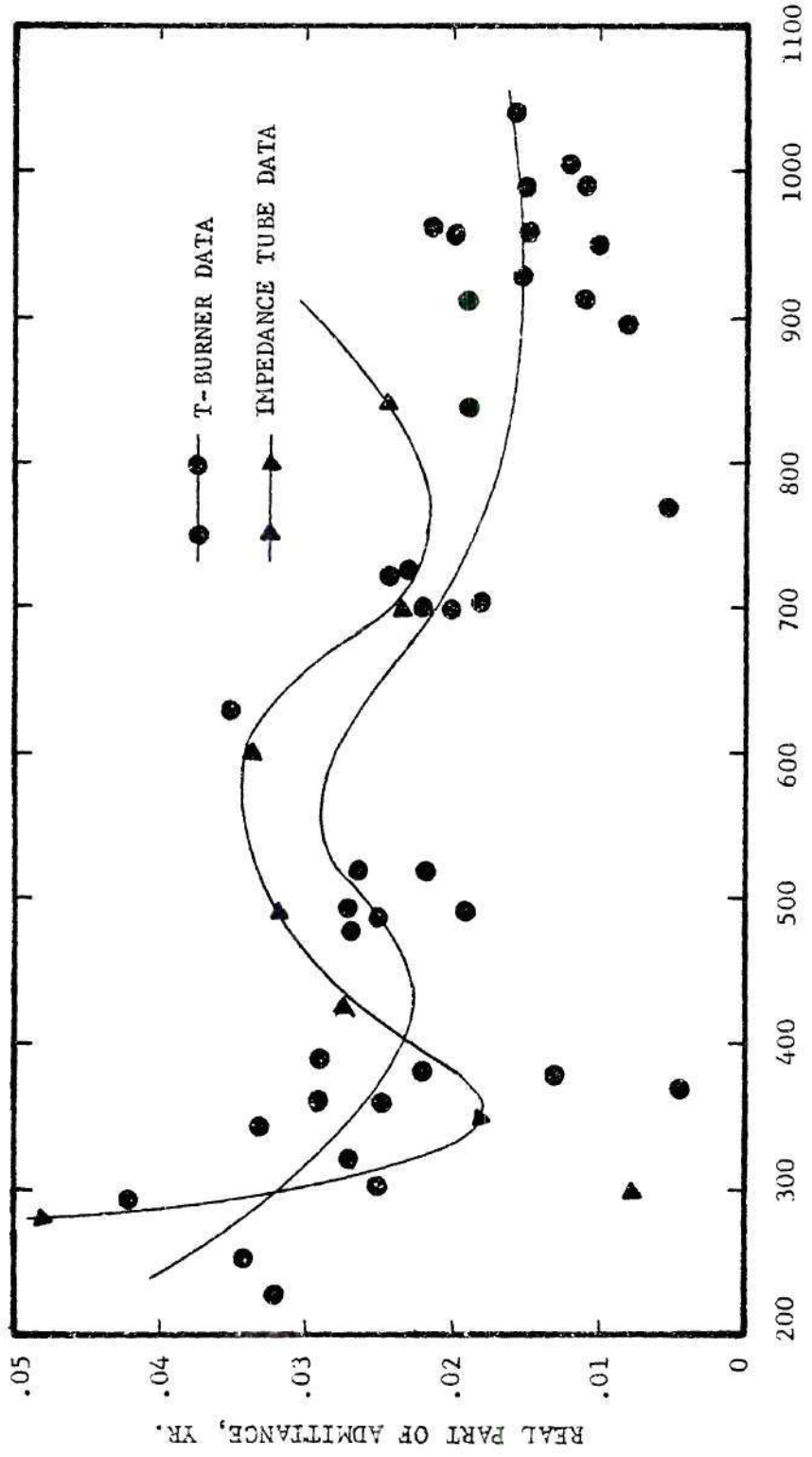

Figure 6-31. Frequency Dependence of Real Part of Admittance of A-13 Propellant Obtained by Two Experimental Techniques.

Table 6-12. Conversion of T-Burner Data into Admittance Values

Propellant: A-13
Chamber Pr: 300 Psig.

D_{inch}	L_{inch}	$\bar{r}_{inch/sec.}$	$\bar{f}$ Hz	$\bar{p}'_{Psi}$	α_g	α_d	Y_r
1.0	32.5	.198	.360	8	5.9	6.6	.035
1.0	25.5	.198	770	12	3.4	8.5	.015
1.0	25.5	.188	480	8	4.5	13.2	.037
1.0	14.0	.192	1040	12	15.1	12.3	.026
1.0	14.0	.208	960	23	9.8	13.8	.025
1.0	14.0	.188	1000	11	10.0	12.4	.022
1.0	14.0	.184	960	14	12.9	16.0	.030
1.0	14.0	.185	960	10	10.2	20.0	.031
1.0	25.5	.190	490	9	10.9	7.4	.037
1.0	25.5	.181	490	6	3.8	10.2	.029
1.0	14.0	.188	990	15	13.3	7.9	.021
1.0	14.0	.178	950	13	10.5	8.4	.020
1.0	14.0	.174	940	21	13.3	10.5	.025
1.5	43.5	.181	240	12	3.7	9.1	.05
1.5	43.5	.192	230	20	3.4	6.3	.042
1.5	43.5	.187	250	15	3.6	7.4	.044
1.5	43.5	.196	300	9	4.5	6.0	.035
1.5	37.5	.191	320	17	3.2	8.5	.037
1.5	37.5	.192	290	18	5.9	9.2	.052
1.5	31.5	.192	380	18	5.1	7.1	.032
1.5	31.5	.187	360	18	5.9	8.1	.039
1.5	25.5	.182	520	18	7.7	8.7	.032
1.5	25.5	.184	520	16	8.5	10.0	.0363
1.5	25.5	.190	490	17	7.1	10.0	.035
1.5	19.5	.188	910	18	11.1	7.6	.021
1.5	19.0	.181	700	16	11.4	8.0	.028
1.5	19.0	.182	700	33	12.8	10.8	.0337
1.5	19.0	.188	840	25	11.8	12.5	.029
1.5	19.0	.188	720	28	12.1	12.5	.034
1.5	19.0	.189	700	26	12.5	10.0	.032
1.5	19.0	.182	700	26	12.1	8.9	.03
1.5	31.5	.172	380	21	5.0	3.8	.023
1.5	31.5	.104	370	6	2.9	2.3	.014
1.5	31.5	.181	340	24	7.9	6.7	.043
2.5	20.0	.200	630	110	16.0	4.1	.045
2.5	31.0	.183	390	27	8.1	7.2	.039
2.5	200	.181	720	121	11.4	12.1	.033
2.5	15.0	.152	910	123	16.6	9.5	.029
2.5	15.0	.181	930	114	16.0	7.2	.025

9 has been converted into admittance values using Equation (2-4). These values are also listed in Table 6-12. A considerable amount of scatter is observed both in the T-burner data and in the impedance tube data. In spite of the observed scatter, the admittance values obtained from both methods are of the same order of magnitude and their variation with respect to the frequency also shows similar trends. This suggests that the impedance tube technique is comparable to T-burners, in measuring the admittances of burning solid propellants.

2. Admittances of Reactive Gaseous Injection

As stated earlier in this chapter, the uneven burning of the propellant, short duration of the test and limited number of pressure measurement points to describe the standing wave in the impedance tube, result in considerable scatter in the measured admittance values. Furthermore, the low sampling rate in the A to D converter per data point adds to this scatter. However, in a parallel study where these shortcomings were overcome with a steady burning, longer test duration, large number of pressure measurements to describe the standing wave and higher sampling rate, the admittance values obtained show very little scatter and they agree very well with the theory. In this study the admittances of reactive gaseous rocket injectors were measured using the modified impedance tube technique. The experimental procedures and the experimental data obtained in this study are briefly presented in this section to demonstrate the capability of the impedance tube technique in the measurement of admittance values at elevated temperatures.

The experimental set-up developed in the gaseous rocket injector investigation is shown schematically in Figure 6-32. It consisted of a

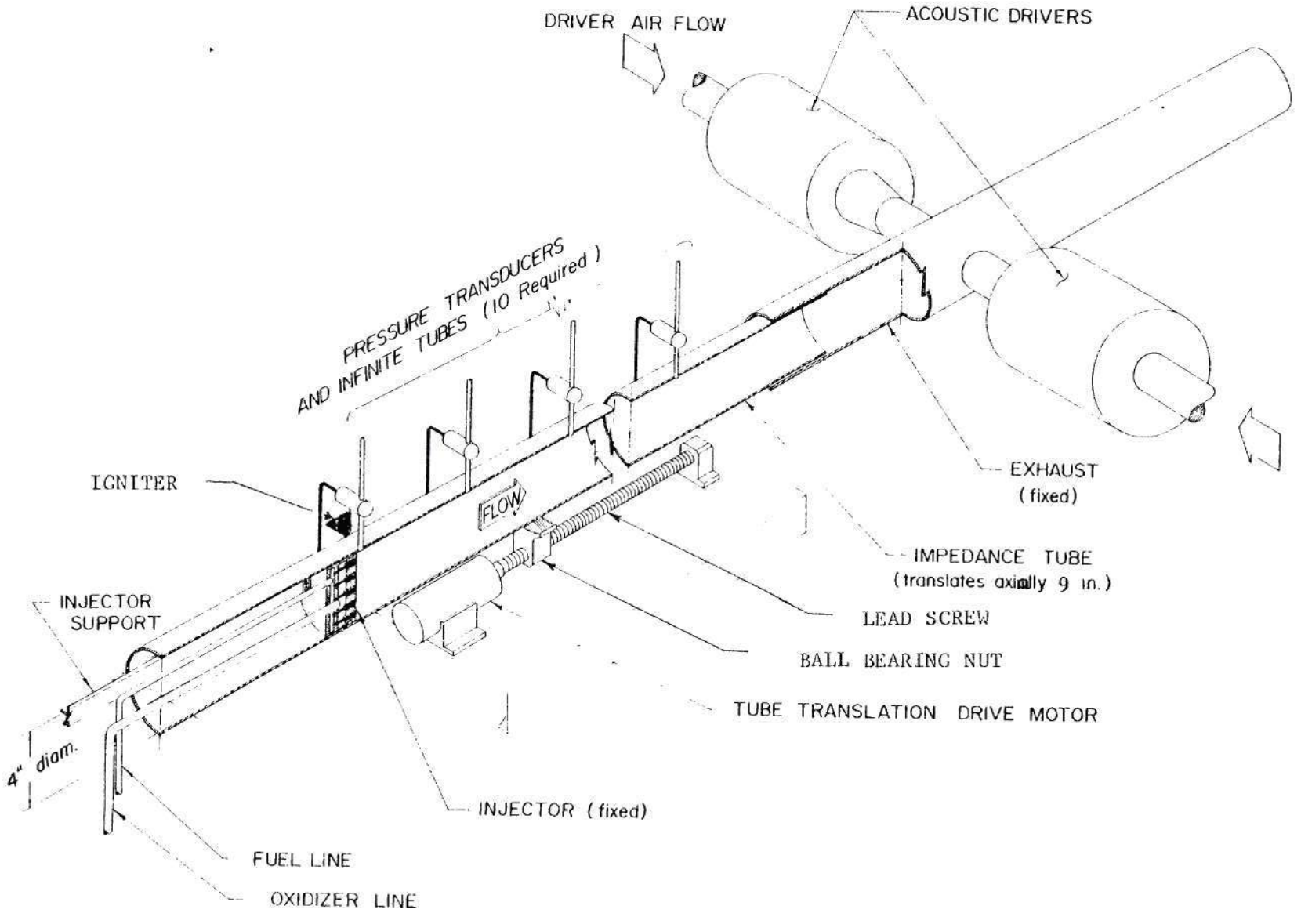

Figure 6-32. Sectioned View of the Test Apparatus.

4 inch diameter modified impedance-tube with a sound source capable of generating simple harmonic waves of a desired frequency and intensity placed at one end of the tube and the injector system under investigation placed at the other end. Storage cylinders and pressure regulators were employed to provide a continuous and steady flow of the required fuel and air. Combustion was initiated by means of a propane-air torch situated a short distance downstream of the injector face. Dynamic pressure transducers and thermocouples installed at desired locations along the walls of the impedance tube provided data that described the structure of the standing acoustic wave pattern and the steady state temperature distributions in the tube.

During an experiment, acoustic drivers were used to establish a standing wave of a desired frequency with a maximum sound pressure level of 160 to 165 db in the tube. Desired flow rates of fuel and air were established and combustion was then initiated by means of the torch. Upon stabilization of the flow conditions in the burner tube, the structure of the standing acoustic wave and the steady state temperature distribution in the tube were determined by axially moving the impedance-tube relative to the injector and acoustic drivers which remain fixed in their positions. The axial movement of the tube was remotely controlled and was achieved by using a tube translation system consisting of a stepping motor which drives a lead screw having a ball bearing nut. The nut, in turn, was rigidly attached to the impedance-tube. By suitably spacing the pressure transducers along the impedance-tube, a short movement (i.e., in this investigation the required

movement was was 8 inches) of the tube provides a complete description of the standing wave in the tube. The measured pressure data were then input into the computational scheme described in Chapter III to determine the injector admittance. These tests were repeated at different frequencies to determine the frequency dependence of the admittance of the test injector. Two series of tests have been conducted during this investigation. In the first series of tests acetylene was employed as the fuel while during the second series of tests methane was employed as the fuel.

Typical plots of the measured axial distribution of the pressure amplitudes and phases for an equivalence ratio of 1.31 and at driver frequencies of 954,805 and 750 Hz are presented in Figures 6-33 through 6-38. The data presented in these figures compare the axial distribution of the pressure amplitudes and phases measured under nonreactive conditions with corresponding data obtained under reactive conditions.

In the injector study, the admittance sign conventions are the reverse of those used earlier in this thesis. When the real part of the complex admittance is a positive number, which implies wave damping at the injector face, the phase distribution along the impedance tube has a positive slope indicating the propagation of acoustic energy towards the injector end. On the other hand, when the real part of the complex admittance is negative in sign, which implies wave amplification at the injector end, the phase-distance curve in the burner tube has a negative slope indicating transmission of acoustic energy away from the injector.

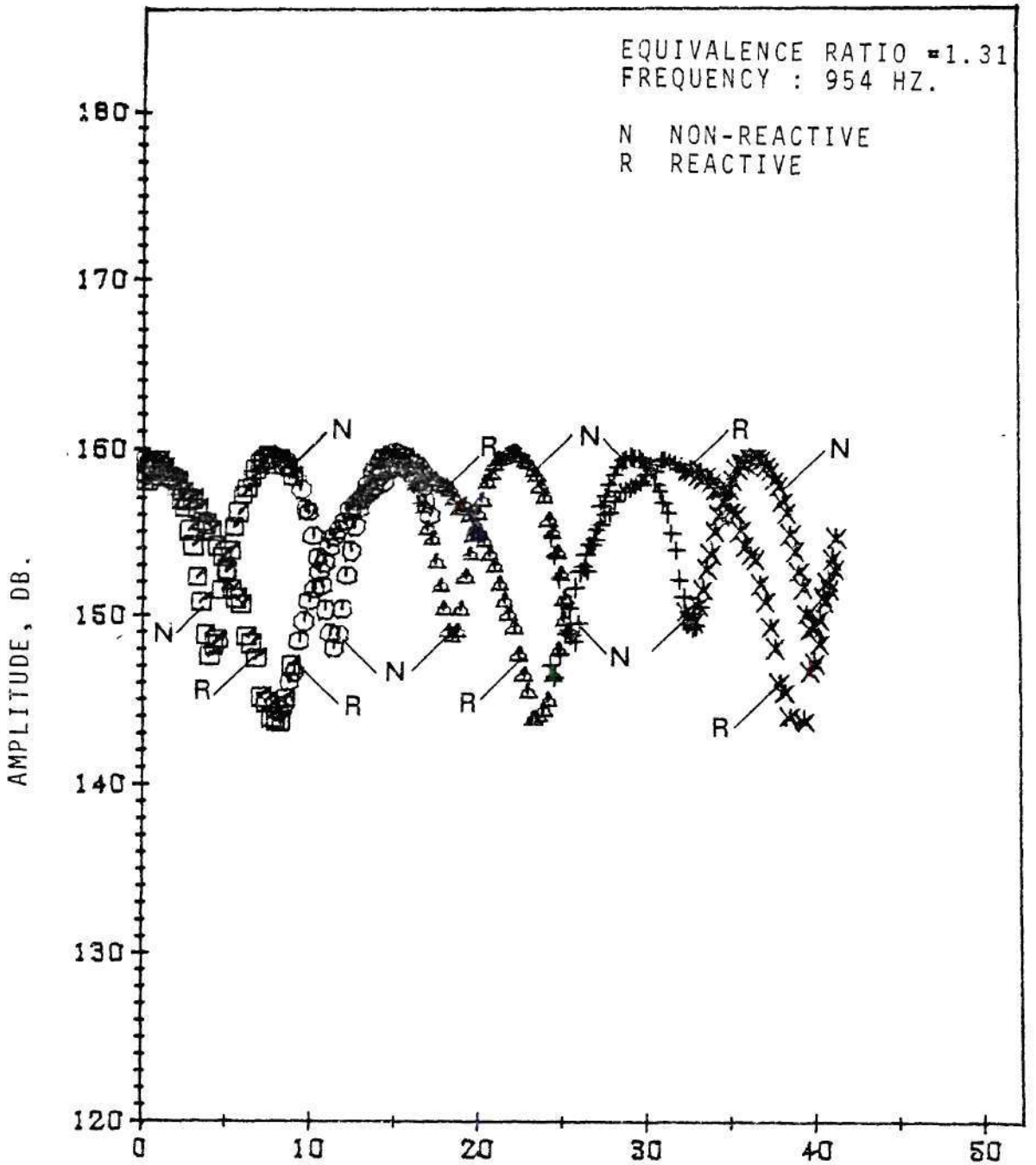

Figure 6-33 Pressure Amplitude Along Impedance Tube.

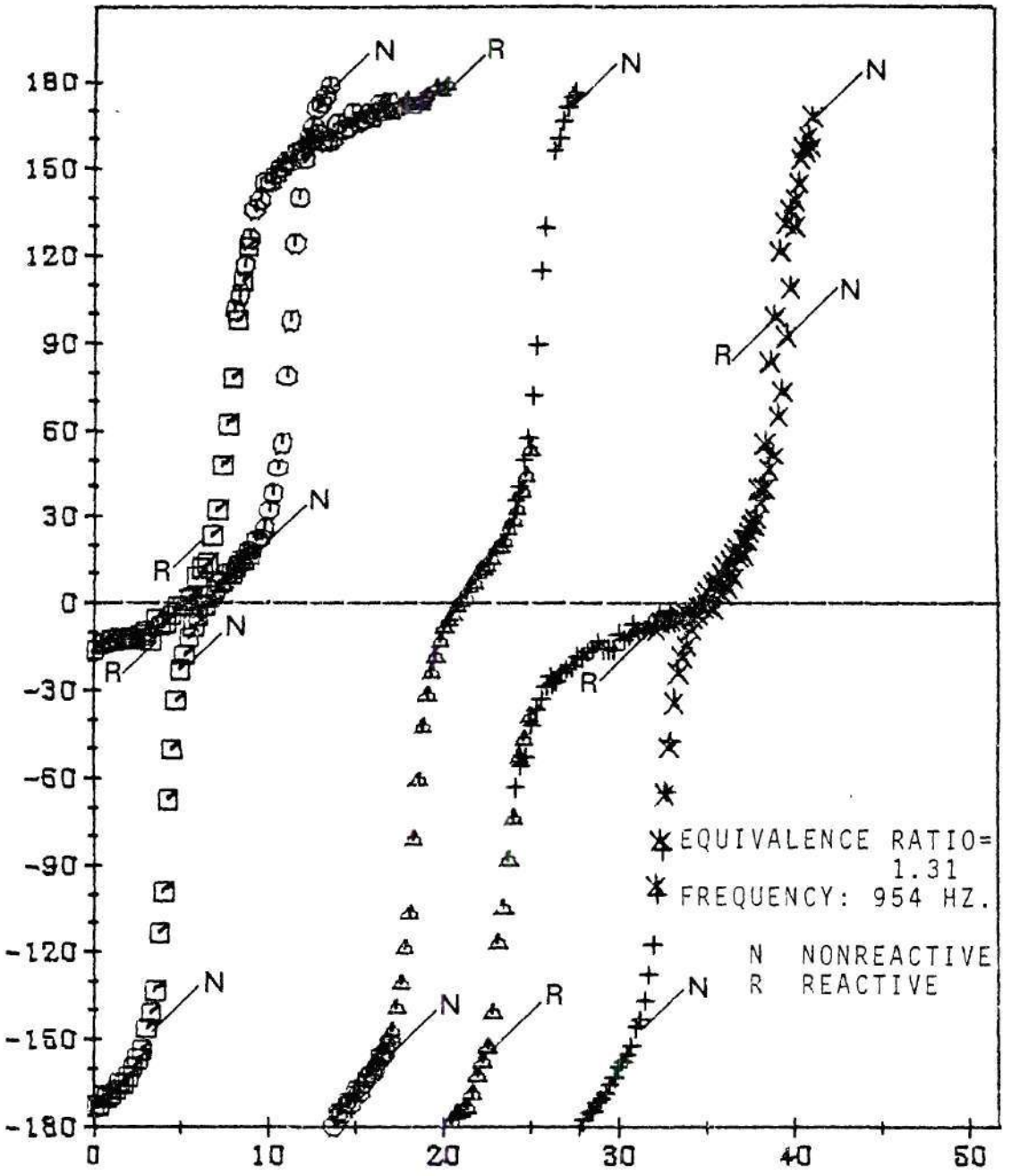

Figure 6-34. Pressure Phase Along Impedance Tube.

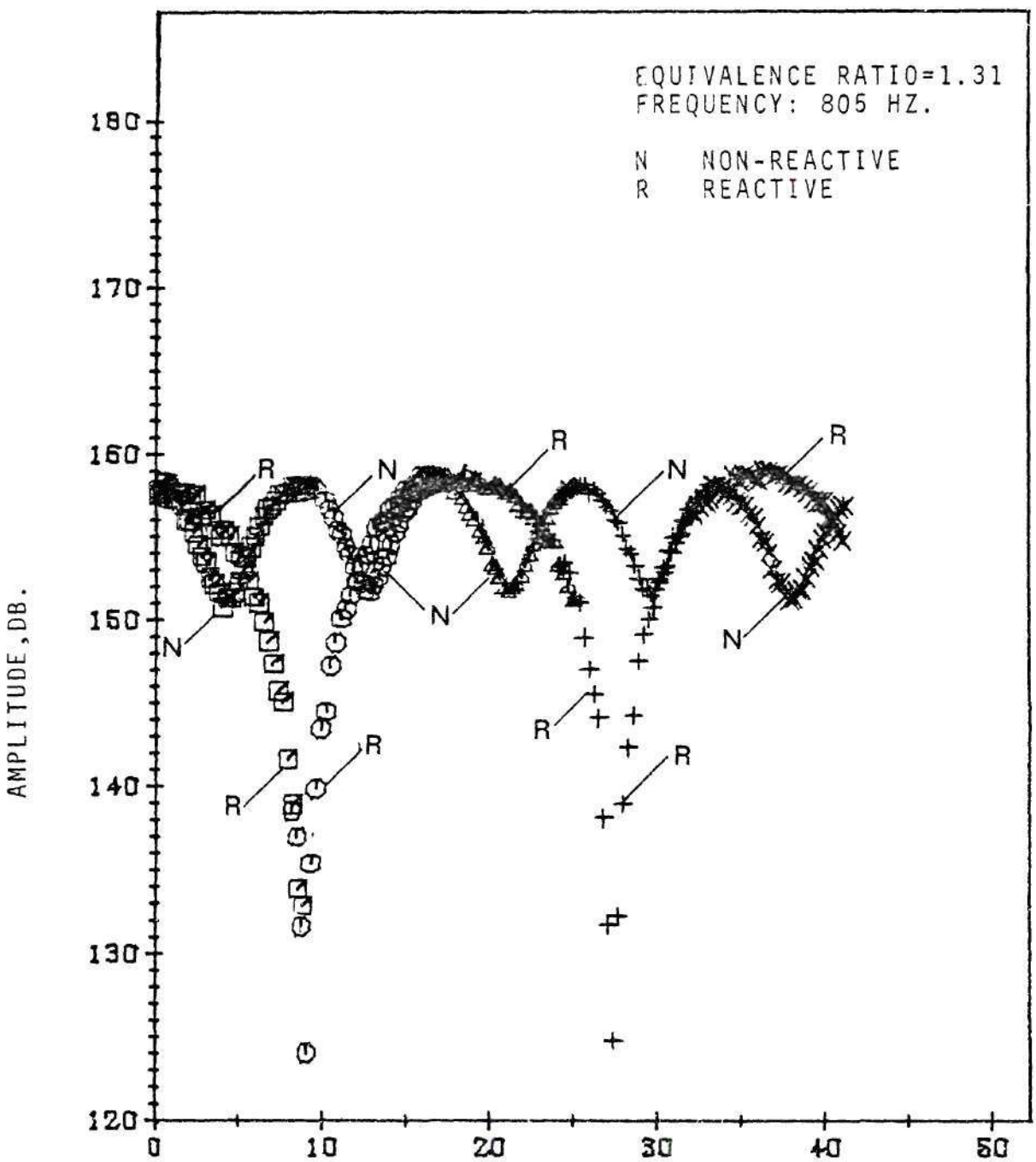

Figure 6-35. Amplitude Along Impedance Tube.

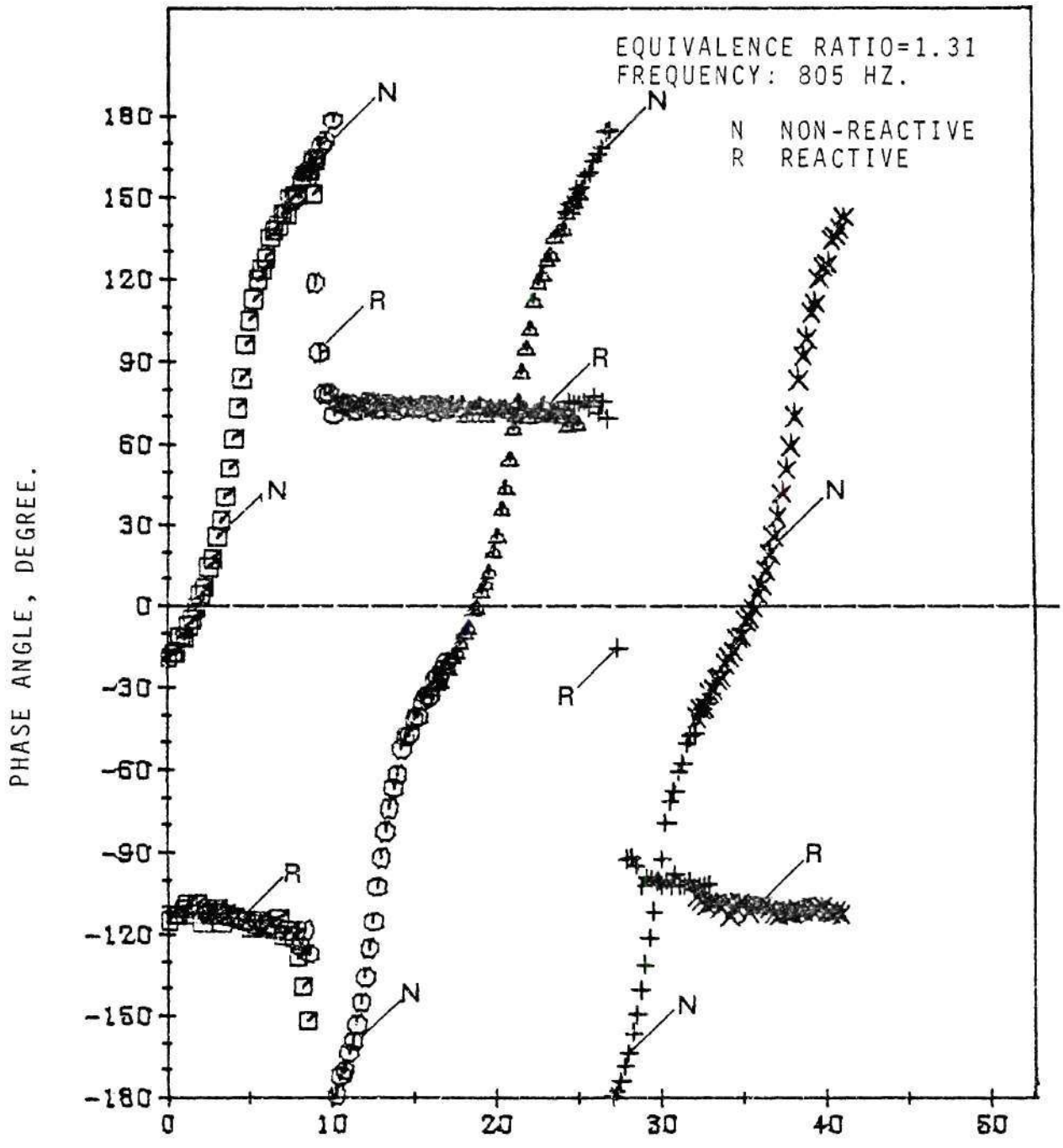

Figure 6-36. Pressure Phase Along Impedance Tube.

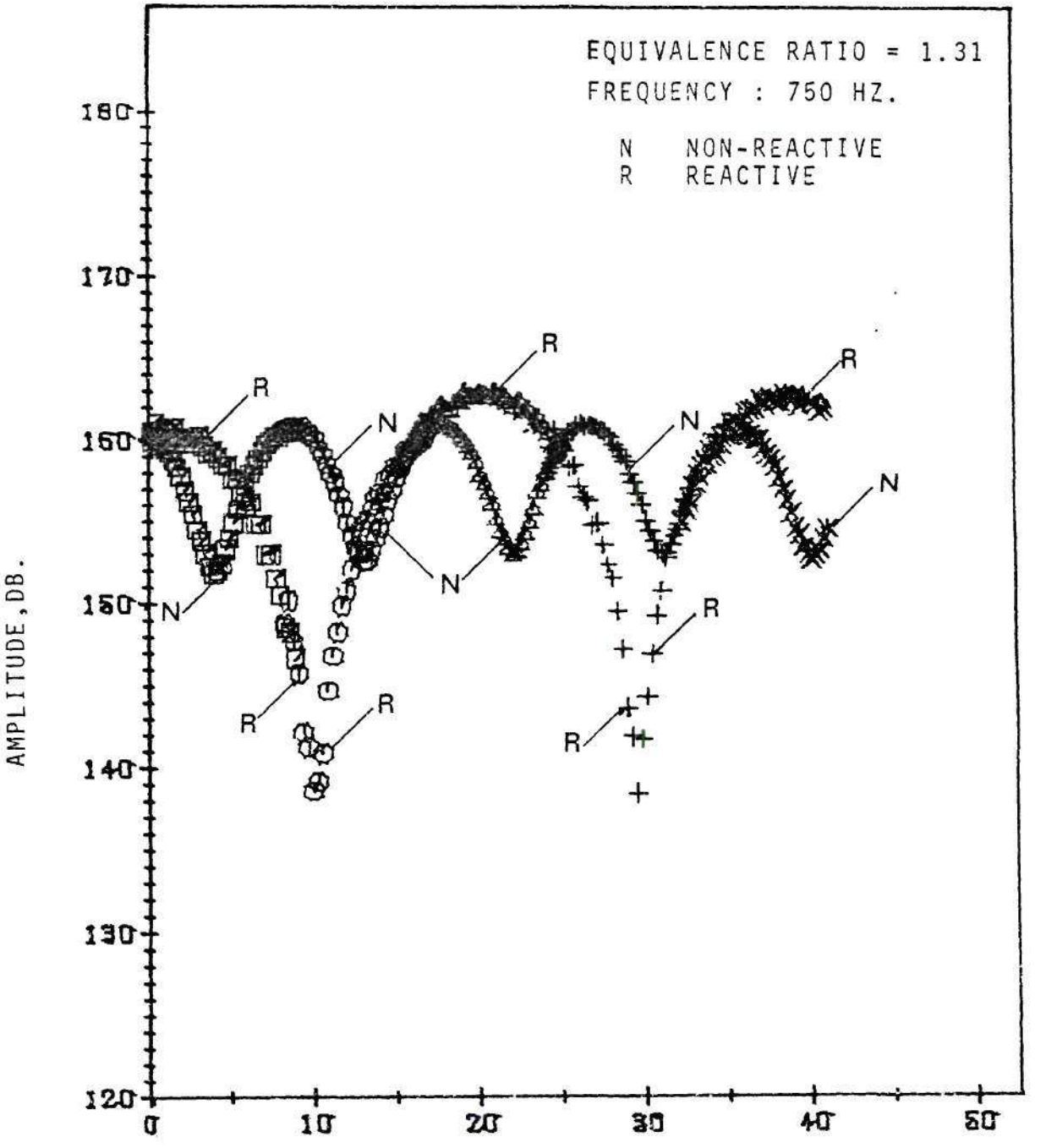

Figure 6-37. Pressure Amplitude Along Impedance Tube.

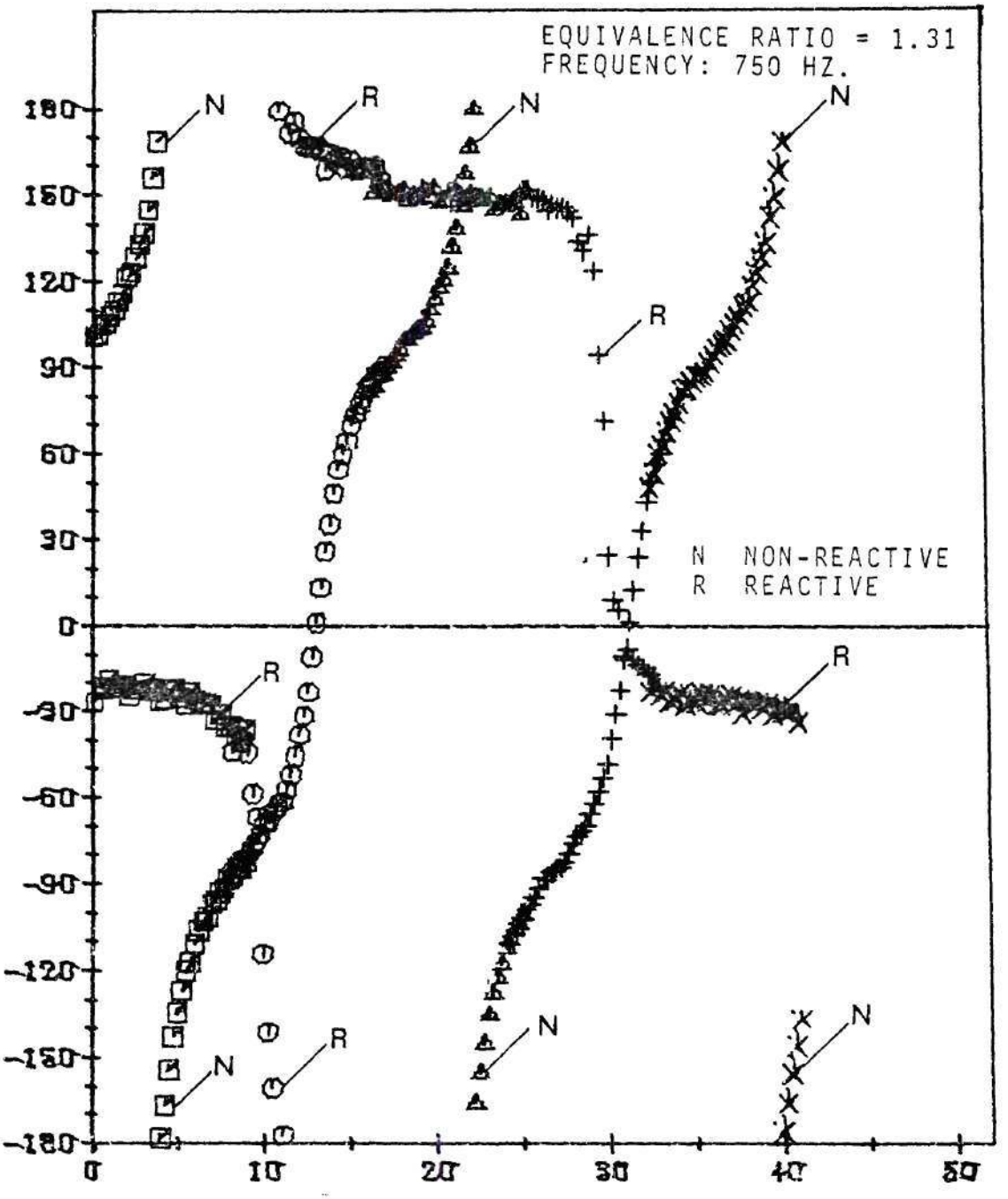

Figure 6-38. Pressure Phase Along Impedance Tube.

An examination of Figure 6-34 indicates that the phase-distance curves have a positive slope under both reactive and non-reactive conditions. This, in turn, indicates that the acoustic energy was moving from right to left along the burner tube and hence the injector was acting as a damping device under both reactive and non-reactive conditions. However, an examination of the amplitude curve in Figure 6-33 indicates that a decrease in the damping provided by the injector occurred when the operating condition of the system changed from a non-reactive to a reactive state. A similar examination of Figure 6-36 indicates that while the phase-distance curve under non-reactive conditions has a positive slope, the phase-distance curve under reactive condition has small negative slope. This indicates a change in the direction of the acoustic energy propagation in the impedance tube as the system changed from a non-reactive to a reactive condition. In other words, this indicates a change from a damping to a mild driving response factor at the injector face.

Figure 6-38, which is similar to Figure 6-36, also indicates that the nature of the phase distance curve changes from a positive to a negative slope as the operating condition of the system is changed from a non-reactive to a reactive state. However, the phase-distance curve of Figure 6-38 has a considerably larger negative slope when compared to the almost square looking phase-distance curve of Figure 6-36. This indicates a stronger driving capability at the injector face under the operating conditions of Figure 6-38 when compared to those of Figure 6-36. This trend is also evident from a comparison of the reactive pressure amplitude data of Figure 6-37 with the corresponding reactive data of Figure 6-35.

Figures 6-39 and 6-40, respectively, describe the frequency dependence of the injector surface admittance for equivalence ratios of 1.02 and 1.31. An examination of these two figures indicates a certain amount of scatter in the measured data. Comparing the measured admittances with theoretically predicted admittances shows that the two sets of data agree qualitatively where the value of combustion time τ_b are taken to be 0.00085 and 0.0012, respectively, corresponding to equivalence ratios of 1.02 and 1.31. The results of this study indicate that under suitable conditions strong coupling between the combustion and the injector can result in driving of acoustic oscillations in the combustion chamber. Also, a reasonable agreement between the measured injector admittances and those predicted by the Feiler and Heidmann[33] model is indicated.

Therefore, the injector study discussed above clearly proves the capability of the modified impedance tube technique to measure driving and damping admittances. The injector study has so far proven better in exploiting the potentials of impedance tube technique as compared to solid propellant study, because of its experimental advantages. Due to the translatory motion of this impedance tube, a continuous pressure measurement could be made to obtain a more accurate pressure wave, and a larger number of data points to be used in the computational schemes. In contrast, in the solid-propellant case only a few discrete pressure data could be used in the data reduction procedure. The injector experiment can be run for a considerably longer time, during which a desired driving frequency is set and the whole system gets enough time to get stabilized, whereas in the solid

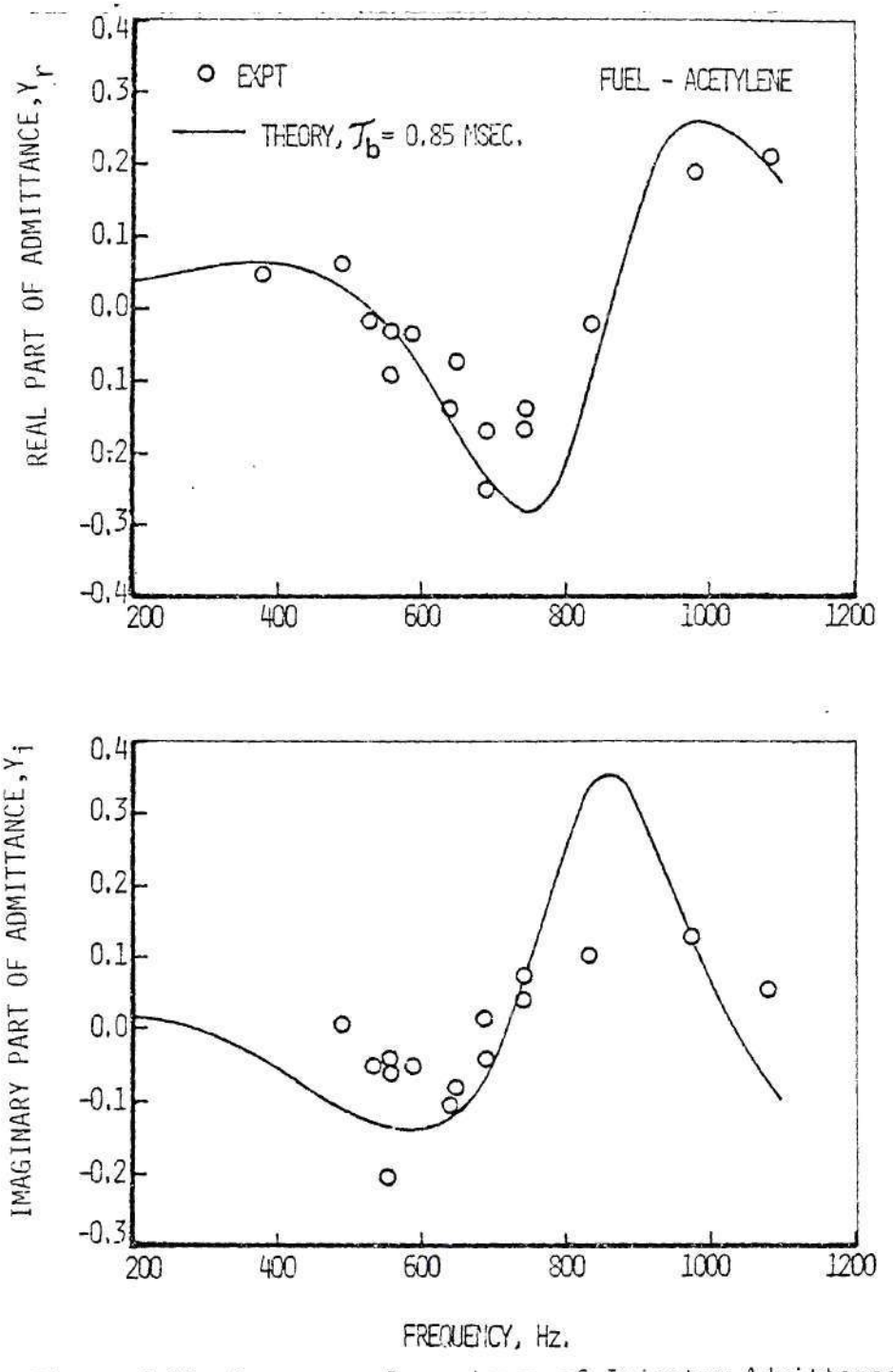

Figure 6-39. Frequency Dependence of Injector Admittance; q=1.02

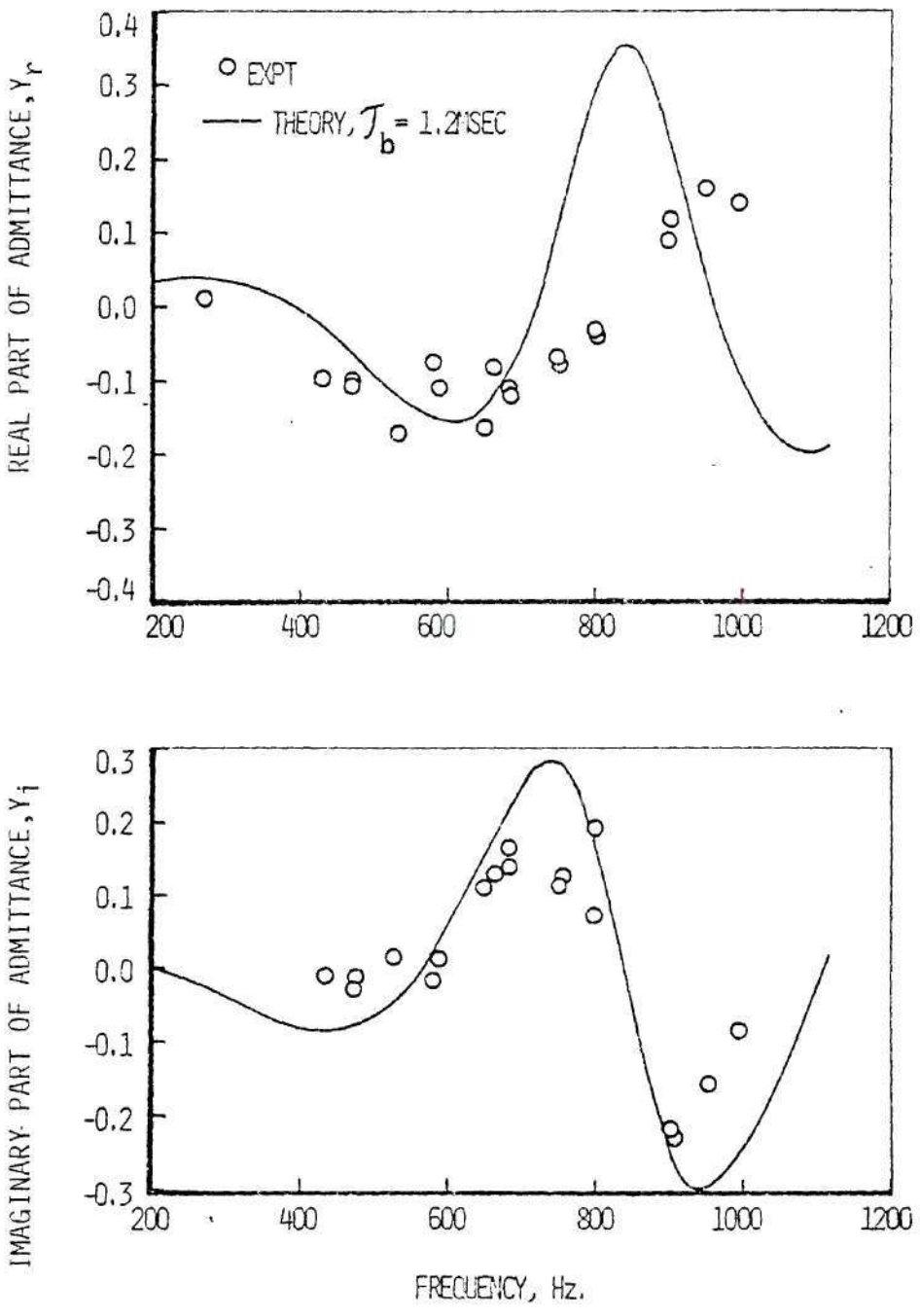

Figure 6-40. Frequency Dependence of Injector Admittance; q=1.31

propellant investigation the duration of the complete test is only about 2 to 3 seconds. Therefore, it is not possible to set a frequency at cold condition which would create a good sinusoidal pressure oscillation during the burning of the propellants. Also, in the solid propellant study due to the short duration of each test run a steady state condition was not achieved and therefore, all the measurements were made under quasi-steady conditions. With all these limitations and shortcomings the admittance data measured so far in the solid propellant study, are qualitatively comparable with T-burner results (see Figure 6-31).

The application of the modified impedance tube technique in the measurement of admittance values at elevated temperature environments has evolved significantly since the beginning of this work. The insight and experience gained by this study has sufficient promise, to call for pursuing further investigations with precision measurements. This technique has additional advantages as compared to conventional T-burners. In principle this technique is capable of measuring the admittances of stable or weakly unstable propellants, and can control the frequency and maintain a zero growth rate of the oscillations, so that the driving capabilities of different propellants are determined under identical conditions. Also, the same experimental arrangement is used for determining the admittances of burning solid propellants at different frequencies.

APPENDIX A

MEAN TEMPERATURE DISTRIBUTION IN IMPEDANCE TUBE

In determining the admittances of burning solid propellants using the impedance tube technique, the axial distribution of mean temperature in the impedance tube is needed. In principle, the axial distribution of steady state temperature in the impedance tube can be obtained using standard temperature measuring devices. However, as will be shown in this appendix, such axial temperature measurements can lead to errors in the values of admittances, particularly when radial temperature gradients are present in the tube. Under such conditions one needs to know a bulk or average axial temperature distribution in the tube before one can evaluate the required acoustic characteristics from the measured standing wave data. The objective of this appendix is to develop a method for obtaining the required axial distribution of the bulk temperature from the measured standing wave data.

In the first section of this appendix, expressions for axial mean temperature distributions in the impedance tube are derived for the cases of fixed and variable wall temperatures. In the next section, experimental determination of the axial steady temperature distribution is discussed. Initially, the one dimensional bulk temperature distribution is obtained using measured temperature data in the impedance tube.

To check this result, an estimate of the bulk axial temperature distribution is made using measured locations of the pressure wave nodal points. Owing to the large discrepancy between these two results, direct measurements of temperature data are discarded. It is also shown that the scheme based on measuring the nodal coordinates of the pressure wave structure, though accurate, has several practical limitations. The problem is resolved by employing a non-linear regression technique to determine the steady axial temperature distribution using the measured acoustic data.

Analytical Consideration

1. Axial Distribution of Mean Temperature

During an impedance tube experiment, the burning solid propellant sample produces a stream of hot gases that flows in the tube towards the exhaust nozzle. Heat transfer from the hot combustion products to the cooler impedance tube walls result in a temperature gradient along the axis of the impedance tube. In this section, the determination of the mean temperature distribution along the axis of the impedance tube is considered.

From heat transfer considerations it can be shown that the heat transfer $d\dot{q}$ to an element of the impedance tube wall of width dx is given by the following expression:

$$d\dot{q} = h(\overline{T} - T_w)\,\pi\, D\, dx \qquad \text{(A-1)}$$

where the various quantities are defined in the nomenclature. On the other hand, from conservation of energy for a fluid element in the

differential tube section of width dx gives:

$$d\dot{q} = -\bar{\rho}\,\bar{u}\,C_p\,\frac{\pi}{4}\,D^2\,d\bar{T} \tag{A-2}$$

Combining Equations (A-1) and (A-2), the following expression for the steady temperature gradient is obtained:

$$\frac{d\bar{T}}{dx} = -\frac{4h}{\bar{\rho}\,\bar{u}\,DC_p}\,(\bar{T} - T_w) \tag{A-3}$$

Since the flow in the impedance tube is turbulent, the semi-emperical expression for the heat transfer coefficient h that was developed by Bertz[22] for a turbulent boundary layer is employed in this investigation. This is given by:

$$h = \frac{C_o}{D^{0.2}}\left(\frac{\mu^{0.2}\,C_p}{P_r^{0.6}}\right)_o (\bar{\rho}\,\bar{u})^{0.8}\,\sigma \tag{A-4}$$

where

$$\sigma = -\frac{1}{\frac{1}{2}\left[\frac{T_w}{T}\left(1 + \frac{\gamma-1}{2}M^2\right) + \frac{1}{2}\right]^{(0.8-\omega/5)}\left[1+\frac{\gamma-1}{2}M^2\right]^{\omega/5}} \tag{A-5}$$

The subscript "o" denotes a quantity evaluated at a stagnation condition while C_o and ω respectively, represent a constant coefficient and the temperature exponent of the viscosity law. Since at high temperatures the value of ω varies between 0.5 and 0.75,[34] an average value of 0.6 is chosen for ω in this study. When mach number M is

small, which is the case in most impedance tube investigations, $\frac{\gamma-1}{2} M^2 << 1$ and the expression for σ simplifies to:

$$\sigma \approx \frac{1}{[\frac{1}{2}(T_w/T + 1)]^{.68}} \tag{A-6}$$

Using the steady state result that $\bar{\rho}\,\bar{u}$ = constant and assuming that C_p and P_r are also constants, it can be shown that Equation (A-4) reduces to $h = C_1\sigma$, where C_1 is a constant. Using this relationship, Equation (A-3) can be rewritten in the following form:

$$\frac{d\bar{T}}{dx} = -\frac{(\bar{T} - T_w)}{\Lambda} \tag{A-7}$$

with the boundary condition $\bar{T}$ (at X = o) = T_c

where

$$\Lambda = C[1 + T_w/\bar{T}]^{0.68} \tag{A-8}$$

The quantity C in Equation (A-8) is a heat transfer parameter whose value depends upon the steady flow properties (i.e., μ, C_p, P_r, etc.) associated with the convective heat transfer coefficient h.

If T_w and Λ are assumed to be constants along the axis of the impedance tube, then Equation (A-7) can be integrated to obtain the axial temperature distribution as:

$$\bar{T} = T_w + (T_c - T_w)e^{-x/\Lambda} \tag{A-9}$$

Hence, knowing the flame temperature T_c and the constant wall temperature T_w, the impedance tube axial temperature distribution $\bar{T}$ can be determined from Equation (A-9). An average value of Λ in the following form may be used in Equation (A-9) to obtain a reasonable axial temperature distribution in the impedance tube.

$$\bar{\Lambda} = \frac{1}{x_o} \int_o^{x_o} C[1 + T_w/\bar{T}]^{0.68} dx \qquad \text{(A-10)}$$

where x_o is the length of the impedance tube.

2. Variable Wall Temperature

Contrary to the assumption that the impedance tube wall temperature T_w is a constant, wall temperature measurements taken during this investigation indicates that T_w varies along the length of the impedance tube. The wall temperature measurements were made using special thermocouple holders. These holders could place the thermocouples into the impedance tube in such a way that the thermocouple tips remain flush to the inner surface of the impedance tube wall with small cavities around them. During an experiment the thermocouples could sense the temperature of the gas in the small cavities surrounding the thermocouple tips at the impedance tube wall and thereby the wall temperatures were measured.

Using the measured wall temperature data that is shown in Figure A-1, an expression of the following form is obtained for wall temperature distribution.

$$T_w = A + Be^{Gx} \qquad \text{(A-11)}$$

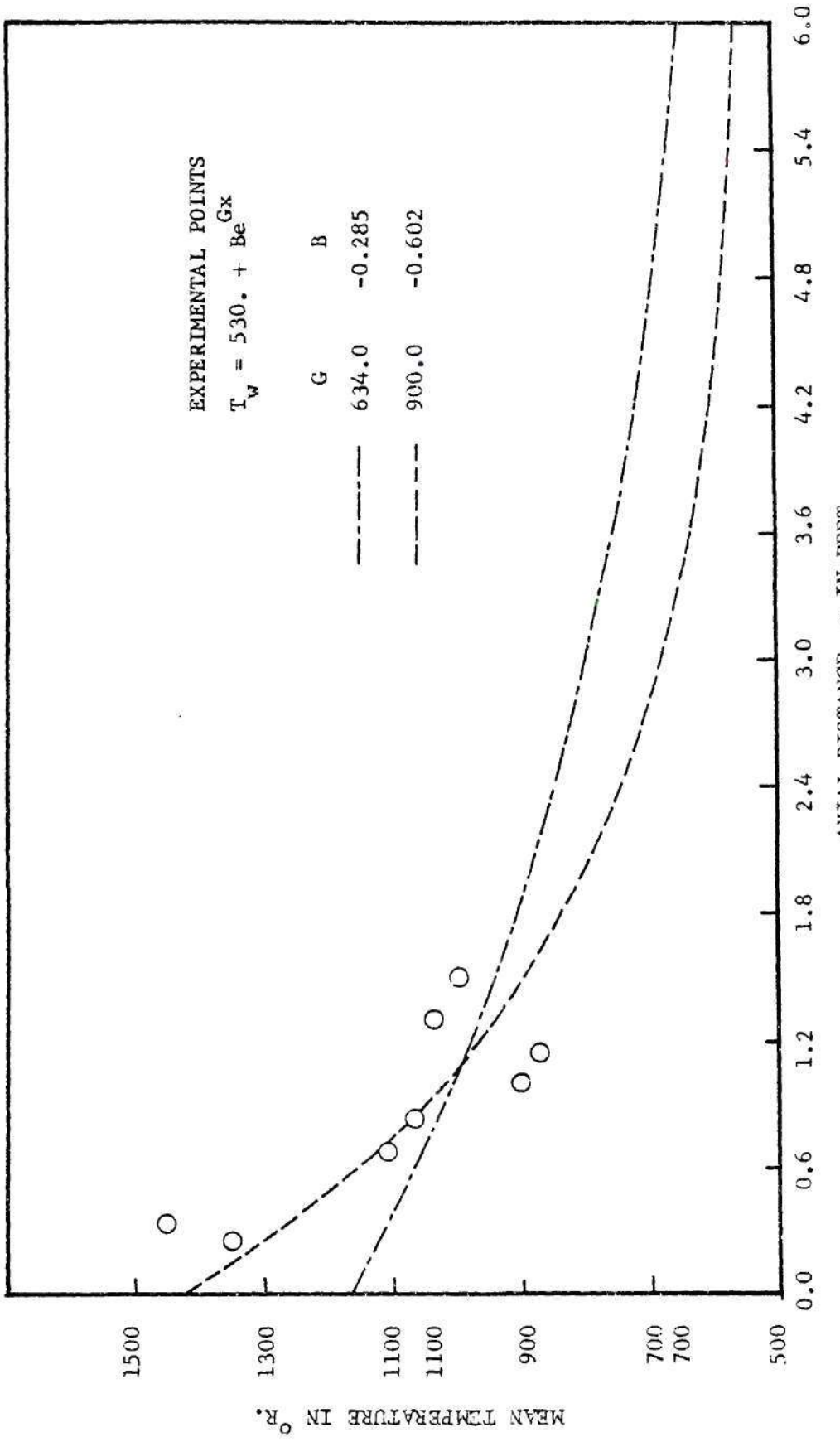

Figure A-1. Wall Temperature Distribution Along the Impedance Tube Axis.

In this expression, the following two sets of values for A, B and G are found to yield reasonable fit between the expression (A-11) and the measured data

	Set I	Set II
A	530	530
B	900	634
G	-0.602	-0.285

Axial temperature distribution in the impedance tube with a variable wall temperature can be obtained by integrating Equation (A-7) numerically, with the boundary conditions, $\overline{T}$ (at $x = o$) = T_c and T_w (at $x = o$) = T_{w_o}. An approximate expression for the axial temperature distribution in the impedance tube with variable wall temperature is given by

$$\overline{T} = T_w + (T_c - T_{w_o})e^{-\frac{x}{\Lambda}} \qquad \text{(A-12)}$$

which is a modified form of Equation (A-9).

3. Comparison of Axial Temperature Distributions

Axial temperature distributions in the impedance tube, computed using Equations (A-7) through (A-12) are presented in Figures A-2 through A-5. In Figure A-2 three temperature profiles are presented, which are obtained using a constant value for the wall temperature (T_w = 810 °R). One of these profiles is obtained by integrating Equation (A-7) while the other two are evaluated using Equation (A-9) with an average value for Λ (i.e., using Equation (A-10)) in one of them and using Equation (A-8) in the other. Figures A-3 and A-4 show

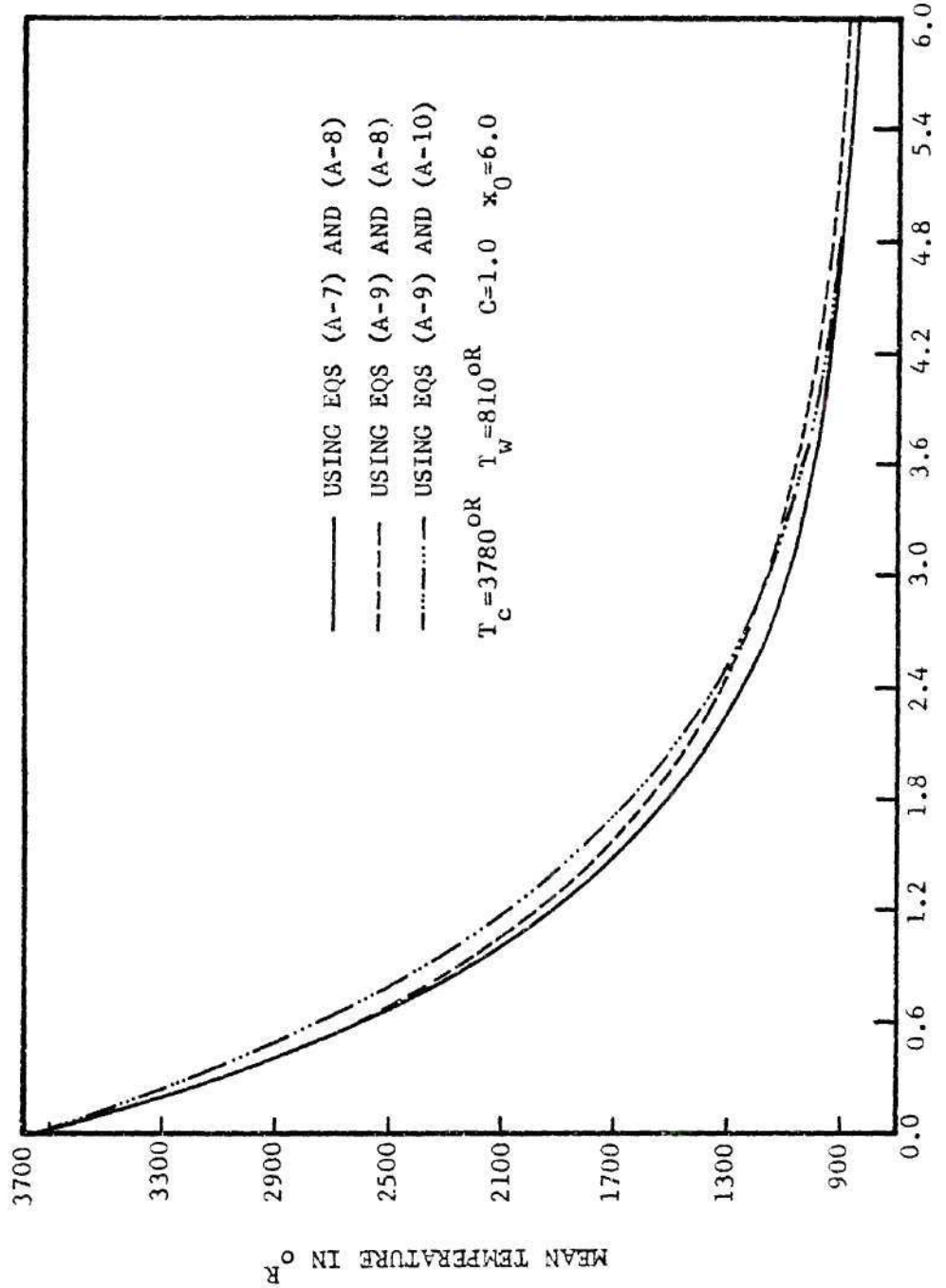

Figure A-2. Mean Temperature Distribution Along the Impedance Tube Axis for a Constant T_w.

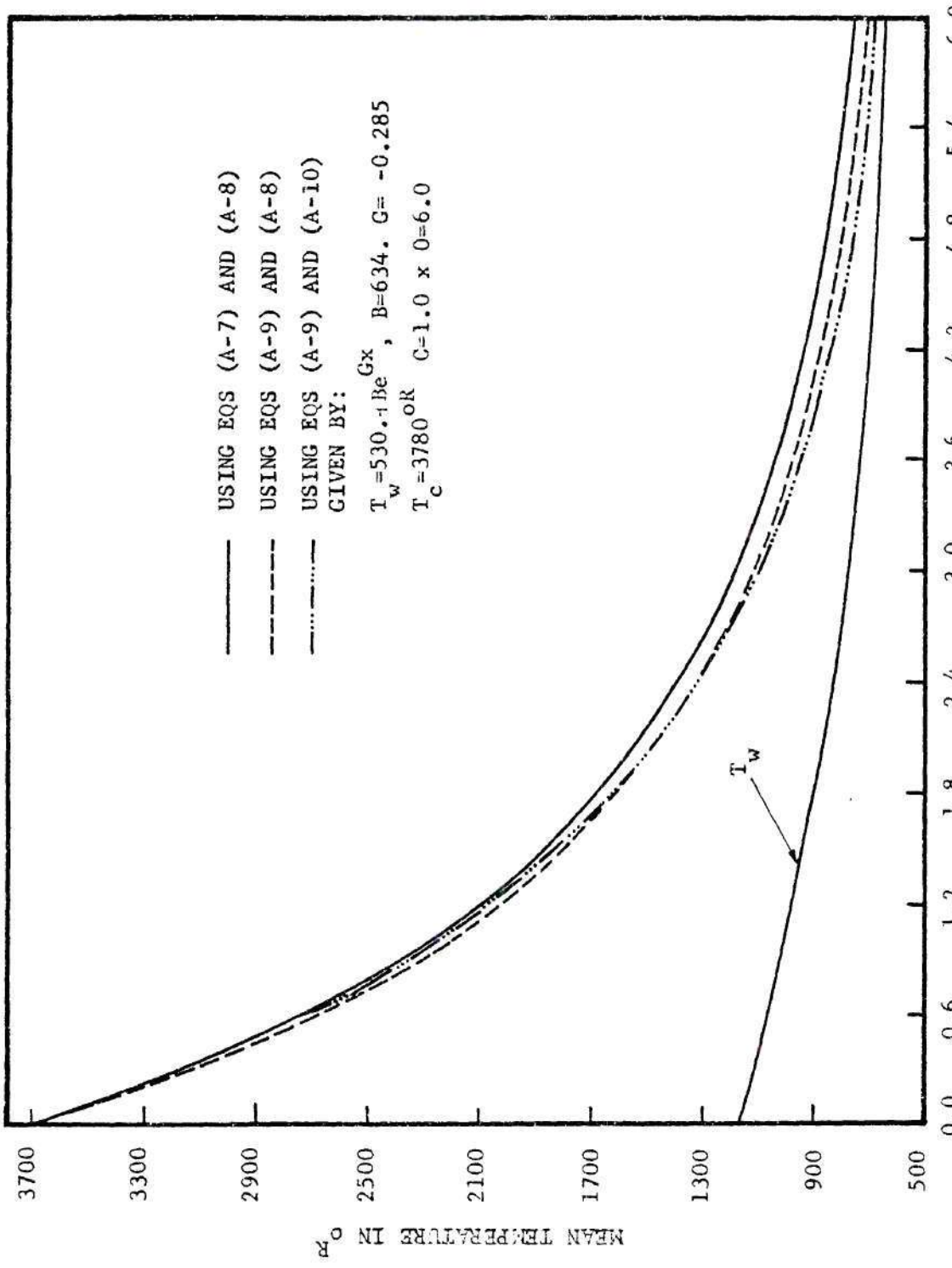

Figure A-3. Mean Temperature Distribution Along the Impedance Tube Axis for a Variable T_w.

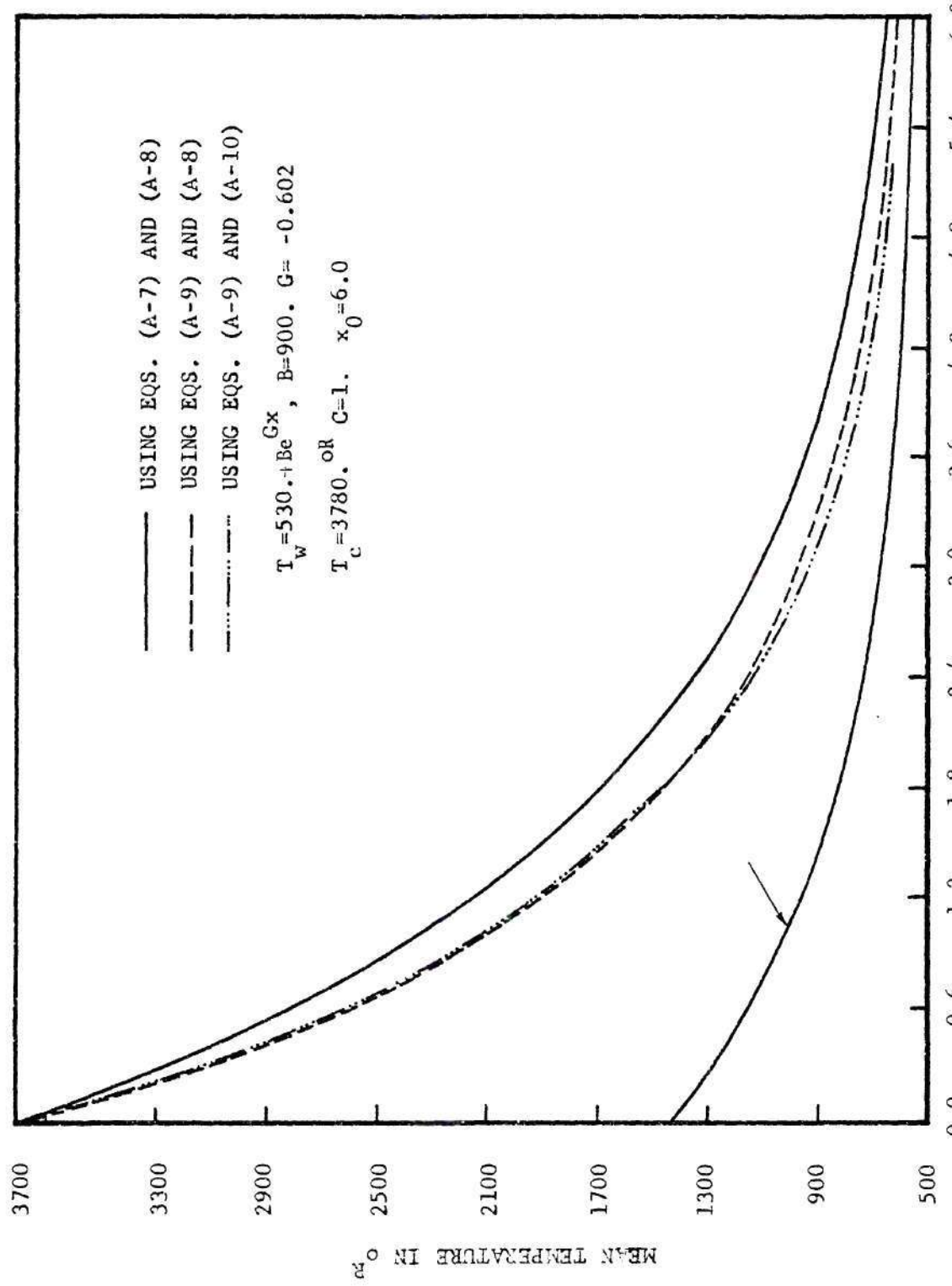

Figure A-4. Mean Temperature Distribution Along The Impedance Tube Axis for a Variable T_w.

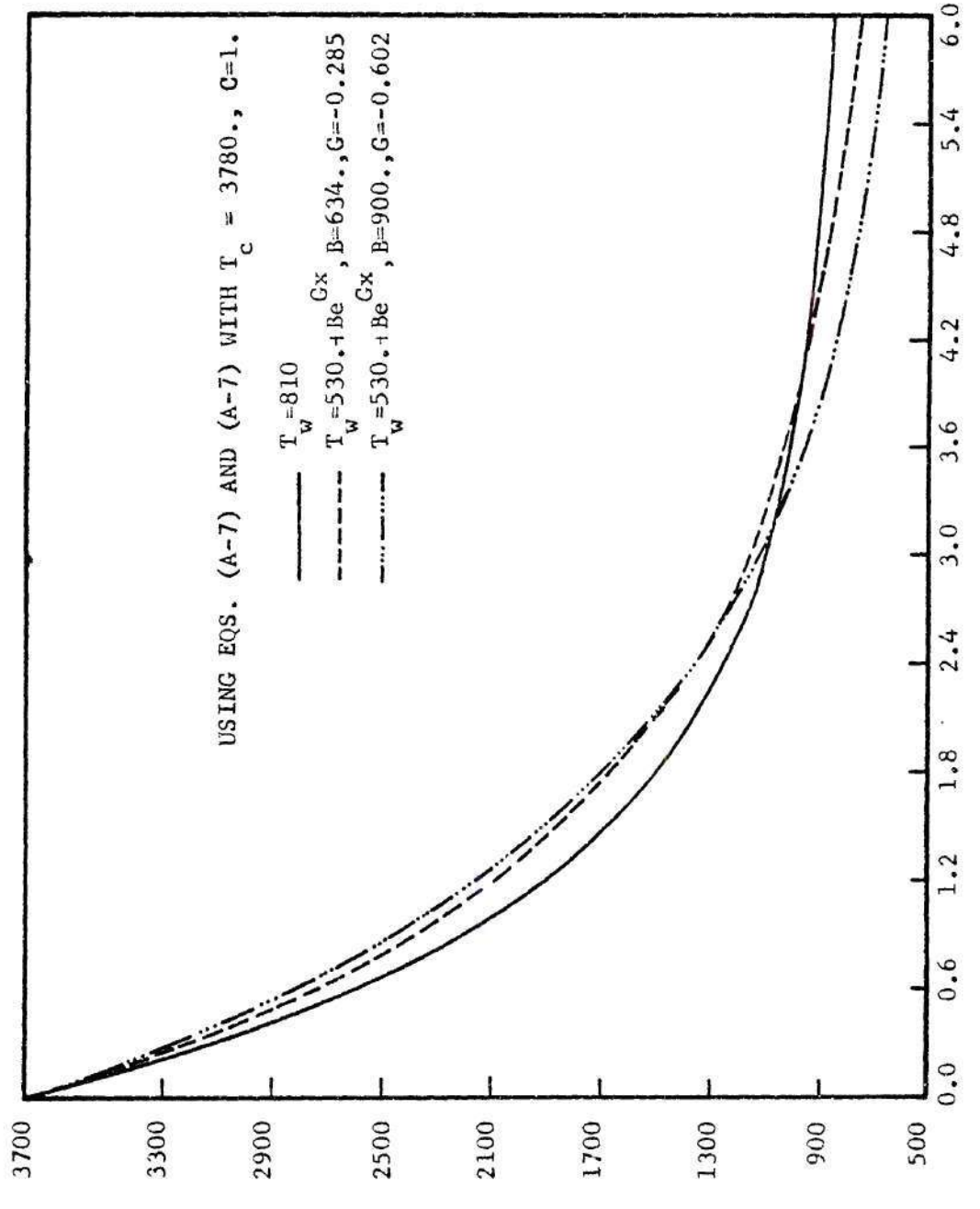

Figure A-5. Comparison of Mean Temperature Distributions Along the Impedance Tube Axis.

the mean temperature profiles which are obtained using Equation (A-11) for wall temperature distribution, i.e., using Sets I and II, respectively, keeping the rest of the parameters the same as in Figure A-2 and using Equation (A-12) in place of Equation (A-9). Figure A-5 presents a comparison of the temperature profiles that are obtained using Equation (A-7) for three different wall temperature distributions. Therefore, Figure A-5 shows the effect of wall temperature distribution over the mean temperature profile in the impedance tube. It is observed from Figure A-5 that the temperature distribution obtained using a constant wall temperature differs considerably from those obtained with variable wall temperatures. Since there is no basis for assuming a constant wall temperature, the wall temperature distributions obtained using Equation (A-11) are probably a better representation in the steady state temperature distribution in the impedance tube.

However, the axial temperature distribution in the impedance tube can not be readily predicted using Equations (A-7) through (A-12), since the heat transfer parameter C involved in these equations is not known. To evaluate the constant C, it is necessary to know the properties of the gas flowing in the impedance tube. Since most of these flow properties are not known reliable approaches for determining the heat transfer parameter C and the mean axial temperature are needed. The resolution of these problems are discussed in the ensuing sections.

Determination of the Mean Temperature Distributions Using Experimental Data

1. Axial, Radial and Weighted One Dimensional Temperature Distributions Using Measured Temperature Data

As mentioned in the introduction, it is possible to measure the temperature at any desired axial location in the impedance tube to obtain the axial temperature distribution. Therefore, a series of tests were conducted and temperature measurements were made at different radial locations, along the length of the tube using Platinum/Platinum 13% Rhodium thermocouples. These measurements show (i.e., see Figure A-6) the presence of a radial temperature gradient along the length of the tube. Therefore, in view of the presence of radial temperature gradient in the tube, the question comes up regarding the best radial location to be used for the measurement of a bulk axial temperature distribution that is consistent with a one dimensional flow model. Since it is difficult to locate such a radial position in the impedance tube, an alternate method is sought to obtain an average or bulk temperature distribution to fit in with the one dimensional flow model. This bulk temperature distribution may be obtained from Equation (A-9), which requires knowledge of the value of C, the heat transfer parameter defined in Equation (A-8). Assuming that Equations (A-9) and (A-12) are valid in each radial location, the values of C are evaluated using the measured temperature data for the corresponding radial locations. The results indicate that the heat transfer parameter C is different for different radial position r of the impedance tube.

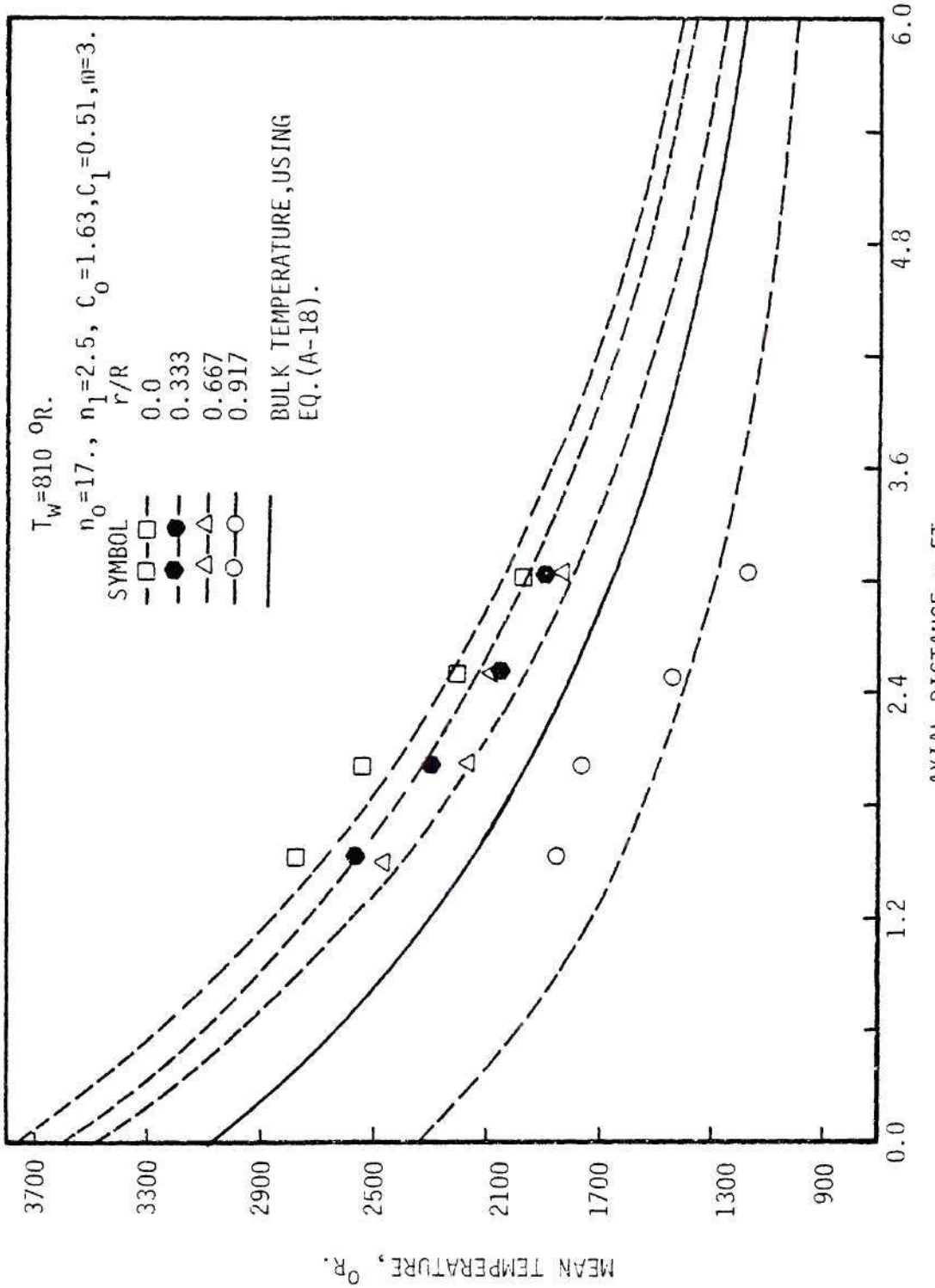

Figure A-6. Axial Variation of Mean Temperature at Various Radial Locations and a Bulk Temperature for Constant Wall Temperature.

Incorporating this radial variation of C, a functional relation is constructed for the steady state temperature, in terms of the axial and radial coordinates of the impedance tube as follows:

$$\bar{T}(x,r) = T_w(x) + \left[(T_c - T_{w_o}) \left(1 - (\frac{r}{R_o})^{n(r)}\right) e^{-(\frac{r}{R_o})^{n(r)}} \right] e^{-\frac{x}{\Lambda(x,r)}} \quad \text{(A-13)}$$

where,

$$\Lambda(x,r) = C(r)[1 + \frac{T_w(x)}{\bar{T}(x,r)}]^{0.68} \quad \text{(A-14)}$$

$$n(r) = n_o e^{n_1\{(\frac{r}{R_o})-1\}} \quad \text{(A-15)}$$

$$C(r) = C_o e^{C_1\{1-(\frac{r}{R_o})^m\}} \quad \text{(A-16)}$$

Using the measured temperature data the parameters n_o, n_1, C_o, C_1 and m are evaluated from a least square fit. The axial temperature distributions obtained at various radial locations using Equation (A-13) are plotted in Figures A-6 through A-8 by dashed lines for different wall temperature distributions. These plots show close agreement with the measured temperature values. Figure A-9 shows the radial variation of mean temperature at various axial locations for different wall temperature distributions.

The main objective of this section is, however, to obtain a bulk axial temperature distribution in the impedance tube which would be consistent with the one dimensional wave structure that is used in

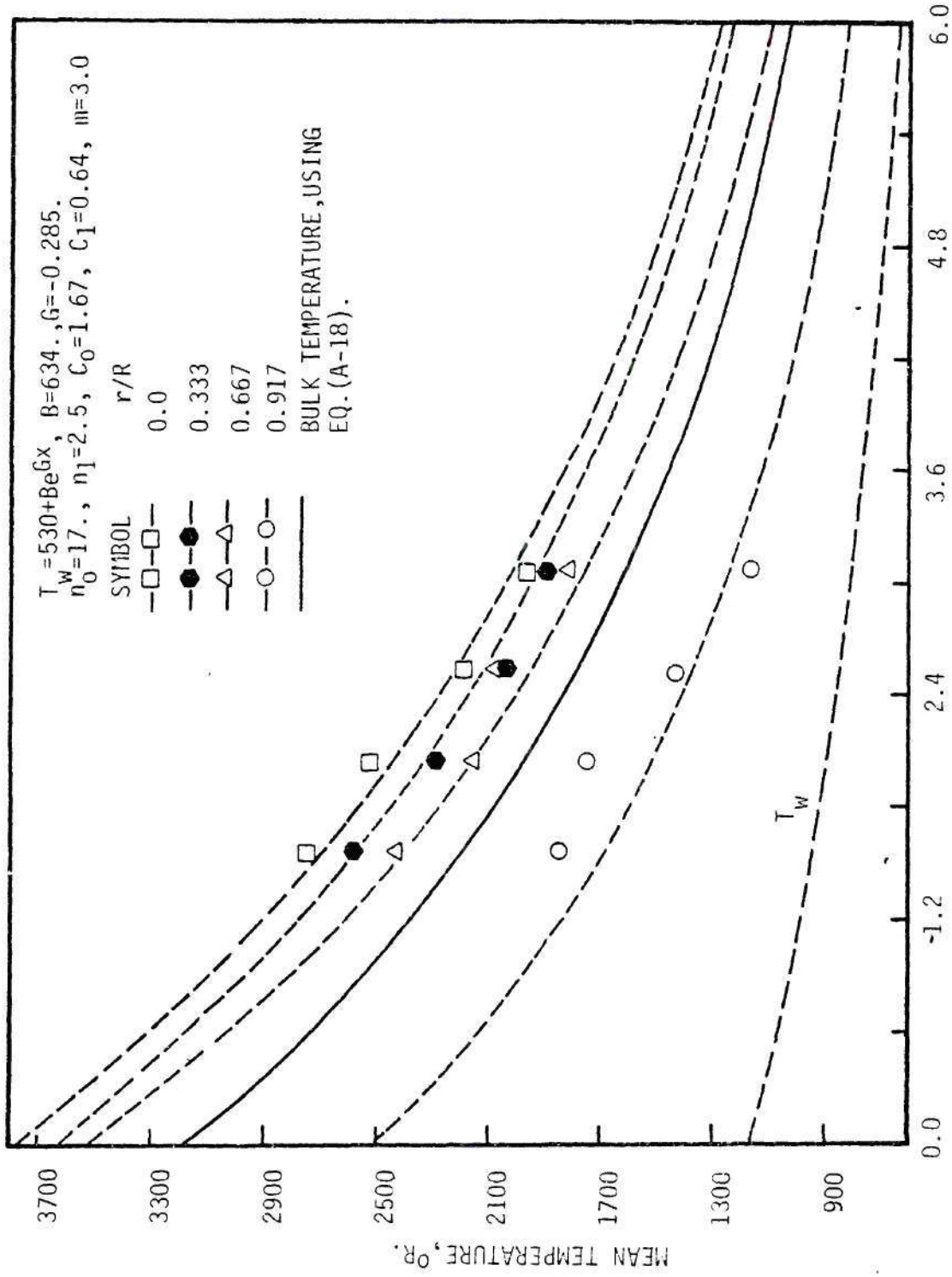

Figure A-7. Axial Variation of Mean Temperature at Various Radial Locations and a Bulk Temperature for a Variable Wall Temperature.

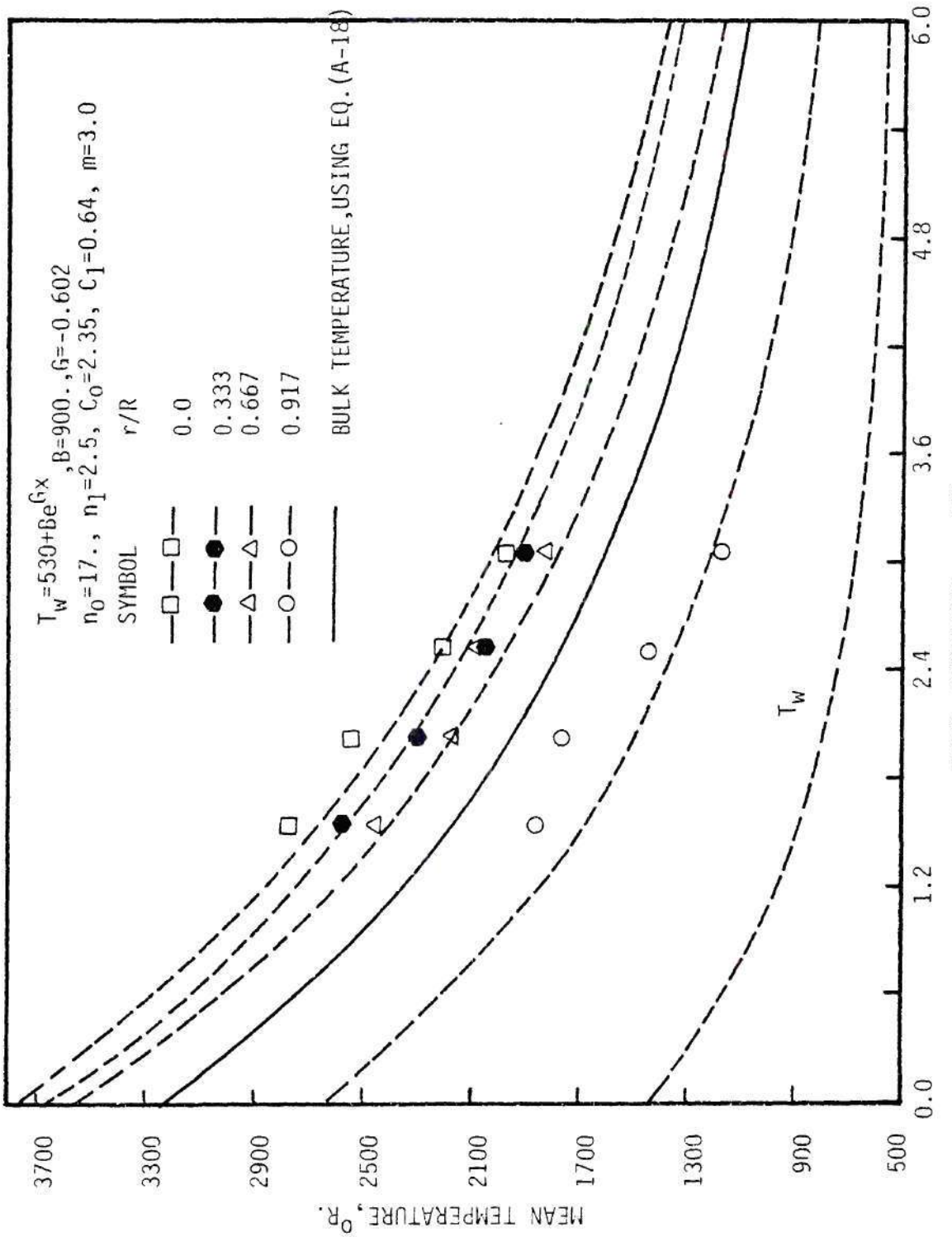

Figure A-8. Axial Variation of Mean Temperature at Various Radial Locations and Bulk Temperature for a Variable Wall Temperature.

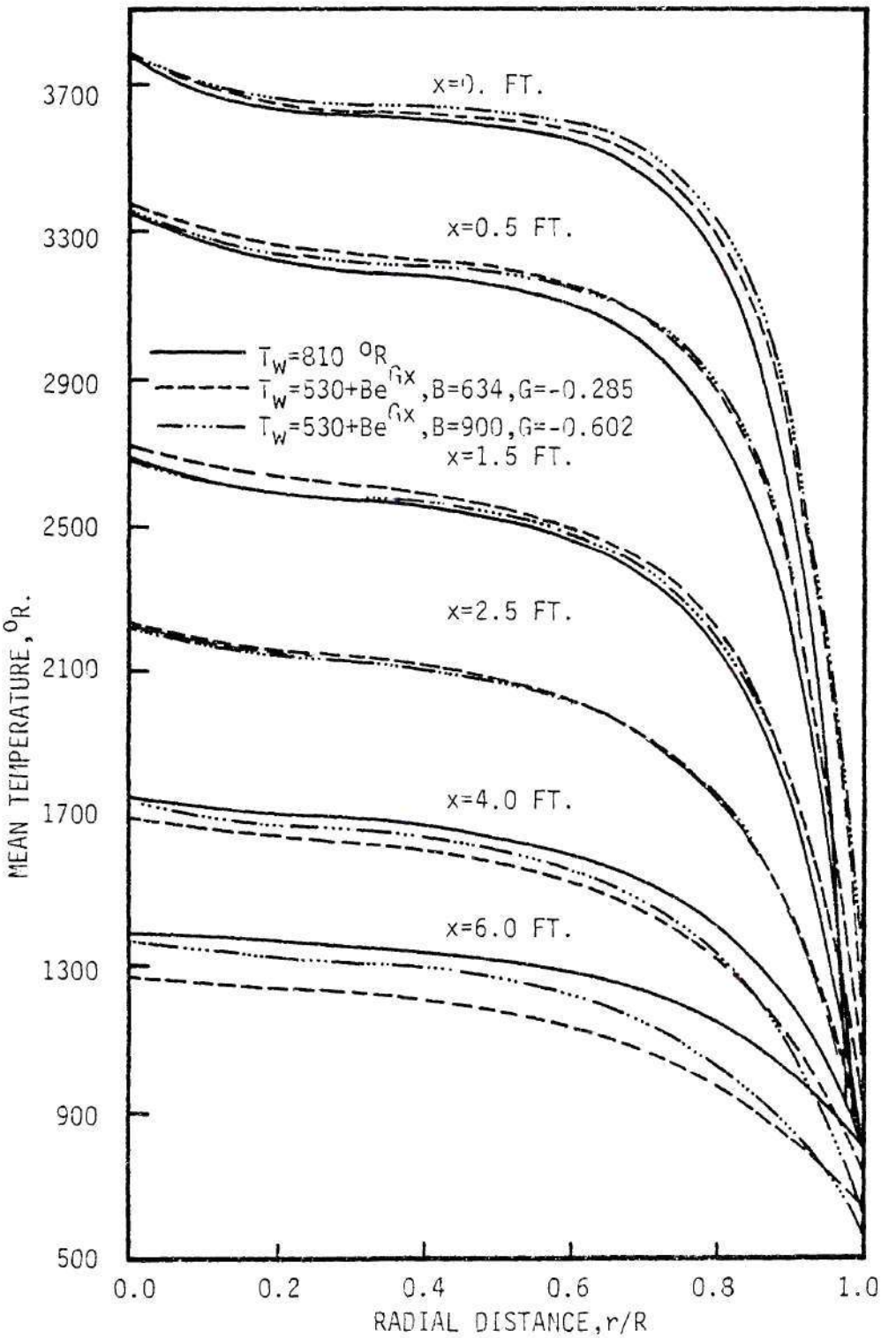

Figure A-9. Radial Variation of Mean Temperature at Various Axial Locations.

the impedance tube measurements. To obtain the bulk temperature an area average of $\overline{T}(x,r)$, using Equation (A-13), is obtained; that is,

$$\overline{T}_A(x) = \frac{1}{\pi R_o^2} \int_o^{R_o} \int_o^{2\pi} \overline{T}(x,r) r \, dr \, d\theta \qquad \text{(A-17)}$$

which reduces to

$$\overline{T}_A(x) = 2 \int_o^1 \overline{T}(x,r) \left(\frac{r}{R_o}\right) d\left(\frac{r}{R_o}\right) \qquad \text{(A-18)}$$

The weighted temperature distributions $\overline{T}_A(x)$ are obtained by integrating Equation (A-18) numerically for various wall temperature distributions and are plotted by solid lines in Figures A-6 through A-8.

2. One Dimensional Axial Temperature Distribution Using Nodal Locations of the Pressure Wave

It is necessary to assure the compatibility of the bulk temperature distribution given by Equation (A-18), with the wave structure in the impedance tube. Hence, an alternate approach is developed to determine the effective axial temperature distribution. In this approach the following simplified expression, similar to Equation (A-12), for the bulk temperature distribution in the impedance tube is assumed.

$$\overline{T}_A(x) = T_w(x) + (\overline{T}_c - T_{w_o}) e^{-\frac{x}{\Lambda}} \qquad \text{(A-19)}$$

where

$$\Lambda = \bar{C}\left[1 + \frac{T_w(x)}{\bar{T}_A(x)}\right]^{0.68} \qquad \text{(A-20)}$$

In Equation (A-19), $\bar{T}_c$ is an average value of $\bar{T}_A(x)$ at $x = o$, evaluated using Equation (A-18). In the present approach the value of the heat transfer parameter $\bar{C}$ is evaluated using measurements of two successive nodal positions x_o and x_1 of the standing pressure wave formed in the impedance tube. The coordinates x_o and x_1 are related to one another by the following expression: (see Figure 2-4)

$$x_1 = x_o + \frac{\lambda(x)}{2} \qquad \text{(A-21)}$$

An average speed of sound for the flow between the positions x_o and x_1 can be obtained from the relation

$$\bar{c}_{av} = \frac{1}{(\lambda/2)} \int_{x_o}^{x_1} [\gamma R\, \bar{T}_A]^{\frac{1}{2}}\, dx \qquad \text{(A-22)}$$

Using the relationship $\bar{c}_{av} = \lambda f$, where f is the frequency of the standing wave in the impedance tube, Equation (A-22) can be rewritten as

$$J\lambda^2 = \int_{x_o}^{x_1} [\bar{T}_A]^{\frac{1}{2}}\, dx \qquad \text{(A-23)}$$

where:

$$J = f/2\sqrt{\gamma R} = \text{constant}$$

substituting the expression for $\bar{T}_A$ into Equation (A-23) and using Equation (A-20), a transcendental equation for $\bar{c}$ is obtained. Once

this equation is solved for $\bar{C}$, the bulk axial temperature distribution in the impedance tube is obtained.

Figures A-10 and A-11 are the plots of x_o and x_1 with respect to frequency for three different propellants, respectively, obtained from the experiments conducted at a chamber pressure of 15 psi. Using these data the bulk temperature distributions are computed and are compared with the temperature distributions obtained using Equation (A-18), (see Figure A-12). It is observed that the effective temperatures computed from the nodal locations of the standing wave structure (Equation (A-23)), are lower than the bulk temperatures deduced from the thermocouple measurements (i.e., see Equation (A=18)). This discrepancy can be attributed to the area weighting (see Equation (A-18)), used to obtain the one dimensional bulk temperature, which need not necessarily be consistent with the one dimensional descriptions of the impedance tube wave structure.

3. Non-Linear Regression Technique to Obtain Axial Temperature Distribution Using Oscillatory Pressure Data

The average axial temperature distribution obtained using nodal locations along the standing pressure wave could, in principle, be used in the evaluation of the admittances of the burning solid propellant samples placed in the impedance tube. However, the accuracy of the temperature distribution depends upon how accurately the positions of the pressure nodes could be located. Since the locations of the pressure transducers in general do not coincide with the locations of pressure nodes, these nodal locations are obtained by extrapolation

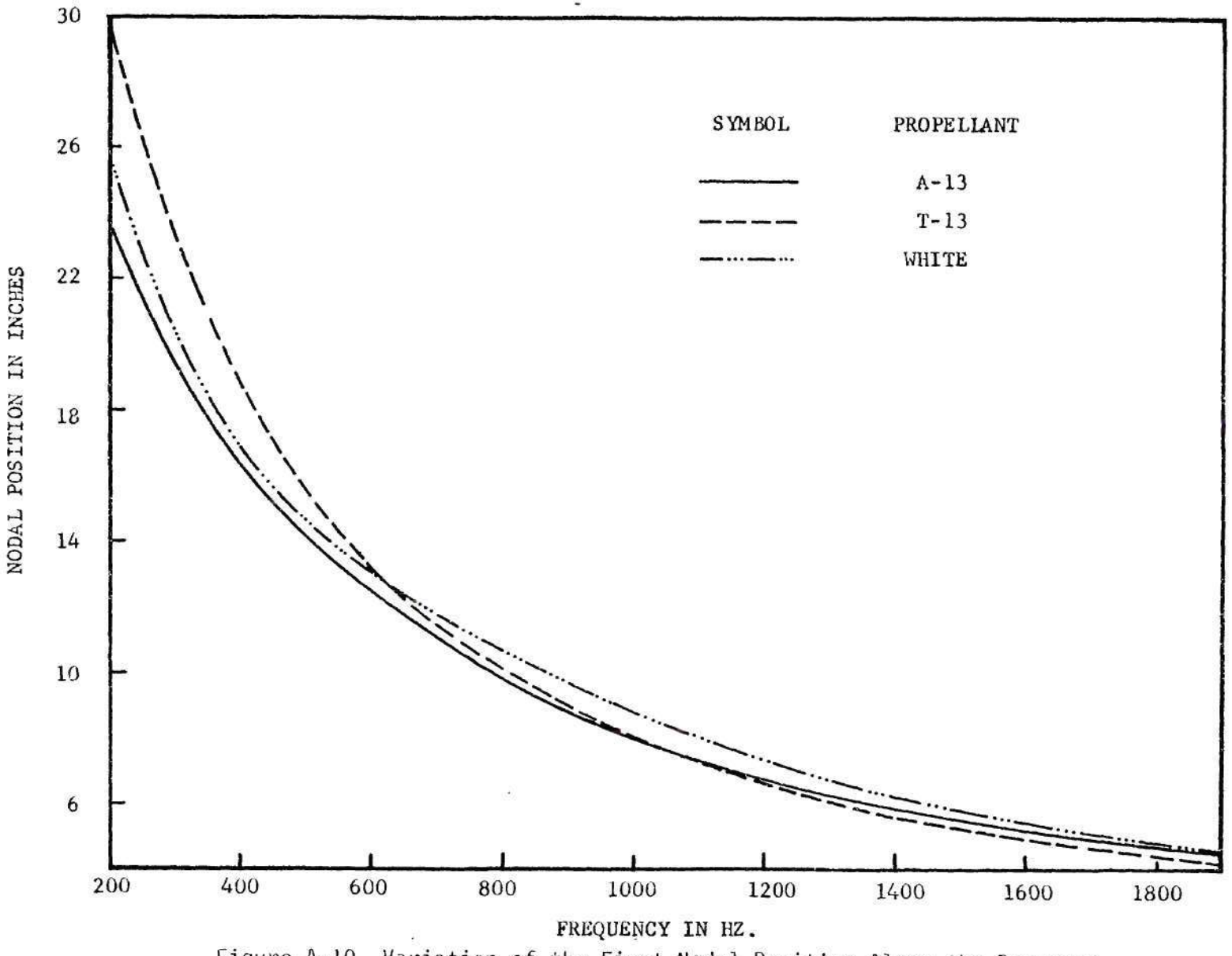

Figure A-10. Variation of the First Nodal Position Along the Pressure Wave with Respect to the Frequency.

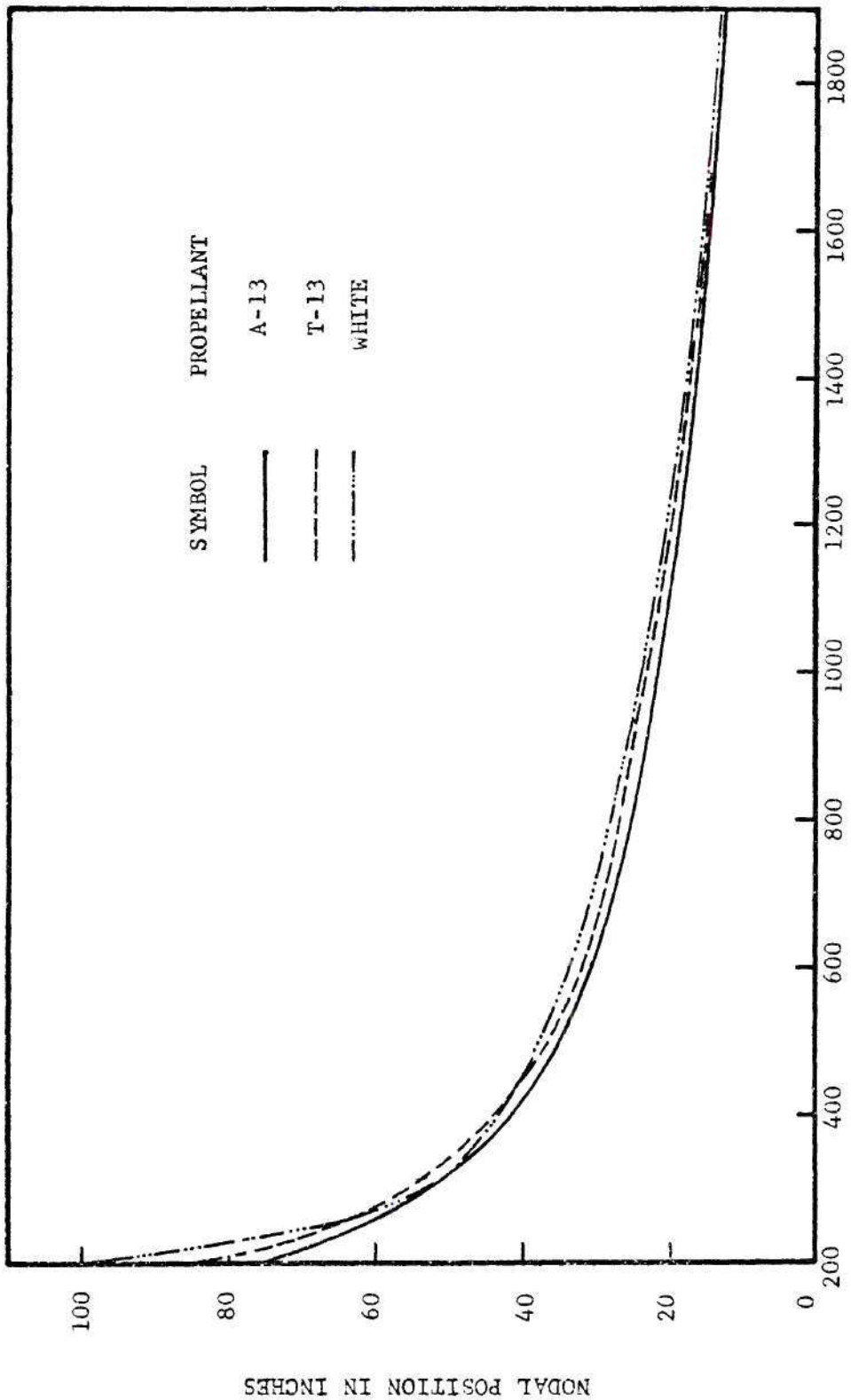

Figure A-11. Variation of the Second Nodal Position Along the Pressure Wave with Respect to the Frequency.

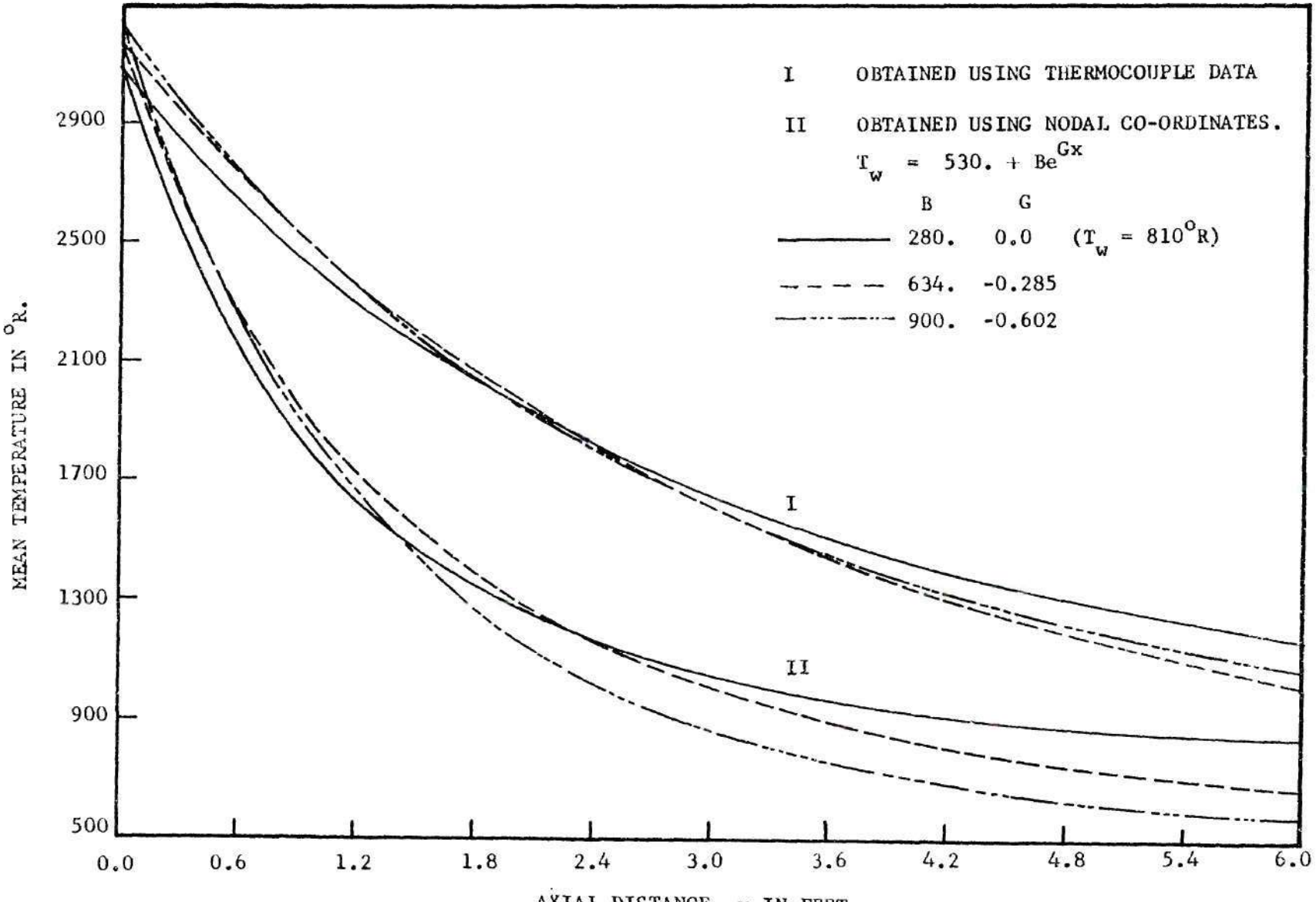

Figure A-12. Comparison of Effective Temperature Distributions Obtained Using Thermocouple Data and Nodal Locations.

of the measured pressure data -- a process which inevitably results in errors in locating these nodes. Hence, an alternate technique which reduces the inaccuracies involved in locating the pressure minima has been developed. This method employs the nonlinear regression technique to determine the constant $\overline{C}$ in Equation (A-20) from the measured amplitude and phase data.[25] The nonlinear regression technique involves determining the value of $\overline{C}$ which provides the best fit between the theoretically predicted wave pattern in the impedance tube and the experimentally measured pressure amplitude and phase data. The best fit is found by determining the value of $\overline{C}$ which minimizes the root-mean-square deviation between the theoretically predicted impedance tube wave structure and the corresponding experimental data. This technique gives a temperature profile which is consistent with the measured wave structure.

To find the minimum root-mean-square deviation, the following function F, which is a measure of the error, is minimized:

$$F = \sum_{i=1}^{n} (E_i - T_i)^2 \qquad \text{(A-24)}$$

In Equation (A-24), E_i represents an experimentally measured quantity (i.e., amplitude or phase) at location x_i and T_i is the corresponding theoretically predicted quantity which depends among other parameters, upon the constant $\overline{C}$. If a minimum of F with respect to $\overline{C}$ exists, then the gradient of F must vanish at that minimum and the following relationship holds:

$$\frac{dF}{d\bar{C}} = -2 \sum_{i=1}^{n} \left[(E_i - T_i) \frac{dT_i}{d\bar{C}} \right] = 0 \qquad \text{(A-25)}$$

A Newton-Raphson iterative scheme is used to obtain a solution of Equation (A-25), utilizing a linearized version of this equation which involves the expansion of T_i in a first order Taylor series with respect to the parameter $\bar{C}$. The resulting linear algebraic equation can be expressed in the following form:

$$\sum_{i=1}^{n} (E_i - T_i^m) \left.\frac{dT}{d\bar{C}}\right|_{(i,m)} = \left[\bar{C}^{m+1} - \bar{C}^m \right) \sum_{i=1}^{n} \left.\left(\frac{dT}{d\bar{C}}\right)\right|^2_{(i,m)} \Bigg] \qquad \text{(A-26)}$$

where m represents the m^{th} iteration.

Equation (A-26) can be rewritten as follows:

$$A^m[\bar{C}^{m+1} - \bar{C}^m] = B^m$$

$$\bar{C}^{m+1} = \bar{C}^m + B^m/A^m \qquad \text{(A-27)}$$

where

$$A^m = \sum_{i=1}^{n} \left(\frac{dT}{d\bar{C}}\right)^2_{(i,m)}$$

and (A-28)

$$B^m = \sum_{i=1}^{n} (E_i - T_i^m) \left.\frac{dT}{d\bar{C}}\right|_{(i,m)}$$

Equation (A-28) is a linear algebraic equation for the unknown $\overline{C}^{m+1}$ and it can be readily solved once A^m and B^m are computed. The computation of these elements requires the determination of the derivative $\left.\frac{dT}{d\overline{C}}\right|_{(i,m)}$. Since these derivatives cannot be determined analytically, numerical values for these derivatives are obtained using finite difference methods.

Computations were performed at a number of frequencies for the propellant A-13, using the oscillatory pressures measured during the tests conducted at low chamber pressures and the corresponding effective axial temperature distribution was obtained. Such a temperature distribution is plotted in Figure A-13 where it is compared to that obtained using the measured nodal locations along the standing wave for the same propellant, A-13. Figure A-13 shows close agreement between the temperature distributions obtained by both methods. Therefore, the non-linear regression technique is used for the purpose of getting the mean temperature distribution, which gives the freedom to place the pressure transducers at any locations along the axis of the impedance tube.

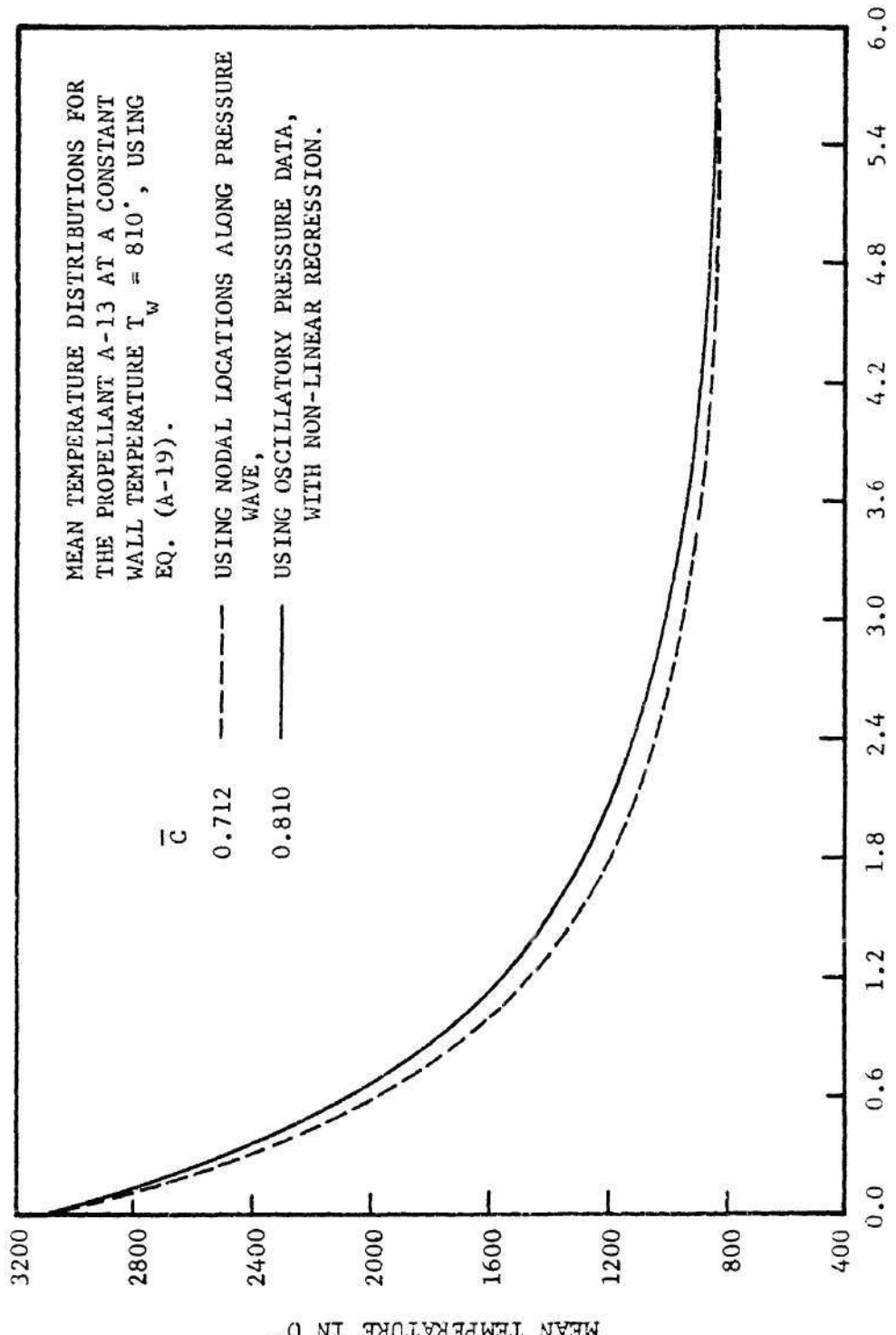

Figure A-13. Mean Temperature Distributions for the Propellant A-13 at a Constant Wall Temperature Using Eq. (A-19) by Two Different Approaches.

REFERENCES

1. Zinn, B. T., Salikuddin, M., Daniel, B. R., and Bell, W. A., "Solid Propellant Admittance Measurements by the Driven Tube Method," AFOSR-TR-75-1531, August, 1975.

2. Janardan, B. A., Daniel, B. R., Bell, W. A., and Zinn, B. T., "Measurements of Reactive Gaseous Rocket Injector Response Factors," Presented at the Spring Meeting Central States Section. The Combustion Institute Lewis Research Center, March 28-30, 1977.

3. Lawrie, W. E. "Development of new Sound Absorbing Materials for Noise Suppressors. Part I: Development of Equipment for Evaluating Acoustical and Durability Properties of Sound-Absorbing Materials at Elevated Temperatures," 1959, W.A.D.C., Technical Report, No. 58-460.

4. Christie, D. R. A., "Measurement of the Acoustic Properties of Sound Absorbing Material at High Temperatures," 1976, Journal of Sound and Vibration 46, 347-355.

5. Price, E. W., "Experimental Solid Rocket Combustion Instability," Tenth Symposium (International) on Combustion, Combustion Institute, pp. 1067, 1965.

6. Williams, F. A., "Combustion Theory," Addition-Wesley Publishing Co., Inc., Palo Alto, Calif., 1965, pp. 220-226.

7. Scott, R. A., "An Apparatus for Accurate Measurement of the Acoustic Impedance of Sound Absorbing Materials," Proceedings of the Physical Society, Vol. 58, 1946, pp. 253-264.

8. Chemical Propulsion Information Agency, T-Burner Manual, CPIA Publication No. 191, Silver Spring, Maryland, November, 1969.

9. Perry, E. H., "Investigations of the T-Burner and its Role in Combustion Instability Studies," Ph.D. Thesis, Daniel and Florence Guggenheim Jet Propulsion Center, California Institute of Technology, Pasadena, California, May, 1970.

10. Derr, R. L., "Evaluation of a Variable Area T-Burner for Metalyzed Propellants," Lockheed Propulsion Company Technical Report AFRPL-TR-72-97, February, 1973.

11. Price, E. W., Mathes, H. B., and Crump, J. E., "Evolution of Laboratory T-Burners for Study of Solid Propellant Combustion Instability," Naval Weapons Center Technical Note 608-109 (Revision 1), China Lake, Calif., August 1972.

12. Oberg, C. L., Ryan, N. W., and Baer, A. D., "A Pulsed T-Burner Technique," AIAA Journal, Vol. 6, No. 5, May 1968, pp. 920-921.

13. Brown, R. S., and Erickson, J. E., "Measuring Combustion Response by a Forced Oscillation Method," AIAA Paper No. 72-1054, presented at the AIAA/SAE 8th Joint Propulsion Specialist Conference, New Orleans, La., November 29 - December 1, 1972.

14. Barrere, M., Nadaud, L., and Thuillier, J. N., "Survey of ONERA and SNPE Work on Combustion Instability in Solid Propellant Rockets," AIAA Paper No. 72-1052, presented at the AIAA/SAE 8th Joint Propulsion Specialist Conference, New Orleans, La., November 29 - December 1, 1972.

15. Fonner, S. N., Hudson, R. L., and Nall, B. H., "Admittance Measurements of Solid Propellants by an Acoustic Oscillator Technique," AIAA Journal, Vol. 2, No. 6, June 1964, pp. 1123-1129.

16. Kuentzmann, Paul and Lengelle, Guy, "Recent Research Activity at ONERA on Combustion Instability and Erosive Burning," 1977 Joint AFOSR/AFRPL, Rocket Propulsion Meeting, Lancester, California.

17. Scott, R. A., "An Apparatus for Accurate Measurement of the Acoustic Impedance of Sound Absorbing Materials," Proceedings of the Physical Society, Vol. 58, 1946, pp. 253-264.

18. Bell, W. A., "Experimental Determination of Three-Dimensional Liquid Rocket Nozzle Admittances," Ph.D. Thesis, School of Aerospace Engineering, Georgia Institute of Technology, Atlanta, Georgia, July 1972.

19. Zinn, B. T., Daniel, B. R., Janardan, B. A., and Smith, A. J., Jr., "Damping of Axial Instabilities by Minuteman II, Stage III, Minuteman III, Stage III, Exhaust Nozzles," Air Force Rocket Propulsion Laboratory Interim Report, AFRPL-TR-72-71, August 1972.

20. Zinn, B. T., Daniel, B. R., Bell, W. A., and Salikuddin, M., "Solid Propellant Admittances Measurements by the Driven Tube Method," AFOSR-73-2571, August 1974.

21. Zinn, B. T., Daniel, B. R., Salikuddin, M., and Bell, W. A., "Determination of Response of Burning Solid Propellants by the Impedance Tube Method," AIAA Paper 75-227, Presented at the AIAA 13th Aerospace Sciences Meeting, Pasadena, Calif., January 20-22, 1975.

22. Bertz, D. R., "A Simple Equation for Rapid Estimation of Rocket Nozzle Convective Heat Transfer Coefficients," Jet Propulsion, January, 1957.

23. Rubin, S., "Review of Mechanical Impedance and Transmission Matrix Concept," J. of Acoustical Society of America, Vol. 4, No. 5, May 1967.

24. Pfahl, Robert, C., Jr. and Mitchel, Barry, J., "Nonlinear Regression Methods for Simultaneous Property Measurement," AIAA Journal, Vol. 8, No. 6, June 1970.

25. Zinn, B. T., Salikuddin, M., Daniel, B. R., and Bell, W. A., "Solid Propellant Admittance Measurements by the Driven Tube Method," AFOSR-73-2571, August, 1976.

26. Zinn, B. T., "Longitudinal Mode Acoustic Losses in Short Nozzles," Journal of Sound and Vibration, 1972, 22(1), pp. 93-105.

27. Richard, A., Dobbins, S., Temkin, "Measurement of Particulate Acoustic Attenuation," AIAA Journal, Vol. 2, No. 6, 1966.

28. Samuel Temkin, Richard A. Dobbins, "Attenuation and Dispersion of Sound by Particulate Relaxation Process, "The Journal of the Acoustical Society of America, Vol. 40, No. 2, 1966.

29. Zinn, B. T., Daniel, B. R., Salikuddin, M., and Bell, W. A., "Determination of the Acoustic Responses of Solid Propellants by the Impedance Tube Method," presented at the Twelfth JANNAF Combustion Meeting, Newport, R.I., August 11-15, 1975.

30. Doebelin, Ernest, O., "Measurement Systems: Application and Design," McGraw-Hill, Inc., 1966, Section 6.

31. Bell, W. A., Craig, J. I., and Strahle, W. C., "Study of Unsteady Combustion of Heterogeneous Solid Propellants by Analysis of Acoustic Emissions," paper presented at 15th AIAA Aerospace Sciences Meeting, Los Angeles, California, January 24-26, 1977.

32. Coates, R. L., Horton, M. D., and Ryan, N. W., "T-Burner Method of Determining the Acoustic Admittance of Burning Propellants," AIAA Journal, Vol. 2, No. 6, June 1964.

33. Feiler, C. E., and Heidmann, M. F., "Dynamic Response of Gaseous Hydrogen Flow System and its Application to High Frequency Instability," NASA TN D-4040, June, 1967.

34. Schlichting, Hermann, "Boundary-Layer Theory," McGraw-Hill Book Company.

VITA

Mohammed Salikuddin was born in Baripada, India on March 29, 1946. He first graduated in 1964 with a Bachelor of Science degree with Physics Honours from Utkal University. Then he joined Indian Institute of Technology, Kharagpur in 1964 in Aeronautical Engineering Department and graduated in 1968 with a Bachelor of Technology Degree with Honours. Then he was employed as an Associate Lecturer in the Department of Aeronautical Engineering, Indian Institute of Technology, Kharagpur until 1972. During this period, while he was a full time employee he completed his Master of Technology degree from the same Institute in 1972. Since then he has been attending the School of Aerospace Engineering of the Georgia Institute of Technology.